Understanding the evolution of galaxies using a novel definition of the Green Valley

James Angthopo

A dissertation submitted in partial fulfillment

of the requirements for the degree of

Doctor of Philosophy

of

University College London.

Department of Space and Climate

University College London

December 20, 2021

I, James Angthopo, confirm that the work presented in this thesis is my own. Where information has been derived from other sources, I confirm that this has been indicated in the work.

Abstract

Green Valley (GV) galaxies are essential to the understanding of galaxy formation and evolution, which, in turn, is necessary to understand our Universe. In this thesis we explore a novel way to define the GV, using the 4000Å break strength, which is more resilient to dust and less model dependent, thus carrying less inherent systematics compared with traditional methods. This method finds a cleaner stratification between each GV region; divided into lower (lGV), middle (mGV) and upper (uGV) green valley. We find comparable results between novel (4000Å break) and traditional (dust-corrected colour) methods of selecting GV galaxies - i.e., similar fractions of AGN galaxies and matching transition timescales. However, a more in-depth analysis finds nuanced differences, such as more homogeneous stellar population properties between different types of galaxies in the novel definition. Furthermore, we find results suggesting a more rapid transition from Blue Cloud (BC) to GV than from GV to Red Sequence (RS). This thesis also tests how well hydrodynamical simulations, EAGLE and IllustrisTNG (TNG100), are able to reproduce the observed trend on the 4000Å break vs stellar mass plane. We find both simulations match the location of the BC, however produce the RS and GV at a higher 4000Å break value than observations. Comparison of GV galaxies between observation and simulations find both simulations to overproduce quiescent fractions. As this is mostly seen for $M_\star \gtrsim 10^{10.5}\,M_\odot$, it is assumed mostly to be due to the subgrid physics of AGN feedback. Finally, we also compared "Twin" galaxies, having similar overall properties such as morphology, colour, stellar mass, etc, but one hosts an AGN and the other doesn't. From this, we find AGN galaxies to be generally more evolved and metal rich than their non-AGN "twin".

Impact Statement

The work I have carried out during my PhD provides an alternative path from which we can improve our understanding of galaxy evolution. This thesis proposes a novel way to select galaxies that are transitioning from highly star forming to quiescent (i.e. no longer forming stars). The main advantage of this novel method is its resilience to dust and is model independent. The dust content of the galaxy changes its appearance such that the observables may suggest older and more metal rich populations with respect to the real properties, thus introducing significant degenerates. The studies outlined in this thesis explore the properties of galaxies that are in transition, selected using this novel method. This is then compared with the traditional method to test for similarities and differences. Additionally, we also analyse how well the state-of-the-art hydrodynamical simulations can reproduce the observational trends for this new way of defining and selecting transitional galaxies. Therefore, this definition is impactful in two different ways. Firstly, the new method can be effortlessly implemented in upcoming surveys and observations from facilities such as James Webb Space Telescope (JWST), WEAVE, Dark Energy Spectroscopic Instrument (DESI), etc. Secondly my work makes use of both observation and simulation data, thus providing the simulation community with an alternate avenue upon which they can constrain and improve their models. The improvements to simulations in turn will help the observational community to better understand the physical mechanisms associated to galaxy formation and evolution. All the work outlined in this thesis have either been published, after peer review, or is under peer review in a well established journal, MNRAS. My work has been well received and cited by researchers in the field of galaxy formation and evolu-

tion. Finally, the work produced during my PhD has also been presented in multiple conferences across Europe and US.

My work directly deals with improving our understanding of galaxy evolution. Therefore, such information can be very useful beyond academia, as many people are interested in the field of Astrophysics, regardless of their background. Better understanding of galaxy formation and evolution can be used in outreach programmes or TV documentaries such as “Wonders of the Universe” and “Stephen Hawking’s Universe” to attract the new generation of astronomers and astrophysicists. Finally, my work consists of using large volumes of data, thus exploiting different types of statistical analysis. Hence, the methods used in this thesis can be useful to a wider audience in the era of “Big Data”.

Acknowledgements

This work has been supported by the UK Science and Technology Facilities Council (STFC) PhD studentship.

Firstly, I would like to thank my supervisor Dr. Ignacio Ferreras, for not only being an amazing supervisor but also being a great mentor in general. I am grateful for the numerous opportunities you provided, through multiple collaborative projects. Without your unwavering support, especially during the tough times, the completion of this thesis would not have been possible. Finally I would like to thank you for making sure my stay in Tenerife went as smoothly as possible.

Secondly, I would like to thank all the staff members at MSSL for all the support that was readily provided to me, especially Prof. Daisuke Kawata and Ms. Philippa Elwell for helping me resolve the many administrative issues I faced. I would also like to express my gratitude to the IAC for hosting and offering me a space to carry out my research, and their administrative staff for helping my transition from UK to Spain. Within the IAC, I would like to express my appreciation to the TRACES and Theory groups for letting me attend and present in their meetings, and participate in the many discussions that occurred within.

I am thankful to the students of the MSSL group for making my first year of PhD a joyous time. I would like to show my appreciation to the Cranleigh Crew (Sam and Matt) for sharing the house together, filled with many eventful nights and weekends. The movie nights and many debates within the house was a breath of fresh air and a break I needed at the end of each work day. I am also very appreciative to Brian and Mónica (my academic sister aka hermaníta) for keeping in touch with me after my move. It was also great to spend time with both of you in

Tenerife, trying to show you around with the little knowledge I had of the Island.

At the IAC, I would like to show my appreciation to the many students who made me feel welcome at the institute and made sure my lunch times were never boring and filled with interesting conversations. Within the students I would like to thank Núria for volunteering to help me when I first arrived at Tenerife and for introducing me to other students at the IAC. Thank you for all the help you provided me with finding accommodation and my Spanish. Thanks to the "Memetastic" group for the constant source of memes and laughter. Also thank you to the Russian Rollercoaster group for being there after the pandemic and the many dinners at La Bourmet; I will miss the sweet potatoes and "tres pimientos" sauce (R.I.P, the sauce will be missed but never forgotten). I am especially thankful to Carlos for being a great friend and always being there when I needed someone to talk to. Also, thanks a lot for helping me to set everything up when I moved houses. I would also like to thank my family for all their support and providing me with the opportunity to pursue a career that I am passionate about.

Finally I would like to thank Rashi for not only being there in my times of need but also being there to celebrate the good times. I appreciate the constant support and encouragement given to me when I was feeling anxious and stressed. I am grateful for the many sound advice you gave to me. Thank you for putting up with my stubbornness and my "unique" sense of humour. Thank you for making my PhD experience as amazing as it has been.

Contents

List of Figures

List of Tables

Chapter 1

Introduction

Throughout history there have been constant efforts to better our understanding of galaxy formation and evolution. Much progress has been made, in multiple avenues, however there are still many unanswered questions, one key question being the quenching of star formation.

The understanding of galaxy evolution, therefore quenching of star formation, will eventually help us to better understand our Universe. We believe our Universe consists mainly of three components (i) baryons (ii) dark matter (DM) and (iii) dark energy (DE). Baryons usually refer to observable matter, which is considered to make up 5% of the Universe. The vast majority of the cosmic budget is in the form of dark matter and dark energy. We have yet to directly observe dark matter, as one hypothesis suggests these are weakly interacting massive particles (WIMPs), or dark energy. While we have not observed dark matter or energy directly, we have inferred them from observations, i.e., the existence of DM from the relation between galactic rotational velocity and their radii and DE are used to explain the acceleration of expansion of the Universe.

1.1 Galaxy formation

There are many steps to galaxy formation and evolution. Below is a list of some of the physical processes which is deemed important to galaxy formation and evolution, where most of the information are taken from Mo et al. (2010) and Ferreras (2019).

1.1.1 Gravitational instability

The initial conditions of the Universe are thought to be homogeneous and isotropic, however had such conditions remained unchanged, there would be no structure formation. Therefore, the dominant hypothesis suggests quantum fluctuations to produce instability at the beginning of the Universe. This instability destroys both homogeneity and isotropy of the Universe causing dense clusters to form, which have an increased gravitational pull. This causes a positive feedback effect that further increases the density and gravity in these regions. While gravity in some areas increases, more and more matter is accreted creating under-dense regions, where the matter is pulled from. Note such effects are thought to grow exponentially, formulated as $\delta \propto e^t$, for galactic scales, while on cosmological scales, this growth rate of the density is described as $\delta \propto t^\alpha$, due to the expansion of the Universe, where $\alpha > 0$ usually. The values of the parameters are normally determined/constrained through cosmological modelling.

1.1.2 Gas Cooling

Owing to the gravitational instability, regions of the Universe become dense enough such that cooling effects, introduced by bremsstrahlung emission, atomic excitation and de-excitation, and recombination become important. The temperature of the halo usually determines which of these effects are in place to cool the gas. Furthermore, the rate of cooling is heavily dependent on the composition of the gas (Sutherland and Dopita, 1993), as hydrogen and helium act as inefficient coolants, while gas with metals tend to cool faster. Once the over-dense region cools enough, a large quantity of gas can flow in. This eventually leads to the build-up of molecules, which are fundamental to the transformation of gas into stars. Eventually, such behaviour will lead to the formation of proto-galaxies, surrounded by dark matter halos. In addition, the formation of disc galaxies is thought to arise due to the conservation of angular momentum of the infalling gas during this phase of galaxy formation.

1.1.3 Star Formation

Further cooling of gas in dark matter halos leads to additional infall of gas, where after an extended period of time, the gas will lose energy through photon emission or hydro-processes, whereas DM only loses energy through rare collisions. This causes the collapse of gas under its own gravity and DM's pull, leading to a rapid increase in density and temperature. With the presence of effective cooling, this becomes a runaway process, where eventually the gas starts fragmenting and clumping together, which eventually produces pre-stellar cores. These processes can occur in similar regions, leading to the formation of a galaxy. Note, while large efforts have been made to study such topics, fundamental questions remain unanswered. One such area of research regarding star formation is the initial mass function (Salpeter, 1955; Kroupa, 2001, 2002; Chabrier, 2003), which determines the number of stars with different stellar mass produced at the initial formation of the system.

Furthermore star formation can be categorised into two groups. The first state of star formation is termed the self-regulated star formation, which occurs in large areas of the galaxies, i.e. the disc of galaxies. The second state is known as star bursts, which occurs in a dense, small region of galaxies, i.e. the centre of galaxies, where there is a large accumulation of gas.

1.1.4 Feedback processes

Note at the infant stages of unravelling the mysteries of the Universe, it was thought that the gas cooled efficiently, and stars formed, where eventually enough stars would form to create a galaxy. However, such prediction produced large disagreement with the observations, that reveal an abundance of hot gas and relatively low amount of cold gas and stars. Therefore, there must be some physical mechanism that is heating up the gas, hence preventing stars from being formed so efficiently.

A possible explanation invokes feedback processes. In this subsection we will discuss the two prominent feedback mechanisms that are thought to be the root cause of lack of stars/cool gas in the local Universe.

1.1.4.1 Supernovae

One such mechanism is known as supernova feedback, where stars at the end of their life explode, releasing a large quantity of energy into their surroundings. This energy will heat up the gas in the vicinity as well as eject it from the galaxy; the ejected material is known as a galactic wind. Both heating and ejection will quench star formation in galaxies as they will no longer have sufficient cool gas from which to continue forming new stars (Dekel and Silk, 1986). Supernovae are largely classified into Type Ia and Type II. Type II supernovae occur at a shorter timescale compared to Type Ia supernovae and are more prominent in late-type galaxies (LTGs), due to short lived massive stars. In such an event, there is a violent core collapse, where most of the iron remains trapped within the core as a neutron star or a black hole. In contrast, Type Ia supernovae are found in both LTGs and early-type galaxies (ETGs). These occur due to low mass binary systems $M_\star \lesssim 8\,M_\odot$, where a white dwarf accretes matter from a companion star in a binary system steadily increasing its mass. If the mass of the star reaches above the Chandrasekhar limit ($M_\star = 1.44\,M_\odot$) the star will collapse causing a supernova. This will release a large amount of Fe into the interstellar medium (ISM). However, this process typically takes longer than Type II supernova owing to the presence of a white dwarf. Note, the frequency and type of supernovae are strongly dependent on the initial mass function (IMF), which remains a heavily debated topic. Such mechanisms are sufficient to explain the lack of cool gas or low efficiency in the conversion of gas into stars, especially in moderate to low mass galaxies, however for more massive galaxies other physical mechanisms are necessary to explain the observations.

Via the study of a galaxy's chemical composition, we are better able to understand not only their chemical enrichment history (CEH), but also the types of supernovae they have experienced. Type II and Ia supernovae not only vary in timescales, but they differ in the elements they release into the ISM. The core collapse, Type II, supernovae mostly release α elements, thus increasing the amount of Mg in the ISM. In contrast, Type Ia supernovae, will release large quantities of Fe into the ISM. Therefore the analysis of abundance ratio between these two el-

ements, will enable us to infer the CEH of the galaxy. For example high [Mg/Fe] implies very little Type Ia supernovae/high occurrence of Type II supernovae. In contrast, low [Mg/Fe] suggests a higher incidence of Type Ia supernova, therefore a different CEH.

1.1.4.2 AGN feedback

For high mass systems, we need processes that are more energetic and affect larger areas. One such mechanism proposed to explain the lack of stars/cold gas in massive galaxies is the presence of active galactic nuclei (AGN). Every galaxy has a super-massive black hole (SMBH) at its centre, which is believed to co-evolve along with its host galaxy (Somerville et al., 2008), due to it accreting large amounts of gas from its surroundings. This in turn causes the presence of AGN activity, which generally releases a large quantity of energy along a perpendicular direction to the spin of the super massive black hole (SMBH). Furthermore, the energy from AGN can heat or eject the surrounding gas, preventing further star formation (Nelson et al., 2018; Dashyan et al., 2019).

Similar to supernovae, AGN are also thought to work predominantly in two modes. One of the AGN modes is mostly observed at high redshift, known as the quasar-mode, where there is a very high level of material accretion. This results in a high level of energy injected into the surrounding. The second mode of AGN feedback is known as radio-mode, which has a lower accretion rate. This mode is also called maintenance mode, and prevents the cooling by continuously heating up the gas, essentially quenching star formation. These events are thought to turn on and off with timescales of 10^5 yr, where the whole life cycle of AGN is believed to last for several Gyr (Schawinski et al., 2015). However, we still do not understand the details of how AGN behave such as their life-cycle or when and where the SMBH forms.

1.1.5 Mergers

Galaxies under gravity never form in isolation, as the growth of the inital density fluctuations of dark matter creates dense and sparse regions. In each dense re-

gion, there are usually filaments of galaxies, forming the well-known cosmic web. Therefore, it is very likely that throughout their life-time, there will be interactions between galaxies/dark matter halos. These interactions may cause the merging of two dark matter halos and their galaxies. If such merging happens between halos of similar masses, known as major merger, then the gas of the initial galaxies is shock-heated and settles back into hydrostatic equilibrium in the form of one new halo and galaxy (Barnes and Hernquist, 1998). However, if the merging happens between halos of different masses, then such an event is less efficient, which leads to the smaller galaxy and its halo acting as a satellite. This satellite halo will orbit the larger halo for a large period of time, where the gas from the satellite can be accreted by the central halo via various mechanisms. Depending on the environment and stellar mass of the galaxies, the satellite galaxy can experience galaxy harassment (Richstone, 1976), strangulation (Balogh et al., 2000; Balogh and Morris, 2000) or ram-pressure stripping (Gunn and Gott, 1972), where in each scenario, its gas can be removed, causing the halting of star formation. Additionally, such processes, especially major mergers, are thought to lead to the morphological transformation of galaxies, from disc to spheroid, due to such events disrupting the dynamical properties of the galaxies.

Both major and minor mergers can be sub-categorised into two more types of merging events. The first is known as dry mergers, where two galaxies that are quiescent, with little to no on-going star formation, or have little gas, merge together. In this instance, the quiescent galaxies prominently remain quiescent but increase in stellar and halo mass. The second type of mergers is coined wet mergers, where there is at least one galaxy with plenty of gas. Wet mergers provide the more massive galaxy with a fresh supply of gas which in turn reignites star formation.

1.2 Galaxy Properties

The previous section briefly describes the initial stages of galaxy formation, whereas in this section we will describe the properties of galaxies that are observable and the physical processes associated with them. As galaxies are objects con-

taining many stars clumped together to form various stellar populations, the study of their various properties will enable us to extract their formation history.

1.2.1 Morphology

One of the very first discoveries about galaxies were related to their morphological variety (Hubble, 1926a,b). Based on their morphology alone, Hubble proposed a classification system, shown in Fig. 1.1, which he was able to observe using Mount Wilson's 100-inch telescope.

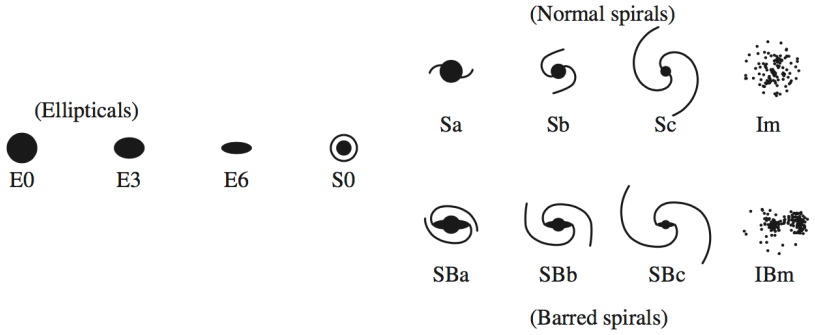

Figure 1.1: This shows the different types of galaxy morphology as proposed by Hubble. One key aspect of this figure is that it does not show the evolution of galaxy morphology, even though elliptical galaxies are generally early type (older) galaxies, while spiral galaxies are late type (younger) galaxies. This figure is taken from Abraham (1998).

Galaxies are primarily classified into either disc or elliptical, based on how their stars, gas and dust are distributed. Elliptical galaxies have little cold gas and dust and appear spheroidal with no spiral arms. Due to its shape, its gas, dust and stars are mostly dominated by random motion (Mo et al., 2010). Note, most early type galaxies (ETGs) happen to be elliptical. Furthermore, ETGs encompass Lenticular galaxies too, which have large bulge and disc, with no spiral arms. These galaxies typically have a Hubble classification of S0. They can contain large amounts of dust within their discs, similar to disc galaxies, however, they have very little ongoing star formation. On the other hand, disc galaxies are flat and disc like with, some, displaying spiral arm like features. For such systems, most of the motion of gas, stars and dust in the outer-parts are supported by rotational motion. Some spiral galaxies also have a bulge at the centre, whose structure is upheld by

random motion, like elliptical galaxies. These are known as classical-bulges. Typically, late type galaxies (LTGs) are disc galaxies. As previously mentioned, the disc galaxies can be transformed into ellipticals, via mergers.

Along with the two main classifications, an additional group exists - these galaxies are known as Irregular. These are less common in the present Universe and do not fit into either the disc or elliptical morphology. Irregular galaxies are usually smaller in size, and do not have any structural shape. They have a high amount of ongoing star formation, hence they appear bright. These galaxies also have a lot of gas and dust present.

There are multiple ways of identifying the morphological classification of galaxies. The simplest solution consists of visual inspection (Lintott et al., 2008; Smethurst et al., 2015). However, systems less prone to the subjectivity of visual inspection consist of the use of non-parametric measurements known as CAS - concentration, asymmetry and smoothness. Elliptical galaxies will have a high concentration and smoothness and low asymmetry due to their homogeneous structure, while the opposite is true for the spiral galaxies. Further information on the CAS system can be found in Conselice (2003). Another method implemented to classify galaxy morphology consists of comparing the bulge-to-total light fractions (B/T), which estimates, roughly, how bulge- or disk-dominated a galaxy happens to be. This is determined by the use of the Sérsic index (n) (Sersic, 1968; Ciotti and Bertin, 1999), which determines the surface brightness at a given distance. The profile can be simplified as

$$I(R) = I_0 e^{-(\frac{R}{R_e})^{1/n}}, \tag{1.1}$$

where I_0 is the intensity at the centre of the galaxy, $R = 0$, R is the projected radius of the galaxy where the flux is being measured, R_e is the half-light radius. The parameter n determines, how quickly light decays as we move away from the centre of the galaxy.

1.2.2 Colour

In addition to their morphology, galaxies also vary in their colour. Colour is defined as the flux ratio between two different filters. These filters can cover any spectral waveband. Galaxies vary in their colour owing to their stellar populations, as young stars are more luminous at near-ultraviolet (NUV) wavelengths whereas the old stars will emit most their photons in redder wavelengths, i.e. optical and near-infrared (NIR). Therefore by contrasting the magnitude of a galaxy in different wavelength ranges, we are able to infer the properties of their stellar populations. By using stellar population models (Bruzual and Charlot, 2003; Maraston, 2005; Conroy and Gunn, 2010; Vazdekis et al., 2012), their star formation history (SFH) can be determined. However, this is rather complicated, as the colour of a galaxy is also sensitive to its chemical enrichment history (CEH), as well as dust. Both an increase in metallicity or dust can redden the galaxy therefore creating an entanglement between the three properties of galaxies. The entanglement between age and metallicity, specifically, is known as the age-metallicity degeneracy (Worthey, 1994; Ferreras et al., 1999), which is an issue yet to be fully solved.

The colours of galaxies can be measured photometrically and spectroscopically. For each galaxy in a given filter, the apparent magnitude is calculated by

$$m_x = -2.5 \log 10 \frac{\int F(\lambda) x(\lambda) d\lambda}{\int C(\lambda) x(\lambda) d\lambda}, \tag{1.2}$$

where the subscript x indicates the passband chosen, as shown in Tab. 1.1 (York et al., 2000). $F(\lambda)$ is the spectral energy density of the observed galaxy, $C(\lambda)$ is the energy density for the given waveband for either the Vega star or an AB reference, $x(\lambda)$ is the response function of the filter in a certain waveband and finally λ is the integrating variable regarding wavelength (Roche et al., 2009; Blanton and Roweis, 2007).

1.2.3 Dust

As mentioned above, the colour of a galaxy enables us to probe the SFH or CEH. However, understanding such processes is complicated due to the presence of dust,

Table 1.1: This table shows the 5 standard spectroscopic wavebands, ugriz, adopted to calculate fluxes in SDSS (York et al., 2000).

Filter	Central wavelength (Å)	Waveband (Å)
u	3543	2980. - 4130.
g	4770	3630. - 5830.
r	6231	5380. - 7230.
i	7625	6430. - 8530.
z	9134	7730. - 11230.

which consists of fine particles that absorb and scatter photons from the stars. Dust can affect the spectroscopic and photometric observations of a galaxy in two different ways: (i) Light may get absorbed and scatted away from the line of sight towards the observed, this is commonly known as dust extinction, (ii) light originating from sources not on the line of sight can be scattered into the path towards the observed. This second point complicates the correction of the dust effects, as it depends on wide range of properties including dust composition as well as the distribution of dust within the light emitting region. The cobined effect of (i) and (ii) is termed dust attenuation. Due to the nature of dust, the extinction/attenuation curve is non-trivial, as it scatters more light at bluer wavelengths than redder wavelengths, making the galaxy appear redder than they should (Cardelli et al., 1989; Fitzpatrick, 1999). While we can correct for such effects, this process is very complicated. For example, a simple model treats dust as a homogeneous screen in front of the galaxy (Calzetti et al., 2000), whereas a more realistic modelling assumes that dust particles are densely located around star forming regions, with young stars, while other regions with less gas have little dust (Charlot and Fall, 2000). Depending on the assumption of dust geometry and distribution, the dust extinction/attenuation curve can vary drastically (Tress et al., 2018; Salim and Narayanan, 2020, and references within), hence any correction applied will have some level of systematic associated to it.

1.2.4 4000Å and Balmer breaks

Beyond colour, spectra (the distribution of flux as a function of wavelength) provide a more accurate representation of the stellar populations in a galaxy. From

the spectrum of a galaxy, we are able to probe various properties using targeted absorption features, as well as the overall shape of the continuum (the latter being the information that standard colours usually provides). These features are matched against stellar population models to better constrain their SFH and CEH. This thesis is based on the adoption of the 4000Å break as a proxy of evolution, therefore we include this sub-section, where we will briefly discuss this spectral window.

The 4000Å break in a galaxy is caused by the pile up of absorption lines in the spectra of stellar atmospheres. To understand better the origin of this break and its dependence with the age and metallicity of the stellar populations, we show in Fig. 1.2 a few stellar spectra from the MILES library (Sánchez-Blázquez et al., 2006), roughly corresponding to solar metallicity, and for a range of effective temperatures, as labelled. Let us consider, for simplicity, the evolution of a simple stellar population, i.e. all stars are formed at the same time, with the same chemical composition. As the population ages, the hotter, more massive – and thus short-lived – stars will die out earlier, so that the contribution to the integrated spectra will be dominated by stars at progressively lower temperature. The figure shows that the population will become redder, and a prominent break at 4000Å will form, mostly contributed by lower-mass stars. Such behaviour results in the 4000Å break being sensitive to the average age of the galaxy (Bruzual, 1983; Poggianti and Barbaro, 1997). However, in addition to this age sensitivity caused by the temperature dependence of the dominant stars, the break is produced by a large number of "metal" absorption lines, so that chemical composition will also affect the variation of the break. Moreover, this metallicity dependence will be more prominent at the older ages when the spectra is dominated by the older, hence cooler, stars.

Note also the presence of the Balmer break, at a shorter wavelength (3645Å). This feature is caused instead by the pile up of Balmer absorption lines of Hydrogen (i.e. photo-excitation transitions from the energy level n=2, as a resonant photon is being absorbed). At the lowest energy, the n=2 to n=3 transition produces the absorption of a photon at a wavelength of 6563Å (termed Hα), with the next one in the series caused by a n=2 to n=4 jump at 4861Å (Hβ), and so on. Since

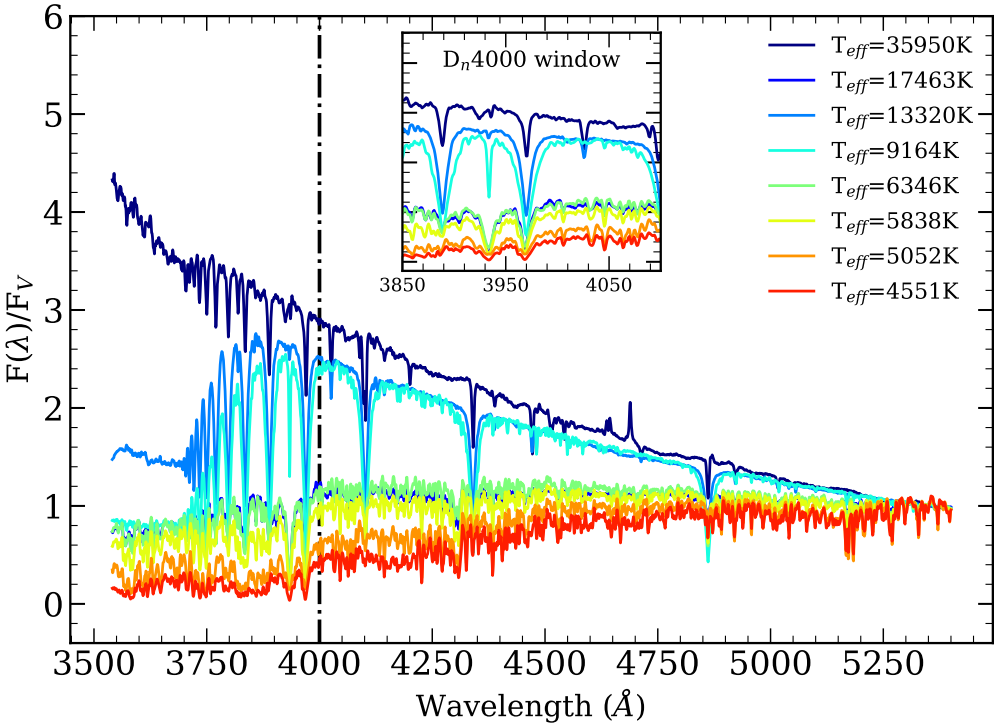

Figure 1.2: Stellar spectra of different effective temperature from the MILES library (Sánchez-Blázquez et al., 2006), characterised by Cenarro et al. (2007). Each colour corresponds to a different effective temperature, as indicated by the legend. The vertical dashed-dotted line at 4000Å marks the position of the break used in this thesis to characterize green valley galaxies. The inset shows a zoomed-in portion of this region. Note the spectra are all normalized to have the same V band flux.

the energy levels scale like $E_n \propto 1/n^2$, as the transitions involve higher values of n (from the original state n=2 that characterizes the Balmer series), the absorption lines are found at progressively smaller steps, asymptoting towards a wavelength corresponding to the n=2 to n=∞ transition (i.e. ionisation from a n=2 state), which takes place at 3645Å, termed the Balmer break. At shorter wavelengths, photons will induce this ionisation of Hydrogen from n=2, and will be absorbed, producing a decrease in the net flux blueward of the break. Note this break is evident in the star with $T_{\rm eff}$ ∼17,000 K, shown in the figure. The prominence of the break at these temperatures can be explained by a combination of the energy transitions involved and the temperature of the gas in the stellar atmosphere (Saha, 1921). This temperature dependence will therefore induce an age sensitivity of the Balmer break

in stellar populations, and, as it is only caused by hydrogen, it does not have a direct dependence on metallicity – only indirectly through blending of neighbouring lines in the same spectral region at the effective resolution of the observation. However, please note these two breaks (Balmer and 4000Å) are independent, and can be distinguished at the resolution of the SDSS spectrograph.

In addition to the Balmer break, the lower order Balmer absorption lines are also defined as strongly age-sensitive indicators. The lowest order feature, Hα, however, suffers from strong contamination if ionised diffuse gas is present (in star-forming galaxies or AGN), and even small levels of star formation can affect quite substantially the absorption line. Hβ is one of the most commonly used age-indicators, quite often matched against a metal-sensitive index, such as [MgFe] (see, e.g. Kuntschner and Davies, 1998). It is one of the traditional Lick indices (Trager et al., 1998), and has undergone a number of revisions, to decrease its sensitivity to chemical composition (e.g. Cervantes and Vazdekis, 2009). The higher order lines Hγ and Hδ are also used in the analysis of stellar populations (Worthey and Ottaviani, 1997), and are less dependent on emission line corrections, as the corresponding emission lines are significantly weaker than Hα or Hβ. However, they also suffer from a substantial sensitivity to variations in the non-solar abundance ratios (Thomas et al., 2004), so the best approach to constrain the population properties is to combine a range of line strengths with different sensitivity to these parameters.

1.2.5 Redshift

Cosmological redshift affects the spectra of galaxies in two ways. Studying galaxies at varying redshift means we are essentially observing them at different distances. Thus, galaxies that are at high redshift will have increasingly higher receding velocities, which in turn will introduce a Doppler shift on the wavelengths. Additionally, the expansion of the Universe will also cause the wavelengths to be ”stretched”. This ”stretching” effect is formulated as

$$z = \frac{\lambda_{obs} - \lambda}{\lambda}, \tag{1.3}$$

where λ is the wavelength a photon is emitted at and λ_{obs} is the wavelength we observe the photon at. This effect may necessitate the use of different instruments, that have different wavelength coverage, to observe galaxies, in the same spectral window at rest-frame, at higher redshift.

The second effect imposed by different redshifts is more physical, where we are essentially looking at different cosmological times. Thus, observations at higher redshift equates to the analysis of galaxies as if they were the progenitor version of what is seen at present time, statistically. Galaxy surveys at multiple redshifts will be equal to observations at different stages of their evolution. Therefore, the direct study of changes to their intrinsic properties over varying redshift bins will help us better understand galaxy evolution, as these results will be from direct observations rather than modelling. Our understanding of galaxy evolution mainly comes from low redshift surveys, where their SFH is inferred. However, in recent years, there have been multiple surveys looking at intermediate redshift, such as LEGA-C (van der Wel et al., 2016) and VANDELs (McLure et al., 2018), which have enabled us to study the properties of galaxies at higher redshift. Furthermore, more observations will be employed in the near future, such as JWST (Gardner et al., 2006), WEAVE (Dalton, 2016), MSE (McConnachie et al., 2016) and WAVES (Driver et al., 2019), which focus on galaxies at higher redshifts, enlarging the sample size, enabling for better statistical robustness.

1.2.6 Environment

Galaxy environment can be largely divided into four categories, in ascending order of density, (i) void (ii) field (iii) groups and (iv) clusters. Environment is thought to play an important role in galaxy evolution, indicated by trends such as the morphology-density relation, which finds an over-representation of elliptical galaxies in cluster regions and spiral galaxies to dominate the fields (Dressler and Shectman, 1987). This is mostly thought to be due to galaxies in dense spaces undergoing galaxy-galaxy interactions such as harassment, strangulation and ram-pressure stripping, which are various forms of interaction (Pasquali, 2015). In addition, galaxies in dense environments are also likely to experience mergers, which

in conjunction in the aforementioned mechanism will cause morphological transformations. This will result in differences between the properties of galaxies in dense-vs-sparse regions. Therefore, galaxies in clusters are thought to be redder, older, more metal rich, have lower SFR and gas fraction than their field counterparts (Kauffmann et al., 2004).

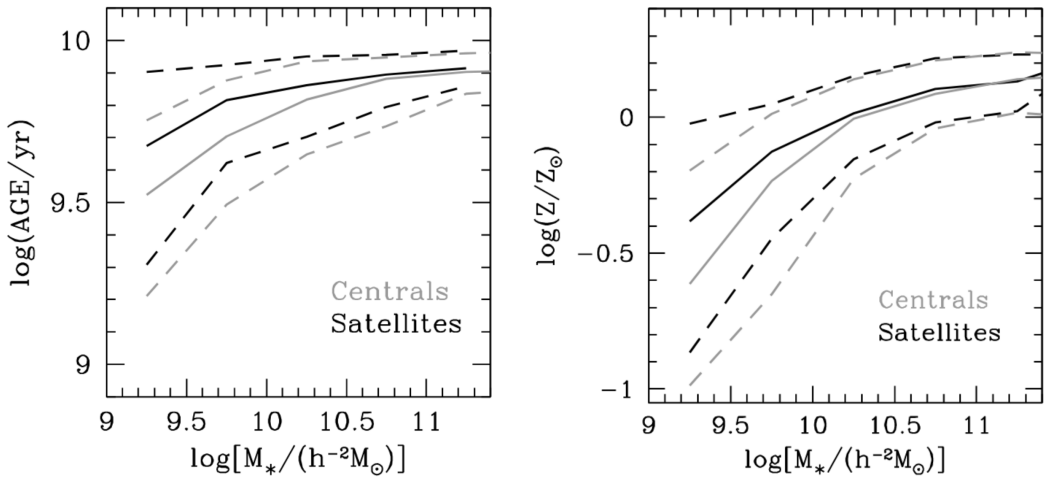

Figure 1.3: Relation between age (left) and metallicity (right) for different stellar masses of centrals (grey lines) and satellites (black lines). The dashed lines show the 16th and 84th percentile, while the solid line show the median value. Both figures are taken from Pasquali (2015), which is an amended figure from Pasquali et al. (2010).

Note, while galaxy environment is thought to be important, previous studies have noted its impact depends on (i) stellar mass of the galaxy and (ii) whether the galaxy is considered central (i.e. most massive system in the halo) or satellite (i.e. orbiting the most massive system). While we find differences in stellar populations between high- and low-density environments, most of these differences are seen in low mass galaxies, with $\log \mathrm{M}_\star/\mathrm{M}_\odot \leq 10.5$ (Peng et al., 2010), which are most likely to be satellite systems. Additionally, looking at satellite systems, we find comparable trends between cluster and field, where the satellites are older, more metal rich, have lower SFR and gas fractions compared to centrals (Thomas et al., 2010; Rogers et al., 2010; Pasquali et al., 2012; La Barbera et al., 2014), see Fig. 1.3.

1.2.7 Luminosity function

One of the fundamental properties of galaxies is related to their luminosity. The luminosity function is defined by the number of galaxies in a given luminosity bin. Typically, the luminosity function is fit by a Schechter function (Schechter, 1976),

$$\Phi(L)dL = \Phi_0 \left(\frac{L}{L^\star}\right)^\alpha \exp\left(-\frac{L}{L^\star}\right)\frac{dL}{L^\star} \tag{1.4}$$

where $L_\star$ is the characteristic luminosity, α is the slope of the faint end and Φ_0 is the normalisation factor. Note the luminosity function varies with the properties of galaxies mentioned above, such as their morphology, colours redshift and environment. For example, red galaxies have higher characteristic luminosity, higher $L^\star$ value, shallower faint-end slope, and lower α value, compared to blue galaxies (Baldry et al., 2004). Note the luminosity is directly related to the mass of the system as a greater number of stars means a more massive and luminous galaxy . Therefore, the luminosity function can be converted to study the mass function of the system (Bell et al., 2003). This will vary in a similar manner to the luminosity function, where there will be a higher density of red galaxies in the high mass regime and a greater number of blue galaxies in the low mass regime.

1.2.8 Scaling relations

Most of the aforementioned observable properties of galaxies are strongly correlated with one another; most importantly the mass, size, luminosity and colours of galaxies. There are three important scaling relations; the Tully-Fisher relation (TFR), fundamental plane (FP) and colour-magnitude (CM) relation. The TFR correlates the total luminosity of the galaxy to their rotational velocity, which can be defined in its simplest form as $L \propto v_{max}^4$ (Tully and Fisher, 1977).

The FP plane is a 3-dimensional relation between the size, velocity dispersion and surface brightness of early type galaxies (Bernardi et al., 2003). This can be formulated as

$$\log R_e = a \log \sigma + b \langle \mu_r \rangle_e + c \tag{1.5}$$

where R_e is the effective radius of the galaxy, $\langle \mu_r \rangle_e$ is the mean surface brightness

within R_e and σ is the velocity dispersion. Note a, b and c are some constant factor which can be obtained from observations - for example a,b,c are found, in r band, to be *1.390*, *0.314* and *-8.867*, respectively, for elliptical galaxies from the Sloan digital sky survey (La Barbera et al., 2010). Within this FP, each of the properties are also correlated to one another. One relation is known as the Faber-Jackson relation which relates the total luminosity, which combines the surface brightness (μ_r) and size of the galaxy, to the velocity dispersion as $L \propto \sigma^{\alpha}$ (Faber and Jackson, 1976), where $\alpha > 0$, thus indicating that the luminosity of a galaxy scales with its velocity dispersion. The second relation is known as the Kormendy relation which formulates the trend between the size (R_e) and surface brightness (μ_r) of the galaxy as $\mu_r \propto R_e^{\gamma}$, where $\gamma < 0$, hence the surface brightness decreases as the size of the galaxy increases (Kormendy, 1977).

The final relation, colour-magnitude (Bower et al., 1992a,b), again relates mostly to ETGs that are quiescent. This relation shows that the more luminous, more massive, ETGs also happen to be redder, with a very low level of scatter. As mentioned previously, age, metallicity and dust result in galaxies having redder colours, however, ETGs are known to have very little dust (Calzetti et al., 2000), therefore this reddening with stellar mass can be mostly associated to the age and metallicity of galaxies. This enables us to study the SFH of galaxies. However, one of the biggest issues with the interpretation of this relation, regarding their stellar populations, is the effect of the age-metallicity degeneracy mentioned above. Sophisticated methods for studying ages and metallicities of stellar populations in galaxies, through spectroscopy, have helped mitigate this age-metallicity degeneracy. For instances, Graves et al. (2009) study such relations, where they find that the metallicity, measured using [Fe/H], might be the main driver of the tight correlation between the colour-magnitude relation at fixed velocity dispersion, whereas the age of the galaxy causes the small spread that is observed.

1.2.9 Nuclear Activity

Most of the flux we observe from galaxies is expected to come from their stars and gas. However, most galaxies will have, in their core, a supermassive black hole

(SMBH). If there is sufficient gas in the galaxy, the SMBH will accrete this gas, emitting a large amount of radiation at various wavelengths. The flux from such process can be great enough to contaminate the flux observed from the galaxy in two distinct ways. The flux from the AGN will have its own continuum, therefore contaminating the stellar continuum. Hence, to study the stellar populations of a

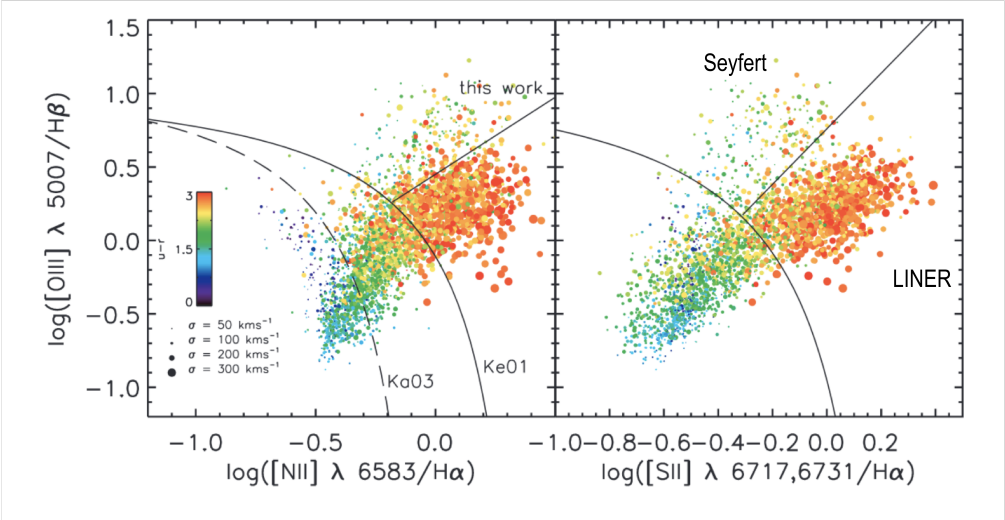

Figure 1.4: Both figures show the demarcation line for different types of nebular emission activity. On the left panel the line labelled Ka03 is from Kauffmann et al. (2003), which marks the upper limit of SF galaxies. Between Ka03 and Ke01 (Kewley et al., 2001, both solid curved lines) lines, resides the composite galaxies, strong star forming galaxies and AGN. The straight line on the left panel separates strong, Seyfert, and weak, LINER, AGN. Finally, the straight line on the right panel from Kewley et al. (2006), also separates LINER and Seyfert AGN. This figure is taken from Schawinski et al. (2007), with slight amendments.

galaxy, the AGN continuum must be accounted for and subtracted. Additionally, powerful AGN can heat up the surrounding gas, therefore causing a large broadening of emission lines, such as [OIII] or Hα. AGN activity takes place in the centre of the galaxy, thus while its flux typically originates from a small region, its impact is thought to be felt within the whole galaxy and in some extreme instances by their surrounding galaxies (Dashyan et al., 2019).

Note, as the AGN affects the spectra of the galaxy, we are able to identify if a galaxy hosts an AGN or not by studying targeted emission line ratios, in optical wavebands. Fig. 1.4 shows an updated figure of the BPT diagnostic diagram

(Baldwin et al., 1981), which plots the ratio between [OIII]/Hβ and [NII]/Hα. The emission lines are caused by different physical mechanisms, thus, enabling the categorisation of galaxies depending on their ratios. Each of these plots shows the regions where different types of galaxies, SF, composite, LINER and Seyfert AGN lie - see caption for more detail. Owing to the lack of emission lines in quiescent galaxies, as they have no star formation, they cannot be located in the BPT diagram.

1.3 Simulations

The properties of galaxies can be observed or simulated. Both of these methods complement to each other to better our understanding of galaxy formation and evolution. Observations improve our understanding by showing the relation between different galactic properties thus enabling us to infer the physics behind the physical mechanisms. Simulations, on the other hand, enable us to encode the behaviour of these processes, in order to reproduce the observed results. Hence, observations can be used to constrain the simulations and the simulations facilitate the interpretation of the observational results. In terms of simulations, they come in two main flavours (i) Semi-Analytic Modelling (SAM) (ii) Hydrodynamical simulations. In both types of modelling, there are still large amounts of disagreement in their detailed results but modelers have mostly come to the consensus on what physical processes are key to reproduce the observed galactic properties.

1.3.1 Semi-Analytic Models

This type of simulation is the most simplistic of the two, as SAMs do not solve the fundamental equations regarding gravity or hydrodynamics for the particles. Instead these models are built on top of the DM halo merger tree and the galaxies are defined by their global properties, such as their stellar mass, SFR, BH mass, stellar metallicity, etc (Somerville and Davé, 2015, and references within for more detail). The evolution of galaxies in such simulations is determined by sets of simplified equations that are supposed to encapsulate the behaviour of the galactic properties, such as stellar feedback, growth of black hole, AGN feedback, star formation, etc. The parameters of the physical equations are fine-tuned such that they are able to

reproduce the observational trends at $z = 0$. Due to the simplistic nature of these simulations, they are very cost effective and easy to run. Therefore, multiple simulations with slight changes in the parameter values can be done in a short time to study their effects. Additionally, the effect of various physical mechanisms, such as stellar feedback or AGN feedback, can be tested by simply ”turning them off” or ”on”.

1.3.2 Hydrodynamical simulations

These are the second types of simulations, which are more sophisticated as they solve the equations of motion and gravity (Springel and Hernquist, 2003). However, similar to the SAMs, they also use simplified equations, sub-grid physics, to model the remaining physical processes, such as heating and cooling of gas, star formation, seeding of black hole and its accretion. Such simplification of physics is necessary owing to the resolution limit, lack of computational power and our limited knowledge of such processes. The parameters of the sub-grid equations are also fine-tuned to reproduce the observed trend at $z \sim 0$, such as the luminosity function (Schaye et al., 2015), colour-bimodality (Trayford et al., 2015; Nelson et al., 2018), mass-metallicity relation (Pillepich et al., 2018b), etc. These simulations follow galaxy formation and evolution in a cosmological box, typically varying from 50 Mpc (McAlpine et al., 2016; Pillepich et al., 2019; Nelson et al., 2019a) to 300 Mpc (Springel et al., 2018; Pillepich et al., 2018a), allowing us to analyse the particles within, at different redshift intervals.

1.4 Outline of this thesis

The main objective of this thesis is to study the properties of galaxies that are currently quenching their star formation therefore in transition from young to old. In this section, we will first briefly describe the overall concept of galaxy evolution and then describe the different chapters of this thesis.

To understand the evolution of galaxies, the aforementioned galactic properties must be studied with regards to various physical mechanisms. Fig. 1.5 shows a simple schematic diagram describing some of the potential channels of galaxy evo-

lution. Here we see, two distinct regions occupied by young and old galaxies. The existence of such population in observations will be discussed in Chapter 2.2.

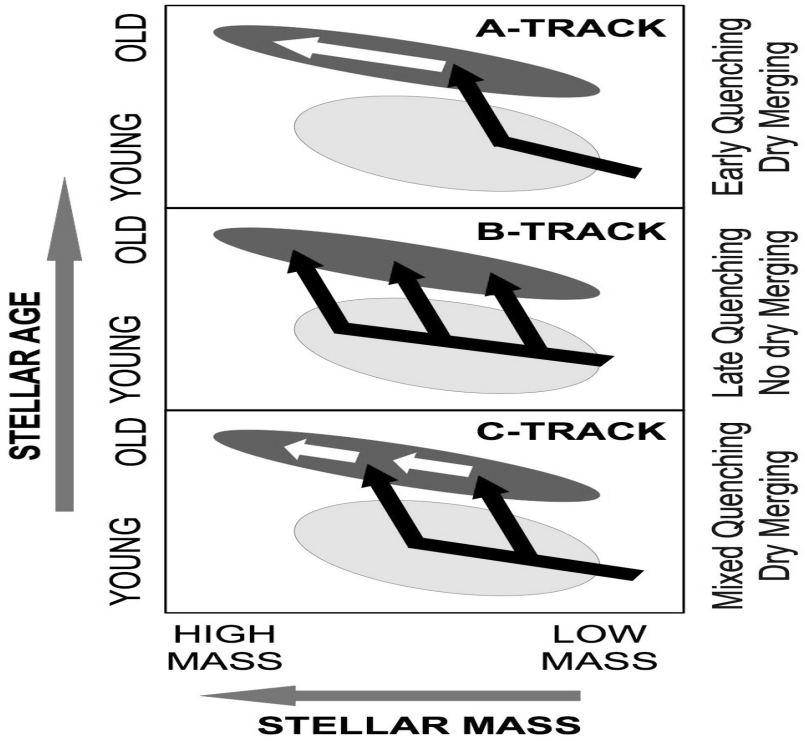

Figure 1.5: Diagram illustrating different evolutionary tracks that a galaxy might follow as it goes from young to old. As seen from diagram, there are 3 distinct path that a galaxy could follow for their evolution. A-Track shows early quenching of star formation followed by multiple merging events. B-Track shows the opposite where galaxies appear to have late quenching, where galaxies have accumulated most of their mass through conversion of their gas into stellar masses, then it quenches its star formation. C-Track is a mixture of the previous 2 tracks. This diagram is an amended diagram from Faber et al. (2007), also shown in Ferreras et al. (2013b).

Due to the collapse of gas particles under their own gravity, galaxies are formed with low mass and young stellar populations. As they convert more of their gas into stars, they will experience a steady increase in their stellar mass and will follow the tracks shown by the black arrows in A-, B- or C-track. Eventually, owing to feedback mechanisms, such as supernovae or AGN, or environmental processes, such as ram-pressure stripping, strangulation or harassment, these galaxies will run out of cold gas, quenching their star formation. Once the quenching of star formation begins, the average age of the galaxies increases causing them to transition from

the region occupied by young to old galaxies. Depending on the mechanism under which these galaxies quench their star formation they will follow the black arrows of A-, B- or C-track. For example, quenching via the A-track could be due to environmental mechanisms, as the galaxies have relatively low stellar masses, whereas quenching via track C could be due to AGN feedback, as these galaxies are more massive, or it could be a combination of various physical processes. Depending on the dominant physical mechanism for stopping star formation, the time taken to transition from the young stellar population region to the old galaxies area will vary; as discussed in Chapter 2.2. Furthermore, in the A and C evolution tracks, once these galaxies quench their star formation they can experience dry mergers. This increases their stellar mass, while keeping their average age relatively old, as shown by the white arrow tracks. In some instances, galaxies will undergo wet-mergers, ignite new episodes of star formation, in which case they will experience an increase in stellar mass but a drop in the average age.

1.4.1 Chapter 2

The general idea of galaxy evolution is well understood, however the details are very much a debated topic. For instance, the average age of the galaxies are estimated or inferred from the galaxy properties. Therefore, to understand the evolution of galaxies, we must recreate such a schematic diagram using observable parameters. Chapter 2 of this thesis will try to summarise the past effort into doing exactly this. Here we introduce the concept of Blue cloud (BC), Green Valley (GV) and Red sequence (RS), which is used as a substitute for young, transitioning and old galaxies, respectively. We will discuss the various parameters used in previous studies to define the evolutionary sequence. For each definition, we will outline the properties of galaxies in transition, the timescales associated to the transition from young to old and finally the different physical mechanisms associated to these timescales.

1.4.2 Chapter 3

Many of the past methods of defining the evolutionary sequence require some form of correction or modelling - the use of colour requires dust correction, or the use of the star formation rate requires some form of modelling of the stellar initial mass function. Therefore, in this chapter we present a new way of defining the evolutionary sequence, which consists of using the 4000Å break. We then compare this novel method against a traditional method, based on the colour of the galaxy, finding it to be more resilient to the systematics associated to dust correction. Furthermore, since it is an observable, measured directly from the spectra, its calculation does not require any modelling. After dividing the GV region, defined using both 4000Å break and colour, into terciles -lower GV (lGV), middle GV (mGV) and upper GV (uGV) - we study and compare the properties of transitioning, GV, galaxies. Overall, we find similar results between both definitions of the GV, which are also in agreement with previous studies (Martin et al., 2007), such as the high fraction of AGN galaxies in GV. However, unlike traditional methods, we find the new GV definition provides a cleaner stratification between different regions of the evolutionary sequence and yields a more homogeneous stellar population between different types of galaxies i.e., star forming, quiescent and LINER.

1.4.3 Chapter 4

To fully understand galaxy formation and evolution, observations and simulations must be compared. While many works are still needed for simulations, they are able to reproduce many of the fundamental relations seen in observations at $z \sim 0$ (Trayford et al., 2015; Pillepich et al., 2018a; Nelson et al., 2018). In this chapter, we test how well two state-of-the-art simulations, EAGLE and IllustrisTNG, reproduce the evolutionary sequence, when using the novel definition. Such evaluation finds that both simulations reproduce the location of the BC fairly well but fail to match the location of observational GV and RS, where IllustrisTNG does slightly worse than EAGLE. Furthermore, comparison of galaxies in the GV between observations and simulations finds that simulations typically find a higher fraction of quiescent galaxies, as well as older galaxies, suggesting that the quenching mech-

anism implemented in both simulations is too strong. The disagreement between simulations and observations is greatest at high stellar mass, $\log M_\star/M_\odot \gtrsim 10.5$, suggesting AGN feedback to be too strong, as many studies have found AGN to be important in quenching star formation at high stellar masses (Kauffmann et al., 2003; Schawinski et al., 2007; Trayford et al., 2017; Lacerda et al., 2020).

1.4.4 Chapter 5

AGN are thought to be important in quenching star formation in galaxies, however the exact mechanisms of AGN are poorly understood. In this chapter, we try to understand the exact role of AGN by continuing the study of del Moral-Castro et al. (2019) and del Moral-Castro et al. (2020), where they select a sample of nearby "Twin" galaxies - these are pairs of galaxies with overall similar properties such as stellar mass, ellipticity, magnitude in r band and morphology, but one hosts an AGN and the other does not. We compare the properties of 10 pairs of "Twin" galaxies in terms of their location on the evolutionary sequence, defined using 4000Å break, finding that AGN galaxies are more evolved than their SF counterpart - even if they are considered "twins". Further analysis shows that AGN galaxies are older and more metal rich than their "twin" SF galaxies, indicating that galaxies hosting AGN have a different star formation history (SFH) than SF galaxies. Independent of the galaxy type, we find evidence of inside-out quenching, where the stellar populations in the central region are older and more metal rich than in the outer region. We compared the properties of "twin" galaxies with a larger sample from SDSS, finding the difference between AGN and SF galaxies to be statistically small but significant and physical.

Chapter 2

Green Valley

This chapter will focus mostly on the Green Valley (hereafter GV) - consisting of how it is traditionally defined and the properties of galaxies selected under such definitions. While we mainly focus on results in the optical wavebands and from observations, we will also discuss some of the discoveries made from different wavelength ranges and simulations.

2.1 Exploration of galaxy bimodality/ Defining GV

Strateva et al. (2001) was one of the earliest works to uncover and explore the bimodal distribution, with $\sim$ 150000 galaxies from SDSS (York et al., 2000), using $(u^\star - r^\star)$ vs $g^\star$ (see Fig. 2.1). The galaxies were distributed such that they yielded a high density at the blue and red colours, with a sparse region in between. This bimodal behaviour was also seen in other colours - $u^\star - g^\star$, $g^\star - r^\star$ and $r^\star - i^\star$ - however $u^\star - r^\star$ showed the cleanest signal. Each mode was fitted with a Lorentzian profile. Later works opted to use slight variations of this diagram, such as, $u - r$ vs M_r (Baldry et al., 2004) - where the distributions were fitted with a Gaussian profile. Additionally, multiple functional forms were fit to define the locus regions of BC and RS, which varied from a high order polynomial to the Schechter function.

Other surveys, such as GALEX (Martin et al., 2005), enabled further exploration of this bimodal distribution by providing a cleaner/wider separation between BC and RS; via the use of UV data. Galaxies were observed in the near-ultraviolet (NUV) as well as the far-ultraviolet (FUV), and galaxy bimodality was explored via

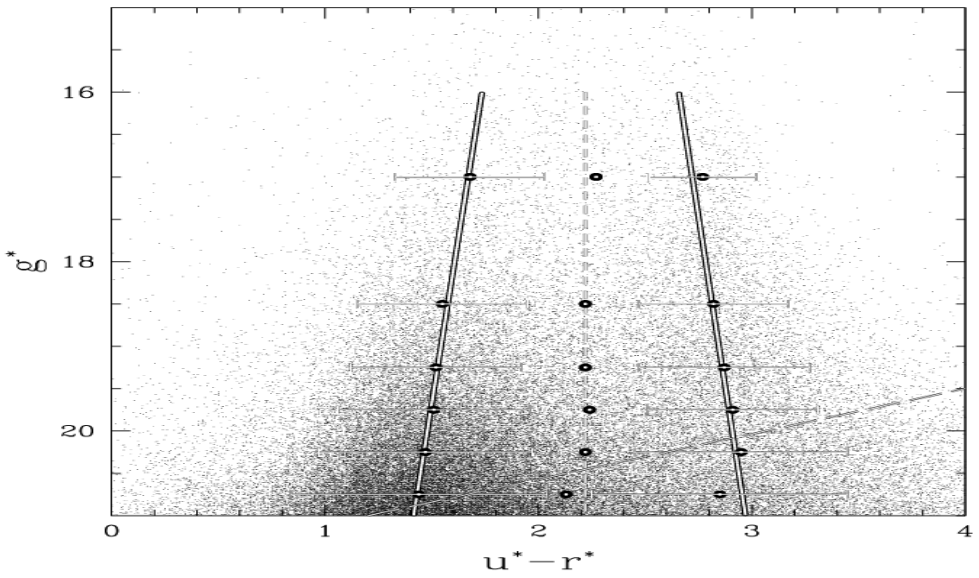

Figure 2.1: Colour, $u^{\star} - g^{\star}$, vs magnitude in $g^{\star}$ diagram, where the scattered data points are galaxies. The solid lines show the dense regions which can be thought of as the blue and red found for the distribution of SDSS galaxies. The dashed line down the middle separates the blue and red peak at different $g^{\star}$ bin. This figure is taken from Strateva et al. (2001).

(NUV-r)$_{0.1}$ and (FUV-r)$_{0.1}$ vs $M_{r,0.1}$ (Wyder et al., 2007; Martin et al., 2007), see Fig. 2.3. Note, the $_{0.1}$ subscript here indicates the measurement being carried out at an equivalent redshift, $z = 0.1$. At shorter wavelengths (NUV and FUV), spectra are highly sensitive to young stars, while older stellar populations affect the redder wavelengths. Therefore the combination of ultraviolet (NUV or FUV) and optical (r) magnitudes provide a cleaner separation between young and old stellar populations compared to the use of only optical magnitudes. Using a double Gaussian to fit the galaxy distribution in (NUV-r)$_{0.1}$ vs $M_{r,0.1}$ was insufficient due to the existence of surplus galaxies amid the bimodal distribution (see Fig. 2.2). Therefore, the sparse region in between was thought to be a region (Wyder et al., 2007), and not just the tail of the two distributions.

Another approach to study quenching of star formation and evolution in galaxies consists of analysing galaxies over long cosmological periods. Faber et al. (2007) makes use of both DEEP2 (Davis et al., 2003) and COMBO-17 (Baade et al., 1999) surveys to study the change in the luminosity function of blue and

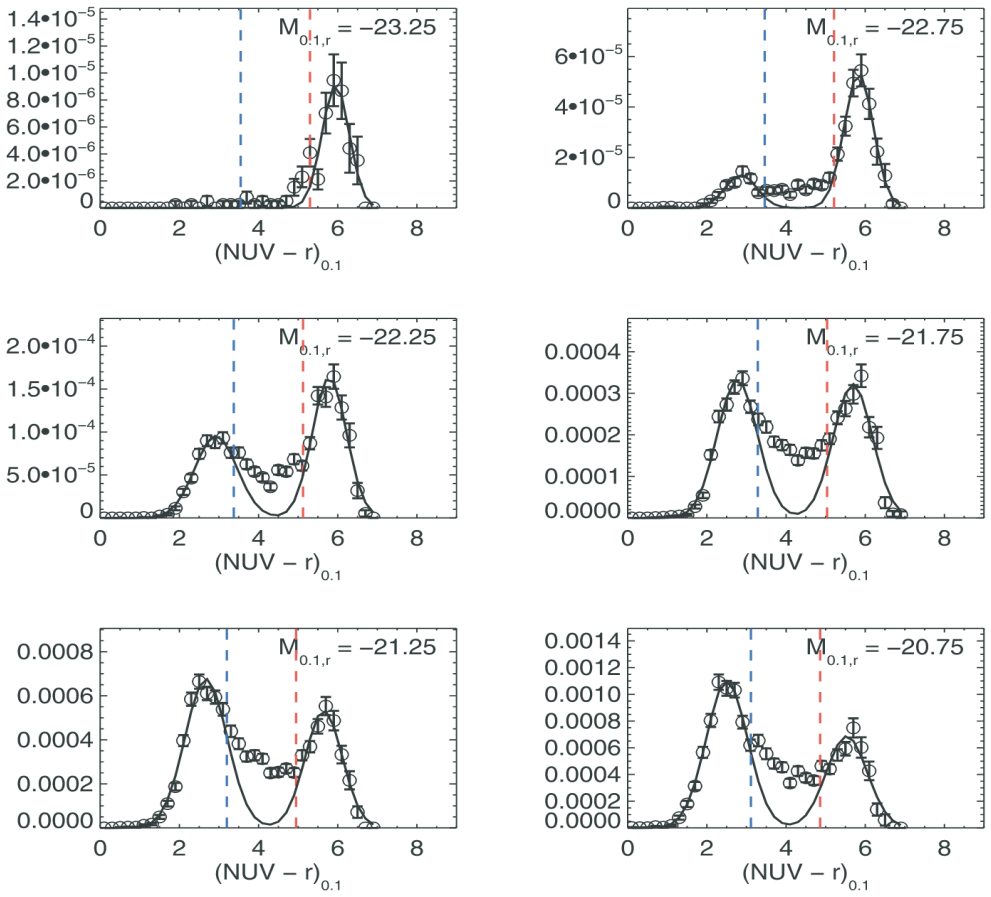

Figure 2.2: Histogram density of galaxies for different colours defined as $(NUV\text{-}r)_{0.1}$ for different absolute magnitude in r bins, $M_{0.1,r}$. The width of each magnitude binds are 0.5 wide, with the text showing the mid point. The observed data points are shown by empty circles with error bars while the double gaussian fit is shown in the solid line. The blue and red lines show the limits of the blue and red galaxies considered when fitting the Gaussian function, independently. Note the excess galaxy in between (Wyder et al., 2007)

red galaxies. Analysis of the luminosity function shows a differing evolution for blue and red galaxies, where the number density of blue galaxies remains constant from $z \sim 1$ to present time, as the Schechter function (ϕ^*) appears constant for the different redshift bins. In contrast, there is an increase in the number density of red galaxies from $z \sim 1$ to $z = 0$, as ϕ^* increases by ~ 0.5 dex between the 2 redshift ranges (Faber et al., 2007). Note the rise in the number of red galaxies only pertains to L^* (the luminosity where the gradient of the slope changes rapidly).

Recent studies have opted to use galaxy colour, as a proxy for age, to split the galaxies into different regions in combination with their stellar mass - $u^\star - r^\star$ or

$g^\star - r^\star$ vs stellar mass (Schawinski et al., 2014; Bremer et al., 2018; Kelvin et al., 2018; Phillipps et al., 2019), see Fig. 2.3. Furthermore, colour-stellar mass diagrams have also been explored in state-of-the-art hydrodynamical simulations to define the evolutionary sequence (Trayford et al., 2015, 2017; Nelson et al., 2018; Correa et al., 2019). Galaxies are binned into different stellar masses, and within each bin the galaxies are divided, either through their morphological classification, galaxy type (i.e. star forming or quiescent) or simply their colour. From the distribution of galaxy parameters, they define the location of BC, RS and thus GV in between them - usually characterizing the border between each region with a linear fit. While the simulations do very well in reproducing the general distribution of galaxies as well as reproducing their bimodality, a detailed analysis shows some inconsistency. For example, the slope of the RS, in colour vs stellar mass plane, is found to be inconsistent between observation and simulation, where simulation RS slopes are shallower than those from observations. This is noted to be owing to the mismatch in the mass-metallicity relation (Trayford et al., 2015; Nelson et al., 2018).

Additionally, rather than using the colours of galaxies, which can be thought of as an observable parameter, previous papers have also opted to use their SFR (Salim et al., 2007; Schiminovich et al., 2007; Koyama et al., 2019; Trussler et al., 2020). Note, the calculation of SFR requires modelling, therefore can be prone to systematics depending on the choice of IMF, M/L ratio and SSP models. Again, they classify the galaxies into different stellar mass bins - as it is thought to be one of the fundamental parameters (Kauffmann et al., 2003). In each individual bins, the average SFR is calculated and depending on the position within the diagram a BC (or main star forming sequence, MSFS), GV (deviation from MSFS) and RS (further deviation away from MSFS) is defined (Peng et al., 2015; Trussler et al., 2020). A linear fit is then used to define the borders of BC, GV and RS for all stellar masses (see top right panel of Fig. 2.3).

Other than using optical colours and parameters derived from the optical wavebands, many papers have tried to study the bivariate distribution using galaxies observed in the NIR or MIR (Walker et al., 2013; Lee et al., 2015). These works

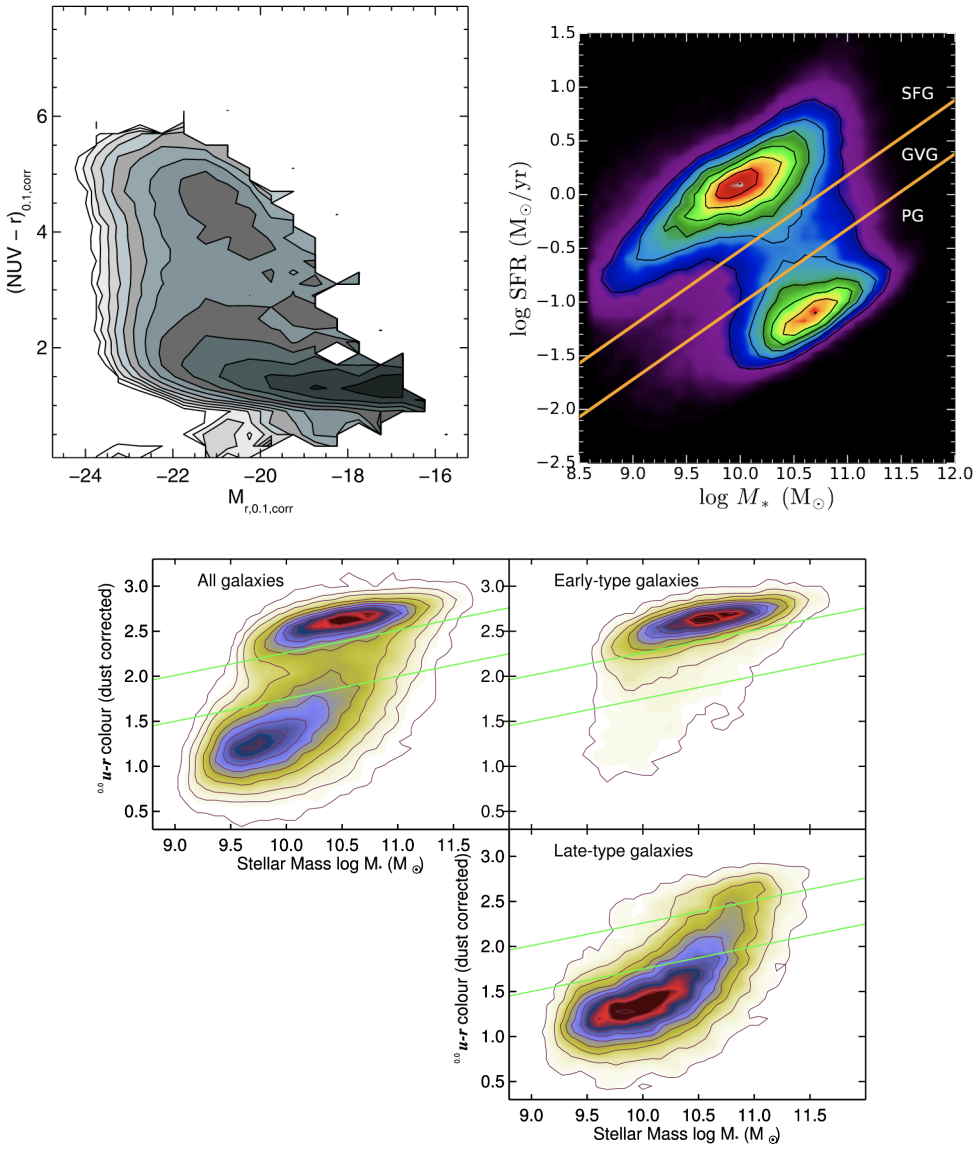

Figure 2.3: Here we show 3 different ways that the evolutionary sequence of galaxies are shown. *Left panel:* distribution of galaxies from GALEX survey in colour, $(NUV - r)_{0.1,corr}$, vs absolute magnitude, $M_{r,0.1,corr}$ shown in Wyder et al. (2007). Similarly, *right panel* shows the distribution of SDSS on SFR vs stellar mass plane defined in Trussler et al. (2020). *Bottom panel:* shows the BC, GV and RS defined on the colour, $u-r$ (dust corrected), and stellar mass plane from Schawinski et al. (2014).

involve surveys such as *NOAO Extremely Wide-Field Infrared Imager* (NEWFIRM, Whitaker et al., 2011), NEWFIRM Medium BAND Survey (NMBS, van Dokkum et al., 2009), *All-Wavelength Extended Growth Strip International Survey* (AEGIS, Davis et al., 2007), *Wide-field Infrarred Survey Explorer* (WISE, Wright et al., 2010), etc. In the infrared, analogously to optical, magnitudes in two filter bandpasses can be subtracted, to obtain their colour, to define the distribution of galaxies - such as U-V (Brammer et al., 2009), U-B (Mendez et al., 2011), or difference between the combination of MIR wavebands, 3.4, 4.6, 12, and 22 μm (Lee et al., 2015).

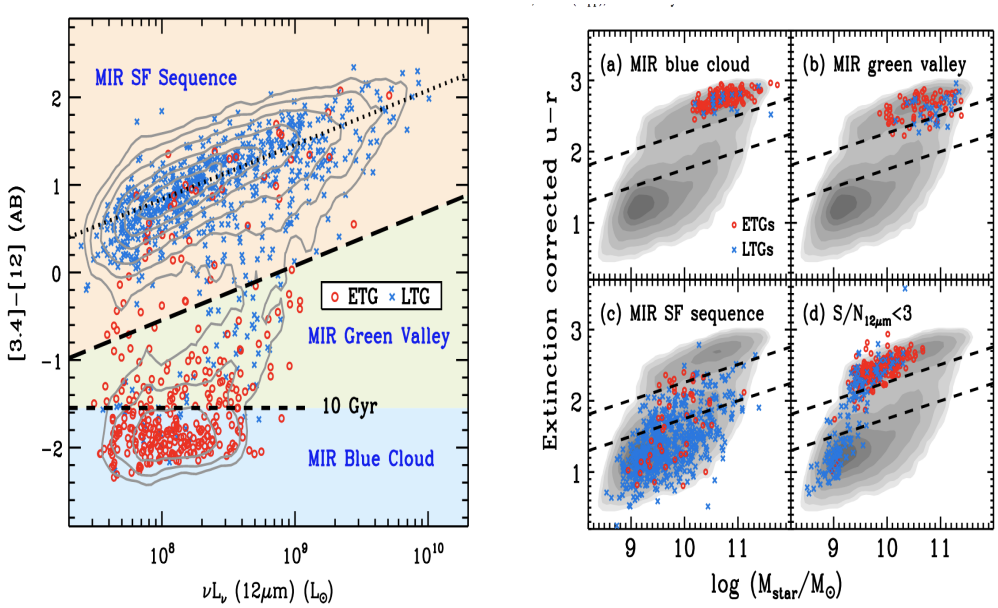

Figure 2.4: *Left:* shows the distribution of galaxies in the MIR vs luminosity plane, where various evolutionary regions have been defined. The MIR SF Sequence, MIR GV and MIR Blue cloud correspond to the optical BC, GV and RS, respectively. *Right:* maps the MIR selected regions from the left panel on the optical optical colour vs stellar mass plane. Each panel shows the distribution of galaxies at differing location of evolutionary sequence in MIR vs luminosity plane (Lee et al., 2015).

Defining the galaxy distributions using IR observations can produce bivariate distributions of galaxies (see left of Fig. 2.4). However, galaxies identified to be SF or transitioning in the IR plane are typically found in the RS for optical colours (see right of Fig. 2.4). Furthermore, a recent study which analysed a sub-mm survey, H-ATLAS (Valiante et al., 2016), define a so-called "green mountain" (GM),

where the most luminous galaxies in IR have a unimodal distribution, with the peak located at the GV in optical $g^\star - r^\star$ (Eales et al., 2018). The differing distribution between optical and sub-millimeter observations was attributed to Malmquist bias, where in the optical, samples are over-represented by galaxies that are most luminous in the optical wavebands and galaxies, which are most luminous in IR, are over-represented in the submillimeter survey.

2.2 Properties of GV galaxies

In this section, we will discuss various properties that GV galaxies possess, which were obtained using the GV definitions mentioned above. Note, that while colour can be used to define the evolutionary sequence of the galaxies, they are heavily affected by dust. Wyder et al. (2007) found the effect of dust causes an artificial spread of the BC and Salim et al. (2009) found it to be as high as 1/4 of the colour variation in BC. Dust can also a produce misplacement of BC galaxies into GV/RS (Brammer et al., 2009). The effect is most prominent in BC for star forming galaxies, as these galaxies have the highest amount of dust, whereas galaxies that are considered quiescent have very little gas and dust, so these are the least affected. Correcting for dust, by adopting an attenuation law (Cardelli et al., 1989; Calzetti et al., 2000), can mitigate such effects, however depending on the chosen law, there can be a significant level of systematics (Salim and Narayanan, 2020).

2.2.1 Morphology

The SFH of galaxies in the GV can be explored using various line indices, i.e. $D_n(4000)$ (Balogh et al., 1999) and $H\delta_A$ (Worthey, 1994). For a passively evolving population, $D_n(4000)$ is sensitive to a longer timescale compared to $H\delta_A$, thus galaxies with different SFH will be located on different areas of this space. Using such diagrams, galaxies are thought to transition smoothly from BC to RS, as the stellar population of the galaxies get older (Kauffmann et al., 2003; Brinchmann et al., 2004). Furthermore, study of the stellar population properties yielded a low level of scatter for galaxies in BC and RS, but a high level of scatter in the GV, suggesting a significantly lower homogeneity in the GV (Martin et al., 2007). One

such reason could be owing to galaxy morphology. While BC and RS are dominated by LTGs and ETGs respectively, the GV is found to host a mixture of both galaxy types (Brammer et al., 2009; Schawinski et al., 2014). This result is further supported, when studying the evolution of galaxies in a limited mass range, $10.25 \lesssim \log \mathrm{M}_\star/\mathrm{M}_\odot \lesssim 10.75$, as a morphological transformation occurs first in the BC, followed by the quenching of star formation (Bremer et al., 2018). In addition, the study of GV galaxy morphology using their Sérsic index, effective radius and stellar mass surface density (obtained from K-band surface brightness profiles) further supports this scenario, as it shows that most of the GV galaxies already have some kind of prominent bulge (60%) with some remnants of a disc (Bremer et al., 2018). In contrast, using a different waveband to support such transitioning reason finds slightly different results. A study using infra-red data on the A2199 supercluster finds MIR SF sequence is dominated by LTGs (93%). These galaxies are thought to first quench their star formation, becoming GV LTGs (32%) then transform into GV ETGs (68%). Finally, these galaxies evolve into ETGs (90%) that dominate the MIR blue cloud (MIRBC) galaxies (Lee et al., 2015). Note such discrepancy between results can be expected if the GV galaxies are defined in different wavebands. Therefore, while both studies are comparing GV galaxies, they are defined in a different manner, thus they could be selecting the same sets/types of galaxies to belong to differing regions (see right of Fig. 2.4). Furthermore, the two studies cited above have galaxies in different environments, where we discuss the impact of environment below.

For the study of galaxy morphology, we can make use of an extended set of five parameters related to the surface brightness distribution, thus providing more information than the standard classification. These parameters are (i) concentration, (ii) asymmetry, (iii) smoothness (CAS) (Conselice, 2003) (iv) Bulge-to-Total Decomposition (B/T) (Simard et al., 2002) and (v) Gini Coefficient/M_{20} (Lotz et al., 2004). For GV galaxies, both colour and stellar mass are shown to have intermediate values between the blue and red galaxies, where the median stellar mass for blue, green and red galaxies are $\log M_\star/M_\odot$ =9.6, 10.3 and 10.7, respectively (see Fig. 2.5). Simi-

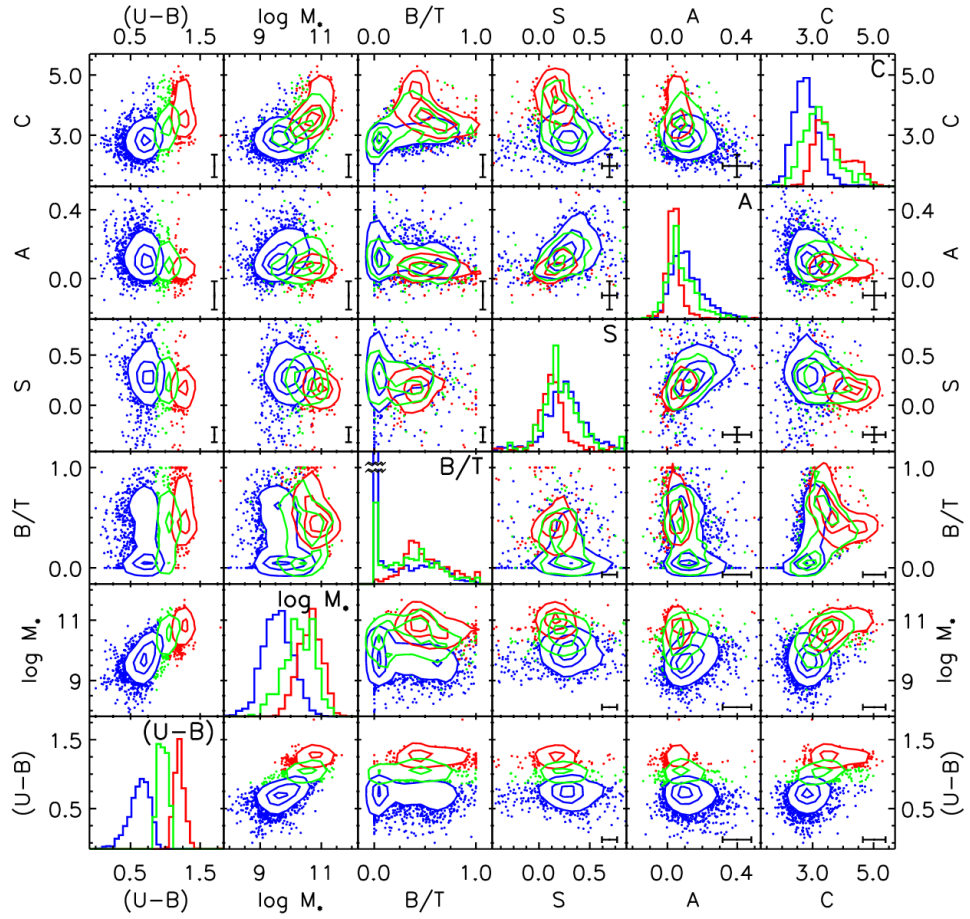

Figure 2.5: The bivariate distribution of galaxies from AEGIS, within the redshift range $0.4 \leq z \leq 1.2$ in multiple planes. Displayed are the galaxies colour (U-B), in rest frame, concentration (C), asymmetry (A), smoothness (S), bulge-to-total light fraction (B/T) and stellar mass. The data points, contours and histograms in blue, green and red shows the result for BC, GV and RS galaxies, respectively. The diagonal panels show the normalised histogram of various parameters. This figure is taken from Mendez et al. (2011).

larly, all morphological parameters, concentration, asymmetry, smoothness and B/T indicate that GV galaxies tend to have intermediate properties between BC and RS galaxies (see Fig. 2.5). The main exception to this rule is that BC galaxies have a higher fraction of mergers (19%±1%) than both GV (14%±2%) and RS galaxies (12%±2%), indicated by asymmetry and Gini Coefficient/M_{20} (Mendez et al., 2011). Note, this suggests a fraction of these galaxies could have undergone rejuvenation events (Thomas et al., 2010).

Furthermore, a more detailed analysis - study of the structure of GV galax-

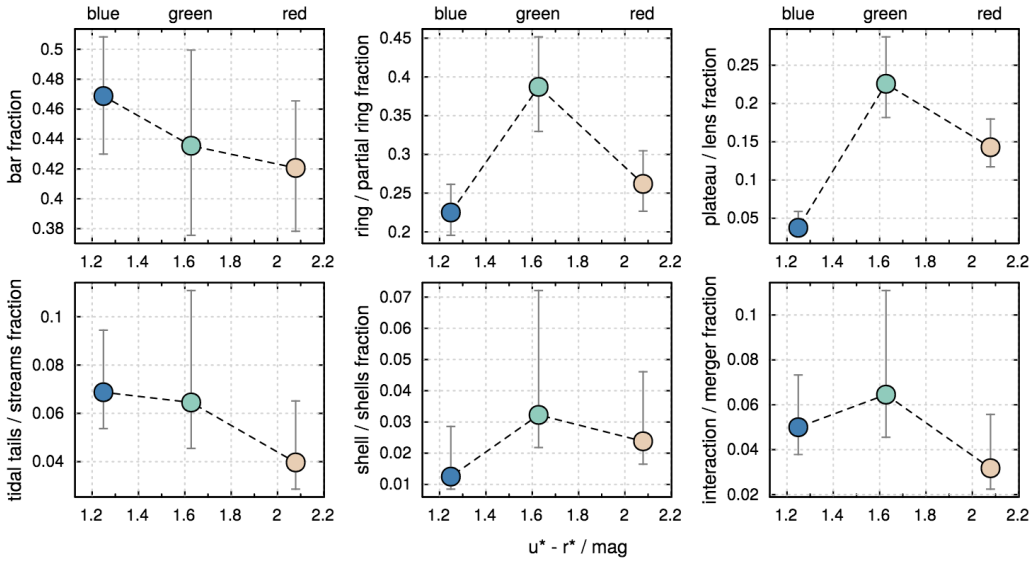

Figure 2.6: Fractions of galaxies with different structure for blue (blue), green (green) and red (peach) galaxies, defined using the galaxy colour ($u^{\star} - r^{\star}$). This figure can also be found in Kelvin et al. (2018).

ies - within a limited mass range $10.25 \lesssim \log \mathrm{M}_{\star}/\mathrm{M}_{\odot} \lesssim 10.75$, reveals an over-representation of rings and morphologically lens-like (they have a faint/shallow surface brightness in the middle but a sharp edge) galaxies ($53.23^{+6.14}_{-6.34}\%$) compared to BC ($37.30^{+4.48}_{-4.08}\%$) and RS ($25.00^{+3.72}_{-3.10}\%$). The aforementioned features are also more likely to be found in barred galaxies, by an increased factor of $\sim 20-30\%$, compared to their unbarred counterpart (Kelvin et al., 2018). One possible explanation for over-representation of such structure in GV could be owing to the higher fraction of S0-Sa type galaxies found in the GV. While there is a strong indication for GV galaxies favouring rings and lens like structure, there is little evidence supporting the higher fraction of galaxies with bars or tidal features (see Fig. 2.6), in agreement with a lower fraction of mergers in the GV. Such results suggests that the quenching of star formation could be non-violent, where the gas supply is gradually exhausted, favouring inside-out quenching.

2.2.2 Transition timescale

In addition to galaxy morphology, the GV also holds the information regarding quenching timescales/time taken to evolve from BC to RS. It was the dominant

belief due to the sparsity of the GV, that the transition must occur rather rapidly. However, based on SFH modelling and galaxy formation simulations, it has been found that such timescale can have a high variance (Schawinski et al., 2014; Wright et al., 2019; Correa et al., 2019). While there is a variety of timescales associated with transitioning galaxies, most studies assume an exponentially decaying SFR over time. Such SFH is formulated as

$$SFR(t) = SFR(0)e^{-t/\tau}, \tag{2.1}$$

where $SFR(0)$ represents the peak of SF activity, and τ is the rate of decay of star formation, also quoted as the *e*-folding time (Lee et al., 2010; Schawinski et al., 2014; Smethurst et al., 2015; Phillipps et al., 2019). Note while such modelling is sufficient for a rough estimation of the SFR decay, this does not explore in detail the nuances of SFH in actual galaxies - such as galaxies with later episodes of star formation or galaxies with constant SFR.

As mentioned in the previous section, the spectral indices, $D_n(4000)$ vs $H\delta_A$ can be used to determine the SFH of galaxies - especially those with SFH defined in equation 2.1. Hence, by constructing various SFH, with different rate of quenching, the transitioning timescales for galaxies are found to vary from 50 Myr to 7 Gyr. However, in the majority of cases, 50%, the transition timescale has been found to be ~ 2 Gyr (Martin et al., 2007). The vast variation in the transitioning can be partially explained by separating the galaxies into late- and early-types. It has been noted that, most fast transitioning galaxies are ETGs, which have a transitioning time of $\tau \lesssim 250$ Myr (see Fig. 2.7). Galaxies with slow quenching/transitioning timescales are usually LTGs, that have timescales of $\tau \gtrsim 1$ Gyr (Schawinski et al., 2014; Smethurst et al., 2015). This behaviour is reproduced in simulations, where elliptical galaxies have slightly shorter quenching timescales, $\tau \sim 1.0$ Gyr, compared to disc galaxies, $\tau_Q \sim 1.5$ Gyr (Correa et al., 2019). This large variation in the transition timescale suggests that galaxies of differing morphologies are likely to experience a very different form of quenching. Note, such studies based only on GV galaxies during transition can lead to some bias. Most GV galaxies are likely to

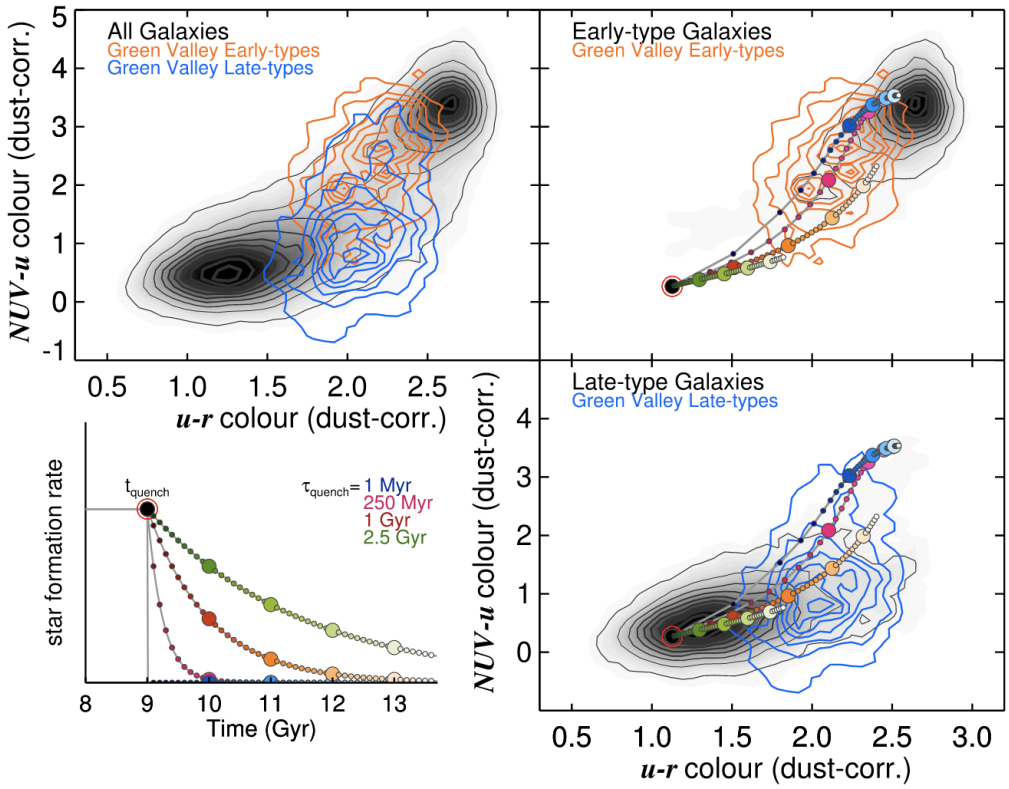

Figure 2.7: Distribution of galaxies in colour-colour space. The black contours shows the galaxy distribution of all galaxy type(top left), all ETGs (top right) and LTGs (bottom right). In each of these panels the blue and orange contours show the GV LTGs and ETGs respectively. Bottom left panel shows the different SFH, assuming different quenching timescales, where blue quenches the most rapidly and the green data points quench the slowest. Each small (big) points show evolution in spaces of 100 Myr (1 Gyr). Most ETGs galaxies seem to follow the most rapid quenching timescale ($\tau_Q \leq 250$ Myr) and LTGs locus reside close to the evolution track shown by slow quenching timescale, $\tau_Q \geq 1$ Gyr (Schawinski et al., 2014)

have rather long transition timescales, whereas galaxies that transition very rapidly are most likely to be found in the RS already (Martin et al., 2007; Smethurst et al., 2015, and references therein).

A more general study, without the separation of morphology, of different evolutionary stages currently finds transitioning timescales varying between 1.5-4.0 Gyr. Furthermore, the rate of decay or the e-folding times are estimated to be $\tau \sim 4$ Gyr for GV and 6 Gyr for BC galaxies (Phillipps et al., 2019). By evolving the galaxies colour, they also showed that, similarly to how GV galaxies end up in RS, BC galaxies should also evolve to GV, i.e., eventually quench their SF.

The timescale for which the galaxies end up quenching their star formation is also shown to depend on the model used. Assuming a "closed-box", where there is no expulsion of material via outflow, or a "leaky-box" (i.e material loss through outflow, models can give differing timescales). Assuming the "leaky-box" model, for the same set of galaxies slightly longer times are found, 5-7 Gyr, with a shorter decay rate, $e-$folding timescale ~ 1 Gyr, compared to the "closed-box" model; 2-5 Gyr for quenching timescale and $e-$folding $\sim 2-4$ Gyr (Trussler et al., 2020). Additionally, they found that while the "closed-box" model was able to match the observations in most instances, the "leaky-box" model mostly failed at reproducing the observed trend for stellar mass higher than $10^{9.8} M_{\odot}$. This, along with results from other studies (Kauffmann et al., 2003; Brinchmann et al., 2004; Phillipps et al., 2019), heavily suggests that the quenching timescale is strongly dependent on stellar mass. As previously mentioned, a similar exercise can be carried out for RS galaxies to estimate their past transitioning timescales, which find their quenching timescales to be shorter than current GV galaxies. This supports two main hypotheses (i) quenching in the local Universe is slower than at high redshift (ii) most current GV galaxies have a longer quenching timescale and galaxies that quench rapidly are mostly in the RS (Martin et al., 2007; Salim, 2014). The long quenching timescale is further supported by the existence of the Green Mountain (GM), when selecting galaxies based on sub-millimeter surveys (Eales et al., 2018).

In addition to observational studies, the quenching timescales are also studied in detail using state-of-the-art hydrodynamical simulations such as EAGLE (Schaye et al., 2015; Crain et al., 2015) and IllustrisTNG (Pillepich et al., 2018a; Marinacci et al., 2018; Springel et al., 2018; Nelson et al., 2018; Naiman et al., 2018). EAGLE has used both colour and sSFR - in contrast to TNG100, which has only used colour - to define the evolutionary sequence, finding the median transition timescale to be $\Delta t_{green} \sim 1.6$ Gyr, with 10th-90th percentile spread is $\sim 0.7-3.8$ Gyr (Trayford et al., 2017; Wright et al., 2019; Nelson et al., 2018). Such large variation in quenching timescales are mostly associated to the differing halo mass and stellar mass. For low mass systems, $\log \mathrm{M}_{\star}/\mathrm{M}_{\odot} \lesssim 9.6$, the quenching timescale is esti-

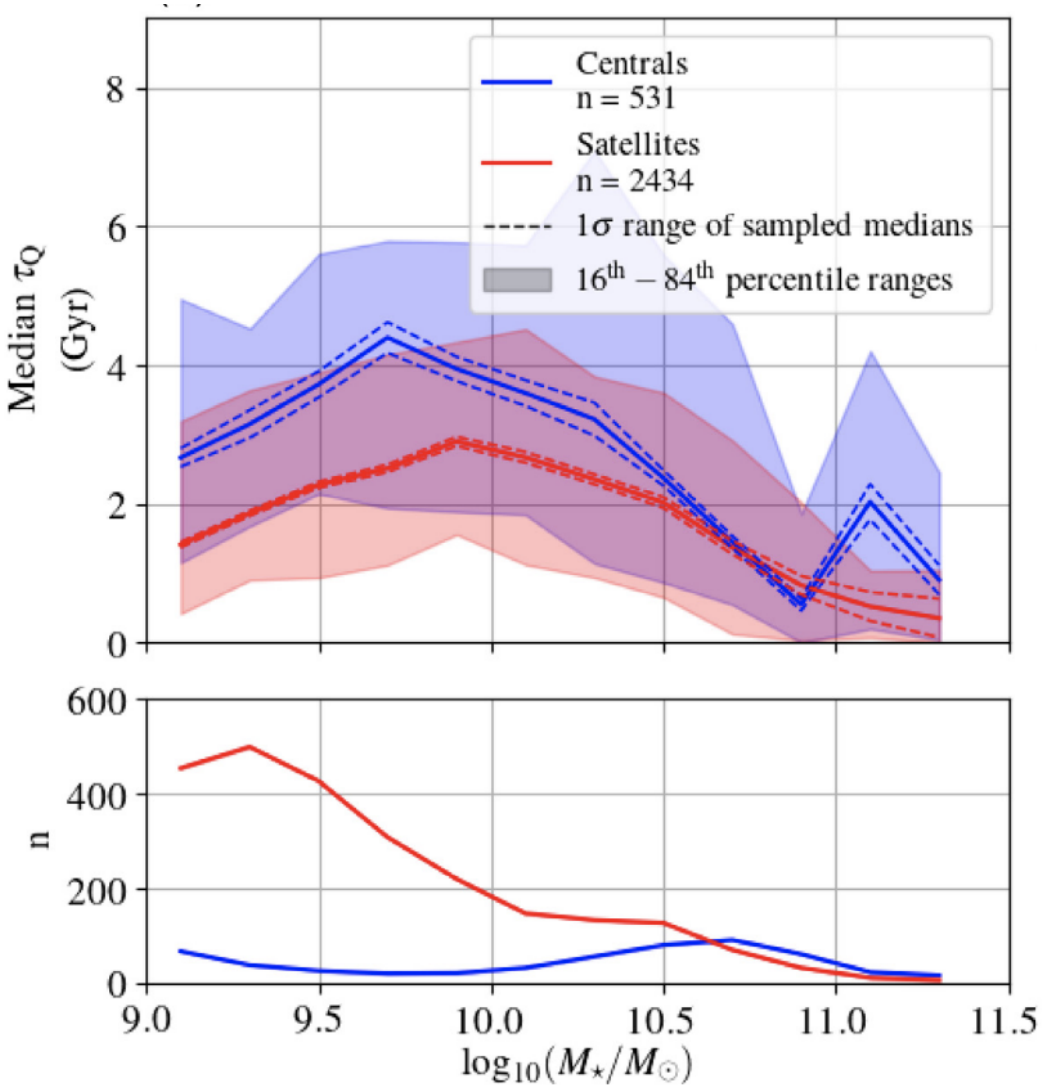

Figure 2.8: This shows the median timescale for galaxies to become passive at current redshift, $z = 0$. The galaxies have been separated in centrals (blue) and satellites (red), where the solid lines show the median value, dashed line show 1σ and shaded regions show 16^{th} and 84^{th} percentile. Both central and satellite galaxies show an increase in τ_Q with mass for low mass, then a decrease in τ_Q with increase in mass for high mass - indicating different modes of quenching. The blue and red lines at bottom panel show the number of galaxies in each stellar mass bin considered (Wright et al., 2019)

mated to be $\tau_Q \sim 4(3)\,\mathrm{Gyr}$ for central (satellite) galaxies. This is noted to decrease, $\tau_Q \gtrsim 3.0\,\mathrm{Gyr}$, for intermediate mass galaxies $9.7 \lesssim \log \mathrm{M}_\star/\mathrm{M}_\odot \lesssim 10.3$. Finally for the highest stellar mass objects, $\log \mathrm{M}_\star/\mathrm{M}_\odot \gtrsim 10.30$, both central and satellite galaxies have the shortest quenching timescales $\tau_Q \lesssim 1.5\,\mathrm{Gyr}$ (Wright et al., 2019) - see Fig. 2.8.

2.2.3 Quenching mechanisms

Both observational and simulation studies (Phillipps et al., 2019; Correa et al., 2019), find heavy dependency between stellar mass and quenching timescale. There could be multiple reasons for this. One such possible avenue could be as different quenching mechanisms are dominant in different stellar mass bins. It is strongly believed that environmental quenching plays an important role in low mass galaxies and mass quenching is significant in high mass systems. In this section, we will describe such physical processes relevant to different stellar masses.

At low stellar mass, it is strongly believed that environment plays an important role (Kauffmann et al., 2004; Peng et al., 2010; La Barbera et al., 2014), where galaxy-galaxy interactions would lead to quenching. Galaxy interactions can cause tidal stripping, where the gas from one galaxy, usually the one with smaller stellar mass, is accreted, by the more massive galaxy (Johnston et al., 1999). However, a more common scenario of the environmental effect is known as ram-pressure stripping. This occurs when a satellite galaxy falls into a dense cluster - as shown by Kauffmann et al. (2004), where galaxies in the densest environments happen to be RS galaxies. In such instance, the gas, from the interstellar medium (ISM) of the infalling galaxy is rapidly removed by the surrounding intracluster medium (ICM), which in turn causes rapid quenching of star formation (Abadi et al., 1999; Schawinski et al., 2007). Due to the density and temperature of the intergalactic medium (IGM), infalling galaxies are unable to accrete additional gas, further contributing to the quenching of star formation, known as strangulation (van den Bosch et al., 2008). Such a combination of processes is expected to produce very rapid quenching timescales, $\tau \sim 200\,\mathrm{Myr}$ (Steinhauser et al., 2016) - $\tau \sim 2\,\mathrm{Gyr}$ (Wright et al., 2019), as mentioned above. Note, Trussler et al. (2020) assume various models in terms of galaxy quenching and evolution. At $\log \mathrm{M}_\star/\mathrm{M}_\odot \lesssim 9.8$, the leaky-box model, which mimics the tidal stripping/ram-pressure stripping behaviour, finds a good fit to the observed mass-metallicity relation. However, at higher stellar mass such model fails to match the observation. Instead, a closed box model, which behaves similarly to only galaxy strangulation/starvation, is able to

match the observed trend. Note, such a mechanism is expected to take a longer time to quench the star formation of a galaxy, $\sim 5\,\mathrm{Gyr}$, as it is not a pure dynamical process. This hypothesis is supported by the low fraction of GV galaxies with tidal features found by Kelvin et al. (2018). Furthermore, this is consistent with simulations where the longest quenching timescales are found in intermediate mass bins $9.7 \lesssim \log \mathrm{M}_\star/\mathrm{M}_\odot \lesssim 10.3$, for both central and satellite galaxies (see Fig. 2.8). Moreover, local events such as supernovae are also expected to suppress star formation in galaxies by heating and evaporating the dense star-forming clouds or by ejecting the gas reservoir from the galaxy into the intergalactic medium (Silk and Rees, 1998; Bower et al., 2006; Dalla Vecchia and Schaye, 2012).

Finally, in the high stellar mass regime, $\log \mathrm{M}_\star/\mathrm{M}_\odot \gtrsim 10.3$, owing to a drop in the quenching timescale, $\tau_Q \lesssim 1.5\,\mathrm{Gyr}$, it is speculated that AGN feedback with combination of major merging quenches the star formation. In addition, the quenching timescales of galaxies are thought to be independent of their environment (Kauffmann et al., 2004; Peng et al., 2010; La Barbera et al., 2014). On the observation end, the GV is found to contain high fraction of AGN, as high as 50% (Martin et al., 2007). A more detailed study reveals that most galaxies hosting AGN happen to be high mass, and strong AGN ($\mathrm{L[OIII]} > 10^7 \mathrm{L}_\odot$) are more important at the initial stages of quenching star formation as these galaxies still have relative high sSFR. In contrast, weak AGN galaxies have sSFR that deviate from the main sequence region to the quiescence area, indicating that such AGN maintain the quiescence state (maintenance mode) by preventing the gas within the galaxy from cooling down (Kauffmann et al., 2003; Ho, 2008; Salim, 2014). Furthermore, rather than using single aperture fibre studies, surveys of galaxies using Integral Field Spectroscopy (IFS) have shown AGN to reside predominantly in the BC/GV region (Sánchez et al., 2018; Lacerda et al., 2020) - see Fig. 2.9. Note, for such studies, these galaxies have been classified as AGN using the BPT scheme (Baldwin et al., 1981). There are two major caveats that might result in inconsistencies with other studies (i) the emission lines used to classify galaxies into low-ionization nuclear emission-line region (LINER) could be due to emission from old hot stars (Belfiore et al., 2016)

(ii) a galaxy classified as SF in the optical might still harbour an AGN at the center of the galaxy that is more readily observed in different wavebands. Furthermore, study of galaxies at different scales indicate that the presence of AGN heavily favour inside-out quenching as most galaxies would have older stellar populations in the central region compared to the outer region (Lacerda et al., 2020). Such results are in agreement with most state-of-the-art simulations as they have found the AGN is necessary to reproduce the fundamental scaling relations and bimodal distribution of the galaxies (Somerville et al., 2008; Hopkins et al., 2008; Schaye et al., 2015; Trayford et al., 2015). Note the initial Illustris simulation (Vogelsberger et al., 2014; Genel et al., 2014; Sijacki et al., 2015) only implemented one mode of AGN feedback, but were unable to reproduce the bimodal distribution of galaxies in the high stellar mass regime at our current redshift. Therefore, in IllustrisTNG (Pillepich et al., 2018a; Weinberger et al., 2018) a more efficient AGN feedback mode was implemented, which properly reproduced the observed properties of galaxies even at high stellar mass. The mismatch, specifically at high stellar mass, with one mode of AGN, provided strong evidence for the need of AGN to quench star formation.

Furthermore, simulations provides us with an unique ability to study the impact of AGN by running multiple simulations, with same sub-grid physics and initial conditions but with one major difference - one implements a black hole seed mass and AGN sub-grid physics, while the other run has no AGN (Hirschmann et al., 2017; Dashyan et al., 2019). Such simulations find that AGN greatly impacts the gas contents and the SFH of not only their host galaxies but also their satellite galaxies, where simulations with AGN consistently produce a higher fraction of quiescent galaxies for a given cosmological time. Similarly, they also find that galaxies have a lower fraction of gas for AGN simulations for a given time and radii compared to no-AGN simulations (Dashyan et al., 2019).

Note, so far we have mainly discussed negative feedback of AGN, which causes quenching of star formation. However, there have been studies showing the AGN imparts a positive feedback, where it enhances the star formation rate. This was most evident when looking at SFR computed using IR luminosities, which

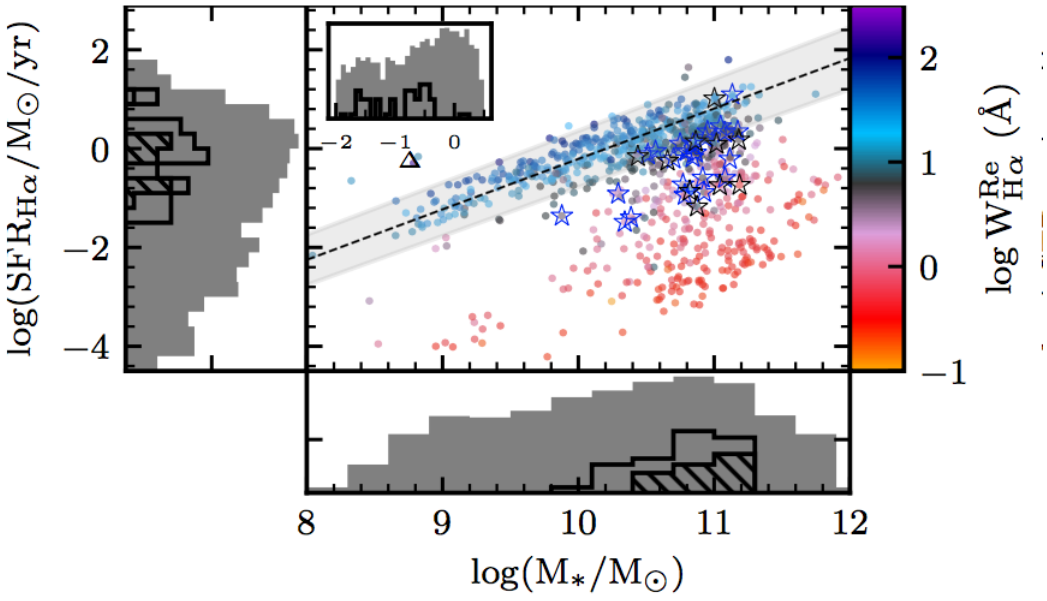

Figure 2.9: The figure shows the integrated SFR, calculated from Hα, vs stellar mass. The dotted data points show non-AGN galaxies, while the black and blue star symbol show galaxies hosting AGN, type 1 and 2, respectively. The dotted black like shows the SFMS, where the filled area represents the 1σ variations. The left and bottom panels show the histograms of all galaxies in grey, and AGN type 1 and 2 in hatched and unfilled, respectively. The inset shows the distance, Δ(logSFR), of individual galaxies from the SFMS (Lacerda et al., 2020).

found that galaxies in the GV that host an AGN are at the upper end of the star forming main sequence (SFMS), above the non-AGN counterpart (Mahoro et al., 2017). Additionally, AGN galaxies in the GV showed a higher fraction (38%) of galaxy-galaxy interactions compared to their non-AGN counterpart (19%) (Mahoro et al., 2019). This suggests the high SFR of GV galaxies, in IR, could be due to a combination of AGN feedback, through positive feedback, and galaxy-galaxy interaction - albeit galaxies without signatures of interaction but with evidence of AGN feedback still had higher SFR than their no-AGN counterparts.

2.2.4 Reverse evolution?

So far all evolutionary tracks assume a transition from BC to GV to RS. However in reality, the picture is more complex than this owing to rejuvenation. Galaxies in both the field and dense environments can undergo minor mergers, which

gives the galaxy a fresh supply of gas initiating star formation (Faber et al., 2007; Gaibler et al., 2012). Such events will cause RS galaxies to move "down" to GV or BC, as seen by the higher fraction of merging galaxies in Mendez et al. (2011). Such galaxies tend to generally have younger stellar populations as well as lower α/Fe abundance ratio (Thomas et al., 2010). However, such galaxies are hard to identify as they might simply be galaxies that have formed recently. Simulations have also seen such behaviour where galaxies do not simply evolve from BC to RS and stay there. IllustrisTNG galaxies tend to be constantly moving up and down the evolutionary sequence. However, only a fraction, 10%, at highest stellar mass, $\log \mathrm{M}_\star/\mathrm{M}_\odot \gtrsim 11.0$, of galaxies will truly experience 'rejuvenation' - sufficient enough star formation to cause them to move from RS to GV or BC - and an even smaller fraction (1%) will experience multiple rejuvenation episodes (Nelson et al., 2018).

2.2.5 Green Valley and the evolution of galaxies

The study of galaxy formation and evolution is one of the key facets of astrophysics, where many important discoveries have been made over the past decades. Owing to the complexity of the physics, there are still many unknowns, especially with regards to the fundamental mechanisms under which galaxies quench their star formation and the timescales associated to these processes. Attempts to answer such questions have been made via the use of (i) high quality surveys (York et al., 2000) and (ii) cosmological hydrodynamical simulations (Schaye et al., 2015; Pillepich et al., 2018a). One of the main discoveries, pertaining to galaxy evolution, is the existence of a bimodal distribution in optical wavebands (Strateva et al., 2001). This bimodal distribution can be constructed using properties such as their colour-magnitude (Graves et al., 2007; Baldry et al., 2004; Martin et al., 2007), colour-stellar mass (Schawinski et al., 2014; Trayford et al., 2015; Nelson et al., 2018), SFR-stellar mass (Schiminovich et al., 2007; Wright et al., 2019; Trussler et al., 2020), UVJ bi-colour (Williams et al., 2009) and recently $\mathrm{D}_n(4000)$-velocity dispersion (Angthopo et al., 2019). The existence of such bimodal distributions has been attributed largely to the ability to categorise galaxies into two distinct groups -

Star Forming (SF) and Quiescent (Q). Regions occupied by SF, primarily late-type galaxies (LTGs), and Q galaxies, predominantly early-type galaxies (ETGs), are labelled blue cloud (BC) and red sequence (RS), respectively, in the colour-mass diagram. The region between BC and RS, coined the Green Valley (GV), is thought to host transitioning galaxies.

The GV population is thought to define a class of its own , rather than a mix between BC and RS (Wyder et al., 2007). Therefore, the study of GV galaxies has given us a unique insight into how galaxies evolve. Previous studies find multiple evolutionary paths (Faber et al., 2007; Salim, 2014; Schawinski et al., 2014), where ETGs are thought to have shorter quenching timescales, $\tau \lesssim 250\,\mathrm{Myr}$, compared to LTGs, $\tau \gtrsim 3.5\,\mathrm{Gyr}$ (Schawinski et al., 2014). Furthermore, low mass systems ($\log \mathrm{M}_\star/\mathrm{M}_\odot \lesssim 9.6$) are thought to quench their star formation mainly due to environmental reasons, i.e. strangulation, galaxy harassment and ram-pressure stripping (Kauffmann et al., 2004; Peng et al., 2010; Pasquali et al., 2010, 2012; La Barbera et al., 2014). These have relatively low quenching timescales $\tau \sim 2\,\mathrm{Gyr}$ (Wright et al., 2019). Intermediate mass systems ($9.6 \lesssim \log \mathrm{M}_\star/\mathrm{M}_\odot \lesssim 10.3$) quench their star formation through stellar feedback, such as supernovae (Somerville et al., 2008), starvation (Phillipps et al., 2019) or AGN feedback (Dekel and Silk, 1986; Dalla Vecchia and Schaye, 2012) and are expected to have longer quenching timescales, $\tau \sim 5\,\mathrm{Gyr}$. Finally, most massive systems have the shortest quenching timescales $\tau \lesssim 1.5\,\mathrm{Gyr}$, as they quench mostly through major mergers, AGN feedback and halo heating (Faber et al., 2007; McIntosh et al., 2014). Therefore, the different quenching mechanisms being dominant in different stellar mass regimes explain the strong correlation between stellar mass and quenching timescale.

Chapter 3

A detailed exploration of Green Valley galaxies

3.1 Introduction

In the previous chapter, we discussed the main results from the literature regarding the green valley (GV). This entailed the selection and different definition of the GV to select transitioning galaxies, as well as the study of their galactic properties, such as their morphology, structure, and galaxy type (i.e. Star forming, Composite, AGN or Quiescent). We also summarised the main results regarding their stellar population properties, such as their average age and metallicity, as well as their quenching/transition timescale from BC to RS. However, we also pointed out some of the caveats of the traditional methods, as they require various forms of correction/modelling i.e. the use of colour to define the GV requires dust correction - which varies depending on the dust attenuation models used, hence hosting inherent systematics - or the use of SFR requiring some form of modelling. In this chapter, we propose a novel way of defining and selecting the transitioning galaxies, with uses the 4000Å break, and compare our results with a more traditional approach based on the colour of galaxies. This work is based on the following published papers Angthopo et al. (2019) and Angthopo et al. (2020), hereafter A19 and A20, respectively.

3.2 Sample Selection

3.2.1 Spectroscopic Data

We select the sample and retrieve the spectra from Data Release 14 of the Sloan Digital Sky Survey (SDSS, Abolfathi et al., 2018). SDSS is a full-sky survey that includes spectroscopic observations of galaxies with Petrosian *r*-band magnitude in the range $14.5 < r_{AB} < 17.7$. Our selection criteria identifies targets with relatively high signal-to-noise ratio, snMedian_r>10. Furthermore, we limit our study within the redshift interval 0.05<z<0.10. After the implementation of our selection criteria, the data set comprises 228,880 spectra. We choose the stellar velocity dispersion as the main stacking parameter, instead of the standard choice of either the total luminosity or the stellar mass of the galaxy. The velocity dispersion (σ) is found to correlate more strongly with the underlying population properties (see, e.g., Bernardi et al., 2003; Thomas et al., 2005; Ferreras et al., 2019), and is less prone to potential systematics, as it is measured in a straightforward way from the absorption line spectra. The velocity dispersion can be mapped onto stellar mass (M_*) by use of an empirical scaling relation obtained from SDSS data: $\log M_*/M_\odot = (1.84 \pm 0.03)\log(\sigma/100\,\mathrm{km\,s^{-1}}) + (10.3 \pm 0.3)$, with the uncertainties quoted at the 68% level. Note also that the velocity dispersion of the spheroidal component correlates well with black hole mass, more strongly than does stellar mass (Gültekin et al., 2009). This will enable us to refine AGN fractions in the GV. The sample is divided into six velocity dispersion bins between σ=70 and 250 $\mathrm{km\,s^{-1}}$ in steps of $\Delta\sigma$=30 $\mathrm{km\,s^{-1}}$. We note that with the adopted range of σ, along with the constraint on the S/N of the spectra, the estimates of velocity dispersion provided by the SDSS SpecObj catalogue are reliable [1].

The SDSS spectra cover the wavelength range 3800–9200 Å, with variable resolution, from R=1,500 at λ=3,800 Å, increasing to R=2,500 at λ=9,000 Å (Smee et al., 2013). The spectra are dereddend with respect to foreground extinction, adopting the standard Milky Way dust law (Cardelli et al., 1989). The correction required was determined by the extinction parameter A_g, quoted in the SDSS cat-

[1] http://classic.sdss.org/dr7/algorithms/veldisp.html

alogues, evaluated in the g band. Once the foreground dust correction is applied, the spectra are brought to the rest frame, and the individual estimates of the 4000Å break are measured, adopting the following definition (Balogh et al., 1999):

$$\mathrm{D}_n(4000) = \frac{\langle \Phi^R \rangle}{\langle \Phi^B \rangle}, \text{ where } \langle \Phi^i \rangle \equiv \frac{1}{(\lambda_2^i - \lambda_1^i)} \int_{\lambda_1^i}^{\lambda_2^i} \Phi(\lambda) d\lambda \tag{3.1}$$

and $(\lambda_1^B, \lambda_2^B, \lambda_1^R, \lambda_2^R) = (3850, 3950, 4000, 4100)$Å. Note that our definition contrasts with the traditional approach, originally defined by Bruzual (1983) that integrate $\Phi(\nu)$ in wavelength space. We believe our definition has an easier interpretation, as the flux ratio between two spectral intervals that straddle the 4000Å break. These two definitions can be compared via a rescaling with a constant factor $\sim$1.07 between the old and the new definition, with a slight dependency upon the underlying population, see Fig. 3.1.

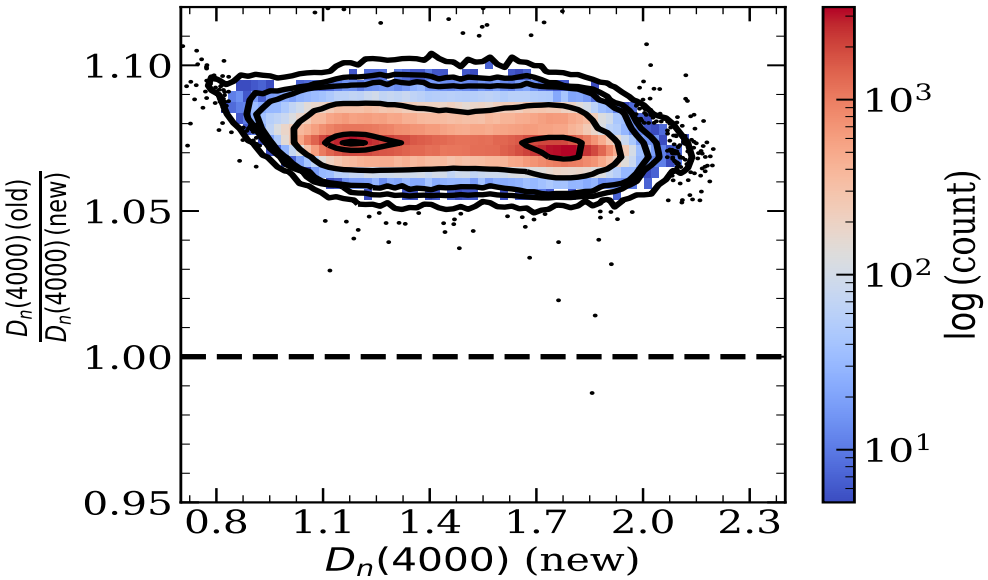

Figure 3.1: The ratio of $\mathrm{D}_n(4000)$ index measured using following Eq. 11 of Bruzual (1983) and $\mathrm{D}_n(4000)$ index calculated using Eq. 3.1. The density plot and contours show the distribution of ratio for the SDSS galaxies. The dashed black line marks the 1.0 value.

We use the $\mathrm{D}_n(4000)$ index to define the GV. For comparison, we contrast the newly defined GV with the traditional one based on colours from broadband pho-

tometry. We adopt $^{0.1}(g-r)$ as the reference colour, i.e. all galaxies are measured at a fiducial redshift z=0.1. The colours are taken from the flux ratios as measured within the 3 arcsec fibres of the SDSS classic spectrograph – to be consistent with the analysis of the observed spectra – and the K-correction needed to bring them to the fiducial redshift is measured directly from the spectra, following the standard approach (see, e.g. Hogg et al., 2002), adopting a standard cosmology ($\Omega_m = 0.3$; $\Omega_\Lambda = 0.7$, $H = 70\,\mathrm{km\,s^{-1}\,Mpc^{-1}}$). As reference, our K-correction in $(g-r)$ stays below 0.14 mag (below 0.085 mag in 90% of the sample), and the median correction applied is $+0.04 \pm 0.03$ mag. The colour is also corrected for *intrinsic* dust absorption, following the dust parameters of Kauffmann et al. (2003) and adopting the Calzetti et al. (2000) attenuation law. Note we use A_V as baseline for the correction, where we find, at z=0.1, $A_g^{0.1} = 1.16 A_V^{0.1}$ and $A_r^{0.1} = 0.88 A_V^{0.1}$.

3.2.2 Defining the Green Valley

For the definition of the Green Valley, there are multiple methodologies one can follow. In this section we will describe in detail the main approach, which were adopted in A19 and A20, as well as outline a different approach that was implemented to make a catalogue for our $\sim 228,000$ SDSS galaxies - identifying each galaxy as belonging to BC, GV or RS.

3.2.2.1 A19 and A20 method

We base our definition of the GV on the relative distribution of the star-forming (SF) and quiescent (Q) subsamples. We make use of the MPA-JHU SDSS catalogues (Kauffmann et al., 2003; Brinchmann et al., 2004) that provide a classification of the galaxy spectra from nebular emission lines into star-forming (BPT=1,2), composite (BPT=3), Seyfert AGN (BPT=4), LINER AGN (BPT=5) or quiescent (BPT=-1), where the latter class means no emission lines are present. We follow a probability-based approach, defining a probability distribution function (PDF) for the BC, $\mathscr{P}_{\mathrm{BC}}$ (defined using the SF galaxy distribution, BPT$=1$), and a PDF for the RS, $\mathscr{P}_{\mathrm{RS}}$ (defined using the Q galaxy distribution, BPT $= -1$). These functions are assumed to depend on two parameters only, the stellar velocity dispersion (σ)

and an additional parameter (π); that serves as a proxy of the stellar age of the underlying populations. We model the PDFs as a Gaussian distribution described by the formulation:

$$\mathscr{P}_k(\pi;\sigma) \equiv \frac{1}{s_k(\sigma)\sqrt{2\pi}} e^{-\frac{1}{2}\left[\frac{\pi-\mu_k(\sigma)}{s_k(\sigma)}\right]^2}, \tag{3.2}$$

where $\mu_k(\sigma)$ and $s_k(\sigma)$ are the mean and the standard deviation of the distribution of π corresponding to galaxies in the velocity dispersion bin given by σ, respectively. We now propose the ansatz that these Gaussian distributions be interpreted as the probability distribution function (PDF) of blue cloud galaxies (for k=SF) and red sequence galaxies (for k=Q). Once the PDFs are defined for the BC and RS, the green valley subset is assumed to follow a probability distribution function given by:

$$\mathscr{P}_{GV}(\pi;\sigma) \equiv \frac{1}{s_{GV}(\sigma)\sqrt{2\pi}} e^{-\frac{1}{2}\left[\frac{\pi-\mu_{GV}(\sigma)}{s_{GV}(\sigma)}\right]^2}, \tag{3.3}$$

where the width of the Gaussian is chosen

$$s_{GV}(\sigma) \equiv \frac{1}{2} s_{Q}(\sigma), \tag{3.4}$$

and the mean is given by

$$\mathscr{P}_{SF}[\mu_{SF}(\sigma);\sigma] \equiv \mathscr{P}_{Q}[\mu_{Q}(\sigma);\sigma]. \tag{3.5}$$

We emphasize these constraints are purely empirical and defined ad hoc. The constraint on the mean implies that at the peak of the GV PDF, a BC galaxy and a RS galaxy are indistinguishable from a probabilistic point of view. The constraint on the width ensures that the GV does not include large fractions of galaxies in the BC or RS regions. However, for a given velocity dispersion bin, it is still possible to select a galaxy as belonging to the GV, even if they reside towards the peak of BC or RS distribution.

Figs. 3.2 and 3.3 present the probability functions obtained for the six velocity dispersion bins, defined using $D_n(4000)$ index and dust corrected colour, ${}^{0.1}(g-r)$, respectively. Both cases show the well-known trend towards higher break strengths

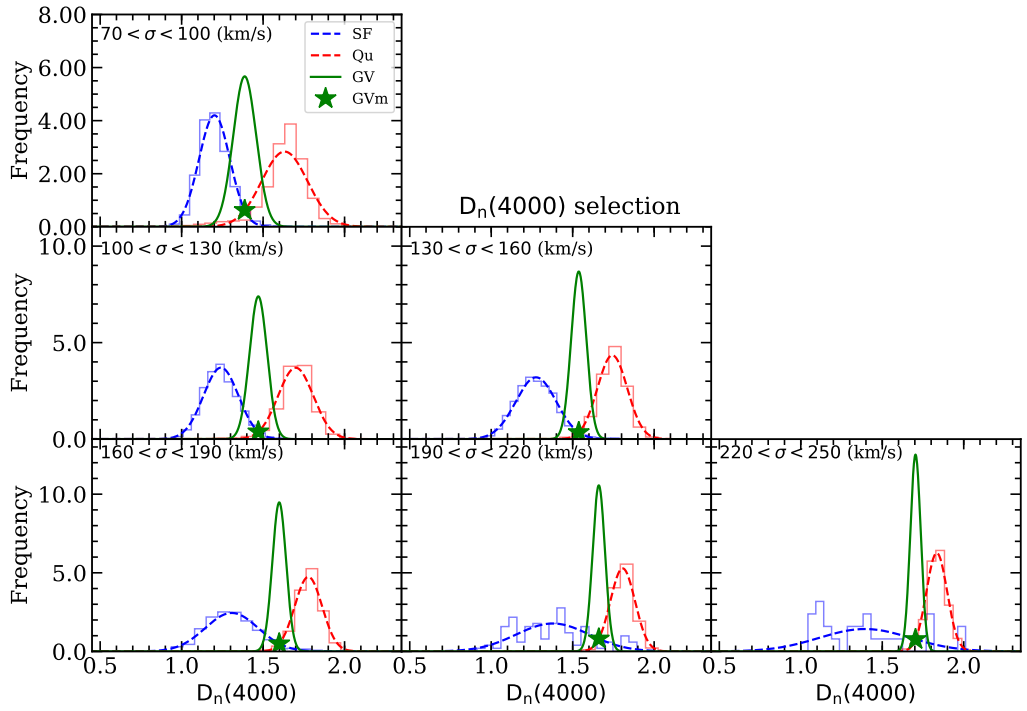

Figure 3.2: This figure presents the distribution of SF (blue) and Q (red) galaxies, which are used to define the probability distribution function (PDF) for the BC ($\mathscr{P}_{BC}$) and RS ($\mathscr{P}_{RS}$), respectively, for different velocity dispersion bins. For the PDF, we assume them to follow a Gaussian distribution. The midpoint of the GV, shown by a star symbol, is located where $\mathscr{P}_{BC} = \mathscr{P}_{RS}$. This shows the definition of the GV population using 4000Å break strength.

or redder colours as velocity dispersion increases. The mean position of the GV is represented by a star symbol. Note the significant difference between the choice of break strength and colour regarding the overlap of the SF and Q subsets. A colour-based approach produces more mixed subsamples that complicates the selection of GV galaxies, whereas the 4000Å break strength produces a sharper separation[2]. Note, $D_n(4000)$ provides an alternative, clean separation between BC, GV and RS *without requiring any dust correction or K-correction.* Therefore, $D_n(4000)$ carries a lower systematic uncertainty from the modelling associated to these corrections. This alternative definition of the GV requires low SNR spectroscopic data, as the 4000 Å break is relatively wide and can be measured even at low spectral resolution (e.g., Hathi et al., 2009; Hernán-Caballero et al., 2013). Note, this methodology can

[2]Colours such as $(u-g)$ or $(u-r)$ produce very similar results to $(g-r)$, however we chose the latter as the observations have markedly lower uncertainties.

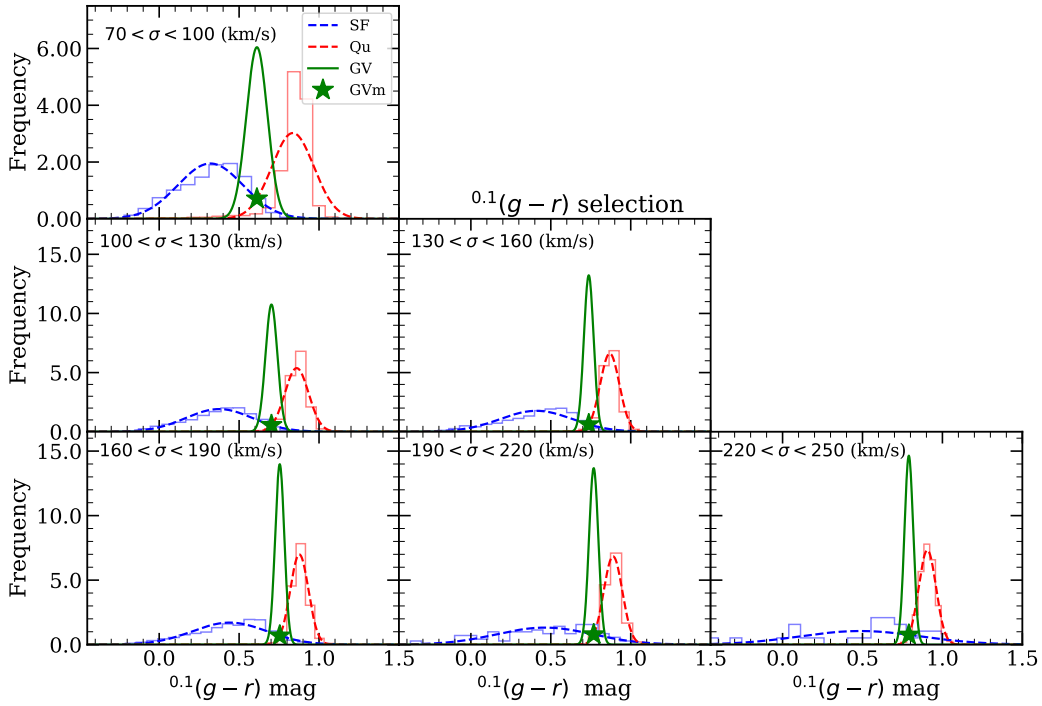

Figure 3.3: Same as Fig. 3.2 but for $^{0.1}(g-r)$ colour (dust-corrected).

be easily used for upcoming/future spectroscopic surveys on the horizon such as WAVES (Driver et al., 2019), WEAVE (Dalton, 2016), DESI (DESI Collaboration et al., 2016) or J-PAS (Benitez et al., 2014).

We apply this method independently within each velocity dispersion bin. The actual selection of GV galaxies follows a Monte Carlo sampling method. For each galaxy within a given velocity dispersion bin, a uniform random deviate (r) is obtained between 0 and 1, and the galaxy is accepted into the GV subset if $\mathscr{P}_{\rm GV}[\pi;\sigma] > r$. Fig. 3.4 presents an example of this selection criterion, within a velocity dispersion bin $130 < \sigma < 160\,{\rm kms}^{-1}$, where the blue, red and green lines show the BC, GV and RS density distributions, respectively. The green star, again, shows the midpoint of the GV. The black line represents the probability of a GV with the given $D_n(4000)$ to be a GV galaxy. The red data points show the r value, randomly assigned to each galaxy, and the black unfilled data points around the red data points indicate the galaxies that are not selected. Note our multiple runs will assign a random r value to the same galaxy, hence in the next iteration there will

be a different set of galaxies, i.e. the vertical location of red dots would change. This shows, while our solution is not unique, galaxies with $D_n(4000)$ or colour value near the green star, μ_{GV}, will have a high probability of being selected as GV during multiple iterations, decreasing as $D_n(4000)$ departs from the μ_{GV}.

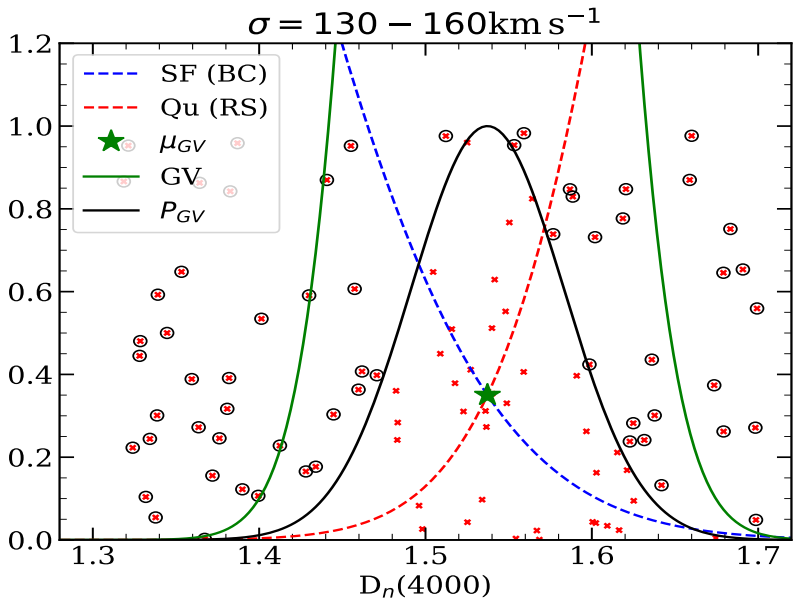

Figure 3.4: Example of selected and unselected galaxies using the method described above. The blue, red and green lines outline the regions of defined BC, RS and GV, respectively. The black line shows the probability of a galaxy with that $D_n(4000)$ value to be selected as GV galaxy, i.e. $\mathscr{P}_{GV}$. The red dots are random values, r, also ranging from 0 to 1, for galaxies with with a given 4000Å break strength. If $\mathscr{P}_{GV} > r$, we select them to be GV galaxy, otherwise we exclude them, indicated by the black unfilled circles.

We will compare here two choices, the dust-corrected colour – defined by $(g - r)$ as observed at a fiducial redshift z=0.1 – and the dust uncorrected strength of the 4000Å break. We adopted the dust correction values from Kauffmann et al. (2003), using the Calzetti et al. (2000) attenuation law, thus enabling a fair comparison to the analysis of Martin et al. (2007), hereafter M07. Note we use A_V, instead of A_z as baseline for the correction. Figure 3.5 shows the location of the three key evolutionary regions following this methodology, according to $D_n(4000)$ (left panel), ${}^{0.1}(g - r)$ (uncorrected, centre panel, shown for reference), or ${}^{0.1}(g - r)$ (dust-corrected, right panel). The points with error bars show the mean and standard

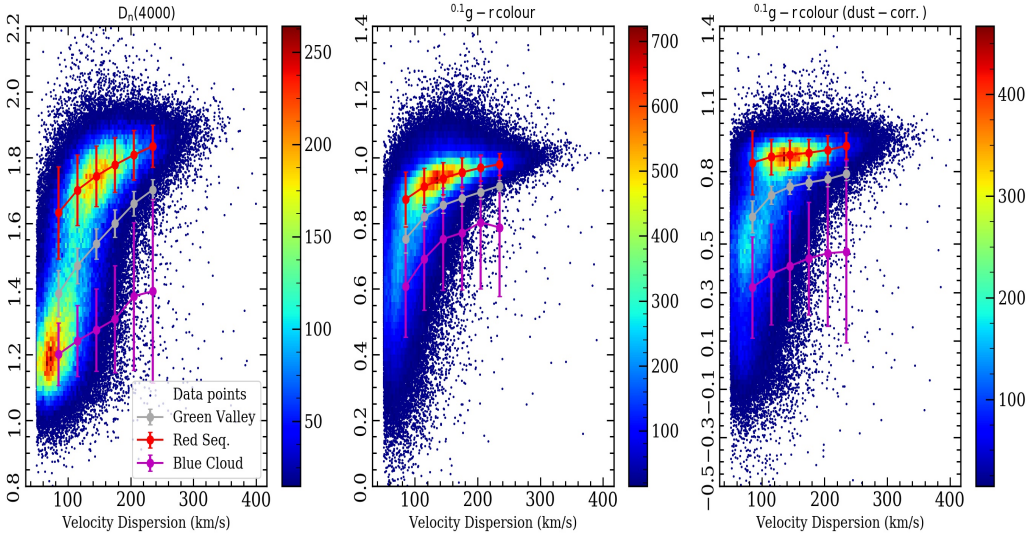

Figure 3.5: *Left:* Distribution of SDSS galaxies with $S/N > 10$ on the $D_n(4000)$ vs velocity dispersion plane. The colour map traces number density of individual galaxies on the diagram, where the colour bar to the right of each panel maps the density to colour. The BC, GV and RS regions are shown by magenta, gray and red data points, where the points locate the mean of each region and errorbars span one standard deviation (i.e. the corresponding to their respective Gaussians in figure 3.2 and 3.3). *Centre:* Distribution of galaxies on the $^{0.1}(g-r)$ colour (dust-uncorrected, shown for reference) vs velocity dispersion plane. *Right:* Equivalent distribution with the dust-corrected $^{0.1}(g-r)$ colour. Note the $D_n(4000)$ measurements have not been corrected for dust, as the correction is negligible for our purposes.

deviation of each subsample. For reference, individual data points are shown as a density plot. Note the impact on the GV definition between the colour distribution before and after the dust correction is applied. Comparatively, the equivalent dust correction for $D_n(4000)$ is smaller, resulting in a minor shift of the mean in the definition of the RS, BC and GV subsets, with a maximum $\Delta D_n(4000) \sim 0.06$ dex, as discussed in Section 3.7.2; a similar exercise for colour yields a maximum change of 0.5 dex. Thus, the 4000Å break strength produces a clean representation, even without dust correction, of the three phases of evolution under study. Once the GV is defined, we further separate it into terciles. The lower tercile represents galaxies closer to the BC, and is hereafter defined as the lower Green Valley (lGV). The upper tercile is closer to the RS and is termed the upper Green Valley (uGV) and the region in between can be classified as middle Green Valley (mGV). If we interpret the GV

as a transition region where galaxies quench their star formation, we can portray the lGV and uGV as the starting and ending stages of this transition, respectively.

3.2.2.2 SDSS Green Valley Probability Catalogue

Note, while the method outlined above is the one we use for this and other upcoming chapters, we are also able to assign to each galaxy, on the $D_n(4000)$ vs velocity dispersion plane, a probability of it belonging to the Blue Cloud ($\hat{\mathscr{P}}_{BC}$), Green Valley ($\hat{\mathscr{P}}_{GV}$), or Red Sequence ($\hat{\mathscr{P}}_{RS}$). Each probability can be written:

$$\hat{\mathscr{P}}_k = \eta_k \mathscr{P}_k(\pi;\sigma), \tag{3.6}$$

where $\mathscr{P}_k$ is given by Eq. 3.2 and η_k is a weight factor dependent on the number of galaxies in BC, GV or RS, in a given velocity dispersion bin.

To assign a probability to an individual galaxy, we firstly obtain the PDF averages: μ_{BC}, μ_{GV}, μ_{RS}, and "widths": s_{BC}, s_{GV} and s_{RS} for 11 bins from 50 to 350 km/s. Then we interpolate between the velocity dispersion bins with a third order polynomial that enables us to find the effective μ_k and s_k in each group, BC, GV and RS, at any velocity dispersion. For each galaxy, we obtain its $\mathscr{P}_k(\mathscr{G}_i)$, along with $\mu_k(\mathscr{G}_i)$ and $s_k(\mathscr{G}_i)$. To determine η_k, we select all galaxies with velocity dispersion within an interval centered at the σ of the chosen galaxy, with width $\Delta\sigma$=15 km/s, and then assign them either to the BC, GV or RS. For any galaxy sitting on adjacent regions, we assign them evenly to their overlapping regions; e.g., if they overlap between BC and GV, they are equally likely to count towards the BC or GV. Thus we obtain η_k for each galaxy. Once we obtain $\hat{\mathscr{P}}_k$, we normalise the total probability to unity. Note we assign galaxies with $D_n(4000)>1.99$, $\hat{\mathscr{P}}_{RS}$=1, and $\hat{\mathscr{P}}_{BC} = \hat{\mathscr{P}}_{GV}$=0, as we know that galaxies with a high 4000 Å break strength are old and quiescent. Likewise galaxies with $D_n(4000)<0.8$ are assigned $\hat{\mathscr{P}}_{BC}$=1, and $\hat{\mathscr{P}}_{GV} = \hat{\mathscr{P}}_{RS}$=0. A small number of galaxies from the catalogue is shown in Tab. 3.1 for reference. The full catalogue can be found in the online version of the paper. Note owing to the methodology used, the probabilities presented here are not unique solutions, but a realisation of the three groups. Thus if one were to carry out

Table 3.1: The normalised probability of a galaxy in SDSS set belonging to either BC, GV or RS; as shown by the final three columns. This table shows an excerpt of the full set, where we give the SDSS spectral identification numbers (plate, Julian date and fibre ID) along with the 4000Å break strength and velocity dispersion (measured within the 3 arcsec diameter fibres of the spectrograph).

SDSS ID				Velocity	Probabilities		
plate	mjd	fibre ID	$D_n(4000)$	dispersion km/s	$\hat{\mathscr{P}}_{BC}$	$\hat{\mathscr{P}}_{GV}$	$\hat{\mathscr{P}}_{RS}$
315	51663	560	1.012	64.5	0.970	0.009	0.021
326	52375	86	1.584	99.2	0.001	0.026	0.973
326	52375	119	1.509	104.6	0.011	0.360	0.629
326	52375	150	1.777	168.2	0.000	0.000	1.000
327	52294	147	1.651	147.9	0.001	0.013	0.986

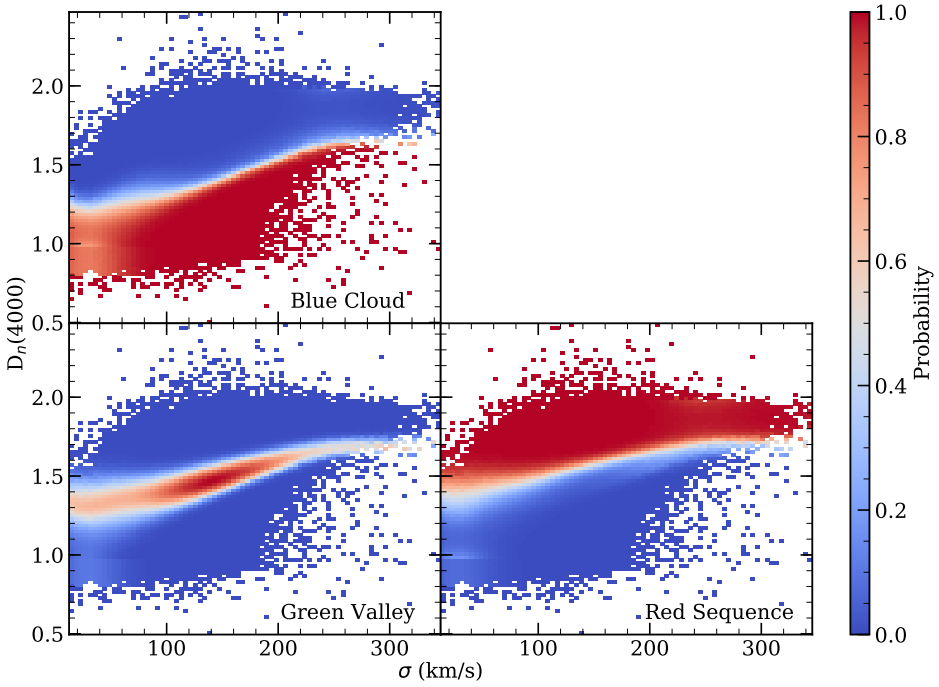

Figure 3.6: The probability of galaxies belonging to the Blue Cloud (*top left*), Green Valley (*bottom left*) and Red Sequence (*bottom right*). Blue colours represent galaxies with a low probability of residing in the three regions, as labelled, while red shows high probability (see colour bar for reference). For ease of visualisation, the resulting density plots have been modified with a Gaussian smoothing kernel.

the outlined steps, the results should not be identical, but statistically equivalent. Fig. 3.6 illustrates the probability density of galaxies residing in BC, GV or RS, obtained following the aforementioned methodology.

3.2.3 Spectral Stacking

For most the analysis in this chapter, we collect subsamples of GV galaxies and then stack them to produce high quality spectra. High S/N is needed for a robust analysis of the stellar population content. However, more importantly, our motivation to stack the spectra is to average out galaxy-to-galaxy variations, leading to a set of "super-spectra" for which the variations between different regions of the selection plane are only caused by the transitional mechanisms that give rise to the BC/GV/RS distribution.

We follow the standard procedure for the stacking of the SDSS spectra (see, e.g. Ferreras et al., 2013a). The stacking was carried on spectra that were dereddened and brought to a rest-frame wavelength in the air system, applying a normalisation according to the median flux in the rest-frame interval 5000–5500Å. The process implies resampling the flux within each spectral pixel following a linear split between adjacent pixels according to the amount of overlap between the original pixel and the sampled pixel. Each resulting stack is then corrected for nebular emission by performing spectral fitting with the STARLIGHT code (Cid Fernandes et al., 2005). In the stacking procedure, we exclude Seyfert AGN (BPT=4) and Composite systems (BPT=3), since prominent AGN luminosity contaminates the continuum, affecting the colours and the 4000Å break strength, parameters used in the definition of the GV. The residuals with respect to the best fit spectrum are then used to fit Gaussian profiles within the standard emission regions, which are then removed from the stacks (see La Barbera et al. 2013 for details). In order to compare the spectral features across the wide range of velocity dispersion, we convolve all stacks with a Gaussian kernel to produce a velocity dispersion of 235 km/s in all cases. Fig. 3.7 compares the stacked data of uGV and lGV galaxies in two important regions: the interval around the age-sensitive Balmer indices Hγ and Hδ (top panels) and the region covering the metallicity-sensitive indices Mgb and $\langle$Fe$\rangle$ (bottom panels). From top to bottom, we show the stacked spectra; the S/N; and the difference between uGV and lGV spectra, in three velocity dispersion bins, as labelled.

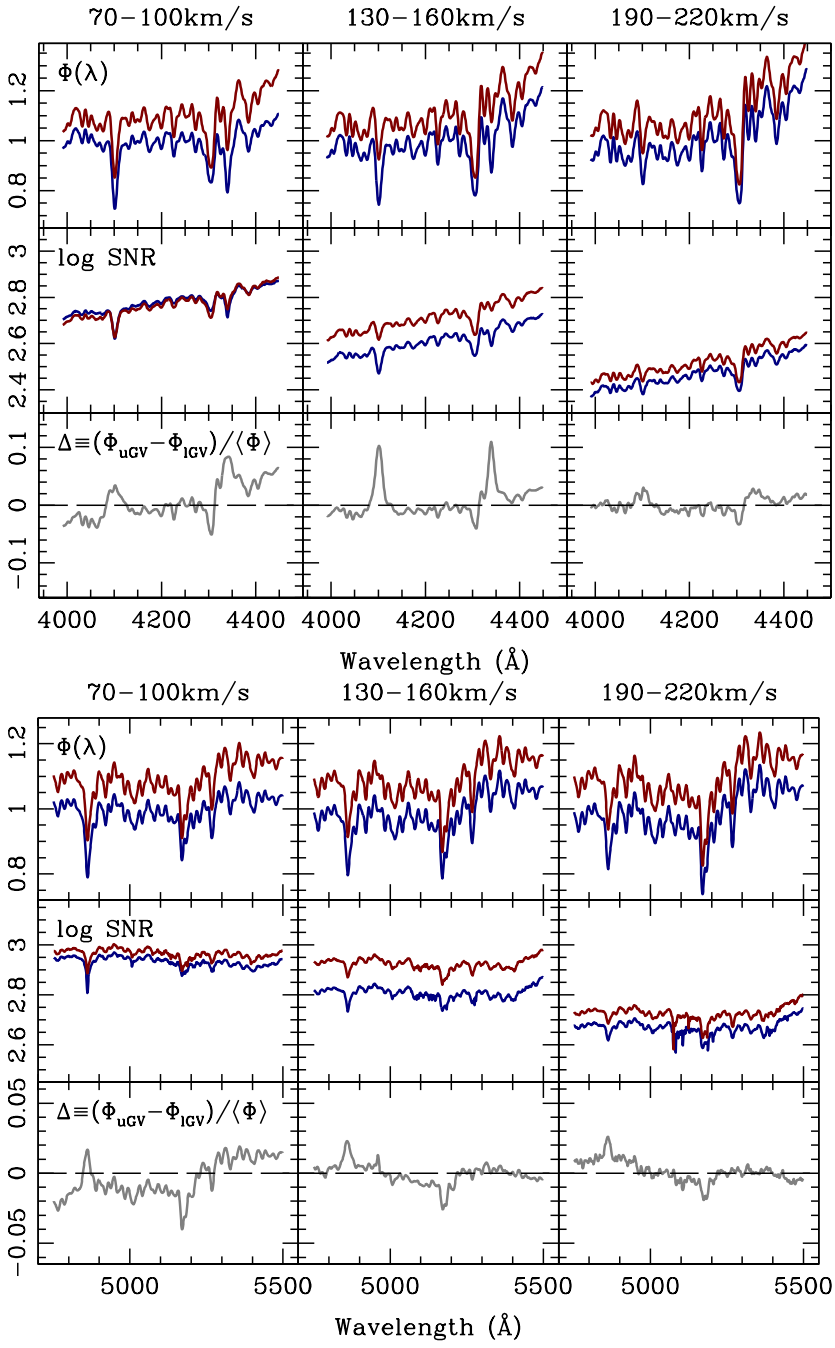

Figure 3.7: Here we compare the stacked spectra within two important spectral windows. The first is located around the Hγ and Hδ absorption lines (top panels) and the second neighbours the Hβ and Mg+Fe complex (bottom panels). In each panel, the top, mid and bottom sub-panels show fluxes of the lGV (in blue) and the uGV (in red), with a small arbitrary vertical offset to avoid crowding; the signal to noise ratio on a logarithmic scale; and the relative flux difference between uGV and lGV spectra. The title on top of each sub-panel shows the velocity dispersion bin we are looking at. Note, we convolve all stacks to a common velocity dispersion equivalent of 235 km/s.

3.2.4 Uncertainty of the stacked spectra

One of the key constraints in our sample selection is the signal to noise ratio of individual spectra (snMedian_r>10) in order to avoid stacking large numbers of noisy data. This constraint results in stacked spectra with a very high S/N (see Fig. 3.7) when computed with the standard statistical noise carried from the individual data. Such high values of S/N lead to underestimated uncertainties on the derived parameters, as the higher values of the best-fit χ^2 reflect the shortcomings of population synthesis models at this level of detail. Therefore to ensure our results have more realistic uncertainties, we adapt the noise level including two estimates – added in quadrature – that take into account additional sources of uncertainty in the stacking procedure. (1) We create Monte Carlo realisations of each stack by using the uncertainty of individual fluxes. We carry out the same analysis for these stacks as our original set, therefore giving us a more robust statistical uncertainty of the derived parameters. (2) For each velocity dispersion bin, we bootstrap the subsample, selecting, at random, only 60% of the galaxies. We carry out the same process as for the original stacks, therefore incorporating the systematical uncertainty in our error bars caused by the sample selection. Bins comprising fewer galaxies are expected to carry a larger uncertainty, accounting for sample selection systematics.

Additional systematics may be expected, inherently to the methodology adopted here. One such systematic relates to the use of SSP models (Bruzual and Charlot, 2003; Vazdekis et al., 2012), that carry their own systematic uncertainties that depend upon the stellar library, isochrones and initial mass function (IMF) chosen. Furthermore, the use of STARLIGHT to perform spectral fitting will carry additional uncertainties. One way to mitigate this systematic would involve comparisons among independent spectral fitting algorithms, such as pPXF (Cappellari and Emsellem, 2004) or FIREFLY (Wilkinson et al., 2017). Another source of uncertainty arises from the emission line correction that we apply to the Balmer absorption lines. However, our use of a battery of emission line diagnostics, and the comparison with spectral fitting – that mask out such regions – mitigates this potential systematic.

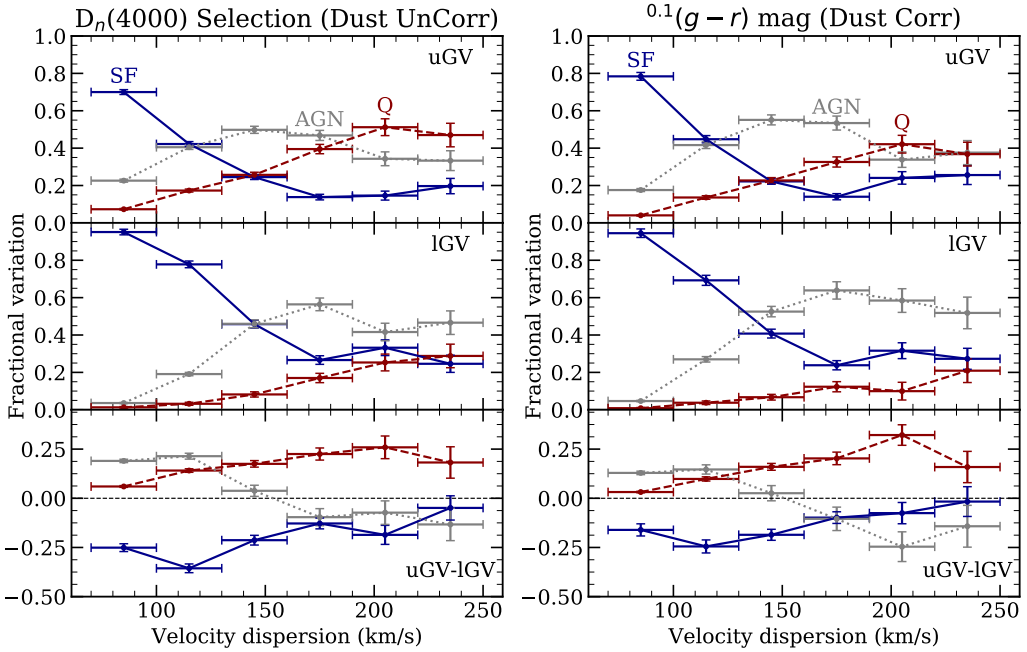

Figure 3.8: Fractions of different types of galaxies in uGV (top) and lGV (middle). The classification of these galaxies are based upon their nebular emission properties, where the standard BPT (Baldwin et al., 1981) diagram, is used to group them into SF (blue), AGN/LINER (grey) and quiescent (red). The left and right panels show results corresponding to 4000Å strength and dust-corrected colour selection of GV galaxies. The bottom panel shows the difference between upper−lower GV.

3.3 Fractions of Galaxy Types

One of the simplest analysis concerns the distribution of segregated samples based on nebular emission. The different types of galaxies are identified following the BPT standard classification system (see Fig. 1.4 and Baldwin et al., 1981). Table 3.2 shows the distribution of galaxy spectra in the upper (uGV) and lower (lGV) green valley, with respect to velocity dispersion. For reference, we show three selection criteria, from top to bottom, the 4000Å break strength, the uncorrected $(g-r)$ colour evaluated at a fiducial redshift of z=0.1, and the dust-corrected colour, all measured within the SDSS spectroscopic fibre.

A graphical version of this Tab. 3.2 is shown Figure 3.8, which shows the fraction of star-forming, quiescent and AGN galaxies as a function of velocity dispersion, on the upper and lower GV, contrasting the difference between a selec-

Table 3.2: This shows the number of SDSS galaxy spectra in uGV and lGV for different velocity dispersion bins, for different definitions of the GV based on the 4000Å break strength, colour without and with dust correction. This also presents the fractional contribution (as percentages) of different galaxy types, i.e. star-forming (labelled SF; BPT flag 1 or 2); quiescent (labelled Q; BPT flag −1), or Active Galactic Nucleus, including LINER emission (labelled AGN; BPT flag 4 or 5).

σ (km/s)	No. Gal	f(SF)%	f(Q)%	f(AGN)%	No. Gal	f(SF)%	f(Q)%	f(AGN)%
	lower GV				upper GV			
D4k selection								
70–100	4265	95.1±1.5	1.3±0.2	3.6±0.3	3845	70.0±1.3	7.3±0.4	22.6±0.8
100–130	2369	77.8±1.8	3.2±0.4	19.1±0.9	2627	42.2±1.3	17.3±0.8	40.5±1.2
130–160	1078	45.8±2.1	8.2±0.9	46.0±2.1	1344	24.5±1.3	25.7±1.4	49.8±1.9
160–190	500	26.6±2.3	17.0±1.8	56.4±3.4	631	13.8±1.5	39.5±2.5	46.8±2.7
190–220	190	33.2±4.2	25.3±3.6	41.6±4.7	254	14.6±2.4	51.2±4.5	34.3±3.7
220–250	118	24.6±4.6	28.8±4.9	46.6±6.3	117	19.7±4.1	47.0±6.3	33.3±5.3
colour selection $^{0.1}(g-r)$ (no dust correction)								
70–100	3384	95.7±1.7	1.7± 0.2	2.6±0.3	3174	83.9±1.6	7.7± 0.5	8.3±0.5
100–130	1844	81.1±2.1	8.5± 0.7	10.5±0.8	1824	56.2±1.8	25.4± 1.2	18.4±1.0
130–160	813	52.6±2.5	24.8± 1.7	22.5±1.7	953	25.6±1.6	52.4± 2.3	22.0±1.5
160–190	311	30.5±3.1	44.7± 3.8	24.8±2.8	353	16.7±2.2	65.4± 4.3	17.8±2.2
190–220	103	18.4±4.2	61.2± 7.7	20.4±4.4	110	10.0±3.0	74.5± 8.2	15.5±3.7
220–250	40	7.5±4.3	72.5±13.5	20.0±7.1	45	8.9±4.4	82.2±13.5	8.9±4.4
colour selection $^{0.1}(g-r)$ (dust corrected)								
70–100	3534	94.5±2.3	0.8±0.2	4.7±0.3	3233	78.4±2.1	4.2±0.4	17.6±0.8
100–130	1623	69.2±2.7	3.8±0.5	27.0±1.5	1722	44.8±1.9	13.6±0.9	41.6±1.8
130–160	1028	40.8±2.4	6.7±0.8	52.5±2.8	1194	22.2±1.5	22.7±1.5	55.1±2.7
160–190	487	23.8±2.5	12.3±1.7	63.9±4.6	586	14.0±1.6	32.6±2.7	53.4±3.7
190–220	231	31.6±4.2	10.0±2.2	58.4±6.3	266	24.1±3.3	42.1±4.7	33.8±4.1
220–250	110	27.7±5.6	20.9±4.8	51.8±8.5	125	25.6±5.1	36.8±6.3	37.6±6.4

tion based on break strength (left), or dust-corrected colour (right). Both methods give the expected decreasing (increasing) trend of star-forming (quiescent) galaxies towards increasing velocity dispersion, reflecting the effect of downsizing. At the massive end (σ=200-250 km s^{-1}), the fraction of AGN in the uGV (lGV) is $\sim$30$\pm$5% ($\sim$50$\pm$7%) according to the $D_n(4000)$ definition, comparable to the equivalent fractions from the dust-corrected colour selection, namely $\sim$37$\pm$6% ($\sim$51$\pm$8%). Our estimate of the fractional contribution of AGN is compatible with the analysis of previous study (see Martin et al., 2007, Fig. 20), further supporting the idea that the 4000Å break strength can be accurately used to define the GV without the need for dust correction. Moreover, looking at the distribution of the 4000Å break strength of M07 in their transition region (see Martin et al., 2007, Fig. 3), the index range is fully compatible with our definition of the GV.

3.4 Line Strength Analysis

In the previous section, we make use of the emission lines and their ratios to identify and study the different types of galaxies in the GV. In this section, we use their absorption feature, which requires emission line correction, to study the stellar population of GV galaxies. These two sets of results can be thought of as a zeroth order analysis, as we are studying directly the observables, with minimal dependency on the need for any modelling.

3.4.1 General Trends

For the study of stellar populations, we select a battery of standard indices from the Lick system: $H\beta$, Mgb, Fe5270, Fe5335, G4300 (Trager et al., 1998), the higher order Balmer indices $H\gamma_F$ and $H\delta_F$ (Worthey and Ottaviani, 1997), as well as the $D_n(4000)$ (hereafter D4k, Balogh et al., 1999) index already used for the definition of the GV. We combine the iron abundance indices into an average $\langle$Fe$\rangle \equiv$(Fe5270+Fe5335)/2, and also measure the standard index [MgFe]$' \equiv \sqrt{\text{Mgb}(0.72 \times \text{Fe5270} + 0.28 \times \text{Fe5335})}$ (Thomas et al., 2003). These indices can be split into two categories – age- and metallicity-sensitive. The Balmer indices, $D_n(4000)$ and G4300 are usually considered age-sensitive, while the others are

metallicity-sensitive. However any and all spectral indices mentioned here (and, unfortunately, elsewhere) suffer from the age-metallicity degeneracy (e.g., Worthey, 1994; Ferreras et al., 1999).

This approach, solely based on the observed line strengths, is meant to assess in a model-independent way the variations between different regions across the GV. Fig. 3.9 shows the line strengths measured in the stacks, where we include the spectra of SF, LINER and Q galaxies, plotted with respect to velocity dispersion. We note these measurements are taken from the stacks that are smoothed to a common velocity dispersion of 235 km/s. Within each subfigure, the left (right) panels correspond to a selection of GV galaxies based on 4000Å break strength (dust-corrected $^{0.1}(g-r)$ colour). Each panel shows independently the trends in the upper, middle and lower GV, as labelled, including an error bar obtained from bootstrapping the sample. For both selection methods, the $D_n(4000)$ index increases strongly with velocity dispersion in all three regions of the GV, in agreement with previous studies (see, e.g., Kauffmann et al., 2003; Graves et al., 2009). However, at low velocity dispersion, the D4k selection produces overall slightly higher values of the break, along with a wider range, towards lower values of the Balmer indices, consistently supporting the hypothesis that the D4k selection produces a GV with older and more homogeneous populations, especially at the low-mass end. At the high mass end, both selection criteria give rather similar results, although the lGV set defined by D4k appears to give marginally lower values than the colour-based lGV. However, this behaviour is not paralleled by the Balmer lines, so the mapping into population trends becomes less trivial. Nevertheless, both D4k- and colour-based definitions of the GV find strong trends in all age-sensitive indices with respect to velocity dispersion, and give robust confirmation of the well-known age-mass relation (see, e.g. Gallazzi et al., 2005).

Both selection methods unsurprisingly produce the lowest (i.e. youngest) break strengths and highest (i.e. youngest) Balmer indices in the lGV at the low-mass end, whereas at high velocity dispersion, the differences between lGV and uGV are minor. We should keep in mind that the age-sensitive indices presented in Fig. 3.9

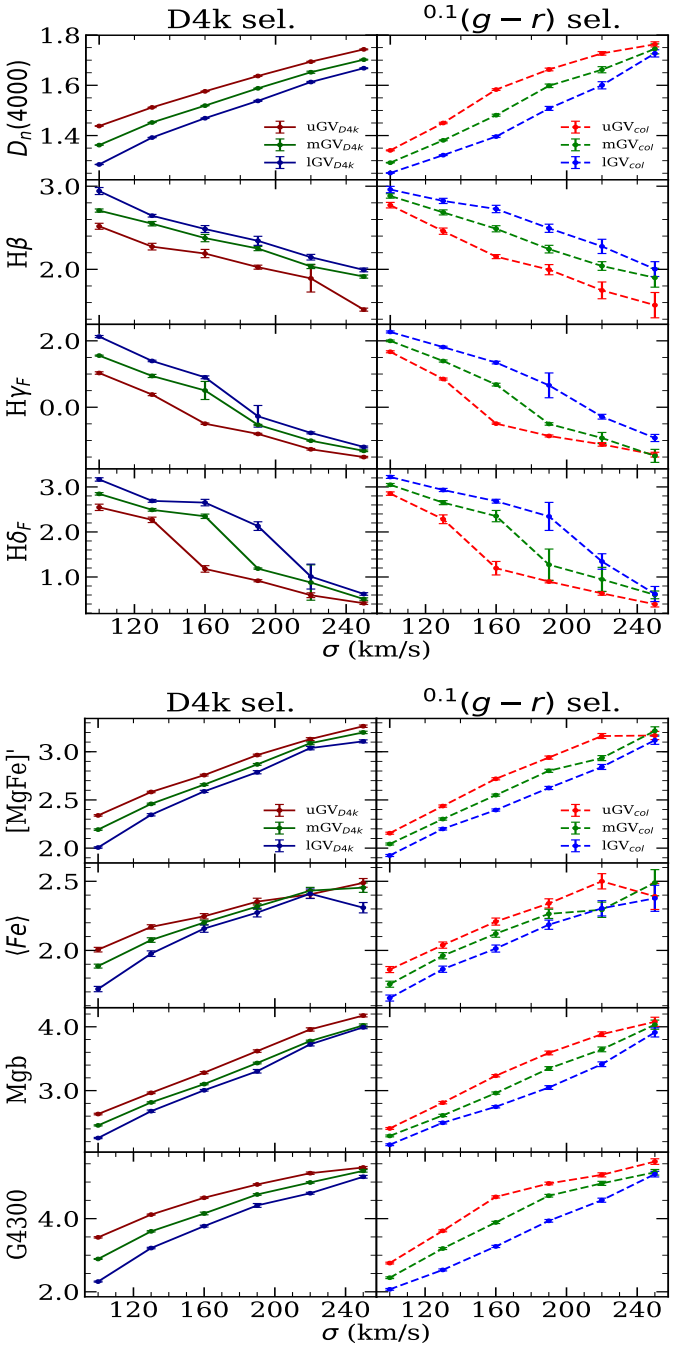

Figure 3.9: Comparison of group of line strengths of GV galaxies selected by 4000Å break strength (D4k) or dust-corrected $^{0.1}(g-r)$ colour (col). Each panel presents the results for lGV (blue), mGV (green) and uGV (red) as labelled. *Top* panel: From top to bottom, shows the age-sensitive spectral indices $D_n(4000)$, $H\beta$, $H\gamma_F$ and $H\delta_F$. *Bottom* panel: From top to bottom shows the metallicity-sensitive indices [MgFe]′, ⟨Fe⟩, Mgb, and the age-sensitive index G4300. All measurements are given as equivalent widths, in Å, except for $D_n(4000)$, which is a dimensionless ratio.

behave differently with respect to the age distribution, with the Balmer indices being more sensitive to recent star formation episodes compared to $D_n(4000)$ (Poggianti and Barbaro, 1997). Regardless of the GV selection method, as we traverse from lGV to uGV, we find a decrease in the line strengths of all Balmer indices, thus indicating a smooth transition from the younger lGV to the predominantly quenched, passively evolving uGV. It is worth noting that the colour-based selection produces overall higher Balmer indices, possibly implying the presence of younger (but dustier) galaxies, with respect to the D4k selection. Even though the colour selection includes an intrinsic dust correction, biases may appear as the correction is prone to systematics regarding the derivation of the dust corrections as well as variations of the dust attenuation law caused by the diverse range of dust geometry and chemical composition in galaxies (see, e.g. Tress et al., 2018; Salim and Narayanan, 2020). Moreover, note that the K-correction applied to bring the observed colour within a fiducial value (z=0.1 in our case) may also introduce an additional systematic: the median K-correction applied is 0.04 mag but there is an obvious dependence with redshift – with the correction trivially vanishing at z=0.1 – and a more subtle trend with the intrinsic colour – with the K-correction being larger in the redder galaxies. The difference in this correction with respect to the intrinsic colour can be as high as $\sim$0.1 mag, thus comparable with the interval that defines the GV. Such behaviour can introduce a correlation in the selection of the GV. In contrast, the 4000Å break selection depends very little on dust correction (see Fig. 3.22) and is independent of K-correction (as the index is directly measured on the rest-frame spectra).

The bottom panels of Fig. 3.9 present the results for metal-sensitive indices along with G4300. The index G4300 increases with velocity dispersion, roughly following a very similar trend as $D_n(4000)$. Note that this index separates more smoothly the lGV, mGV and uGV, confirming a strong correlation with the 4000Å break. For [MgFe]$'$, $\langle$Fe$\rangle$ and Mgb, we find the expected positive correlation with increasing velocity dispersion (e.g., Sansom and Northeast, 2008). The line strength [MgFe]$'$ – that can be approximately considered a total metallicity indicator – shows

that, in general, the D4k selection features slightly more metal rich populations compared to the colour selection, in all GV regions. By comparing $\langle$Fe$\rangle$ and Mgb, we find both produce similar trends. As we move up the GV, from lGV to uGV, the data show increasing metallicity. It is worth mentioning here that the dependence of these indices on age – due to the age-metallicity degeneracy – is such that higher values of the index could also be explained by *older* ages. Section 3.6 is devoted to a comparison of the stacked spectra with population synthesis models via spectral fitting, to be able to break such degeneracies. Moreover, we show below (Section 3.5) an analysis of stellar ages based on simple stellar populations.

Therefore, Fig. 3.9 validates both selection methods for GV galaxies but the D4k method is more insensitive to dust corrections. This results in subtle but measurable differences with respect to the colour-based GV selection method. These differences are especially important at low velocity dispersion, where the contribution from dusty, star-forming galaxies may introduce a larger systematic regarding the dust correction.

3.4.2 Difference regarding (nebular) activity

Rather than simply studying the trends of line strength with regards to velocity dispersion, we can also study variation of the stellar population properties between different types of galaxies, such as quiescent, star-forming and LINER AGN systems. Moreover, as systems with nebular emission are expected to be significantly affected by dust, we want to explore the differences between the D4k selection (minimally affected by dust) and the colour selection (that applies a dust correction, but may be affected by systematics from this correction). Therefore, we make two stacks of galaxies within each velocity dispersion bin within each GV region. One stack consists of only Q galaxies (Q_{stack}) and another is made up of star forming, LINER AGN and Q galaxies (All_{stack}). Comparison between these two stacks provides useful insight on the properties of GV galaxies and the potential biases caused by the selection method. Fig. 3.10 shows the difference in the age-sensitive indices between the Q_{Stack} and All_{stack}. The top and bottom panels show the difference in results for uGV and lGV galaxies, respectively. Solid and dashed lines

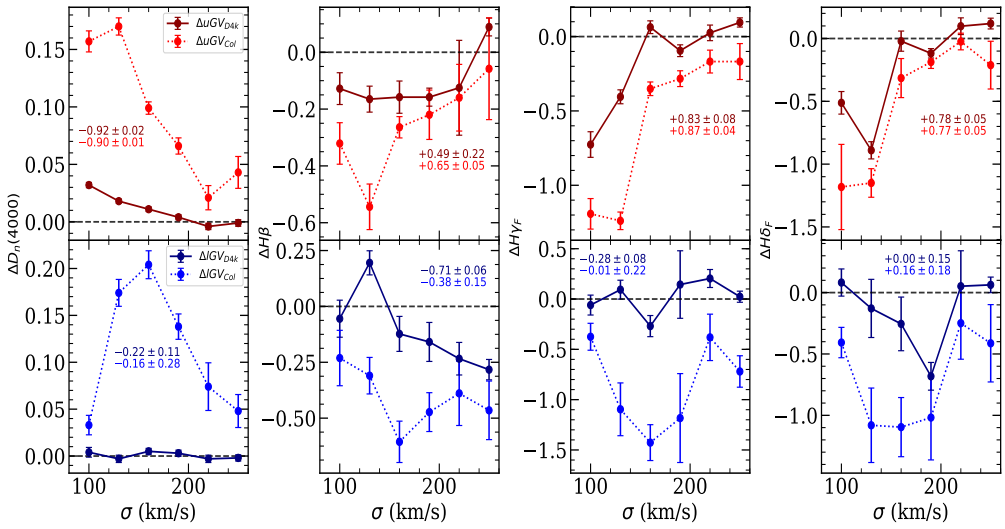

Figure 3.10: Differences in age-sensitive line strengths between uGV (top panel) and lGV (bottom panel) between Q_{stack} (stacks of Q galaxies only) and All_{stack} (stacks consisting of SF, LINERS and Q galaxies). The light red and blue dotted data shows the difference for colour selection, while dark red and blue solid lines show the difference in the D4k selection. Similarly, the numbers in dark (light) red and dark (light) blue show the pcc of $D_n(4000)$ (colour) selection data points. The error in each data points are quoted at the 1 σ level.

show the results for the D4k and colour-based selection, respectively. The numbers in each panel represent the Pearson correlation coefficient (pcc). In uGV galaxies, a decrease in the difference of $D_n(4000)$ with respect to velocity dispersion is evident, for both D4k (pcc $=-0.92\pm0.02$) and colour selection (pcc$=-0.90\pm0.01$). This trend can be attributed to the lower contribution of star-forming galaxies as velocity dispersion increases (see Table 3.2). It should be noted that the variation in $\Delta D_n(4000)$ (leftmost panels) for the D4k selection should be, by construction, minimal, as we are constraining the $D_n(4000)$ index within certain values. Note, in contrast, the different trends found in the Balmer indices. For the uGV, inclusion of SF galaxies increases Balmer absorption in both definitions of the GV, as expected from the decrease in average age. Furthermore, the values of pcc show a stronger correlation/anti-correlation in uGV in comparison to lGV; this effect can be attributed to a lower percentage of SF and AGN galaxies in uGV in contrast to lGV with increasing velocity dispersion. We find a more homogeneous distribution

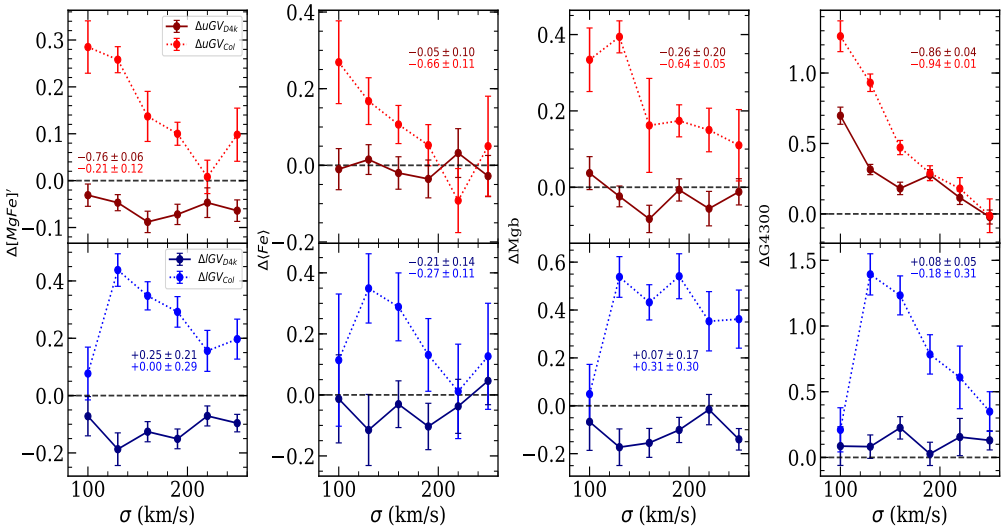

Figure 3.11: Same as Fig. 3.10 but for metallicity sensitive indices and G4300.

of stellar populations when GV galaxies are selected according to D4k, whereas the colour-based selection produces larger differences in the indices in both uGV and lGV.

Fig. 3.11 shows the results for the remaining line strengths. Note the age-sensitive G4300 behaves similarly to $D_n(4000)$, as in Fig. 3.9. Both Figs. 3.10 and 3.11 show that in all cases, *the line strength variations are significantly smaller for the D4k selection, confirming that a more homogeneous distribution of GV galaxies is produced when selecting the sample on break strength.* A colour-based selection, even after a careful dust correction is applied, produces a more complex mixture of galaxies, regarding nebular activity. We argue that the D4k selection results in a more representative sample of transitioning galaxies from the BC to the RS. Note that for the metallicity sensitive indices, the difference between stacks gives a negative value, that may suggest lower average metallicities when stacking only quiescent galaxies. Moreover, note that [MgFe]′ also increases with stellar age, so that an age-dependent explanation would need to invoke *younger* populations in Q galaxies. In contrast, the colour selection yields positive variations in the metal-sensitive indices, as expected if All_{stack} is dominated by younger, metal-poor, star-forming galaxies. This result further supports the idea of population contamination when

adopting colour selection. This contamination seems to affect not only the age- but also the metallicity-sensitive indices at all values of the velocity dispersion, although the difference appears to decrease towards higher velocity dispersion, where the number of SF galaxies, hence contamination from dusty BC galaxies, decreases.

3.5 SSP Analysis

To first order, we can use the information obtained from the various line strength to estimate the physical properties of the galaxies, such as their age and metallicity. Therefore, in this section, we produce easy-to-interpret 'SSP-equivalent' ages, instead of a more complex combination of populations, left to Section 3.6. SSP-derived ages should be interpreted as a luminosity-averaged age, as if the whole stellar content of the galaxy were formed in a single burst. An alternative definition – based on composite age distributions following a predefined functional form of the star formation rate – can be prone to biases due to the specific form adopted. We show both estimates of age in this chapter to be able to assess the actual variations in the underlying populations of GV galaxies. We follow a Bayesian approach, probing a large volume of SSPs from the MIUSCAT population synthesis models (Vazdekis et al., 2012), comparing the observed and the model line strengths with a standard χ^2 statistic:

$$\chi^2(t,Z) = \sum_i \left[\frac{\Delta_i(t,Z)}{\sigma_i}\right]^2, \tag{3.7}$$

where $\Delta_i(t,Z) = O_i - M_i(t,Z)$ is the difference between the observed line strength and the model prediction for the ith index, and σ_i is the corresponding uncertainty. The grid of SSP models comprise 8,192 synthetic spectra. The stellar age ranges from 0.1 to 13.5 Gyr, in 128 logarithmically-spaced steps, and metallicity ([Z/H]), varies from -2.0 to $+0.2$ dex, with 64 steps. We note the original models have a reduced set of metallicity steps (seven in total) and we interpolate (bi)linearly for a given choice of (log) age and metallicity.

Since the signal-to-noise ratio of the data is very high (Fig. 3.7), we need to apply offsets to the individual indices to account for potential variations due to differences in the [Mg/Fe] abundance ratio of the populations or, indeed, due to

an extended age distribution. Our modus operandi involves computing the best fit solution (i.e. giving the minimum χ^2) for a fiducial stack. This fiducial stack is chosen as the one that gives the lowest value of χ^2 for the best fit. We then define the offsets for each line strength from this best fit solution, and apply these offsets (δ_i), such that $\Delta_i(t,Z) = O_i - M_i(t,Z) - \delta_i$ in equation 3.7 – to *all* the stacks in the sample. Given the large S/N of the spectra, we also add in quadrature – as a potential systematic error, and in order to produce conservative error bars – an additional amount corresponding to 5% of the measured line strength. The resulting χ^2 distributions are bivariate functions of age and metallicity. We fix the stellar initial mass function to Kroupa (2001). Note that the results for alternative choices of the IMF, such as Chabrier or Salpeter, give very similar results, and that, within the range of velocity dispersion values considered in this sample, no substantial variations of the IMF are expected (see, e.g. Ferreras et al., 2013a).

3.5.1 Quiescent-only stacks

For the most robust set of results, we focus on the subsample of *quiescent* galaxies in the upper and lower portions of the GV. Note, while SSPs can be used to estimate the ages of various types of galaxies, it is found that this type of analysis is most robust for the interpretation the SFH of Q galaxies, as their stellar populations trace SSPs most closely. Furthermore, the difference in stellar age of the quiescent galaxies serves as a proxy of the time galaxies spend on the GV. We now resort to stacking all the quiescent spectra from SDSS, following standard procedures (see, e.g. Ferreras et al., 2013a). Within a given bin of velocity dispersion, we create one stack in the upper GV and another one in the lower GV. The resulting spectra – mostly featuring S/N above 100 per Å in the regions of interest – are analysed by measuring a set of age- and metallicity-sensitive spectral indices: Hβ, Mgb and $\langle$Fe$\rangle \equiv$(Fe5270+Fe5335)/2 (Trager et al., 1998); Hγ_F and Hδ_F (Worthey and Ottaviani, 1997); [MgFe]$'$ (Thomas et al., 2003) and the 4000Å break strength (Balogh et al., 1999). We correct for nebular emission as mentioned in Section 3.2.3, which follows the methodology laid out in appendix B of La Barbera et al. (2013). The observed line strengths are compared with synthetic stellar population models

(Vazdekis et al., 2012), producing SSP-equivalent ages. The top panels of Figure 3.12 show the SSP-equivalent ages of uGV and lGV galaxies with respect to σ, and the bottom panels plot the age difference between these two regions (Δt_{SSP}), that can be interpreted as a effective quenching timescale. We emphasize that these differences concern GV galaxies spectroscopically classified as quiescent. The well-known mass-age trend is readily apparent, with more massive galaxies (higher σ) featuring older ages (Gallazzi et al., 2005). It is worth noticing that both the colour and break strength selection produce very similar trends. However at the highest values of velocity dispersion ($\sigma > 190\,\mathrm{kms}^{-1}$) the dust-corrected colour selection seems to provide, as absolute SSP ages, older galaxies.

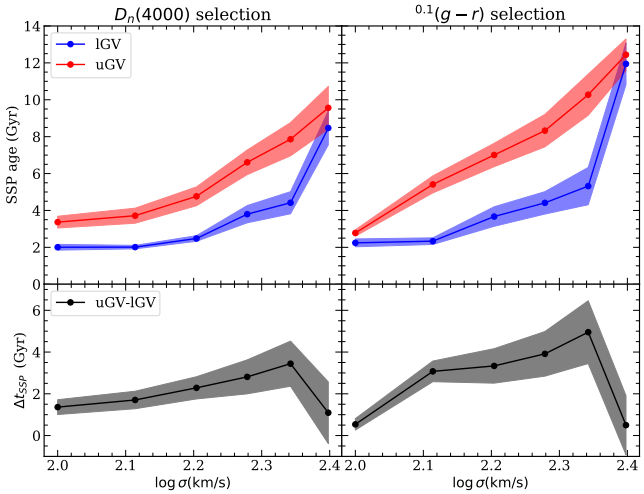

Figure 3.12: This figure presents the SSP equivalent ages for stacked galaxies in lGV (blue) and uGV (red) for different velocity dispersion bins. The left and right panels correspond to the two different GV selection methods; 4000Å break and dust-correct colour, respectively. The bottom panels takes the difference in SSP ages between uGV and lGV galaxies (defined as Δt_{SSP}), thus indicating the transition timescale. The shaded regions extend over the 1 σ uncertainties.

A clearer visualization of this putative GV "traversing time" can be provided by the difference between SSP ages between the uGV and the lGV. The data feature a trend of increasing Δt_{SSP} with velocity dispersion, implying the GV transit times in more massive galaxies become longer, from $\Delta t_{SSP} \sim 1.5$ Gyr at σ=100 kms^{-1} to $\sim$3.5 Gyr at σ=200 kms^{-1}. These values are roughly in line with recent estimates of observed and modelled GV galaxies (Smethurst et al., 2015; Wright et al., 2019;

Rowlands et al., 2018), and our analysis suggests a clear trend with respect to velocity dispersion.

Intriguingly, the figure suggests a mass scale – corresponding to the highest velocity dispersion of the stacks – above which the age difference Δt_{SSP} *decreases*, towards GV transition times around 1 Gyr at σ=250 kms^{-1}. These trends can also be found in M07, where a high fraction of AGN with high luminosity is suggestive of short quenching timescales. In line with M07, we also see a slower quenching regime at lower velocity dispersion (σ <200 km/s). Such behaviour can be interpreted as two different modes of quenching on either side of this mass scale (if we assume that the transition always proceeds from BC to RS), or the presence of a substantial amount of rejuvenation in higher mass galaxies. Rejuvenation might be due to positive feedback from AGN. This is expected to play a role in early gas-rich phases of massive galaxies, where AGN outflows and processing jets are likely to overpressurise interstellar gas clouds and induce star formation, as in Cen A (Crockett et al., 2012; McKinley et al., 2018; Keel et al., 2019).

3.5.2 All Stacks

We can also calculate the SSP equivalent age and metallicity for All_{Stack} to see how the stellar population of different types of galaxies behave. Note, All_{Stack} refers to stacked spectra that include star-forming, quiescent and LINER-like galaxies, which are the stacks used for this section. Fig. 3.13 shows the corresponding probability contours of the bivariate likelihood $\mathscr{P}(t,Z)$ derived from the spectral stacks of the uGV (red) and lGV (blue) galaxies, selected according to 4000Å break strength in solid lines; for comparison, we show the contours for colour selection in faint dashed lines. Both sets of contours are slightly smoothed by a Gaussian kernel, and shown at the equivalent 1, 2 and 3 σ confidence levels, with each panel representing a velocity dispersion bin. Note the expected positive correlation between velocity dispersion and either SSP-equivalent age or metallicity. We note that the method is especially good for determining *relative* variations in the stellar age, whereas metallicity is less well constrained. The difference in age between lGV and uGV galaxies is apparent. We marginalize over metallicity, producing the

trends in SSP-equivalent age shown in Fig. 3.14, with the error bars given at the 1 σ level. We show the uGV and lGV trends with respect to velocity dispersion in the D4k-selected (left) and colour-selected (right) GV. The bottom panels show the age difference between the two. The dashed grey lines in the bottom panels show the analysis when restricting the stacks to quiescent galaxies, as shown in Fig. 3.12. Both sets of stacks feature a similar increasing trend with σ, except at the highest velocity dispersion bin, where the quiescent sample shows a significant decrease. Note, this is as expected as in the All_{stack} includes SF therefore complicating the interpretation of stellar ages using the SSP equivalent analysis. Furthermore, the presence of SF galaxies at high D4k and high velocity dispersion also indicates that such galaxies would have long quenching timescales, as they are expected to have formed at high lookback-time.

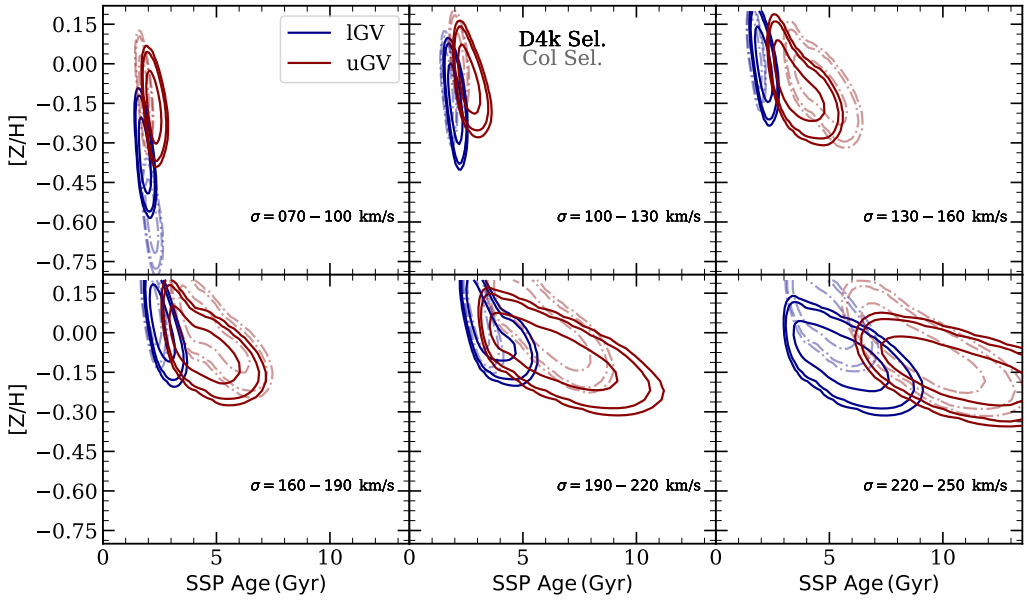

Figure 3.13: The contours represent the likelihood derived from the line strength analysis of SSP-equivalent age and metallicity, where each line represents the 1, 2 and 3 σ levels. These contours correspond to the results from All_{stack}, where the solid lines show the results from the 4000Å break strength and semi-transparent dash-dotted lines present the result for $^{0.1}(g-r)$ dust-corrected colour. The blue (red) contours represent lGV (uGV) stacks.

Rather than looking at only the SSP ages to study the transition timescales, we can use their metallicities to study similar properties. Overabundances in [Mg/Fe]

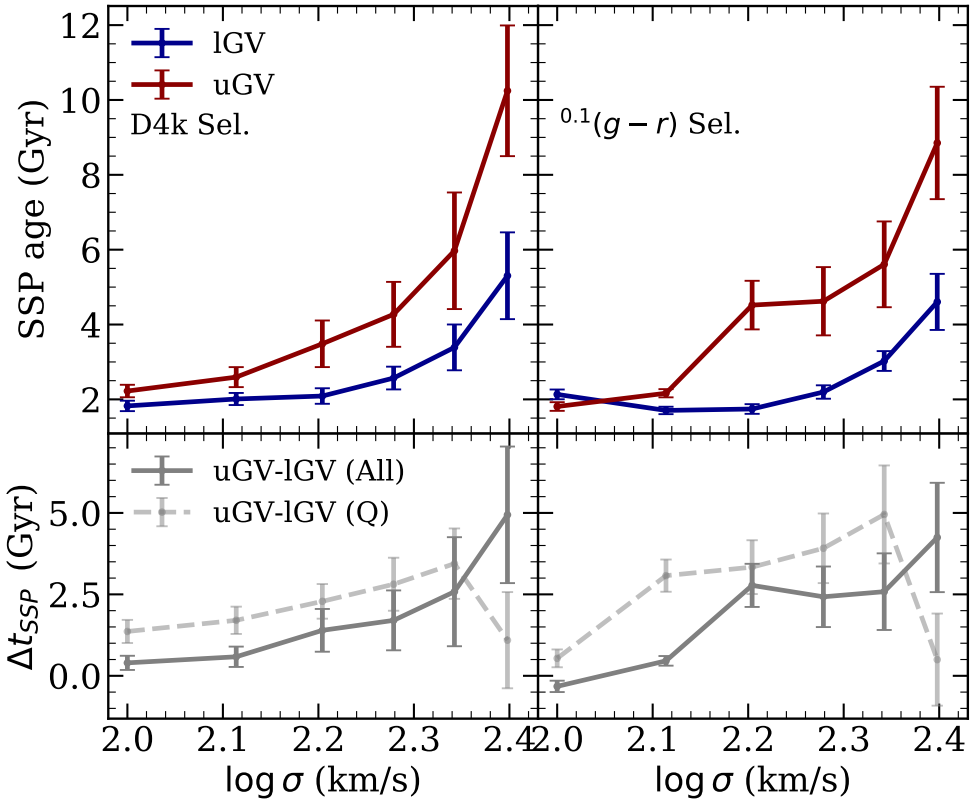

Figure 3.14: The SSP-equivalent ages calculated from age- and metallicity-sensitive line strengths for different velocity dispersion bins for All_{stack}. The blue and red lines show results for lGV and uGV for D4k- (left) and dust-corrected colour (right) definition of GV. The bottom panels show the difference in SSP equivalent ages between uGV and lGV, where the dashed grey lines show the result from Q_{stack} as seen in Fig. 3.12, and the solid grey lines displays the trend for All_{stack}.

are traditionally associated with short and intense star formation episodes where the delayed Fe-rich contribution from type Ia supernovae is not incorporated into stars (see, e.g., Thomas et al., 1999). Standard models based on a single or double degenerate progenitor imply delays between 0.5 and 2 Gyr (Matteucci and Recchi, 2001). Therefore, populations with super-solar [Mg/Fe] are expected to have been formed over similar timescales. Thus, an estimate of [Mg/Fe] provides a stellar clock that has been exploited, for instance, to show that massive early-type galaxies must have formed their central regions within a dynamical timescale. Here we look for potential variations of [Mg/Fe] in the stacked GV spectra, following the proxy adopted in

La Barbera et al. (2013). This proxy allows one to use standard, solar-scaled population synthesis models to measure [Mg/Fe]. The procedure involves constraining a grid of SSP models using two different sets of line strengths, one involving age-sensitive indices along with an Mg-sensitive index (obtaining a metallicity [Z_{Mg}/H]; in this case we use Mgb) and another one involving the same age-sensitive indices plus a Fe-sensitive index (producing [Z_{Mg}/H], here we use $\langle$Fe$\rangle$). The difference, i.e. [Z_{Mg}/Z_{Fe}] is the adopted proxy for [Mg/Fe].

Fig. 3.15 plots [Z_{Mg}/Z_{Fe}] against velocity dispersion for both definitions of the GV, where the numbers in the legend represent the pcc. Our estimate of pcc along with its uncertainty involves 100 Monte Carlo realisations. For each realisation, we remove at random one data point and calculate the resulting pcc; this is done to mitigate the effect of outliers. The pcc is quoted as the median of the distribution and the uncertainty is one standard deviation. The data points are shifted horizontally by an arbitrary amount to avoid overcrowding. In the D4k selection (left panel), the uGV behaves differently with respect to lGV and mGV, which behave in a similar manner to each other. Both mGV (pcc=$+0.77 \pm 0.06$) and lGV (pcc=$+0.59 \pm 0.14$) show a weak but significant correlation with velocity dispersion, whereas the abundance ratio in uGV galaxies (pcc=-0.24 ± 0.14) seems rather constant. Interestingly, the colour-based selection (right panel) shows an increasing trend in all subsamples of the GV, although [Z_{Mg}/Z_{Fe}] appears to flatten in uGV galaxies with $\sigma \gtrsim 150$ km/s. The trends support the scenario of a more extended star formation history in lower mass galaxies (see, e.g., de la Rosa et al., 2011).

3.6 Spectral Fitting

In order to look in more detail at the stellar population content of GV galaxies, we carried out spectral fitting, by use of the STARLIGHT code (Cid Fernandes et al., 2005), to produce best-fit *composite* mixtures. Variations of these mixtures across the GV will inform us of the transition between the lGV to the uGV – note that depending on whether the dominant mode is quenching or rejuvenation, it is possible to evolve *in both directions*. STARLIGHT performs linear superpositions

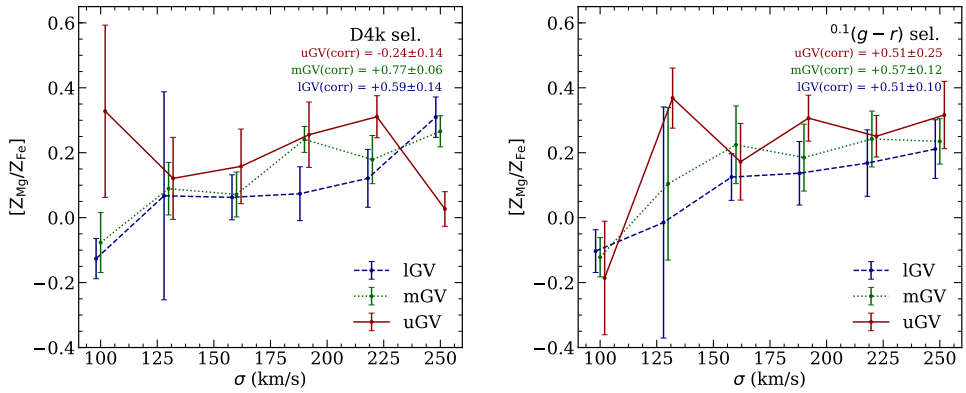

Figure 3.15: This shows the variation in abundance ratio proxy $[Z_{Mg}/Z_{Fe}]$ for different velocity dispersion bins. Left and bottom panels show the result for 4000Å break and colour selection. In each panel, the blue, green and red lines represent the lGV, mGV and uGV galaxies, respectively. Additionally, the numbers quoted on the top right side state the Pearson correlation coefficient (pcc) between $[Z_{Mg}/Z_{Fe}]$ and velocity dispersion, where the colour coding follows that of the lines.

of simple stellar population (SSP) spectra supplied by the user, selecting a best fit by minimizing a χ^2 statistic with an MCMC sampler. For this chapter, we use a grid of N_*=138 SSPs from the models of Bruzual and Charlot (2003, hereafter BC03), adopting a Chabrier (2003) IMF. Our grid consists of 28 distinct stellar ages and 6 different metallicities. The age ranges from 1 Myr to 13 Gyr, spaced logarithmically, and the metallicity varies from [Z/H]=−2.3 to +0.4.

We mask out the standard spectral regions where nebular emission may be prominent. The fitting range we chose – 3500-7500Å– includes a number of age- and metallicity-sensitive regions such as those targeted in the previous section. Spectral fitting provides an alternative approach to individual line strength analysis; the larger amount of information, including the stellar continuum from the NUV, optical and NIR windows, allows for constraints on more complex distributions of stellar ages and metallicities.

3.6.1 Luminosity-weighted parameters

Fig. 3.16 shows the luminosity-weighted averages of some key stellar population parameters of the GV stacks as a function of velocity dispersion. The top (bottom) panels show the D4k- (colour-) based selection, respectively. The blue dashed,

green dotted and red solid lines represent the result for lGV, mGV and uGV, respectively. Each panel quotes the corresponding Pearson correlation coefficient (pcc). In each panel, from top to bottom, we show the average stellar age, $\langle t \rangle$, a parameter, Δt, defined below, that keeps track of the width of the age distribution, the average total metallicity, $\langle [Z/H] \rangle$, and the dust attenuation applied as a foreground screen, A_V. The average age is defined as:

$$\langle \log\, t \rangle = \sum_{j=1}^{N_*} x_j \log\, t_j, \tag{3.8}$$

where x_j is the normalized luminosity weight (i.e. $\sum_j x_j = 1$) and t_j is the age of the j-th SSP in the basis set (see Cid Fernandes et al., 2005, for details). The average age shows the well-established trend, where velocity dispersion, roughly a proxy for galaxy mass, is positively correlated with the average age (e.g., Gallazzi et al., 2005). Galaxies on the uGV are consistently older at all values of velocity dispersion. The age difference between mGV and lGV is less prominent than between these two and the uGV. A possible explanation for this trend is discussed in Sec. 3.7.3. The age difference between the uGV and lGV stays in the region 0.5-1 Gyr, a consistent result with respect to the SSP analysis shown in Sec. 3.5.

The uncertainties of the parameter estimates are obtained by making 20 Monte Carlo realizations of each stack, by adding noise consistently with the uncertainties in each flux bin, and re-running each one of them through STARLIGHT. The realizations produce a distribution from which the standard deviation of the parameter estimates is quoted as the uncertainty. Galaxies in the lGV have a smoother age trend with respect to velocity dispersion.

The second age indicator, Δt (second panel from the top), is extracted from the cumulative stellar mass profile:

$$\mathscr{C}(s) = \sum_j x_j (t \leq s). \tag{3.9}$$

Defining the inverse of this function as $\tau(y) \equiv \mathscr{C}^{-1}(y)$, we take the time interval $\Delta t \equiv \tau(0.70) - \tau(0.30)$, i.e. the time lapse spanning the epochs when the galaxy,

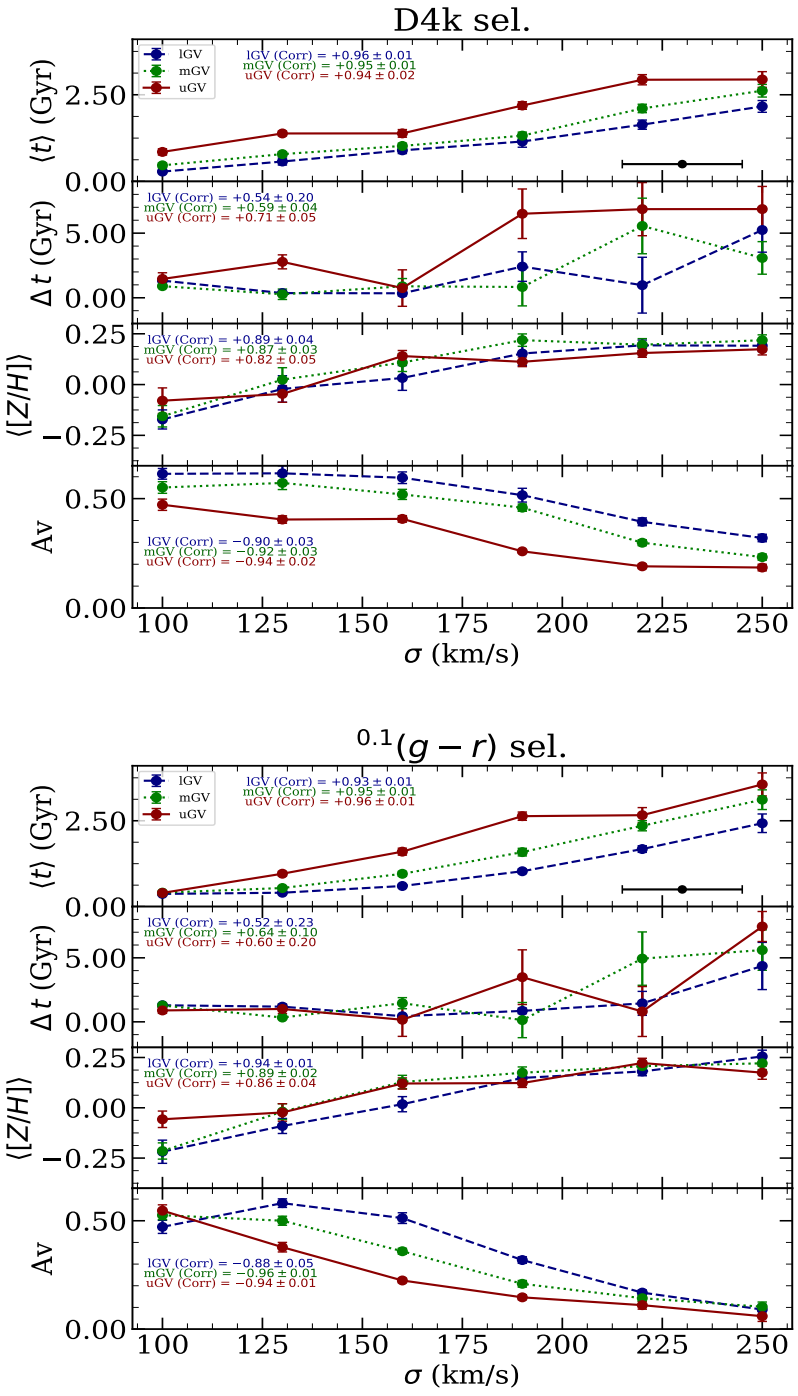

Figure 3.16: Population parameters - from top to bottom, average age, our defined quenching timescale Δt, average metallicity and dust attenuation - for D4k- (top) and colour-selection (bottom). In each panel, the blue, green and red data points are labels for lGV, mGV and uGV, respectively. Again, with the same colour coding, the numbers in each panel indicate the Pearson correlation coefficient for lGV, mGV and uGV.

or its progenitors, formed between 30% and 70% of its total stellar mass. The motivation behind this definition is to provide a GV transition interval that could be related, for instance, with a quenching timescale. However note three important caveats. Firstly, if the galaxy has experienced a rejuvenation episode, the recently formed stars will be given more weight, thus leading to high Δt values: even if the actual quenching timescale is relatively short. Secondly, we are dealing with stacks that include star-forming galaxies. Therefore, our definition of Δt should be considered as an effective GV timescale, rather than a true quenching interval. Additionally, we are considering All_{stacks}, so while we have fewer number of SF galaxies in high velocity dispersion bins, they still represent 19-28% of the galaxies in the stack, depending on the selection method and GV location. This will further complicate this parameter and its interpretation as being a true quenching timescale indicator. Finally, for the purpose of our analysis, we select the time taken to form 30% and 70% of the total stellar mass, however, our definition can be changed such that we could have used 50% and 90% or other similar intervals. We use 30% and 70%, as these intervals have the lowest estimated uncertainty associated to them, whereas the use of 90% will carry a large uncertainty. Owing to these complexities, here, we find Δt increases in all cases, whereas previous results from the literature noted that the quenching timescale evolves in a complex way with velocity dispersion, with an initial increase, followed by a decrease at the massive end (Gabor et al., 2010; Wright et al., 2019), similar to what is found in Fig. 3.12, when considering only quiescent galaxies.

The third panel from the top shows the average total metallicity, calculated in a similar manner to average age, namely:

$$\langle [Z/H] \rangle = \sum_{j=1}^{N_*} x_j [Z/H]_j, \tag{3.10}$$

where $[Z/H]_j$ is the individual SSP metallicity of the jth component. A strong positive trend is also found between total metallicity and velocity dispersion, once more in agreement with previous studies of the general population (see, e.g., Gallazzi

et al., 2005; Graves et al., 2010). At the low mass end, the colour-based selection (panels on the bottom), shows a consistent trend towards a higher metallicity in the uGV with respect to the lGV. However, this trend is less evident in the D4k selection (top panels), which is less sensitive to contamination from dusty, star-forming (and possibly lower metallicity) galaxies, especially in the lGV; resulting in a weaker correlation for D4k selected samples in comparison to a colour-based GV. The D4k selection shows that, within error bars, metallicity does not segregate within the GV at fixed velocity dispersion. *This result suggests a potential bias when selecting GV according to colour.* The next (bottom) panels of Fig. 3.16, for both selection methods, show the monotonically decreasing trend of dust attenuation with σ, consistent with previous studies (e.g., La Barbera et al., 2014), featuring a clear stratification from lGV to uGV, with mGV galaxies having, once more, properties closer to lGV galaxies. This information can also help assess potential biases related to the dust correction needed in the colour-based selection. It is worth mentioning the small difference in A_V at the lowest velocity dispersion in colour-based GV galaxies. One could argue that the dust correction could be partly responsible for this result, whereas the D4k selection shows the A_V stratification between uGV, mGV and lGV at all values of σ.

Fig. 3.17 shows the variation in average metallicity as a function of Δt and average age, as labelled. The results of a D4k (colour) selection of GV galaxies is shown on the top (bottom) panels, following the same colour coding as the previous figure to represent the uGV, mGV, lGV stacks. The marker size maps velocity dispersion. Focusing on the D4k selected sets, we find two different trends in the sample; i) at low metallicity ($\langle[Z/H]\rangle \lesssim +0.1$), GV galaxies have short Δt ($\lesssim$3 Gyr); ii) at higher metallicity, GV galaxies have a broader distribution of Δt, a result indicative of rejuvenation. In this region, galaxies have higher velocity dispersion and feature older stellar populations. Moreover, lGV and mGV galaxies have relatively shorter Δt, with respect to uGV systems, that have $\Delta t \gtrsim$5 Gyr. Therefore, a higher fraction of uGV galaxies at the massive end appear to have undergone more substantial episodes of rejuvenation. The standard age-metallicity relation can be found in the

figure, with a significant stratification towards older populations at fixed metallicity in uGV galaxies. This effect is more pronounced in the D4k selection, whereas the colour-based selection produces a more complex mixture at low velocity dispersion, as expected from the contribution of dust, more prevalent at this end of the distribution.

3.6.2 Star Formation History (SFH)

The next step in the analysis of the spectral fitting constraints is the star formation history, namely the distribution of SSP weights, x_j as a function of age – i.e. marginalized with respect to metallicity. Note that individual SFHs constrained on a galaxy by galaxy basis are rather uncertain with any population fitting code, and STARLIGHT is no exception. However as we are dealing with stacked spectra covering a large number of galaxies, we can assume that the derived SFHs represent statistical trends in the various regions of the GV probed here. Fig. 3.18 shows the luminosity-weighted output for lGV (blue), mGV (green) and uGV (red). The histograms bin the age intervals in a linear manner. The average age and metallicity, quoted in each panel, have been calculated using the SSP ages of the basis set, along with their corresponding weights, following equations 3.8 and 3.10. The left and right panels show the results at the lowest and highest velocity dispersion bins, $70< \sigma <100$ km/s and $220< \sigma <250$ km/s, respectively. The upper (lower) panels show the results for the D4k (colour) selection, as labelled. Note these results are robust regarding the *relative* weight contributions, whereas absolute estimates may carry larger uncertainties. To assess the statistical uncertainty, we perform for each stack a Monte Carlo set of 20 realizations of spectra with the same flux distribution and noise compatible with the stack under consideration, following an identical methodology. The shaded regions in the figure show the expected uncertainty from this comparison. Note that spectral fitting inherently constrains luminosity-weighted properties. A translation into mass-weighted values unavoidably carries additional uncertainties, related to the mapping from luminosity into stellar mass. For instance, a recent episode of star formation can bias the results as the hot, massive stars present in young populations contribute significantly more than their cool,

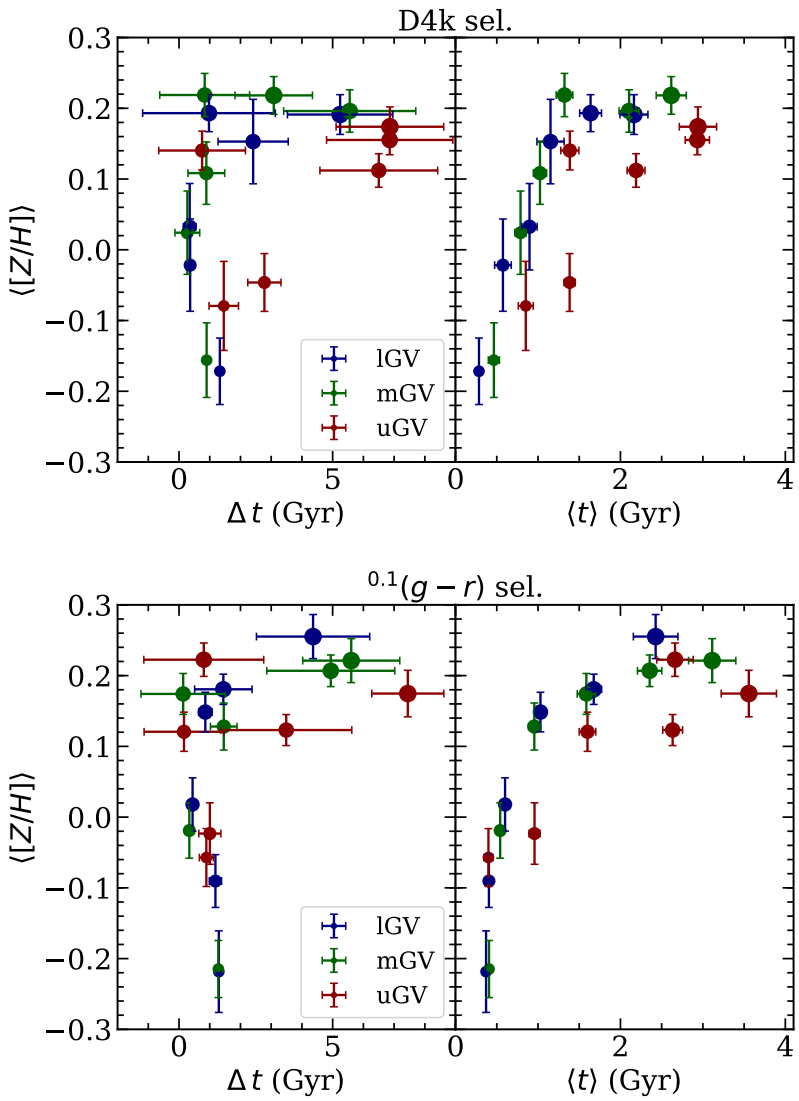

Figure 3.17: Relation between the average metallicity, $\langle[Z/H]\rangle$ and Δt, or average age, $\langle t\rangle$. The blue, green and red data points indicate results for lGV, mGV and uGV galaxies, respectively. The increase in the size of the data points, show an increase in the velocity dispersion and the error bars indicate the 1σ level. The top and bottom panels show the results for 4000Å break and colour selection of GV galaxies, respectively. Finally, note the uncertainty in average metallicity remains constant, whereas the error bar in Δt_Q increases with average metallicity.

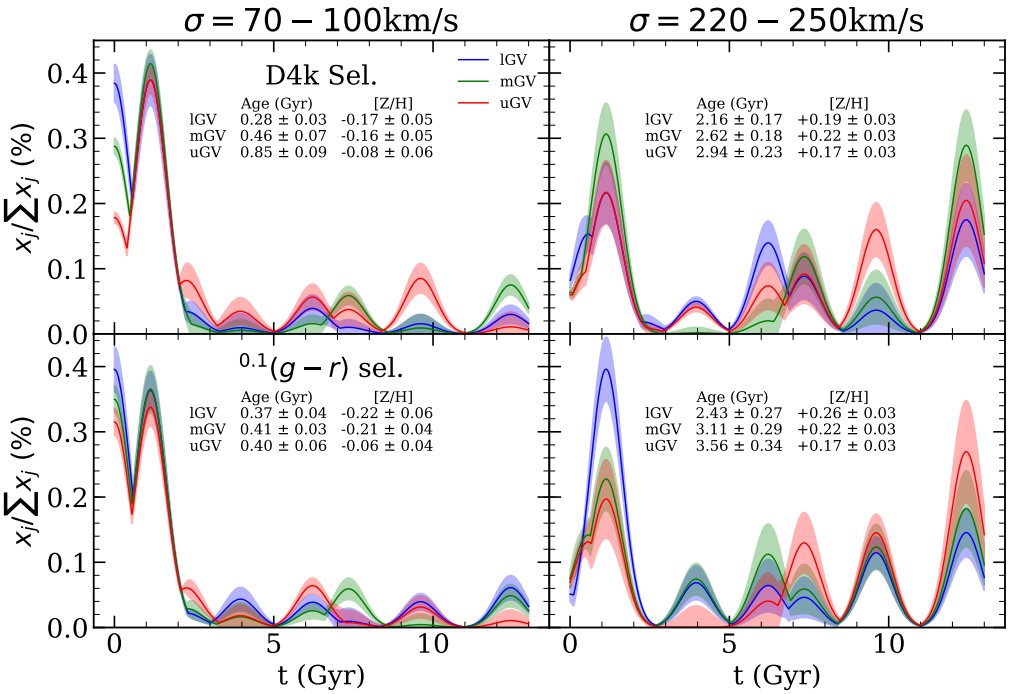

Figure 3.18: The luminosity weighted star formation history for $D_n(4000)$ (top) and colour (bottom) selected GV galaxies, at the lowest, $70 < \sigma < 100$ km/s (left), and highest, $220 < \sigma < 250$ km/s (right), velocity dispersion bins. Note $t = 0$ indicates today. Again the blue, green and red curves shows the SFH for lGV, mGV and uGV, respectively, and the shaded curved have been found by Monte Carlo realization of the spectra and running them through STARLIGHT to obtain their SFH. The text in each panel indicates the average age and metallicity of the stacks.

low-mass (although equally young) counterparts.

At low velocity dispersion (left panels) the stellar populations are mostly young. As we traverse the GV from lGV to uGV, more weight is given to the older components, increasing the average age from $\langle t \rangle \sim 0.3$ Gyr in the lGV to ~ 1 Gyr in the uGV, for the D4k selection, whereas the colour-based selection produces a more homogeneous distribution, with undistinguishable age differences "across the valley", and a significantly larger scatter. In all cases, the SFHs concentrate within the most recent ~ 2 Gyr, with small, subdominant old populations that become, only slightly, more prominent in the uGV. At high velocity dispersion (right panels), the SFHs evolve towards older components, with average (luminosity-weighted) ages $\sim 2 - 3$ Gyr.

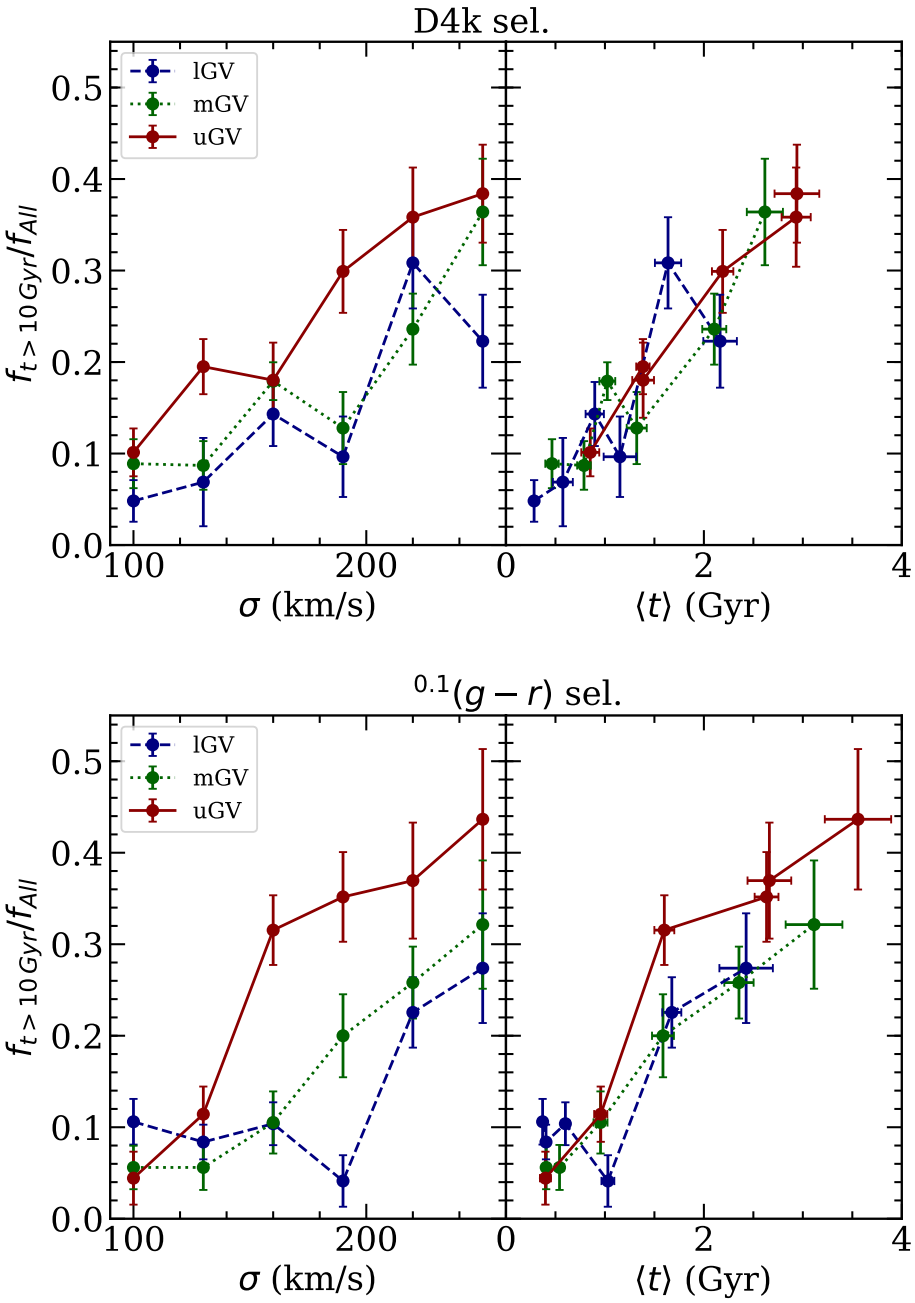

Figure 3.19: The variation in the fraction of old stellar populations ($\gtrsim$10,Gyr) with regards to velocity dispersion (left) or average age (right). The top and bottom panels show results for D4k and colour selection of GV galaxies. The blue, green and red lines correspond to lGV, mGV and uGV galaxies, respectively.

Fig. 3.19 shows the variation of the mass fraction in old (>10 Gyr) stars with respect to velocity dispersion and average age, for the D4k (top) and colour (bottom) selection. Both cases produce similar increasing trends of the old contribution in

the most massive galaxies and towards higher average ages. The latter statement is not trivial, as this diagnostic is sensitive to whether the age distribution changes its width with respect to average age. The D4k selection produces consistently higher old stellar fractions at all values of velocity dispersion, in lGV and mGV, whereas the colour-based selection, once more, shows some mixing at the low mass end. Regardless of the selection process, uGV galaxies display more of a difference with respect to mGV and lGV galaxies. Note that at low velocity dispersion, the colour selection yields a lower fraction in old stars, specially in the uGV. This is interesting as even though both selection methods feature not too dissimilar low fractions of Q galaxies ($7.3 \pm 0.4\%$ for D4k, and $4.2 \pm 0.4\%$ for colour), we see a greater number of SF galaxies in the colour-based selection (namely $70.0 \pm 1.3\%$ in the D4k selection versus $78.4 \pm 2.1\%$ for the colour selection). *This could be a further indication of a possible bias due to dust attenuation that causes BC galaxies to "creep" into the GV (Schawinski et al., 2014).* This theory is further supported at intermediate velocity dispersion bins, $100 < \sigma < 190$ km/s, where even though there is a lower contribution of SF galaxies in the D4k Selection of the uGV, a higher fraction of old stars is found in the colour-based GV stacks.

3.6.3 Mass-weighted population properties

In addition to the luminosity-weighted properties presented above, we can extend the analysis by use of the stellar mass to light ratio ($\Upsilon_\star$) provided by the population synthesis models for each SSP. Although this translation carries additional uncertainty, it is a way to assess whether the older components are more dominant than expected from a simple fit to the observations, which are inherently biased towards the most luminous stars. Mass-weighted parameters provide a more physical interpretation of the SFHs. The analysis is based on models with a fixed initial mass function, namely Chabrier (2003). We stress that within the velocity dispersion probed by this sample, no significant variations from a "standard" IMF are expected (see, e.g., Ferreras et al., 2013a; La Barbera et al., 2013).

Fig. 3.20 is the equivalent of the best-fit stellar parameters shown in Fig. 3.16 for the mass-weighted case, using the same line and colour coding. Similarly to the

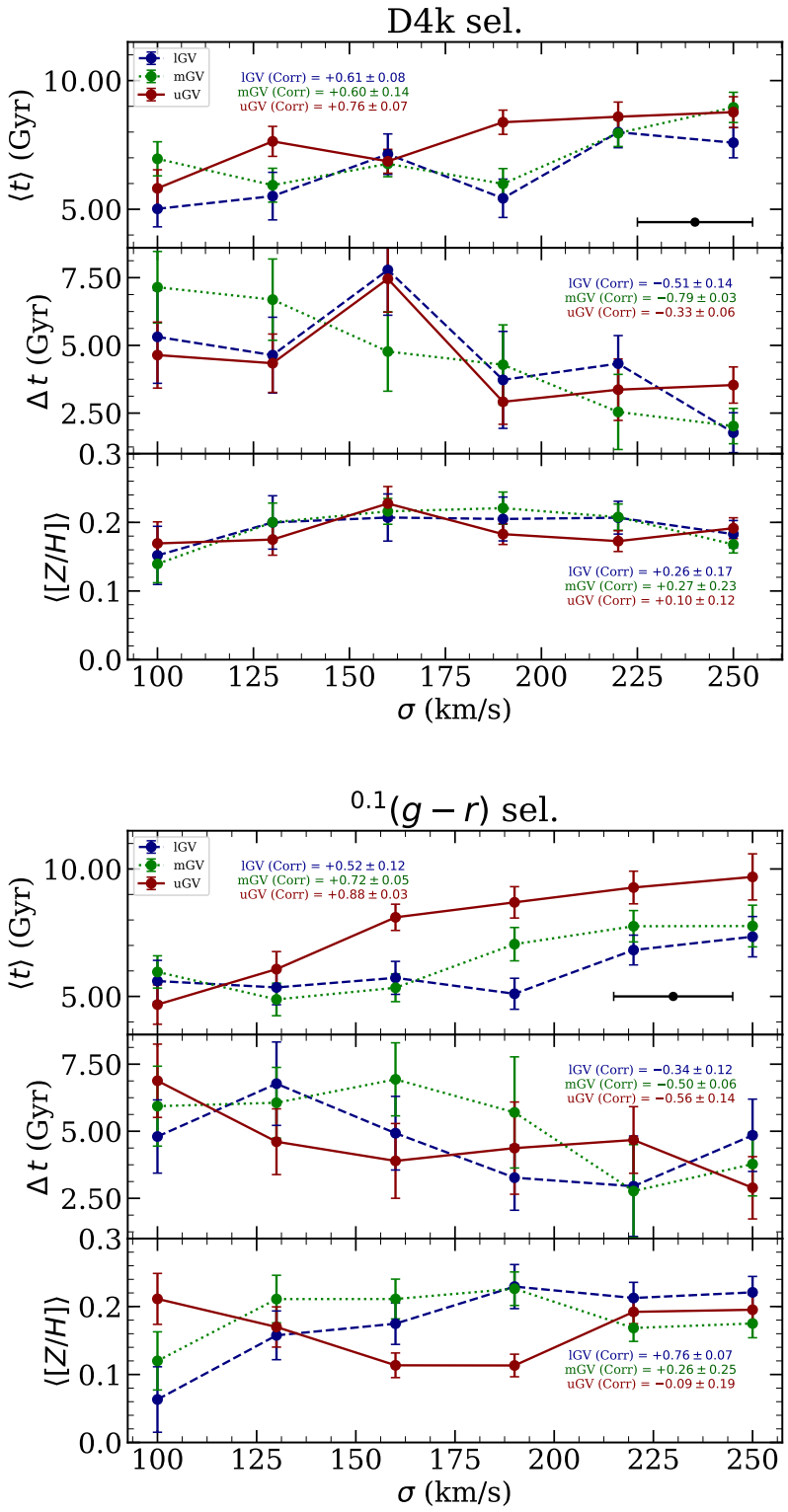

Figure 3.20: This is the equivalent of Fig. 3.16, showing mass-weighted parameters.

luminosity-weighted values, a general increase is found in average age with velocity dispersion but the absolute values are higher, as expected, and plateau at the massive end. Regarding GV sub regions, we also find here more affinity between lGV and mGV, whereas uGV galaxies appear older. This result is consistent regardless of the GV selection method, confirming that a selection based on the 4000Å break provides a homogeneous population. An increased scatter is evident in the mass-weighted estimates, partly due to the added uncertainties regarding the translation from light to mass. The Δt parameter shows a significant difference with respect to the luminosity-weighted counterpart, with overall high values and a *decreasing* trend with velocity dispersion, and no segregation regarding GV location (i.e. lGV, mGV and uGV). Note, though, there is an anti-correlation, that is weaker in comparison to Fig. 3.16. Estimates of average metallicity are now higher, and appear rather flat with respect to velocity dispersion, within error bars.

3.7 Discussion

In this chapter, we define the GV via a novel method, using the 4000Å break and study the stellar population properties of these GV galaxies in detail. We contrast the results obtained from this novel method, to the traditional approach based on the dust-corrected broadband colours. In this section, we explore the implications of this analysis as well as discuss potential biases/caveats.

3.7.1 Aperture Bias

The classic SDSS 3 arcsec diameter fibres map the central region of galaxies, $\sim$3-5 kpc, hence introducing potential biases with regards to stellar mass (velocity dispersion, as more massive galaxies are generally larger. Therefore, for more massive galaxies we are studying the very central regions and lower fraction of the overall galaxies, whereas for less massive galaxies we study an overall higher fraction and region. To assess this bias, we use the JHU/MPA catalogue (Kauffmann et al., 2003) and compare the colour within the aperture with the modelled colour for the whole galaxy (Fig. 3.21). The difference between these two definitions of colour shows a minimal trend with stellar mass. Due to $D_n(4000)$ tracing the average age in a

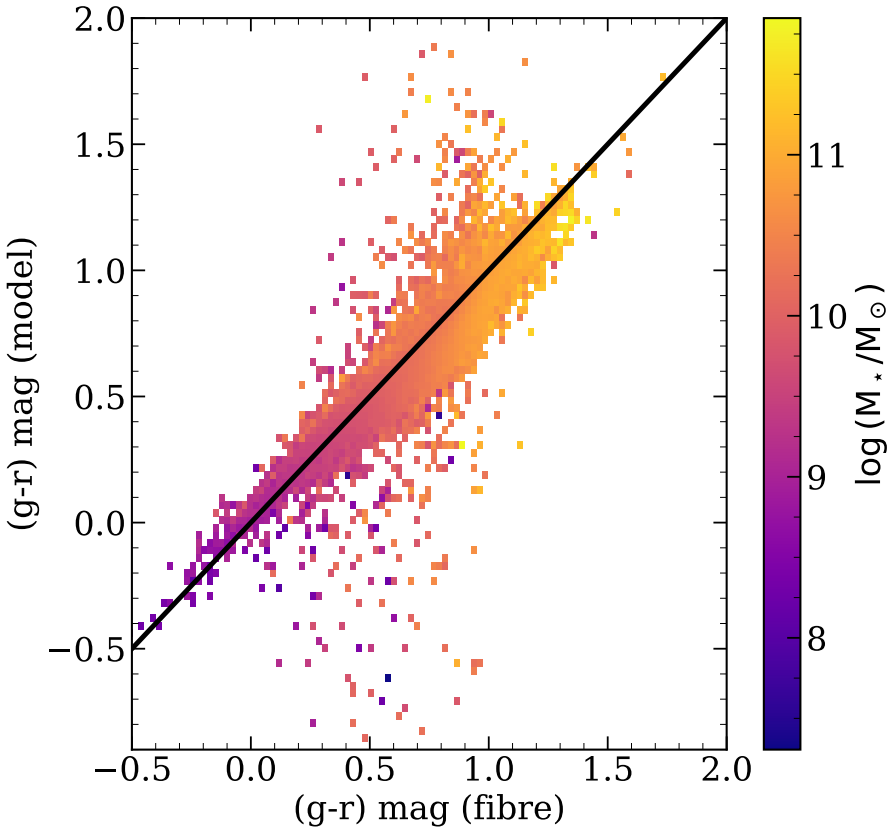

Figure 3.21: Comparison between the (g-r) colour measured inside the 3 arcsec fibre and the same colour measured for the whole galaxy (i.e. through the surface brightness modelling, which is determined from the official SDSS model magnitudes). The data is colour coded with respect to their stellar mass, indicated by the colour bar on the right. Finally, the unity line, 1:1 correspondence, is shown by the black line.

similar manner to colour, we expect a similar, minor, difference between $D_n(4000)$ inside the fibre and $D_n(4000)$ measured in the whole galaxy.

Though there is no bias in relation to stellar mass, we do see an offset between the colour in the fibre and that of the whole galaxy. Therefore, a similar behaviour in $D_n(4000)$ is expected. The inconsistency in colour between fibre and whole galaxy is partially due to biases from surface brightness modelling, as well as from the presence of gradients in population content. One physical mechanism that can give rise to these gradients is the inside-out/outside-in quenching. For instance, inside-out quenching will result in younger populations outside of the reach of the fibre (Kelvin et al., 2018). The opposite will be true when a galaxy is un-

dergoing outside-in quenching. Another cause for such behaviour would be galaxy morphology. More specifically, spiral galaxies with a strong bulge will produce a greater difference between fibre and whole galaxy estimates of both the colour and $D_n(4000)$.

3.7.2 Dust-related systematics

Another potential bias in the analysis could arise due to dust. The traditional selection of GV galaxies, based on colours derived from broadband photometry, is affected by dust attenuation. In order to remove the effect of dust, a model is applied to derive a colour correction term. However, these corrections are subject to uncertainties that depend on the model fitting as well as on additional systematics related to the details of dust attenuation in galaxies. It is worth emphasizing that the net effect of dust is to impose an effective, wavelength-dependent attenuation law. However, in detail, it is a result of a wide range of mechanisms involving scattering and absorption of photons from the illuminating source (i.e. the underlying stellar populations) by the dust particles. The effective attenuation depends not only on the composition of dust, but also on its distribution within the galaxy (see, e.g., Galliano et al., 2018). The dust is typically concentrated around star-forming sites, and motivates the birth cloud model, where a time-dependent dust attenuation provides a suitable description of the net attenuation law (see, e.g., Charlot and Fall, 2000). Observationally, star-forming galaxies feature a wide range of effective attenuation laws beyond the standard ones that fit the Milky Way average extinction curve (Cardelli et al., 1989) or the average attenuation of star-burst galaxies (Calzetti et al., 2000). The variation of the parameters that describe the attenuation law also appear to correlate (Tress et al., 2018; Salim and Narayanan, 2020). Therefore, such trends can lead to significant systematics in the dust correction.

To illustrate the dependence of the 4000Å break and colour-selection of GV galaxies with respect to dust attenuation, therefore the systematics associated with dust correction, we compare in Fig. 3.22 the difference between the trends found for the location of the BC (blue); GV (green) and RS (red), as a function of velocity dispersion. Each one corresponds to the mean of the PDF associated to each

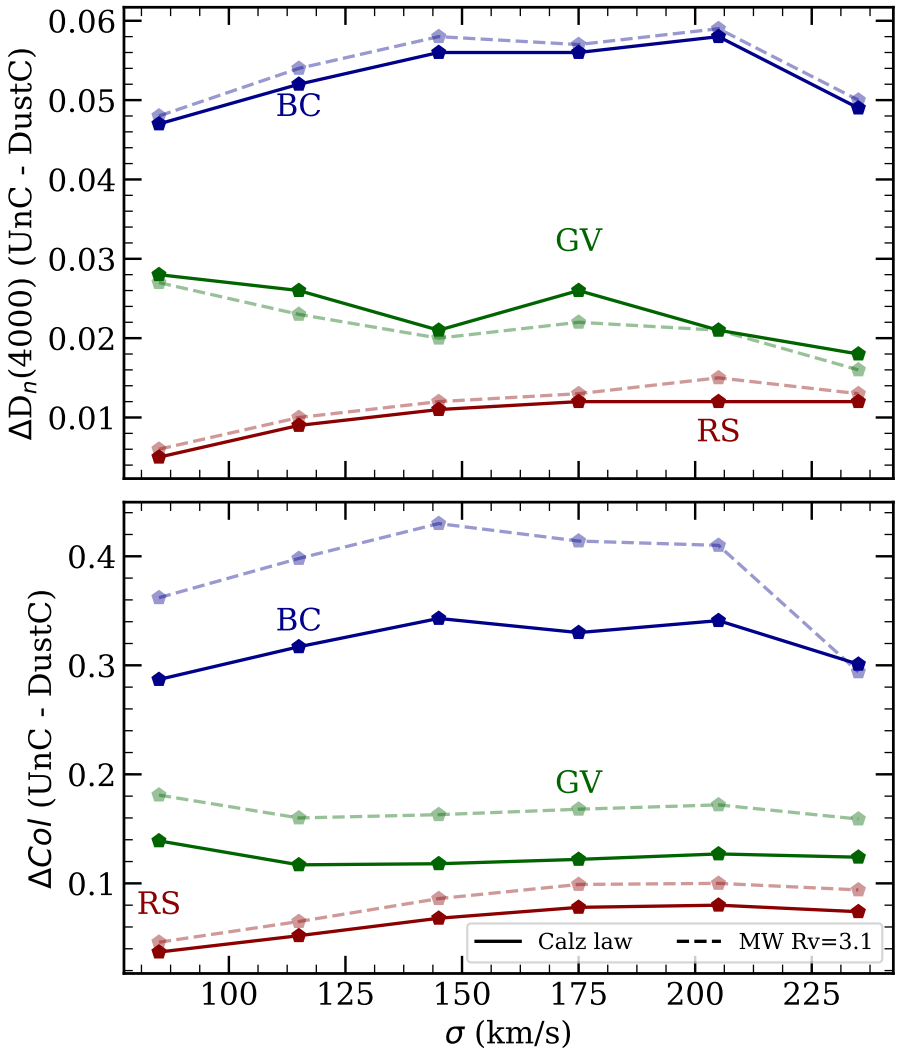

Figure 3.22: This tests the systematics associated with dust correction when defining the evolutionary sequence, i.e. BC (blue), GV (green) and RS (red), using 4000Å break strength (top) and $(g-r)$ colour (bottom). This presents the difference in BC, GV and RS locations after dust correction, where we consider two different dust attenuation law: Calzetti et al. (2000), solid lines, and Cardelli et al. (1989), dashed lines. The systematics associated to each method can be obtained by taking the difference between solid and dashed lines.

sub-population (see Sec. 3.2.2). The top and bottom panels display the difference between BC, GV and RS with and without dust correction for $D_n(4000)$ and colour, respectively. To test for systematics we apply either a Milky Way extinction law (Cardelli et al., 1989, dashed lines) or a Calzetti et al. (2000, solid lines) law. Note the small difference when using the selection based on break strength (top panels), especially on GV galaxies, at the level $\Delta D_n(4000) < 0.03$, whereas the colours (bottom panels) are not only substantially affected – with correction terms comparable to the actual separation between BC and RS, but are also heavily dependent on the attenuation law adopted, and thus prone to systematics from the variance regarding the details of dust composition and geometry.

Due to the systematics of the dust, correction using different dust attenuation laws will change the location of the galaxies in the evolutionary sequence. This will affect the fraction of different galaxy types in BC, GV and RS. This can be analysed from Table 3.2, which shows the fraction of galaxies in the lGV and uGV, when selected according to either D4k or colour, with the latter shown with and without a dust correction. A graphical description of this table can be found in Fig. 3.8. Note the D4k-selected GV yields a larger population of SF galaxies, than the *uncorrected* colour selection, especially towards high velocity dispersion ($\sigma \sim 200$ km/s), along with a lower percentage of Q galaxies. Such a trend could be down to two reasons. Firstly, dust could have reddened the galaxies to different amounts, so that SF galaxies occupy a wider region, leading to broader Gaussian PDFs when performing a colour-based selection. Secondly, due to our GV definition being dependent on the PDF of SF galaxies, the GV might have been shifted towards the RS in the colour-based approach. This explains the large (small) percentage of Qs (SF) population in lGV $72.5 \pm 13.5\%$ ($7.5 \pm 4.3\%$)and uGV $82.2 \pm 13.5\%$ ($8.9 \pm 4.4\%$), at the highest velocity dispersion ($220 < \sigma < 250$ km/s).

The introduction of a dust correction makes the D4k- and colour-based selections closer together (see also Fig. 3.8), illustrating the importance of dust correction when using colours. In more detail, note that the dust-corrected colour-based GV gives a lower fraction of Q galaxies in both lGV and uGV, with respect to the

D4k selection. Although this might seem counter-intuitive, note that the largest effect when applying the dust correction of the colours is to increase the number of SF galaxies. Therefore, we deduce that most of the galaxies that appear on the GV after the dust correction is applied originate from the RS defined by the dust-uncorrected classification – as the effect of the correction is always to make the colours bluer. Another interesting trend can be seen when going from intermediate (σ=160–190 km/s), to high (σ=190-220 km/s) velocity dispersion, where we see an increase in the SF population in both D4k and dust-corrected $^{0.1}(g-r)$ selection of lGV and uGV. Note this trend is not seen in the dust uncorrected $^{0.1}(g-r)$ selection.

Moreover, note the difference in the line strengths between the full GV stacks and those consisting exclusively of Q galaxies – shown in Figs. 3.10 and 3.11. The D4k-selected sample shows a more homogeneous distribution, in contrast with the larger variations found in the colour-based selection. Furthermore, we also find differences in the transition timescale Δt_{SSP}, when considering Q_{stack} and All_{stack}, in Figs. 3.12 and 3.14, where the $D_n(4000)$ selection shows a smoother trend compared to the colour selection in both instances, *suggesting the colour selection gives a more complex mixture of populations at different locations of the GV*. These results illustrate the highly non-trivial issue of the systematics expected in the selection of GV galaxies, and leads us to adopt the D4k selection as a more robust representation of the GV.

3.7.3 Interpretation of the GV as a transition region

We now take the D4k-selected GV as our standard sample. The differences in the stellar population properties of the three different areas of the GV, at fixed velocity dispersion, reflect the nature of the GV as a transition phase. The line strength results allow us to see in a model-independent way these variations. Fig. 3.9 shows a substantial difference in the higher order Balmer lines, especially Hδ_F, with respect to the other indices, such as Mgb, Fe5270, Fe5335. Hδ_F is especially sensitive to recent episodes of star formation (see, e.g., Martin et al., 2007) and thus may imply, when considering stacked spectra, that the contribution from rejuvenated galaxies dominates the flux, especially at high velocity dispersion. Also note that at low ve-

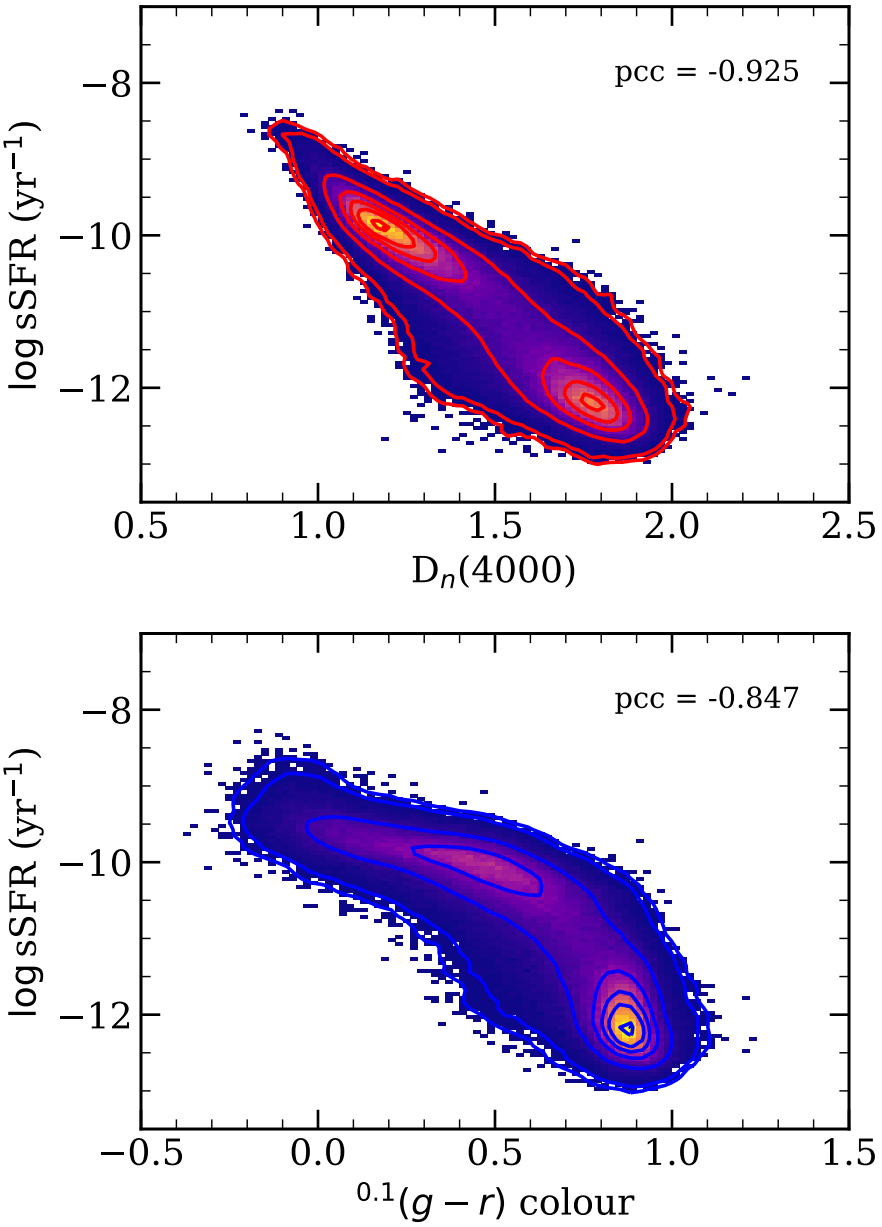

Figure 3.23: Relation between the sSFR and D4k (*top*) and sSFR and dust-corrected colour (*bottom*). The numbers on the top right corner note the Pearson correlation coefficient (pcc), where D$_n$(4000) shows a stronger (anti)-correlation with sSFR, in comparison to colour.

locity dispersion, the trend of Hδ_F is smoother, tentatively meaning that a smoother decaying (or truncated) star formation is in operation, suggesting a quenching mechanism – of otherwise younger populations – at the low-mass end.

Further supporting the results from line strength analysis, the population con-

straints based on SSP ages provide additional evidence towards rejuvenation at high velocity dispersion. The parameter Δt_{SSP} estimates the transition timescales, where we see a drop $\Delta t_{SSP} \sim 1.0$ Gyr for the highest velocity dispersion bin $220 < \sigma < 250$ km/s, when only considering Q_{stack} (Fig. 3.12). However, this behaviour is not seen when we consider All_{stack} (Fig. 3.14), where for the greatest velocity dispersion bin, we see an increase in $\Delta t_{SSP} \sim 5.-$ Gyr - suggesting greater difference in the ages of stellar populations between lGV and uGV, thus a longer transition timescale. Furthermore, we find similar trends when considering results from spectral fitting analysis (Fig. 3.16), where the parameter Δt is defined as an estimator of the width of the stellar age distribution, and stays at $\Delta t \lesssim 2$ Gyr for $\sigma < 170$ km/s (luminosity-weighted) – corresponding to a more compact age distribution – followed by very large values of Δt at the massive end, as expected from the presence of two or more disjoint star formation events across cosmic time, expected when rejuvenation produces a significant young component. Moreover, Fig. 3.19 emphasizes that the fraction of old (>10 Gyr) stars in uGV galaxies is high in massive galaxies and low at small velocity dispersion. Therefore, in this SDSS-based, low-redshift sample, quenching appears at late cosmic times in low-mass galaxies, whereas at the massive end one can only measure recent rejuvenation events on an otherwise old population. The mass-weighted results (Fig. 3.20) feature more scatter – as expected from the added uncertainties in $\Upsilon_\star$,when converting the SSP contributions into mass fractions – but interestingly produce a *decreasing* trend of Δt with velocity dispersion, implying that the rejuvenation events at the massive end cannot involve a large mass fraction of young stars. Nelson et al. (2018) also explored the fractional contribution of rejuvenated galaxies in the IllustrisTNG simulation, finding that $\sim 10\%$ of the subset of massive galaxies ($M_\star/M_\odot > 10^{11} M_\odot$) have undergone rejuvenation once and $\sim 1\%$ have experienced more than one rejuvenation event. Note our analysis shows rejuvenation to be dominant in stacked spectra at the massive end. However, the percentage of different types of galaxies in the stacks (Tab. 3.2 and Fig. 3.8) are roughly in agreement with the numerical simulations. Focusing on the uGV at high velocity dispersion ($220<\sigma<250$ km/s) we

find 19% are star-forming galaxies. If we assume that a fraction of these SF galaxies are simply transitioning from BC to RS, with the remainder representing rejuvenation events, i.e. galaxies that have dropped down from the RS, we might find similar fractions of rejuvenated systems as those found in the literature (Thomas et al., 2010; Nelson et al., 2018). A similar argument can be made for galaxies in lGV and mGV. However, the fractional contribution from star-forming galaxies is higher, and we expect a smaller contribution from rejuvenation events.

Regarding metallicity, we recover the standard mass-metallicity relation, as shown in Fig. 3.16. Although on a speculative tone, note the metallicity trend between uGV and lGV gets inverted between low- and high velocity dispersion (in the luminosity weighted version). Such a trend would be a consequence of fresh, lower metallicity gas contributing to the rejuvenation events at the massive end of the sample.

Concerning the transition from BC to RS, previous work from the literature indicates a rapid evolution through the GV due to its sparsity (see, e.g., Baldry et al., 2004; Taylor et al., 2015). However, this transition time depends on morphology. For instance, Schawinski et al. (2014) distinguish at least two morphologically-related transition paths. Early-type galaxies are thought to traverse the GV in a rapid manner, quenching their star formation very quickly and moving onto the RS, while, in contrast, late-type galaxies are expected to undergo a slower quenching process. This is supported by Kelvin et al. (2018), where they look at structural variations with respect to colour and morphology, and argue in favour of inside-out formation, which is related to slow quenching, instead of a violent transformative event. Additionally, the observational constraints from the stacked spectra give timescales between 2 to 4 Gyr (Phillipps et al., 2019). We are able to recover such trends when using SSP-equivalent ages for Q_{stack}, where we find a variation in transitional timescale ranging from from $1.0-3.5$ Gyr. Carrying out similar analysis by stacking spectra regardless of nebular activity (Fig. 3.14), also yield similar results, albeit there is no drop in transition timescale for the highest velocity dispersion. However, the difference between uGV and lGV luminosity-weighted average ages,

from spectral fitting, results in a lower transition time $\sim$1.0 Gyr. Interpreting Δt as a transition timescale leads to a higher value $\gtrsim$5 Gyr, with respect to Phillipps et al. (2019). Note this is to be expected as (i) STARLIGHT is robust at tracing average parameters but produce weaker constraints on the details of the SFH; (ii) The parameter Δt traces the transition time in a slightly different manner, as it is very sensitive to recent bursting episodes (see Sec. 3.6.1 for details), while the methodology adopted by Phillipps et al. (2019) uses a fixed exponentially decaying SFH, thus making it less sensitive to rejuvenation effects.

In addition, state of the art simulations give further support to a rapid transition through the GV; Wright et al. (2019) state that low velocity dispersion galaxies feature relatively long quenching timescales, $\tau_Q \gtrsim$3 Gyr. This timescale increases with velocity dispersion; but at the highest values of velocity dispersion, they find a drop to $\tau_Q \lesssim$2 Gyr. As for the physical mechanism that produces this transition, it is stated that in low-mass galaxies it is mostly due to processes such as ram pressure stripping, while in more massive galaxies quenching operates though events such as stellar feedback (Wright et al., 2019). Finally, in the most massive systems, major mergers and quasar-mode AGN are thought to quench star formation.

Finally note the similar behaviour between lGV and mGV, in contrast with uGV for the D4k-selected sample. Interestingly, this behaviour between the different GV regions was also seen by Phillipps et al. (2019) in their study of "green" galaxies using sSFR. They noted a lower transition time going from their "lGV" to "mGV" – selected by $\mathrm{sSFR}_{lGV}/\mathrm{sSFR}_{mGV} \sim$1.6, giving 2 Gyr – with respect to their "mGV" to "uGV" – selected by $\mathrm{sSFR}_{mGV}/\mathrm{sSFR}_{uGV} \sim$ 2.5, giving 3–4 Gyr. Fig. 4.5 shows the relation between D4k and sSFR (top) and between colour and sSFR $(bottom)$. The relation with D4k presents a stronger correlation (pcc$=-0.925$) compared to colour (pcc$=-0.847$), therefore it is not surprising that sSFR behaves in a similar manner to the 4000Å break strength. This similarity reinforces the trends found here.

3.8 Conclusions

We present in this Chapter a novel method for the selection of transitioning galaxies, by defining the green valley based on 4000Å break strength, and comparing our results with the the standard selection based on dust-corrected colours from broadband photometry. For both methodologies, we carry out a detailed analysis of the stellar population of galaxies residing in the GV. We make use of a large sample of high quality spectroscopic data from the Sloan Digital Sky Survey (SDSS). The new definition adopts the well-known spectral index $D_n(4000)$ of Balogh et al. (1999), whereas the colour-based approach uses the SDSS-defined, dust corrected colour $^{0.1}(g-r)$, i.e. K-corrected to redshift z=0.1, see Fig. 3.4. The "population" indicator, i.e. either $D_n(4000)$ or $^{0.1}(g-r)$, is plotted against velocity dispersion (σ), and the sample – defined between 70 and 250 km/s – is split into six bins in σ. A probability-based approach is followed, where the star-forming and quiescent samples define a Blue Cloud (BC) and a Red Sequence (RS), respectively, and an intermediate population, i.e., the green valley (GV) is introduced, and further split into three regions, lower (lGV), middle (mGV) and upper (uGV), based on the value of the population indicator.

Our results show overall consistent properties between the new definition, that is more resilient to potential systematics from the dust properties, and the dust corrected selection based on colour, with similar fractions between star-forming (SF) and quiescent (Q) galaxies with respect to velocity dispersion (see Table 3.2). More importantly, both definitions of the GV find a high fraction of AGN in uGV (lGV) - $D_n(4000)$ finds $\sim 30 \pm 5\%$ ($\sim 50 \pm 7\%$), which is similar to the dust-corrected colour selection, $\sim 37 \pm 6\%$ ($\sim 51 \pm 8\%$), see Fig. 3.8. Additionally, the study of SSP equivalent ages finds similar ages and similar transitional timescales for Q_{stack} (All_{stack}), where Δt_{SSP} varies from $1.0-3.5$ Gyr ($0.5-5.0$ Gyr) between both selection methods. This shows the validity of both selection methods in defining the GV, and selecting transitioning galaxies to study their general galactic properties. However, when studying the stellar population properties in more detail, subtle differences are found between these two selection criteria that may affect the interpre-

tation of galaxy evolution between the BC and RS regions. For instance, Figs. 3.10 and 3.11 show the difference between the line strength indices in spectral stacks comprising either the full set of GV galaxies, or only the quiescent subsample. The colour-based selection produces a different, more complex population mixture, part of which may be a systematic bias caused by dust attenuation and the subsequent correction. We also find that the population properties of lGV and mGV galaxies are closer together, with the uGV sample representing an altogether different set, with older, less dusty and more extended population mixtures (see Figs. 3.16 and 3.17).

The population analysis, based on spectral fitting of high quality stacked data, reveals the standard age- and metallicity- positive correlations with velocity dispersion (or alternatively mass). Moreover, we define a parameter, Δt, that describes the width of the age distribution, and find an interesting different between low- and high-σ galaxies (Fig. 3.17). The former have rather narrow widths ($\Delta t \lesssim 0.3$ Gyr), whereas the latter feature more extended distributions ($\Delta t \gtrsim 4$ Gyr). This result is consistent with the idea that at the low-mass end, the data reveal quenching of star formation, whereas massive galaxies display significant (luminosity weighted) late events, which would imply rejuvenation. The mass-weighted equivalent (Fig. 3.20), although presenting more uncertainty from the conversion of light into mass, confirms that these events do not contribute very large amounts in terms of the mass fraction.

Chapter 4

Evaluating hydrodynamical simulations with Green Valley galaxies

4.1 Introduction

In the previous chapter, we explored in detail the stellar population properties of galaxies in the green valley (GV) solely from the observational point of view. To select and define the transitioning galaxies, we used a novel definition of the GV. In this chapter, we use the same method to define the evolutionary sequence of galaxies from simulations, i.e. Blue cloud (BC - occupied by SF galaxies), GV (dominated by transitioning galaxies) and Red Sequence (RS - hosting mostly quiescent galaxies). This novel definition is used to test how well the state-of-the-art cosmological hydrodynamical simulations, EAGLE and IllustrisTNG, are able to reproduce the observational trends. This chapter is based on the work carried out in Angthopo et al. (2021)

4.2 Sample

We present here some details of the simulation and observational data explored in this chapter, while a more detailed explanation of the simulations can be found in the relevant papers quoted below. In this chapter, we focus our description mainly

on the aspects more relevant to the analysis of green valley galaxies, especially on the way AGN feedback has been implemented in the simulations.

4.2.1 The EAGLE (RefL0100N1504) simulation

EAGLE (Schaye et al., 2015; Crain et al., 2015) is a cosmological hydrodynamical simulation, which consists of multiple runs with varying box sizes and resolutions. For this project, we make use of the fiducial EAGLE simulation, termed RefL0100N1504 (hereafter Ref100), that use a comoving box size of L=$68h^{-1}$ Mpc=100 Mpc, which contains 1054^3 dark matter (DM) particles. The baryonic and dark matter particles have a mass of m_g=1.81×10^6M$_\odot$ and $m_{\mathrm{d}m}$=9.70×10^6M$_\odot$, respectively. EAGLE is constructed with the base code of GADGET 3 (Springel, 2005), where EAGLE use and modify the subgrid physics, smoothed particle hydrodynamics (SPH) formulation and the time step definition. In terms of physics, EAGLE uses a flat ΛCDM cosmology, where Ω_m=0.307, Ω_Λ=0.693, Ω_b=0.048, h=0.6777, σ_8=0.8288 - these values are taken from the Planck Collaboration et al. (2014).

Similarly to all other galaxy simulations, EAGLE models their galaxy formation and evolution through a number of prescriptions known as “subgrid physics”. This aims to describe the radiative cooling and photoheating, reionization of hydrogen, star formation, stellar mass loss and Type Ia Supernovae feedback due to star formation and AGN activity, and growth of supermassive black holes (SMBH). Most of the methods in EAGLE follow Schaye and Dalla Vecchia (2008), where the gas pressure, rather than its density, determines the star formation rate, tracing better the Kennicutt-Schmidt law. The simulations are also known to fail matching the observed number of high mass galaxies, as they have an ’overcooling’ problem for stellar feedback. This is thought to be owing to their limitation on the resolution. To solve this issue, the method outlined in Dalla Vecchia and Schaye (2012) is implemented, which assumes stellar feedback to be a stochastic process. Additionally, the gas particle with the highest density is converted to a collisionless particle, that is then treated as a seed of a black hole, which typically has a mass of $m_{\mathrm{B}H} = 10^5 h^{-1}\mathrm{M}_\odot$. This behaviour is only applied to galaxies with a high dark mat-

ter halo mass, above $m_{\mathrm{h},thres}$=$10^{10}h^{-1}\mathrm{M}_{\odot}$. Similarly to stellar feedback, the AGN feedback energy is also injected stochastically. There is thought to be two major modes of AGN feedback, 'quasar-' and 'radio'-mode. However, EAGLE tends to implement only the AGN feedback mode, which behaves more like quasar-mode feedback, as the thermal energy rate being inserted is proportional to the gas accretion rate where the SMBH is situated. Note, this prescription was necessary, due to the lack of resolution of simulations, which is thought to make the two modes of AGN indistinguishable (Naab and Ostriker, 2017).

EAGLE uses the Bondi mass accretion rate, defined in Bondi and Hoyle (1944): $\dot{m}_{\mathrm{B}ondi} = (4\pi G^2 m_{\mathrm{B}H}^2 \rho)/(c_s^2 + v^2)^{3/2}$, where ρ represents the density of the gas near the SMBH, c_s represents the sound speed and v is the relative velocity of the gas with respect to the black hole. The Bondi mass accretion rate is then used to calculate the mass accretion rate for the black hole, formulated as:

$$\dot{m}_{accr} = \dot{m}_{\mathrm{B}ondi} \times \min\left[C_{\mathrm{v}is}^{-1}(c_s/V_\phi)^3, 1\right], \tag{4.1}$$

where $C_{\mathrm{v}is}$ relates to the viscosity and is a free parameter, set at 2π for this simulation; V_ϕ is the rotation of the gas around the black hole. Thus, EAGLE accounts for the angular momentum of individual particles (Rosas-Guevara et al., 2015), in contrast to IllustrisTNG (see below). Note, while the "subgrid" physics that describes the AGN feedback is encapsulated in one equation, thus mimicking one mode of AGN feedback, the accretion rate depends on the mass of the black hole so the AGN feedback behaviour will vary for different stellar mass galaxies (Wright et al., 2019). The mass accretion rate is then contrasted with the Eddington mass accretion rate, and the lower value of the two is chosen to describe the black hole growth. Here we formulate the Eddington mass accretion rate as:

$$\dot{m}_{\mathrm{E}dd} = \frac{4\pi G m_{\mathrm{B}H} m_p}{\varepsilon_r \sigma_T c}, \tag{4.2}$$

where $\varepsilon_r = 0.1$ represents the radiative accretion efficiency, and σ_T is the standard Thomson cross-section. This equation can be quoted in terms of AGN luminosity,

$L_{AGN} = \dot{m}_{BH}\varepsilon_r c^2$, and the Eddington Luminosity can be written as $L_{Edd} = 1.25 \times 10^{38}(m_{BH}/\mathrm{M}_\odot)$ erg/s. Note, we have only discussed some of the "subgrid physics" in this section, however other details regarding the EAGLE simulation can be found in Schaye et al. (2015) and Crain et al. (2015). All of the simulated parameters, both spectroscopic and photometric, are computed within the central 3 kpc of a galaxy, which roughly corresponds to the aperture size of SDSS fibres. Additionally, for the measurement of the specific star formation rate, which is defined as SFR/$M_\star$, we use the SFR and stellar mass within 3 kpc as well, once more mapping the effective extent of the SDSS fibre. However, we use the stellar mass measured over the whole galaxy, for both simulation and SDSS, for all other purposes - i.e. defining the evolutionary sequence.

4.2.2 The IllustrisTNG (TNG100) simulation

IllustrisTNG is an improved version of the original Illustris simulation (Vogelsberger et al., 2014; Genel et al., 2014), which is built upon the AREPO code (Springel, 2010). Similarly to EAGLE, there are multiple runs with different volumes of which we make use of the TNG100 run. The data are publicly available (Nelson et al., 2019b), and has a box size of L=$75h^{-1}$ Mpc$\sim$110 Mpc, with the same number of inital dark matter particles and gas cells, N_{gas}=N_{DM}=1820^3. The mass of the baryonic and dark matter particles are m_{baryon}=$1.4 \times 10^6 \mathrm{M}_\odot$ and m_{dm}=$7.5 \times 10^6 \mathrm{M}_\odot$, respectively (Pillepich et al., 2018a; Marinacci et al., 2018; Springel et al., 2018; Nelson et al., 2018; Naiman et al., 2018). The TNG100 simulation has the highest redshift set at $z = 127$, where the initial cosmological parameters are set as: $\Omega_m = \Omega_{dm} + \Omega_b$=0.3089, Ω_b=0.0486, Ω_Λ=0.6911, h=0.6774 and σ_8=0.8159, following the constraints proposed by the Planck collaboration (Planck Collaboration et al., 2016). The subgrid physics for IllustrisTNG includes radiative cooling, star formation and SN feedback, black hole formation and growth along with AGN feedback; as in EAGLE and the original Illustris project. However, IllustrisTNG incorporates three key improvements with respect to Illustris, which are the growth and feedback of supermassive BHs and galactic winds and stellar evolution and gas chemical enrichment (Weinberger et al., 2018; Pillepich et al., 2018b).

Gas particles in TNG100 are stochastically converted to star particles if the density of the gas reaches a critical threshold, n_H=0.13 cm^{-3}. This number is fine tuned to reproduce the observed Kennicutt-Schmidt law at $z = 0$. Each of the star particles is assumed to have a Chabrier (2003) initial mass function and age. These stellar populations will evolve over time, where they return a fraction of their mass and elements to the neighbouring interstellar medium. Both core collapse SNII, within the mass range $m_\star$=8–100 M$_\odot$, and type Ia SN are included in the TNG100 simulation. The less massive stars, $m_\star$ =1–8 M$_\odot$, evolve through the AGB phase. More detailed information regarding stellar evolution can be found in Pillepich et al. (2018b).

TNG100 has two modes of AGN feedback. During the low-accretion state of SMBH, TNG100 assumes kinetic AGN feedback rather than the bubble model (Sijacki et al., 2007). When the SMBH has a high accretion rate, TNG100 applies a model of thermal feedback, similar to EAGLE, where energy is injected to the surrounding area continuously. On the other hand, during low accretion rates, TNG100 uses kinetic feedback, where BH driven winds are created. The initial black hole seed mass and halo mass threshold are $\mathrm{m}_{BH} = 8 \times 10^5\, h^{-1}\mathrm{M}_\odot$ and $\mathrm{M}_{\mathrm{h},thres}$=7.38 $\times$ 10^{10}M$_\odot$, respectively. Note, these are greater than those of EAGLE, which may be important as discussed below. The rate of accretion is similar to that of EAGLE, however TNG100 tries to distinguish between two modes of AGN feedback - kinetic and thermal. They are differentiated by the definition of the Eddington ratio, formulated as:

$$\lambda_{\mathrm{E}dd} = \frac{\dot{m}_{\mathrm{B}ondi}}{\dot{m}_{\mathrm{E}dd}}. \tag{4.3}$$

The Bondi mass accretion rate is formulated in a slightly different manner to EAGLE:

$$\dot{m}_{\mathrm{B}ondi} = \frac{4\pi G^2 m_{\mathrm{BH}}^2 \rho}{c_s^3}, \tag{4.4}$$

where $c_s = \left[c^2_{\mathrm{s},therm} + (B^2/4\pi\rho)\right]^{1/2}$, thus encapsulates both thermal and magnetic processes. The Eddington mass accretion rate also varies from that of EAGLE

(equation 4.2), as the radiative efficiency of a black hole is twice, ε_r=0.2 (Pillepich et al., 2018b), that of EAGLE, ε_r=0.1 (Crain et al., 2015). The mode of AGN feedback is determined by the accretion rate threshold χ, such that $\lambda_{\mathrm{E}dd} < \chi$ means low accretion rate and results in kinetic feedback and $\lambda_{\mathrm{E}dd} \geq \chi$ enforces thermal feedback, as this resembles a high accretion rate (Weinberger et al., 2017). The threshold, χ, is given by the equation:

$$\chi = \min\left[\chi_0 \left(\frac{m_{\mathrm{BH}}}{10^8 M_\odot}\right)^{\beta}, 0.1\right], \tag{4.5}$$

which introduces a mass dependency. Both χ_0 and β are set as free parameters. The 0.1 threshold sets a hard limit, enabling SMBH with high mass to experience either thermal or kinetic feedback, as without such criterion, all SMBH, at high black hole mass, would only experience kinetic mode AGN feedback (Weinberger et al., 2018). All the parameters of TNG100, with the inclusion of the spectroscopic index $\mathrm{D}_n(4000)$, are measured within an aperture that resembles the central 3 kpc of a galaxy - similar to EAGLE. Note the measurements of the 4000Å break are carried out from synthetic spectra constructed from the SFH of galaxies in both simulations. The creation of these spectra is discussed below in Section 4.3.1. Again, the exception to this is the total stellar mass, which is measured for the whole galaxy.

4.2.3 Observational data (Sloan Digital Sky Survey)

The details of the observational data can be found in Chapter 3. Here we briefly outline the main selection criteria for the observational data. The catalogue consists of galaxies with *r*-band magnitude between 14.5 and 17.7 AB. The coverage of the SDSS spectrograph varies from 3,800 to 9,200Å. The resolution increases from 1500 at 3800Å to 2500 at 9200Å (Smee et al., 2013). We select galaxies in redshift with $0.05 < z < 0.1$, to avoid redshift and aperture bias. Finally, all the spectra must have snMedian_r $>$10, giving us a total of $\sim$228,000 spectra.

In Chapter 3, we chose velocity dispersion as the fundamental parameter, as it has the highest correlation with the population properties, following the well-known observational trend (see, e.g., Bernardi et al., 2003; Ferreras et al., 2019). Veloc-

ity dispersion is a "clean" observable in spectra with high S/N, with significantly fewer uncertainties than stellar mass – another important parameter that correlates strongly with population properties. However, in simulated data, the velocity dispersion of a galaxy is a complicated quantity that depends on many details of the formation process, especially the dynamics associated to the mass accretion history. Additionally, accurate measurements of velocity dispersion are further inhibited owing to the resolution limit of simulations. Stellar mass provides a comparatively more robust indicator of the global properties of a galaxy in a simulation. Therefore, in contrast with Chapter 3, we adopt stellar mass as the main parameter in the analysis of the trends. We convert the six velocity dispersion bins of our previous study, $70<\sigma<250\,\mathrm{km\,s^{-1}}$, to stellar mass bins, by use of the observed trend $\log \mathrm{M}_\star/\mathrm{M}_\odot = (1.84 \pm 0.03)\log\sigma_{100} + (10.3 \pm 0.3)$, derived from stellar masses as quoted in the SDSS galSpecExtra catalogue (Brinchmann et al., 2004), where σ_{100} is the velocity dispersion, measured in units of $100\,\mathrm{km\,s^{-1}}$. Tab. 5.1 shows the mass bins derived using this conversion, along with the newly defined blue cloud (BC), green valley (GV) and red sequence (RS). Note this conversion between velocity dispersion and stellar mass is solely done for the stellar mass bins. For individual galaxies we use the stellar masses given by the galSpecExtra catalogue (Brinchmann et al., 2004).

We follow a similar approach to what is outlined in Chapter 3, where we define BC, GV and RS using the observed distribution of SF and Q galaxies, identified with the BPT diagram (see Fig. 1.4 and, Baldwin et al., 1981), within a fixed stellar mass bin. We define the probability distribution function (PDF) for the BC ($\mathscr{P}_{BC}$) and RS ($\mathscr{P}_{RS}$), respectively, assuming a Gaussian distribution. From these, we define the PDF of GV galaxies ($\mathscr{P}_{GV}$) as another Gaussian peaking at the value of $\mathrm{D}_n(4000)$ for which $\mathscr{P}_{BC} = \mathscr{P}_{RS}$, i.e. both subsets are indistinguishable at this value of the 4000Å break strength. Again the GV is divided into terciles, defining the upper (uGV), middle (mGV), and lower (lGV) green valley. We find good agreement between the BC, GV and RS defined with respect to stellar mass or velocity dispersion, within statistical uncertainties. The only significant deviation

Table 4.1: Blue cloud (BC), green valley (GV) and red sequence (RS) defined using the spectral feature, $D_n(4000)$ index, as proposed in Chapter 3. Here, we use the stellar mass as the fundamental parameters (rather than the velocity dispersion), for a better comparison with the simulations. The values stated in columns 2, 3 and 4 presents the $D_n(4000)$ values associated with the different stellar mass bins, shown in column 1.

$\log M_\star/M_\odot$	BC	GV	RS
10.03 – 10.30	1.20 ± 0.08	1.40 ± 0.07	1.67 ± 0.13
10.30 – 10.51	1.25 ± 0.09	1.47 ± 0.06	1.72 ± 0.11
10.51 – 10.68	1.28 ± 0.10	1.52 ± 0.05	1.75 ± 0.10
10.68 – 10.81	1.30 ± 0.10	1.54 ± 0.05	1.77 ± 0.09
10.81 – 10.93	1.32 ± 0.10	1.57 ± 0.04	1.78 ± 0.08
10.93 – 11.03	1.34 ± 0.12	1.60 ± 0.04	1.79 ± 0.08

was found at the highest mass bin: $10.93 < \log M_\star/M_\odot < 11.03$, where a difference is found in the definition of the GV at the level $\Delta D_n(4000) \sim 0.1$ dex. At the stellar mass, $\log M_\star/M_\odot \gtrsim 10.5$, the BC is sparsely populated, therefore the probability-based methodology is less accurate.

4.3 Data Pre-processing

Before carrying out the analysis, we need to pre-process both the observational and simulation data to homogenise their distributions in order to minimise selection biases, and to produce synthetic spectra from the simulated galaxies with the same instrumental signature as the SDSS data. Note the spectra and the simulation parameters are extracted within a R=3 kpc aperture, to make a consistent comparison with SDSS, while the stellar mass, for both simulation and SDSS, is derived for the whole galaxy. This section focuses on the methodology adopted to prepare the samples so that a direct comparison could be made.

4.3.1 Synthetic spectra

Our comparison uses the $z = 0.1$ snapshot of the simulations, comparable to the redshift range of the SDSS database (differences between $z = 0$ and $z = 0.1$ are minimal for this analysis). In both EAGLE and TNG, we produce a simple stellar population (i.e. single age and chemical composition) for each stellar particle, mixing those populations into composites for all particles in the same galaxy. The stellar parti-

cles have mass above $10^6 M_\odot$, therefore this approach is well justified and does not suffer from any issues related to the sampling of the IMF. Due to the mass resolution of the stellar component in state-of-the-art simulations at present, the low SFR regime is typically sampled by the creation of a few or eventually just one $10^6 M_\odot$ star particle. Note these will in turn produce a bias in the spectra, towards younger luminosity-weighted ages.

To produce spectra comparable to those from the 3 arcsec fibre-fed spectrograph of the classic SDSS data, we combine the spectra from all stellar particles within a 3 kpc galacto-centric radius. For reference, the SDSS fibre radius maps a physical distance of 2.8 kpc at redshift $z = 0.05$ for a vanilla flavoured ΛCDM cosmology with $\Omega_m = 0.3$, $h = 0.7$. The synthetic spectra are taken from the population synthesis models E-MILES (Vazdekis et al., 2016), based on a fully empirical stellar library (Sánchez-Blázquez et al., 2006) and Padova isochrones (Girardi et al., 2000). The E-MILES spectra extend from the far UV to the mid-IR (1680Å to 5 μm), spanning stellar ages from 6.3 Myr to 17.8 Gyr (we restrict the oldest ages to the cosmological age of the Universe at the fiducial redshift, $\sim$12.4 Gyr), and metallicity ranging from [M/H]=-1.71 to $+0.22$. Note, for galaxies that are more metal rich than maximum metallicity in E-MILES models, we artificially decrease it down to $+0.22$. The models adopt a Chabrier (2003) IMF, and we perform a bilinear interpolation in age and metallicity of the E-MILES SEDs. To avoid systematics caused by the modelling of dust attenuation, and taking advantage of the insensitivity of the 4000Å break strength to typical amounts of dust in galaxies (see Fig. 3.22), we do not include dust in the modelling of the synthetic spectra. Finally, the data are convolved to the R$\sim$2,000 resolution of the SDSS classic spectrograph, in quadrature with a Gaussian function mimicking the kinematic kernel that corresponds to each stellar mass bin, following the trend presented above, between stellar mass and velocity dispersion.

Previous work in the literature regarding the dust modelling in EAGLE and TNG100 (Trayford et al., 2015, 2017; Nelson et al., 2018) find a level of agreement with the observational constraints. We emphasize in this chapter that the effect

of dust on the spectra of galaxies represents an additional layer of complexity in galaxy formation models that go beyond the scope of this thesis. Our main aim is to explore the evolution of the stellar population properties across the green valley to probe the more fundamental aspect of how feedback is implemented in models to shape the star formation history of galaxies. The use of the $D_n(4000)$ index to define the location of the GV allows us to bypass the complexity of dust, avoiding potential biases produced by the effect of dust attenuation on other observables, most notably colours based on broadband filters. Fig. 3.22 shows a dust correction on the SDSS data causes a change in the position of the $D_n(4000)$-defined BC, GV and RS by less than 0.06 dex. Just as a test of the actual effect of dust attenuation on our data, we applied the dust model described in Negri et al. (private communication), which is a modification of the dust model of Trayford et al. (2015) for the EAGLE simulation. We found negligible changes in the definition of the BC, GV, RS when using the $D_n(4000)$ index, as expected.

4.3.2 Homogenisation of simulation and observation data

A fundamental step in the comparison between observations and simulations involves ensuring that similar galaxy samples are considered. Different selection effects in observations and simulations will yield samples with incompatible distributions of stellar mass, hence the need for a homogenisation process. More specifically, the Malmquist bias imposed by the r<17.77 AB limit for spectroscopic follow-up (see, e.g., Abolfathi et al., 2018) implies that low mass galaxies ($M_\star \lesssim 10^9 M_\odot$) are missed in SDSS, with a clear trend with redshift. In contrast, simulations are biased against high mass galaxies ($M_\star \gtrsim 10^{10} M_\odot$) due to their volume limitation (see, e.g., Schaye et al., 2015). Therefore, for a fair comparison between these data sets, we must ensure the distributions, in what we regard to be the fundamental parameter, are statistically compatible.

From the original samples, we select sets that are "homogeneous" regarding stellar mass – which is the parameter we assume to act as the major driver of the stellar population content. Note we have to proceed with two different sets of comparisons: one between SDSS and EAGLE and another one between SDSS and

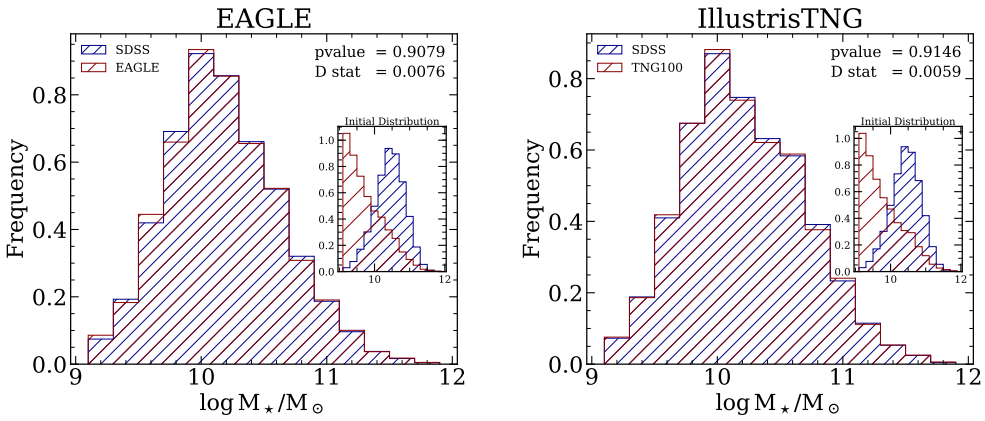

Figure 4.1: Histograms of stellar mass after the homogenisation process between SDSS, in blue, and simulation data, in red - showing EAGLE (*left*) and IllustrisTNG (*right*). The inset panels show, with the same colour coding, the histograms before homogenisation. A KS test is carried out, after the homogenisation process, to confirm the SDSS and simulation data originate from the same parents sample. Each panel shows the corresponding D and p statistic of the test. Note that the SDSS sample requires a slightly different homogenisation sampling depending on the simulated set.

TNG100. Moreover, we homogenise a pair of samples by finding a *pivot* stellar mass, so that below (above) this mass we randomly exclude simulated (observational) galaxies, as we have a lower fraction of observational (simulated) galaxies. Here the *pivot* mass bin is chosen as the one for which there is a greater fraction of observed galaxies in a mass bin compared to the fraction of simulated galaxies. Fig. 4.1 shows the histogram of the homogenised mass distribution of EAGLE (*left*) and TNG100 (*right*) galaxies, with respect to SDSS. The blue and red hatched areas represent SDSS and simulation histograms, respectively. Note various other forms of homogenisation were attempted, which consisted of not using any *pivot* stellar mass. Each method had its own drawback or were unsuccessful. For example, our first attempt simply consisted of using the fractions of galaxies in stellar mass bins from the simulation. However, in the low mass bins, to match the simulated fraction, we would have to use the same observed galaxies multiple times. This approach can be justified, as we could potentially treat the small number of galaxies we do have in a given stellar mass bin as a representative of the larger sample. However, the major caveat is that SDSS favours the brighter subset of the low mass galaxies, potentially

introducing some bias, thus affecting the analysis further down the line. Another attempt considered simply taking the absolute number of galaxies in each stellar mass bin present in simulations - as the total number simulated galaxies were significantly smaller than the total number of observed galaxies. However, this method would yield too few galaxies at high stellar mass, $\log \mathrm{M}_{\star}/\mathrm{M}_{\odot} \gtrsim 10.8$, of the order of unity, making our analysis too susceptible to Poisson noise. Therefore the use of this *pivot* mass for homogenisation enabled us to match the two distributions while including as high number of galaxies as possible for the given data.

To numerically assess the level of homogeneity between the respective stellar mass distributions of observations and simulations, we carried out a Kolmogorov-Smirnov test (hereafter KS-test, see, e.g., Dodge, 2008). When comparing the stellar mass distribution of the original samples, we get high values of the *D*-statistic ($\sim$0.56) between simulated and SDSS data (in both the EAGLE and TNG100 simulations), leading to a low probability that the samples are produced by the same parent distribution. However, after homogenisation, the *D*-statistic becomes, by construction, low ($\sim$6–7$\times10^{-3}$) with high values of the probability ($\gtrsim$90%) that the samples originate from the same distribution. However, note that we compare SDSS individually with either EAGLE or TNG100. We do not aim at creating a joint SDSS-EAGLE-TNG100 homogenised sample as this will reduce further the size of the working sample, restricting the stellar mass range. Therefore we have two sets of SDSS galaxies: one for EAGLE and a different set for TNG100. We note this will lead to some differences between the two sets of galaxy spectra from SDSS, quantified below. Additionally, variations between the two simulation data sets are also expected due to the different cosmological volumes probed, as well as the prescriptions to model the subgrid physics that controls the stellar mass growth in galaxies. We emphasize that this procedure is needed for a fully consistent comparison of the simulations with observational data. Note that in all samples, we make no distinction between satellite and central galaxies, as an environmental analysis is beyond the scope of this thesis (see Chapter 6).

4.3.3 Comparing homogenised samples

Since the homogenisation procedure results in different SDSS subsamples when comparing EAGLE and TNG100 simulations, we want to assess the level of overlap between these two pairs of samples. In each pair (i.e. either SDSS-EAGLE or SDSS-TNG100) we follow the methodology laid out in Chapter 3 (made up of A19 and A20) to define the uGV, mGV and lGV subsamples within each stellar mass bin – defined as the lower-, mid-, and upper-GV, respectively, which are meant to map three regions, defined by splitting the GV into three terciles of the 4000 Å break strength for individual stellar mass bins, that follow the transition from BC into RS. In each subset, for instance the mid green valley, mGV within the 10.30–10.51 (log) stellar mass bin, we cross-correlate the SDSS-EAGLE and SDSS-TNG100, and identify the matching number of galaxies in both sets, expressing this number as a fraction with respect to the total in each bin. Fig. 4.2 shows a comparison of these fractions as a function of stellar mass, where the blue, green and red data points refer to lGV, mGV and uGV, respectively.

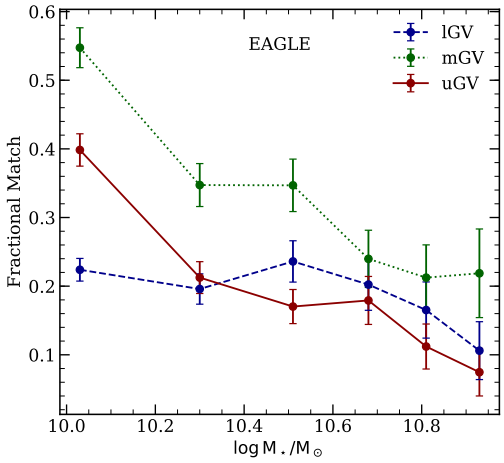

Figure 4.2: Fraction of matching SDSS galaxies in the EAGLE homogenised simulation for lGV (blue), mGV (green) and uGV (red) galaxies. The error bars assume Poisson noise. The fractions are similar when selecting GV galaxies from the homogenised TNG100 sample.

The error bars have been obtained assuming Poisson noise in the count of overlapping galaxies. The fractional match decreases with increasing stellar mass in all subsets. This is due to (i) the independent homogenisation of EAGLE and TNG100,

and (ii) the selection of GV galaxies is probability-based, therefore we do not find a unique solution, being subject to Poisson noise. The difference in fractional match shown in Fig. 4.2 will lead to differences in the retrieved SDSS parameters for EAGLE and TNG100 sample, as seen below, specially in Section 4.4.4 and 4.4.5.

4.3.4 Galaxy Classification

Observationally, galaxies are traditionally classified regarding nebular emission into quiescent (Q), star-forming (SF), Seyfert AGN, LINER AGN, or composites (i.e. a mixture of those). Ratios of targeted emission line luminosities allow us to separate the ionization environments expected in the ISM of galaxies (Baldwin et al., 1981; Cid Fernandes et al., 2011). This is an important classification scheme, as both star formation activity and AGN are essential mechanisms in galaxy evolution, and the path to quiescence still remains an open question (Martin et al., 2007; Dashyan et al., 2019; Man et al., 2019). Our simple methodology does not take into account nebular emission when creating the synthetic spectra from simulations. Therefore, we need to get back to physical parameters in order to classify the simulated galaxies as Q, SF or AGN. Regarding SMBH activity, we compare the black hole accretion rate with respect to the Eddington ratio:

$$\lambda_{\mathrm{E}dd} = \frac{\dot{m}_{\mathrm{accr}}}{\dot{m}_{\mathrm{E}dd}}. \tag{4.6}$$

However, a non-trivial issue is to define the actual values of the threshold ratio to segregate galaxies according to AGN activity. Our aim here is to **reclassify** the end product of the simulation galaxies into SF, Seyfert and LINER AGN, and Q based on their inherent properties, obtained from their respective runs. Note, this does not change the simulation itself but how we classify and interpret the end product. This is required for a fairer comparison, as this ensures that the homogenised sample of observed and simulated galaxies have similar baseline fractions of different galactic types to begin with. Therefore, comparison of fractions of different galaxy types, Sections 4.4.2 and 4.5.2.3, is made more robust than if we had a mismatch in a fraction of different galaxy types.

Observational studies find that Seyfert AGN have Eddington ratios between $-2 < \log(\lambda_{Edd}) < -1$ (Heckman et al., 2004; Schulze et al., 2015; Georgakakis et al., 2017; Ciotti et al., 2017), whereas lower accretion rates correspond to radiatively ineffective AGN, i.e. LINER or even no AGN. Some studies suggest a lower limit for LINER AGN around $\log(\lambda_{Edd}) \sim -6$ (Heckman et al., 2004; Li and Xie, 2017), while others choose values as low as $\log(\lambda_{Edd}) \sim -9$ (Ho, 2008, 2009). Studies using SDSS galaxies have calculated the Eddington ratio from [OIII] emission, finding $\log(\lambda_{Edd}) \sim -4$ (Kewley et al., 2006). For the simulated galaxies, we adopt our own Eddington ratio limits, along with specific star formation rate (sSFR), to classify galaxies as Seyfert AGN, LINER AGN, SF (including composite) or Q. Note the sSFR used here has been calculated using the instantaneous SFR. An alternative selection would use the average SFR over some timescale, but previous work from the literature have shown that measuring SFR in different ways makes little difference at low redshift (Donnari et al., 2019, 2021b). Furthermore, the criterion to select the corresponding values of λ_{Edd} and sSFR is to impose equivalent *global* ratios of Seyfert, LINER, SF and Q to those found in the full homogenised SDSS samples. *Note we are interested in the relative mass-dependent variation of these fractions, and that the homogenisation in mass makes the comparison between SDSS and the respective simulation meaningful.*

EAGLE only imposes one form of AGN feedback, therefore it is not possible to differentiate between Seyfert or LINER AGN activity. From the simulations, we retrieve the black hole mass and their accretion rate – at the fiducial redshift $z = 0.1$ – and we use Eq. 4.6 to find λ_{Edd} in each galaxy. Comparing the total fraction of Seyfert AGN with respect to SDSS, we obtain a threshold $\log(\lambda_{Edd}) \gtrsim -2.0$. We proceed similarly with the LINER galaxies, obtaining a range $-4.2 \lesssim \log(\lambda_{Edd}) < -2.0$. Moreover, for LINERs we also impose a constraint on $\log \mathrm{sSFR}\ (\mathrm{yr}^{-1}) \lesssim -10.5$ to make sure SF activity is minimal. Note that most of the SDSS galaxies hosting LINERs have a sSFR similar to Q. Galaxies with $-4.2 < \log(\lambda_{Edd}) < -2.0$ but with $\log \mathrm{sSFR} > -10.5$ are classified SF. Finally, galaxies with $\log(\lambda_{Edd}) \lesssim -4.2$ and $\log \mathrm{sSFR} < -11$ (> -11) are considered

Table 4.2: Outline of the selection criteria adopted to distinguish between different types of galaxy activity: Seyfert/LINER AGN, quiescence (Q) or star-formation (SF). Two galactic parameters are constrained: the Eddington ratio (λ_{Edd}) and the specific star formation rate (sSFR, which is defined as the ratio between the instantaneous star formation rate and the stellar mass). The symbol x indicates the parameter located at the top of each column. Columns 4 and 7 show, within each column, the percentage of both the simulated and SDSS galaxies, the latter in bracket, of the listed type.

	EAGLE			TNG100		
Type	$\log(\lambda_{Edd})$	$\log(\mathrm{sSFR/yr^{-1}})$	%	$\log(\lambda_{Edd})$	$\log(\mathrm{sSFR/yr^{-1}})$	%
Seyfert	$x \geq -2.0$	-	3.86 (2.77)	$x \geq -1.4$	-	3.03 (3.04)
LINER	$-4.2 \leq x < -2.0$	$x \leq -10.5$	9.33 (9.68)	$-4.2 \leq x \leq -1.4$	$x \leq -11.0$	8.69 (10.31)
SF	$-4.2 \leq x < -2.0$ $x < -4.2$	$x > -10.5$ $x > -11.0$	62.99(62.91)	$-4.2 \leq x < -1.4$ $x < -4.2$	$x > -11.0$ $x > -11.0$	58.43 (60.69)
Q	$x < -4.2$	$x \leq -11.0$	23.82 (24.64)	$x < -4.2$	$x \leq$ -11.0	29.85(25.97)

to be Q (SF). These criteria are summarised in Tab. 4.2, where the constraints are shown for both EAGLE and TNG100 simulations. In each case, the table shows the limits on $\lambda_{\mathrm{E}dd}$ and sSFR as well as the fraction of galaxies of a given type in the homogenised simulations. The values in brackets show the percentage of different types of galaxies observed in the SDSS homogenised sample, identified via the BPT diagram (Baldwin et al., 1981; Kewley et al., 2001; Kauffmann et al., 2003). Both observation and simulation data contain SF and composite galaxies (classified with a BPT parameter either 1 or 3 in the SDSS galSpecExtra catalogue of Brinchmann et al. 2004), while we exclude low S/N star forming galaxies (BPT parameter 2).

The TNG100 simulation adopts two modes of AGN feedback – thermal and kinetic feedback – determined by Eq. 4.3 and 4.5, as defined in Weinberger et al. (2018). The fiducial approach fixes $\beta = 2$ and $\chi_0 = 2 \times 10^{-3}$, following Habouzit et al. (2019). However with this choice of parameters we get too many Seyfert AGN galaxies. To solve this, we carry out a similar procedure to EAGLE, adopting our own thresholds. Doing so may introduce a bias, as we exclude Seyfert AGN galaxies, and either consider them to be LINER AGN or SF galaxies in the fraction estimates. However, note the exclusion of Seyfert AGN in the simulation data is justified, for our purposes, as we find a low fraction of Seyfert AGN in the observations. Furthermore, similarly to EAGLE, this is a necessary step as we have to ensure the ratios of Seyfert, LINER, SF, and Q galaxies are consistent, when comparing the properties of observational and simulation data. The comparison between the homogenised SDSS and TNG100 sets gives $\log(\lambda_{\mathrm{E}dd}) \gtrsim -1.4$, slightly different to that of EAGLE. This is due to different subgrid physics regarding black hole growth and AGN feedback, as well as TNG100 having a larger black hole seed. For LINER AGN we find $-4.2 \lesssim \log(\lambda_{\mathrm{E}dd}) < -1.4$ gives consistent fractions with respect to the observations. In TNG100, the threshold $\log \mathrm{sSFR} = -11.0$ gives a similar fraction of Q/SF galaxies with respect to the observations. Note this choice produces a slightly higher percentage of Q galaxies in TNG100 (29.85%) compared to the observations (25.97%). Furthermore, a slightly higher discrepancy between TNG100 and SDSS than EAGLE and SDSS can be seen for Q fractions,

which might result in the greater deviation from the observation in TNG100 than EAGLE that we see in later sections. However, when trying to get the percentages of TNG100 Q galaxies closer to the SDSS sample, we were unable to reduce the fraction of Q galaxies simply by reducing the log sSFR threshold, owing to there being a lack of galaxies with SFR>0. To decrease the fraction of Q galaxies, such that it matches the observational fraction better, we had to change the Eddington ratio criteria instead, i.e. decrease the lower limit from $-4.2 \lesssim \log(\lambda_{\mathrm{E}dd}) < -1.4$. Such exercise would result in better fractional matching between SDSS and TNG100 Q galaxies (i.e. both would have $\sim 25.97\%$ rather than $\sim 29.97\%$ we see in Tab. 4.2), but this result would cause an equivalent increase in LINER galaxy fraction (i.e. $>> 10.31\%$). Note, this balancing issue was not present in the EAGLE simulation, showing that TNG100 has a harder time reproducing the observational fractions, especially in regards to the SFR.

Finally, note despite the slight variation in the selection criteria and in the homogenisation procedure, the parameter thresholds obtained to produce results matching the SDSS observations are very similar.

4.4 Confronting observations and simulations in the Green Valley

The state-of-the-art simulations explored in this chapter are capable of matching the general fundamental properties of galaxies (Pillepich et al., 2018b; Nelson et al., 2018), as well as the bimodality of galaxies in colour (Trayford et al., 2015; Nelson et al., 2018). Note, while these papers find a qualitative agreement between observation and simulations, they also identify subtle discrepancies. Here, we focus on how well simulations reproduce the bimodality of galaxies on the $\mathrm{D}_n(4000)$ vs $\log \mathrm{M}_\star/\mathrm{M}_\odot$ plane. More specifically, we look at the mass dependence of the fractions of AGN, SF and Q galaxies in the GV. Given that the GV is a transitional region where quenching processes efficiently drive galaxies to quiescence, this comparison allows us to analyse the ability of the subgrid physics imposed in the simulations to reproduce the observational data.

4.4.1 Blue Cloud, Green Valley and Red Sequence

Our first analysis of the data – before focusing on the GV – involves a comparison of the BC, GV and RS between SDSS and simulations. Note similar studies have been already performed on the colour-mass plane, finding general agreement of the simulations with observations (see, e.g., Trayford et al., 2016, 2017; Kaviraj et al., 2017; Nelson et al., 2018) and on the SFR-mass plane (Furlong et al., 2015; Donnari et al., 2019). We revisit this comparison with our new definition of the BC, GV, RS regions, looking for hints that could help improve the simulations.

4.4.1.1 Comparison with EAGLE (RefL0100N1504)

Fig. 4.3 shows the distribution of EAGLE galaxies (*left*) on the $D_n(4000)$ vs $\log M_\star/M_\odot$ plane, after sample homogenisation. The blue, green and red data points with error bars represent the observational (i.e. SDSS) BC, GV and RS. The red and blue histograms on the side panels show the distribution of EAGLE and SDSS galaxies, respectively – likewise for TNG100 on the rightmost panel. We find a mismatch in the distribution, of about $0.1-0.2$ dex at low $D_n(4000)$, but better agreement at high $D_n(4000)$ between SDSS and EAGLE for RS. Combining this with the stellar mass distribution, we see that while there is an overall qualitative agreement, EAGLE seems to produce BC, GV and RS regions with higher $D_n(4000)$, and the mismatch increases from BC to RS. This difference is greatest in the lowest mass bins, $9.5 \lesssim \log M_\star/M_\odot \lesssim 10.5$. The higher value of $D_n(4000)$ at low-intermediate mass could be due to the mass-metallicity relation, being shallower in EAGLE with respect to the observations (Schaye et al., 2015; Trayford et al., 2017).

One reason for the shallowness of the mass-metallicity relation could be due to galaxies having more efficient chemical enrichment at low mass compared with the observations. $D_n(4000)$ is sensitive to metallicity (Balogh et al., 1999), one of the manifestations of the age-metallicity degeneracy. This could be more prominent in our diagram but not in previous studies, such as Trayford et al. (2015), as $D_n(4000)$ has a larger range of values compared to the colour, $(g-r)$, of the galaxy, hence better highlighting the difference. Moreover, the inclusion of only one mode of AGN feedback – resembling quasar-mode AGN, which happens to be dominant in

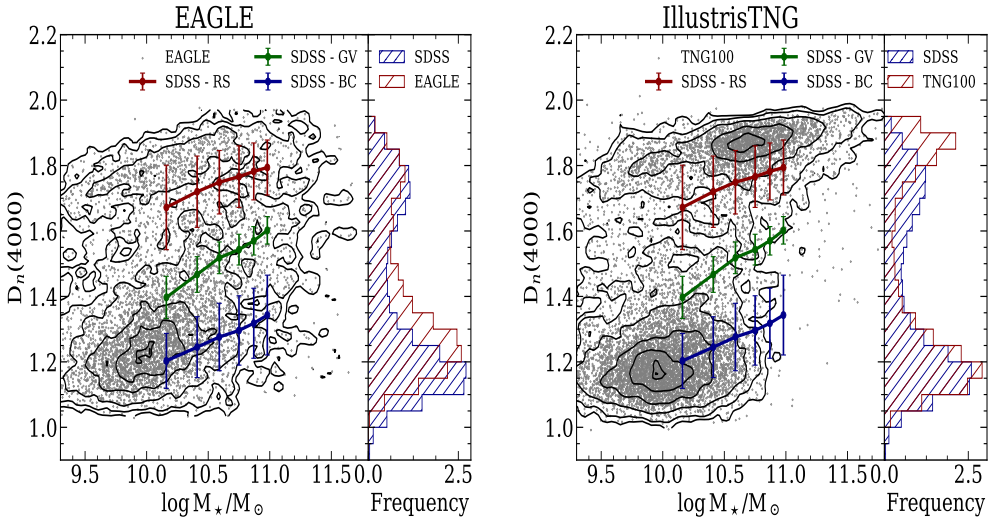

Figure 4.3: Distribution of galaxies on the $D_n(4000)$ vs stellar mass plane. The gray dots represent the simulation data after homogenisation in EAGLE (*left*) and IllustrisTNG (*right*). The contours map areas of constant number density on the plot. The blue, green and red solid lines follow the observational definition of the BC, GV and RS, respectively. The error bars are given at one standard deviation from the mean. The histograms in the adjacent panels display the distribution of 4000Å break strength in observations (blue) and simulations (red).

high mass galaxies (Shankar et al., 2006; Faber et al., 2007; Smethurst et al., 2015) – could offer another potential explanation for this trend. AGN feedback plays an important role in quenching star formation (Martin et al., 2007; Gonçalves et al., 2012; Wright et al., 2019; Dashyan et al., 2019), therefore specially for lower mass galaxies, quasar mode AGN could lead to quenching of star formation that operates too quickly. A combination of these two affects could also cause the trends we see here, where the red sequence features a shallower gradient with respect to the observations.

4.4.1.2 Comparison with IllustrisTNG (TNG100)

In the TNG100 simulated galaxies (see Fig. 4.3, *right*), a better agreement is found in the BC with respect to EAGLE; also evident from the histograms shown on the right. However, there is significant disagreement in the GV and RS, of $\sim 0.1 - 0.3$ dex. Note the gradient of the RS on the $D_n(4000)$ vs stellar mass plane is shallower in TNG100 with respect to SDSS. It is also shallower than the EAGLE data, with

an excess of RS galaxies at low mass ($< 10^{10}\mathrm{M}_{\odot}$). Additionally, at the massive end (above $10^{10.5}\mathrm{M}_{\odot}$), a more drastic decrease in the number of BC galaxies is apparent. Note, the fraction of galaxies in the GV is lower in TNG100 with respect to the observations, specifically for $1.5 \lesssim \mathrm{D}_n(4000) \lesssim 1.8$, as shown by the histogram. Note that previous work in the literature (Nelson et al., 2018) find better agreement when looking at bimodality with respect to (g–r) colour. However, at lower stellar mass, $9 \lesssim \log \mathrm{M}_{\star}/\mathrm{M}_{\odot} \lesssim 10$, they also find a surplus of galaxies in the simulated red sequence, suggesting over-quenching. More specifically, at low stellar masses, recent comparisons find a shallower mass-metallicity trend with respect to the observations (Nelson et al., 2018), which might offer a possible explanation to the excess of RS galaxies in TNG100.

4.4.2 Fractional Variation in the Green Valley

Although we already find limited differences between the EAGLE and TNG100 simulations in the BC, we find a significant difference in the RS, so we focus on the analysis of the GV region, as it is a transition region where quenching processes are expected to leave stronger imprints, and where different feedback prescriptions are expected to be more prominent. Note that we start with $\sim 226\ 872, 13\ 475$ and 22 232 SDSS, EAGLE and TNG100 galaxies, respectively with $\log \mathrm{M}_{\star}/\mathrm{M}_{\odot} \gtrsim 9.0$. After homogenisation we are left with 88 588 (39.05% of total) EAGLE-SDSS and 5 822 (43.21% of total) EAGLE galaxies and 90 709 (39.98% of total) TNG100-SDSS and 9 906 (44.56% of total) TNG100 galaxies. The number of galaxies is further reduced to 630 (10.82% of homogenised sample) for EAGLE and 486 (4.91% of homogenised sample) for TNG100 when considering only the GV. For the SDSS-EAGLE and SDSS-IllustrisTNG samples, we find 6 491 (7.32%) and 6 448 (7.11%) galaxies, respectively in the GV. Even though there are similar fractions of EAGLE and TNG100 galaxies after homogenisation, there is a greater drop in TNG100 compared to EAGLE. Using these GV galaxies we then compare the fraction of different types of galaxies regarding nebular emission (as defined in Sec. 4.3.4), in the lGV, mGV and uGV. The classification separates galaxies into either SF, Q, LINER or Seyfert AGN. Fig. 4.4 compares the fraction of galaxies segregated by type as a

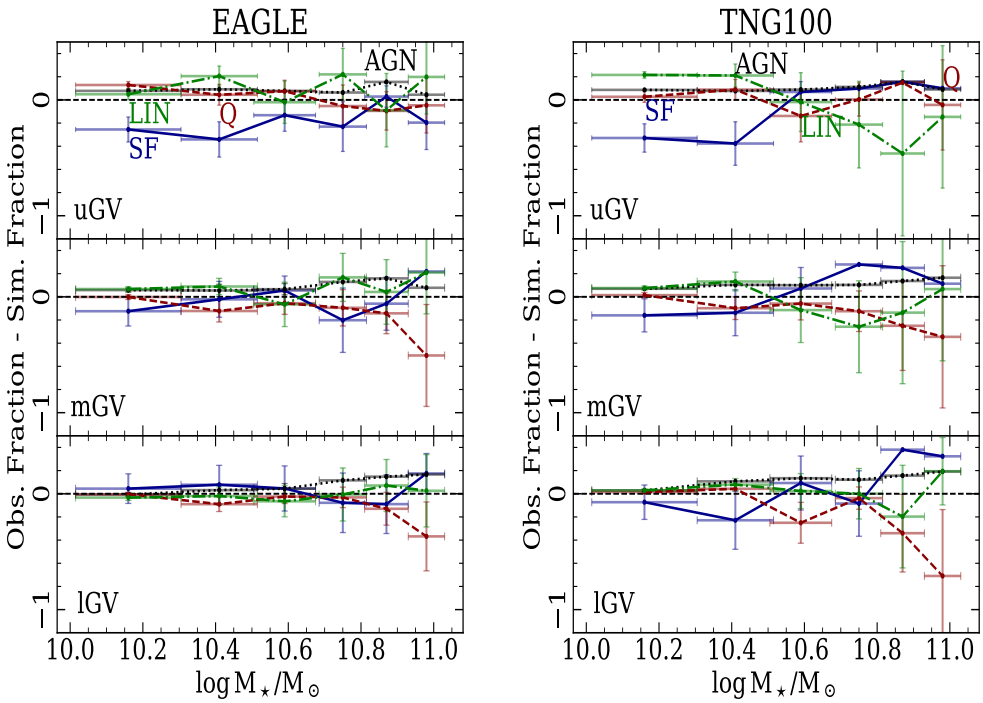

Figure 4.4: Difference between the fractions of observational and simulated GV galaxies as a function of stellar mass. The black dotted, green dash-dot, blue and red lines show the difference for Seyfert AGN, LINER AGN, star forming (includes composite) and quiescent galaxies. Left and right panels show the results for EAGLE and TNG100, respectively. From top to bottom, we show the results for upper (uGV), mid (mGV) and lower (lGV) green valley (see text for details). The error bars show the propagated Poisson uncertainty.

function of stellar mass in EAGLE (*left*) and TNG100 (*right*), with respect to the observational constraints from SDSS. The horizontal dashed line at zero represents the ideal case where simulations and observations match perfectly. The top, middle and bottom panels correspond to the uGV, mGV and lGV, respectively. The lines are colour coded, as labelled. In lGV and mGV, EAGLE is able to reproduce the general trend with respect to SF and Q galaxies at low stellar mass; as most data straddle the zero point. However, for most massive galaxies $> 10^{10.8}\mathrm{M}_{\odot}$, EAGLE tends to overproduce (underproduce) quiescent (SF) galaxies. In uGV, the result is noisier but it is nevertheless able to reproduce the fractions of observed galaxies. Note for low mass, $\mathrm{M}_{\star} < 10^{10.5}\mathrm{M}_{\odot}$, the fraction suggests an overproduction of SF galaxies in simulations. In addition, there is a consistent underproduction of Seyfert

AGN galaxies, however the samples include very few Seyfert AGN galaxies, so the statistics is not so significant. The trend for LINERs galaxies is noisier, so we cannot deduce any mass trend of the mismatch with respect to the observations.

TNG100 also shows a similar level of mismatch with respect to the observational data, with an overproduction (underproduction) of Q (SF) GV galaxies. The overproduction of quiescent galaxies seems to increase with respect to stellar mass, in both lGV and mGV. Similar to EAGLE, there is a reasonable agreement between SDSS and TNG100 in the uGV. Note in lGV and mGV, for the most massive galaxies, $> 10^{10.5}\mathrm{M}_{\odot}$, we find an underproduction of SF galaxies. Whereas in the uGV, TNG100 seems consistent with the observations. The fraction of Seyfert AGN shows little difference. However this is once more owing to low number statistics. The fractions for LINER galaxies is consistent with the observations as it straddles the zero point, similar to EAGLE but noisier.

There could be many reasons for the discrepancies found between the GV galaxies in observations and simulations. We explore them in Sec. 4.5. Note the overabundance of Q galaxies, along with the lack of SF galaxies in the simulation GV may indicate too rapid quenching with respect to the observations. This is consistent with the fact that both EAGLE and TNG100 feature a RS with a greater 4000Å break strength than the SDSS observations.

4.4.3 Specific Star Formation Rate

In addition to the comparison based on the BPT classification of the nebular emission lines, presented above, it is possible to further test the models by comparing the behaviour of the specific star formation (sSFR) rate, defined as the instantaneous star formation rate per unit stellar mass. sSFR is a powerful indicator of the ongoing stellar mass growth. Fig. 4.5 (left) shows sSFR against stellar mass. The blue, green and red dashed lines with error bars show the mean observational sSFR in the lGV, mGV and uGV, respectively, whereas the shaded regions delimit the results from the simulations. Note for galaxies with SFR$= 0$, we set their $\log \mathrm{sSFR}(\mathrm{yr}^{-1})$ at -15.5, and these galaxies are excluded when calculating the mean sSFR for each stellar mass bin. The black and gray data points correspond to individual galaxies

in the GV for simulations and SDSS, respectively. Galaxies with $\log \mathrm{sSFR} < -14$ (hereafter defined in yr^{-1}) represent fully quiescent systems, i.e. with negligible star formation. The text labels on the figures state the percentage of galaxies with SFR=0, thus have had their sSFR set to $\log \mathrm{sSFR} \equiv -15.5$, for their respective stellar mass bins. Note these galaxies might have residual star formation, undetectable due to the resolution limit of simulations. However, the minimum SFR we find is 0.00071 and 0.00032 $\mathrm{M}_{\odot}\,\mathrm{yr}^{-1}$ for EAGLE and TNG100, respectively. These estimates roughly translate to $\log \mathrm{sSFR} = -14.2$ for the most massive galaxies. Therefore, even without the limit in resolution regarding the star formation histories, these galaxies would have a lower SFR than the SDSS sample. Note, for observational galaxies with undetectable star formation, their sSFR have artificially been put around $\log \mathrm{sSFR} = -12.0$ following a gaussian distribution (Brinchmann et al., 2004; Donnari et al., 2019). We argue, since we are focusing on GV galaxies and in a stellar mass range, $\log \mathrm{M}_{\star}/\mathrm{M}_{\odot} = 10^{10.03-11.03}$, that the fraction of galaxies with undetectable star formation should be low. This is further backed up by the low fraction of Q galaxies present in the GV – see Sec. 4.5.2.3. EAGLE produces a trend of sSFR with stellar mass that is close to the observations. The SDSS data feature a wider separation between lGV and uGV, whereas the simulations show significant overlap. Moreover, the simulations show overall higher values of the sSFR with respect to the observations. This mismatch may be due to a systematic offset, as the sSFR of the simulations is retrieved from the output of the star formation activity, whereas the observational constraints are determined indirectly from standard relations involving emission lines (see, e.g., Kennicutt, 1998). However, whilst simulation galaxies have higher SFR in the star-forming subsample, they produce a higher fraction of galaxies with no star formation, thus this trend is consistent with our analysis based on the fraction of Q and SF galaxies, shown in the previous subsection.

The right hand panel of Fig. 4.5 corresponds to the TNG100 simulation. The overall trend with respect to stellar mass is consistent, but the simulations produce values that are systematically higher, and the mismatch is similar with EAGLE

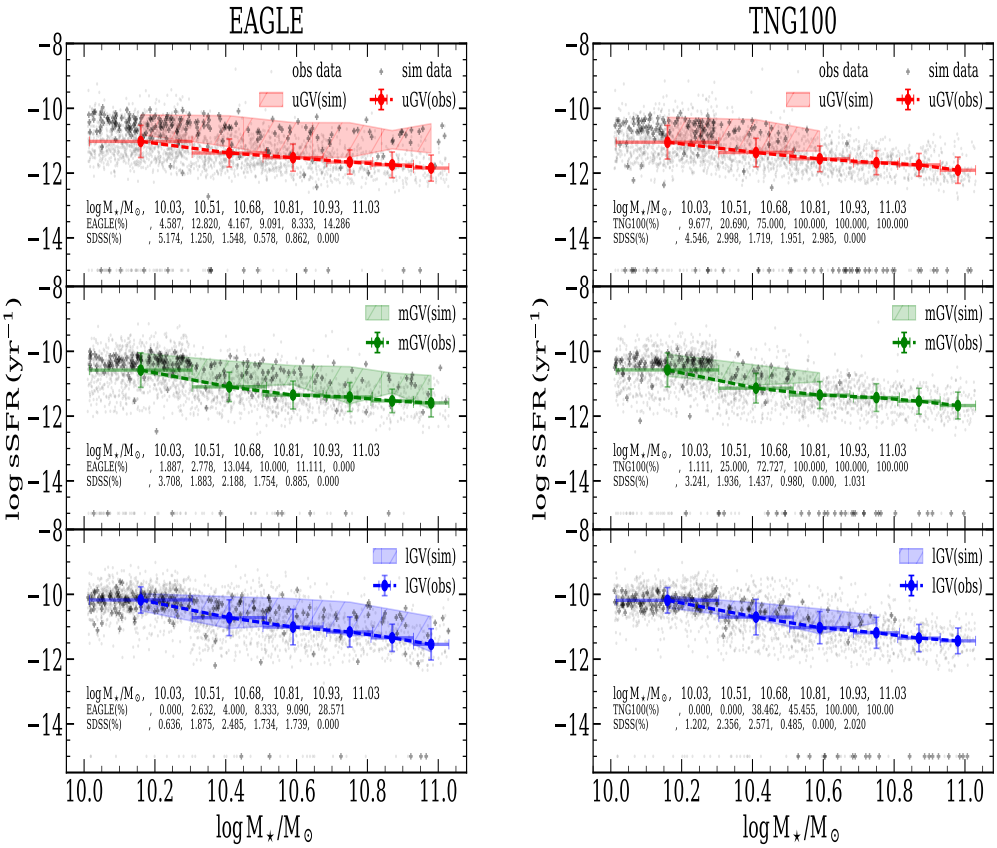

Figure 4.5: Distribution of GV galaxies on the sSFR vs stellar mass plane. The observations (simulations) are shown as gray (black) dots. The results for EAGLE and TNG100 simulations are presented on the left and right panels, respectively. In both panels, the blue, green and red dotted lines, with errorbars representing one standard deviation, show the observational constraints of the lGV, mGV and uGV (bottom to top). The blue, green and red shaded regions show one standard deviation covered by the lGV, mGV and uGV from the simulations, respectively. Note the mean and standard deviation excludes all galaxies without any star formation (SFR $= 0$), i.e. following the convention $\log \mathrm{sSFR}(\mathrm{yr}^{-1})$=$-15.5$, to remove any systematics on the simulations due to the numerical resolution limit. The text labels show the different stellar mass bins and the percentage of galaxies which have their sSFR set to -15.5 for simulations and observations.

galaxies. While the SFR is systematically higher, we do find a higher fraction of galaxies, in TNG100, with no ongoing star formation, thus indicating that some quenching implementation may act as a run away process, disabling any further star formation, unlike what is seen for EAGLE. Furthermore, at the massive end, $\log M_\star/M_\odot \gtrsim 10.6$, most TNG100 GV galaxies lack star formation whereas the observations feature a significant number of SF galaxies, once more supporting the argument towards an excess of Q galaxies in the simulations at the massive end.

All the estimation of the SFR, thus sSFR, have been done using the instantaneous value of SFR for the simulation, whereas the observed SFR is mostly calculated using Hα luminosity, which is sensitive to timescales of 100 Myr. Hence, there could be potential biases. However Donnari et al. (2021a,b) analyse the variation in the quiescent fraction in different stellar mass bins for TNG100, defined using SFR measured over different time periods. They found, regardless of the time interval, - i.e. instantaneous, 100 Myr or 300 Myr - the fraction of quiescent galaxies in a stellar mass bin were very similar.

Even though we are comparing galaxies with similar $D_n(4000)$, the simulated galaxies happen to lie lower on the evolutionary sequence in comparison to observations (Fig. 4.3), thus we are potentially comparing the SFR of upper BC simulated galaxies vs lGV observation galaxies. Therefore, the higher sSFR found for the star forming galaxies is somewhat expected. Note, the caveat is further discussed in Section 4.5.

4.4.4 Average Ages

The next step in the analysis of GV galaxies involves the comparison of the trend in average age, between observations and simulations. For the observational (SDSS) data, we adopt the same procedure as in Chapter 3 (taken from A19 and A20), stacking the spectra, following Ferreras et al. (2013a). The stacks are presented to `STARLIGHT` (Cid Fernandes et al., 2005), to extract star formation histories. This code performs full spectral fitting with an MCMC-based algorithm that finds the best-fit weights of a set of simple stellar populations (SSP). From these weights the

average age is calculated as follows:

$$\langle \log t \rangle \equiv \sum_{j=1}^{N_\star} x_j \log t_j, \tag{4.7}$$

where x_j is the normalised luminosity weight and t_j is the stellar age corresponding to the j-th SSP. For spectral fitting we use 138 SSPs from the Bruzual and Charlot (2003) models, where the age varies from 0.001 to 13 Gyr and total metallicity varies from 10^{-4} to 0.05, with 0.02 corresponding to solar metallicity. The ages in the simulated galaxies are determined directly from the stellar growth of the galaxies, i.e. by taking into account the distribution of stellar particles within a R=3 kpc aperture size; to better match the SDSS classic spectra, taken through optical fibres that map a 3 arcsec diameter. Analogously to the spectral stacking performed in the SDSS data, the star formation histories for each galaxy within the same bin (in stellar mass and location on the GV) are stacked to create a joint distribution of stellar ages from which the average is determined. The uncertainties in both cases are obtained from a bootstrap, where each realization randomly stacks 60% of the galaxies in each stellar mass bin. The uncertainties of average stellar ages vary between $\sim 0.1-0.7$ Gyr for observational constraints, from `STARLIGHT`, and $\sim 0.3-0.5$ Gyr for simulated galaxies. Note that the stellar ages can be weighed either by luminosity or by mass. The former are better constrained by the spectra, whereas the latter are more physically motivated. Similarly to the dilemma between velocity dispersion and stellar mass – where the former is better constrained by the observations, and the latter is the preferred choice for simulations, in this case luminosity-weighted ages are more accurately constrained by the observational spectra, whereas mass-weighted ages suffer less systematic in the simulations.

Taking into account that relative age variations are more robustly constrained than absolute estimates, we decide to quote our results as a relative age difference, given by:

$$\Delta\psi_k(t) = \psi_i^k - \psi_{\mathrm{fid}}, \tag{4.8}$$

where ψ represents either the average age, t, or quenching timescale, τ (see be-

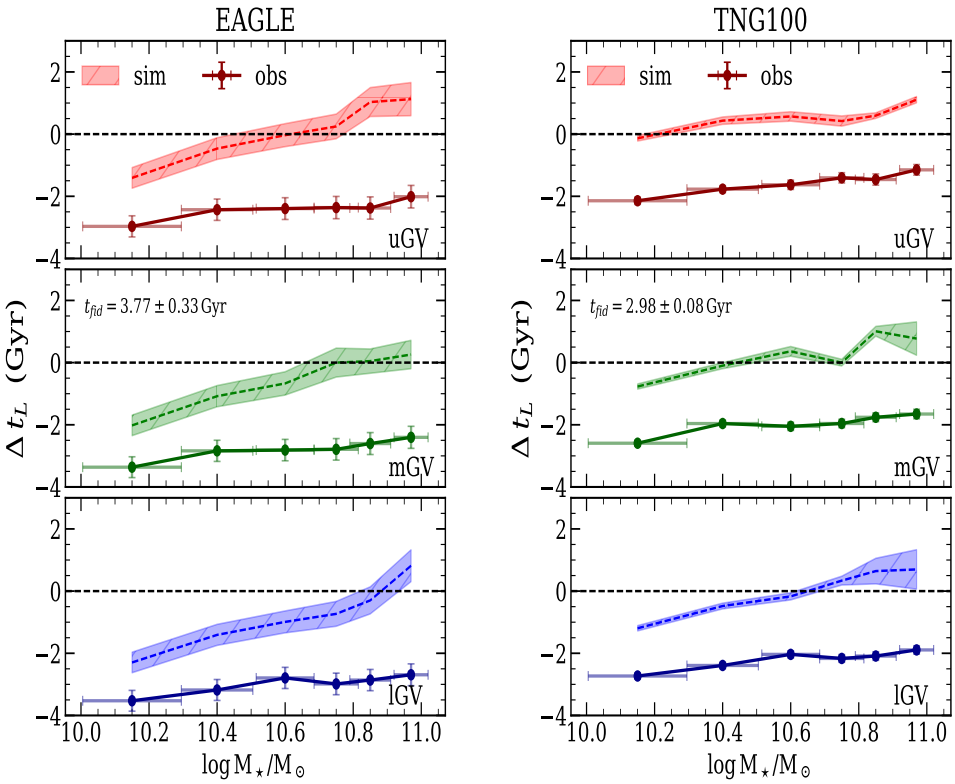

Figure 4.6: Relative luminosity, Δt_L, weighted average stellar ages, shown as a function of stellar mass. Comparison in the relative difference for EAGLE (TNG100) are shown in the left (right) panels, each one separated into panels that correspond (from bottom to top) to the lGV, mGV, uGV. The relative ages are measured with respect to a fiducial one ($t_{\rm fid}$) corresponding to mGV galaxies in the $10.68 \lesssim \log \mathrm{M}_\star/\mathrm{M}_\odot \lesssim 10.81$ mass bin of the simulation data, quoted in each figure (see text for details). The dashed shaded lines show the relative values for the simulated data, while the solid lines present the relative difference in ages for observational data. The uncertainties are obtained from bootstrapping either when stacking the spectra (for observations) or SFH (for simulations)

low). The index k=$\{L, M\}$ denotes whether the parameter is luminosity- or mass-weighted, while i denotes the chosen stellar mass bin. Note for each of the four parameters explored – namely luminosity-weighted average age and quenching timescale, and mass-weighted average age and quenching timescale – we select a single fiducial value throughout, defined as the estimate from simulations in the mGV, at mass bin $10^{10.68} < \mathrm{M}_\star/\mathrm{M}_\odot < 10^{10.81}$. We then subtract this fiducial value, both in simulation and observation parameters, across all stellar mass bins and GV regions. Therefore, by construction, $\Delta\psi_k$ for the fiducial bin will be zero for sim-

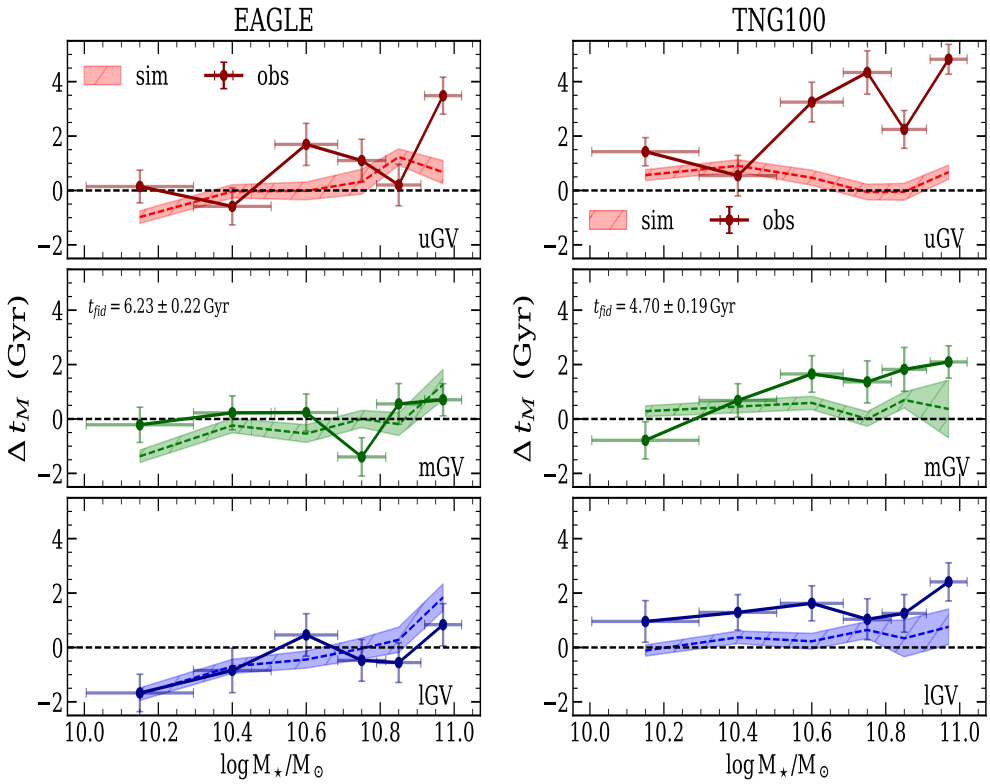

Figure 4.7: Same as Fig. 4.6 but for relative, Δt_M, mass weighted average stellar ages.

ulations, whereas the value of $\Delta\psi_k$ in this fiducial bin for the observed data will account for systematic offsets between observations and simulations.

Fig. 4.6 and 4.7 show the relative, luminosity and mass weighted, average stellar ages in the observations (solid lines) and the simulations (filled dashed lines), with EAGLE (TNG100) shown in the left (right) panels. In each case, the top, mid and bottom panels show the result of uGV, mGV and lGV, respectively. The values quoted in the mid panel show the actual estimate of the stellar age corresponding to the fiducial mass bin. The luminosity-weighted ages show an increasing trend with stellar mass in all cases, consistent with the well-established mass-age relation (Kauffmann et al., 2003; Gallazzi et al., 2005). In all three regions of the GV, EAGLE produces galaxies that are both older, in luminosity weights, than the observed constraints (by about 2.8 Gyr at the fiducial bin), and with a steeper mass-age slope (see Tab. 4.3). The luminosity-weighted estimates show a substantial systematic offset between the spectral fitting results (i.e. the data points) and the constraints

Table 4.3: Slopes of the relation between average age and stellar mass. The slope (α) is obtained from a linear fit to the function $\Delta t_{L,M} = \alpha \log M_\star/M_\odot + \beta$ (see Fig. 4.6 and 4.7). The uncertainty is quoted at the 1 σ level.

	Lum-weighted		Mass-weighted	
	EAGLE	SDSS	EAGLE	SDSS
lGV	$+3.31 \pm 0.49$	$+0.92 \pm 0.20$	$+3.62 \pm 0.72$	$+2.31 \pm 0.95$
mGV	$+2.82 \pm 0.22$	$+0.99 \pm 0.18$	$+2.40 \pm 0.74$	$+0.52 \pm 1.23$
uGV	$+3.09 \pm 0.27$	$+0.91 \pm 0.22$	$+2.23 \pm 0.52$	$+3.11 \pm 1.81$
	Lum-weighted		Mass-weighted	
	TNG100	SDSS	TNG100	SDSS
lGV	$+2.40 \pm 0.16$	$+0.92 \pm 0.18$	$+0.85 \pm 0.28$	$+1.08 \pm 0.69$
mGV	$+1.90 \pm 0.47$	$+0.98 \pm 0.22$	$+0.09 \pm 0.40$	$+3.28 \pm 0.59$
uGV	$+1.16 \pm 0.31$	$+1.10 \pm 0.11$	-0.56 ± 0.58	$+4.14 \pm 1.80$

from the star formation histories of the cosmological simulations (i.e. the shaded regions), in all GV regions and in both EAGLE and TNG100. There is a slightly better agreement with observations in the slope of the luminosity-weighted estimates of TNG100, (see Tab. 4.3), and the fiducial age is also slightly closer to the observational constraints ($\sim$2.0 Gyr).

In both cases, the mass-weighted average ages show better agreement with observations, both regarding the systematic offset and the slope, although with larger error bars. However, note the discrepancy at the massive end of the TNG100 uGV, where observational galaxies have substantially older ages. Note previous work hinted the upper part of the GV could be the least homogeneous, as one could have a more complex mixture of galaxies evolving from the BC to the RS via quenching, as well as galaxies moving "backwards" due to mild, but frequent episodes of rejuvenation (Thomas et al., 2010; Nelson et al., 2018, A20).

Note, the difference in the average age could be solely due to the systematics associated with calculating one based on the chosen spectral fitting algorithm, for observation, and other using their true SFH, for simulation. For this reason, we mostly focus on the relative trends of average age, as these are less affected by such systematics. Alternatively, there is a potential for using a spectral fitting algorithm on the simulated spectra as well, but this brings further complexity, as the spectra is constructed using modelling, introducing a further dependence on the choice of

Table 4.4: Equivalent of Table 4.3 for the quenching timescale, τ_Q. The slope (α) is obtained from a linear fit to the function $\Delta\tau_{Q;L,M} = \alpha \log \mathrm{M}_\star/\mathrm{M}_\odot + \beta$ (see Fig. 4.8and 4.9). The uncertainty is quoted at the 1 σ level.

	Lum-weighted		Mass-weighted	
	EAGLE	SDSS	EAGLE	SDSS
lGV	$+1.32 \pm 0.96$	-0.74 ± 1.16	-1.25 ± 0.70	-1.92 ± 1.17
mGV	$+0.71 \pm 0.98$	-0.03 ± 0.64	$+0.30 \pm 0.48$	-1.83 ± 1.31
uGV	-1.08 ± 1.36	-0.85 ± 1.33	-1.38 ± 0.68	-8.04 ± 2.12
	Lum-weighted		Mass-weighted	
	TNG100	SDSS	TNG100	SDSS
lGV	$+1.61 \pm 0.72$	-0.68 ± 1.12	-0.40 ± 0.89	-1.31 ± 1.66
mGV	-0.13 ± 0.78	-0.20 ± 1.35	$+0.07 \pm 0.72$	-0.20 ± 3.17
uGV	-1.33 ± 0.92	-0.27 ± 2.06	-0.69 ± 0.77	$+1.85 \pm 2.09$

population synthesis model. Therefore, depending on which SSP models we use or IMF we assume, the spectra will vary thus giving us different results through spectral fitting. Therefore, by using the *true* SFH, we ensure the average age is accurate in simulation data, avoiding these biases, even if we do have some systematic differences. Furthermore, as outlined in Section 4.3.3, the number of matching observational galaxies in SDSS-EAGLE and SDSS-TNG100 set is quite low. Despite this, we find the average ages of the observed galaxies, both luminosity and mass weighted, to be very similar. This indicates, while our approach, for selecting GV galaxies might yield highly different sets of galaxies in the SDSS-EAGLE and SDS-TNG100 samples (see Fig. 4.2), their parameters, such as the average age or metallicity, are still comparable.

4.4.5 Quenching timescales

In Chapter 3, we presented a parameter that – under a number of simplifying assumptions – can serve as a proxy of the quenching timescale. It is defined as the time interval between two percentile levels of the stellar age distribution, namely:

$$\tau_Q \equiv t_{70} - t_{30}, \tag{4.9}$$

where t_x represents the cosmic time when the cumulative stellar mass function reaches a percentile level of x. Therefore τ_Q is the time that the system takes to

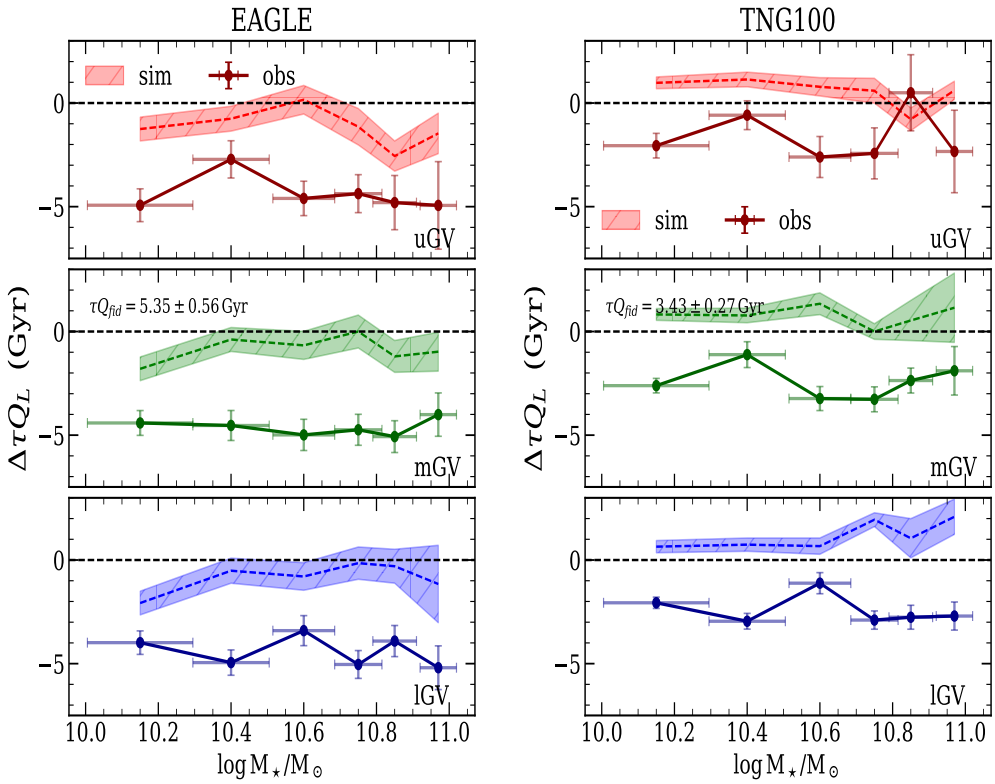

Figure 4.8: Equivalent of Fig. 4.6 for the relative luminosity-weighted quenching timescale, $\Delta\tau_Q$, quoted with respect to a fiducial value ($\tau_{Q,fid}$), also taken from mGV galaxies in the $10.68 \lesssim \log M_\star/M_\odot \lesssim 10.81$ mass bin of the simulation data, and quoted in each figure.

go from a stellar mass content of 30% to 70% of the final amount. Similarly to average age estimates we bootstrap 60% of the galaxies to obtain uncertainties in the range $\sim$ 0.07-2.3 Gyr for the observational data, derived from STARLIGHT, and $\sim$ 0.1-0.8 Gyr for simulated data, directly from the star formation histories. In a simple scenario where the galaxy builds up the stellar content in a monotonic way, this parameter scales with the rate at which stellar mass grows. Ideally, one would consider higher levels of the percentile (i.e. x), in order to represent more accurately the final stages before quenching ensues. However, our choice is motivated by the unavoidable uncertainties of the analysis, notwithstanding the systematics related to the derivation of the star formation history from full spectral fitting, following the STARLIGHT code (Cid Fernandes et al., 2005).

Fig. 4.8 and 4.9 shows the relative trends in both luminosity- and mass-

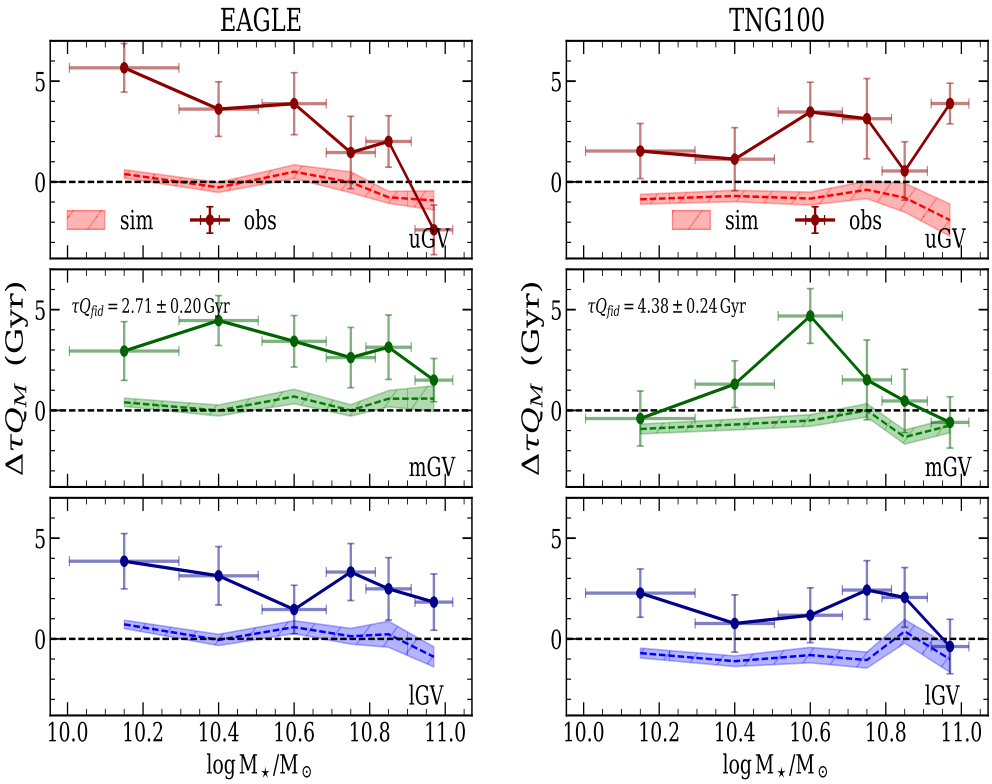

Figure 4.9: Equivalent of Fig. 4.8 for mass weighted quenching timescale.

weighted quenching timescale, respectively. The symbols and panels are analogous to those presented in Fig. 4.6, comparing the results for EAGLE and TNG100 in the left and right panels, respectively. The slopes of these relations, assuming a simple linear trend, are quantified in Table 4.4. We emphasize that τ_Q is less robust than the derivation of an average age, as presented above. Similarly, we can see that there are also large discrepancy between the observational sets of galaxies compared to the average ages. However, we note that the constraints are imposed on stacked spectra of galaxies with very similar properties (same stellar mass and in the same GV region), and feature a high signal to noise ratio. Therefore, the *relative* variations in τ_Q among the stacked data are more reliable than individual measurements of the same parameter. We also note that, similarly to the average age shown above, we present the data as relative to a fiducial bin, chosen to be the $10^{10.68} < M_\star/M_\odot < 10^{10.81}$ interval in mGV simulated galaxies. Two fundamental pieces of information should be looked for in the figures: the general trend with stellar mass, and the overall

offset between SDSS data and simulations. In the luminosity-weighted case (left panels), both simulations reproduce the general trend of the observations, with an overall flat slope. There is a substantial offset between both, with SDSS data featuring shorter values of τ_Q, analogous to the systematic in average age. Interestingly, this offset is reversed in the mass-weighted case, where the comparison suggests that the simulations quench star formation more rapidly. Moreover, this behaviour also appears in the TNG100 comparison.

Note the sign reversal of $\Delta\tau_Q$ between the luminosity-weighted and the mass-weighted cases, that appears in both EAGLE and TNG100. This sign change implies the observations produce shorter τ_Q than the simulations when luminosity-weighted, but longer values of τ_Q when weighed by mass. This result could be caused by the fact that the $D_n(4000)$ index is sensitive to the presence of younger stellar populations from a recent episode of star formation (Poggianti and Barbaro, 1997). However, this could also be explained by the way `STARLIGHT` constrains the weights of individual SSPs when performing spectral fitting. Luminosity weighting puts high weights in a short and recent period of time. Hence the resulting τQ is short. In contrast, the mass-weighted SFH distributes evenly the weights of the different stellar populations, producing a more extended distribution that results in a longer τ_Q. Simulations distribute the weight of the individual star particles evenly for all ages, hence is not so sensitive to the difference between luminosity and mass weighing.

4.5 Discussion

This chapter focuses on how simulations behave regarding the proposed classification of GV galaxies, presented in this thesis, following a probability-based methodology applied to the distribution of 4000Å break strength in a large sample of SDSS (classic) spectra with relatively high signal-to-noise ratio. The definition of the GV along with three sub-regions (lower-, mid-, and upper-GV, denoted lGV, mGV, uGV, respectively) was presented and analysed in Chapter 3. We contrast here the observational properties with two state-of-the-art cosmological simulations, EAGLE and

Illustris TNG. Since the GV can be interpreted as a transition region where galaxies evolve from actively star-forming to quiescent systems, it should be considered a fundamental sample where the physical mechanisms of feedback, described in cosmological simulations by an overly simplified set of equations compared to the real thing, loosely termed subgrid physics, can be put to the test. In a way, constraints based on GV galaxies provide "the next order" in our perturbative approach towards galaxy formation, the lowest order being the standard constraints on the galaxy luminosity/mass function, the Tully-Fisher relation and the mass-metallicity relation (Schaye et al., 2015; Pillepich et al., 2018b).

4.5.1 Potential Caveats

4.5.1.1 Population synthesis models

In order to follow the same definition of the GV in the simulations as in Chapter 3, we had to create synthetic spectra by combining the star formation and chemical enrichment history of the simulations with the E-MILES population synthesis models of Vazdekis et al. (2016). Once the mock spectra were created, we measured the 4000Å break strength following the same $D_n(4000)$ index (Balogh et al., 1999). A possible systematic lies in the choice of models, including stellar evolution/isochrone prescriptions and stellar libraries. One would consider contrasting the results with respect to independent population synthesis models, such as BC03 (Bruzual and Charlot, 2003) or FSPS (Conroy and Gunn, 2010), beyond the scope of this project. We note, though, that our analysis is mostly focused on *relative* variations of the stellar ages, which present significantly smaller systematics than *absolute* age estimates.

4.5.1.2 Green Valley definition

An additional caveat regarding the mismatch between simulations and observations may be due to the actual definition of the GV. Previous studies of the EAGLE and TNG100 samples selected GV galaxies based on colour, or on the SFR vs stellar mass plane (Trayford et al., 2015, 2017; Wright et al., 2019; Nelson et al., 2018; Correa et al., 2019). Our selection, based on 4000Å break strength is motivated by

a fully empirical approach, and requires the "projection" of the output from the simulations on the observational plane by creating synthetic spectra (Sec. 4.3.1) whose $D_n(4000)$ is measured. This step may introduce a systematic that can affect the comparison. An alternative approach would require defining the GV in the simulations independently, similarly to Trayford et al. (2015) and Wright et al. (2019) for EAGLE and Nelson et al. (2018) for TNG100, thus having independent definitions of the GV for EAGLE, TNG100 and SDSS. Using this methodology, we would have different GV locations for EAGLE, TNG100 and SDSS on the $D_n(4000)$ vs stellar mass plane. This would produce independent lGV, mGV and uGV samples in each data set. However this method is counterproductive to the aim of this project, as we are aiming at comparing the empirical definition of the GV, based on SDSS data, with model predictions. Thus by projecting simulations onto the observational plane and comparing the results enables the improvement of the subgrid physics such that the models can reproduce the BC, GV and RS morphology as found in the observations. Moreover, by focusing on the GV in this manner, we isolate the cause of the discrepancy i.e. the overabundance of Q GV population and lack of SF GV galaxies hinting towards over quenching or too rapid quenching in the simulations.

4.5.2 Contrasting observations with simulations

4.5.2.1 Overall distribution

Hydrodynamical simulations have been shown to successfully reproduce the fundamental scaling relations of galaxies. Furthermore, there have been multiple studies on the bimodality that find a qualitative agreement between observation and simulations: in EAGLE, multiple studies have focused on colour (g–r) at $z = 0.1$, to find an overall agreement with the distribution with observation (Trayford et al., 2015). Implementing a more sophisticated treatment of dust attenuation – where younger stellar populations are dustier than older systems – a better agreement with data from the GAMA survey was obtained (Trayford et al., 2017). Note these authors report a red sequence that appears slightly flatter than observed, in agreement with our Fig. 4.3. The flatter red sequence gradient was attributed to a flatter mass-metallicity relation (Schaye et al., 2015). This discrepancy is also evident in the

definition based on the $D_n(4000)$ index, as it is also sensitive to metallicity.

Concerning TNG100-based comparisons, Nelson et al. (2018) correct for dust attenuation, finding a good quantitative agreement of the bimodality with the observations on the colour vs stellar mass plane. We also find good qualitative agreement on the colour vs stellar mass plane, by applying a simple dust correction with the Calzetti et al. (1994) law. However, our analysis based on the $D_n(4000)$ index, which is significantly less sensitive to dust attenuation, shows a greater discrepancy (Fig. 4.3), and this behaviour is similar in the EAGLE simulations. This result would suggest that the prescriptions chosen by the simulations, especially manifesting on the mass-metallicity relation, are able to reproduce and explain the observed colours, whereas the 4000Å break selection of GV suggests these prescriptions are not good enough to explain in detail the properties of the underlying stellar populations. Note that both broadband colours and $D_n(4000)$ suffer from the age-metallicity degeneracy (see, e.g. Worthey, 1994), whereas the latter has a negligible dependence on dust. Therefore, the subgrid physics needed to constrain either may introduce independent biases. We argue here that the 4000 Å break strength is a more fundamental observable, as it removes the highly complex layer of dust production, destruction, geometry, radiative transfer, etc, needed to produce reliable estimates of broadband photometry.

Additionally, the discrepancy between observations and simulations could be to the magnitude limit on the observation, where we do not observe galaxies in SDSS below $r < 17.7$. However, in simulations we do not impose such criteria due to the already small sample size. Therefore, observations might be missing faint galaxies with stronger 4000Å break, found in the simulations. However, we argue, this effect will be most prominent, if at all, in the low mass regime, owing to the Malmquist bias. This could be used to explain the mismatch in the RS gradient, however in high stellar masses $\log \mathrm{M}_\star/\mathrm{M}_\odot \gtrsim 10.2$, this effect will be minimal, i.e. not enough to explain the abundance of galaxies with $D_n(4000) \gtrsim 1.80$ seen in simulation but not observations. Wu et al. (2021) compares the LEGA-C survey with TNG100 at intermediate redshift, $0.6 < z < 1.0$, finding a good match between

the simulated and observed $D_n(4000)$ index. However, they find already that most of the quiescent galaxies, especially for high mass systems with $D_n(4000) > 1.6$, have weaker EW(Hδ) and very little star formation in the recent history, with very few galaxies to have experienced rejuvenation in the last 1 Gyr, which as they evolve to $z \sim 0.1$, would have a stronger $D_n(4000)$ - as seen in this chapter.

4.5.2.2 Overquenching

We discuss here the potential explanation of the mismatch of the bimodality shown with 4000Å break strength as a result of overquenching. Note most of our analysis is carried out on the GV.

Although qualitatively there is good agreement between the two simulations, in EAGLE we find the RS features a $D_n(4000)$ index $\sim$0.1 dex higher than the SDSS constraints at stellar mass $\lesssim 10^{10.5} M/M_\odot$. TNG100 also produces a RS with an even greater $D_n(4000)$ strength, $\sim$0.2 dex higher than SDSS. Both simulations produce the BC in agreement with the observations, therefore indicating a mismatch with respect to feedback/quenching mechanisms that eventually produce the RS. This hypothesis is backed by the fraction of galaxies classified via nebular emission (Fig. 4.4) that shows a higher fraction of Q galaxies in the GV, especially at the massive end. Note that the definition of quiescence versus star formation is less prone to biases than the definition of AGN activity (Tab. 4.2). Therefore, the excess of Q GV galaxies in simulations appears to be quite robust. Luminosity-weighted average ages (Fig. 4.6), consistently show older galaxies in the simulated systems in all GV regions, lGV, mGV and uGV. Between the two sets, TNG100 features the larger discrepancy towards a larger excess of Q galaxies and older average ages. Fig. 4.5 shows the simulated GV galaxies with slightly higher sSFR than the observations, but within 1σ in all lGV, mGV and uGV. The greatest difference between simulations and observations is due to the former lacking any ongoing star formation, where EAGLE and TNG100 have 28% and 100% GV galaxies with $\log \mathrm{sSFR} < -15.5$ at the highest stellar mass bins $\geq 10^{10.81} M_\odot$. While EAGLE produces a consistent level of scatter, $0.5 - 0.8$ dex, matching the observations, a lower scatter, $0.2 - 0.5$ dex, is seen for TNG100 at high stellar mass, $\geq 10^{10.68} M_\odot$.

Previous studies of GV galaxies in both EAGLE and TNG100 suggest quenching timescales $1.5 \lesssim \tau_{GV} \lesssim 7.0$ Gyr (Trayford et al., 2016; Wright et al., 2019; Nelson et al., 2018; Correa et al., 2019), a range that mostly agrees with the constraints derived from SDSS and GAMA data (Schawinski et al., 2014; Phillipps et al., 2019, A20), with a heavy dependence on their stellar mass and morphology. Our study of GV and quenching timescale also gives values within this limit in both observations and simulations, as shown in Fig. 4.8 and 4.9. However, note our sample is less homogeneous than the previous studies, as we stack the SFHs regardless of galaxy type or morphology, thus we are unable to find a clear trend with respect to stellar mass. The mass-weighted quenching timescale supports overquenching/ rapid quenching as the primary reason for the discrepancy between observations and simulations: we obtain more extended SFHs for SDSS than both EAGLE and TNG100, $\tau_Q(obs) > \tau_Q(sim)$. Note both EAGLE and TNG100 reproduce the expected decreasing quenching timescale with stellar mass, as found in the literature (Kauffmann et al., 2003; Gallazzi et al., 2005). However for the luminosity-weighted quenching timescale, we find a reversal of this trend, where the observational constraints show a shorter τ_Q. This effect could be due to rejuvenation (Faber et al., 2007; McIntosh et al., 2014), where a recent episode of star formation will bias the luminosity-weighted estimates towards the younger (i.e. lower M/L) component. Since our estimate of τ_Q is based on the difference in the stellar age distribution at the 30% and 70%, in luminosity weighting, a recent episode of rejuvenation can drastically increase the τ_Q parameter, however if the episode is of a significant fraction, it will have an inverse effect, where τ_Q decreases drastically as seen in Fig. 4.8 and 4.9.

4.5.2.3 Simulation Star Formation Histories

We have shown that various indicators suggest overquenching or a more rapid quenching of GV galaxies in both EAGLE and TNG100 simulations with respect to the observational evidence provided by SDSS spectra. It is also interesting to explore the fact that we find a higher fraction of Q galaxies and lower sSFR in TNG100 with respect to EAGLE, however EAGLE produces slightly older average

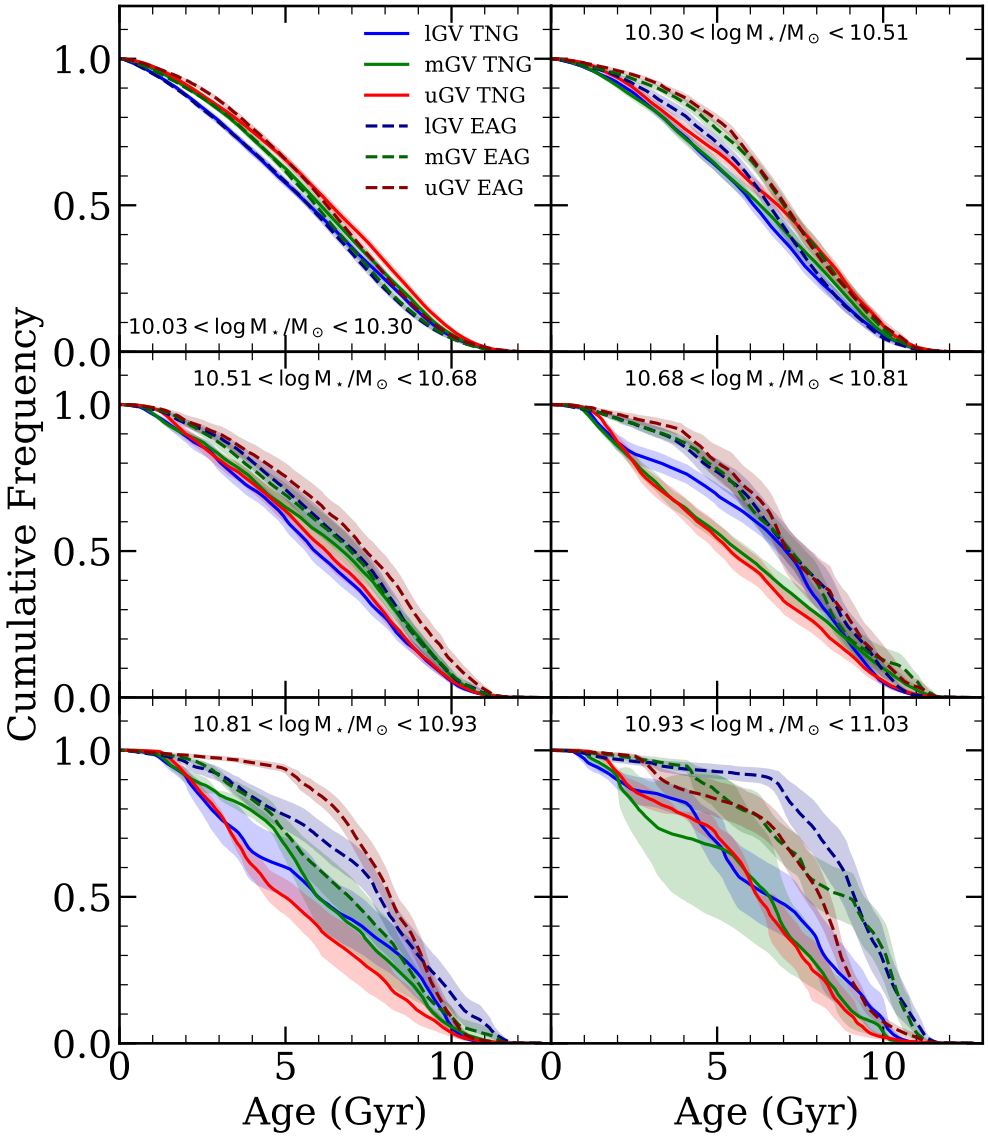

Figure 4.10: Cumulative frequency of the mass-weighted star formation history of galaxies for different stellar mass bins, as labelled. The blue, green and red data points show results for lGV, mGV and uGV respectively. The solid and dashed lines show the mass-weighted star formation history in TNG100 and EAGLE simulations, respectively. The shaded region shows the uncertainty on the SFH, which represents the 1σ variation in the SFH of individual galaxies.

ages and shorter quenching timescales, suggesting earlier and more rapid quenching. This scenario is illustrated in Fig. 4.10, that shows the mass-weighted SFHs, as cumulative functions with stellar age, where blue, green and red data correspond to the lGV, mGV and uGV, respectively. The solid and dashed lines are the results of TNG100 and EAGLE, respectively. At low stellar mass ($\lesssim 10^{10.68}\mathrm{M}_{\odot}$) there is qualitative agreement between the two simulations. We note that in these stellar mass bins, both simulations produce similar average ages. Increasing from this stellar mass range, EAGLE features a quicker accumulation of stellar mass at early times compared to TNG100, as shown by the steeper increase of the cumulative distribution.

The fact that EAGLE galaxies undergo quicker quenching but still feature higher SFRs shows the nuance and complication we face when trying to understand galaxy formation and evolution. Normally, a low sSFR, specially in the GV, is associated to faster quenching. However our results illustrate that this is not always the case as parameters such as SFR, are sensitive to young stars. For instance, estimates based on recombination lines are mostly sensitive to the ionising flux from short-lived O and B type stars, therefore only encompass the very recent SFH.

Therefore in this study we see two distinct and different effects in EAGLE and TNG100 simulations. EAGLE shows a more rapid quenching at early times, whereas TNG100 quenches galaxies at later times, both showing an excess of Q GV galaxies with respect to the observational constraints, but with subtle differences. We argue that this difference may be, partly, caused by the difference in the definition of the black hole seed mass and halo mass threshold. In EAGLE, the choice is $10^5 h^{-1}\mathrm{M}_{\odot}$ for the BH seed and $10^{10} h^{-1}\mathrm{M}_{\odot}$ for the halo mass threshold, whereas TNG100 adopts values about 8 times higher in both cases. This increase in the TNG100 simulation is justified to mitigate slow early growth (Pillepich et al., 2018b), but it might also delay the onset of AGN feedback into a stage that removes all chances of a later stage of star formation at the observed redshift ($z = 0.1$), thus overproducing Q galaxies in the GV.

Fig. 4.11 shows the quenched fraction in both observation and simulation data

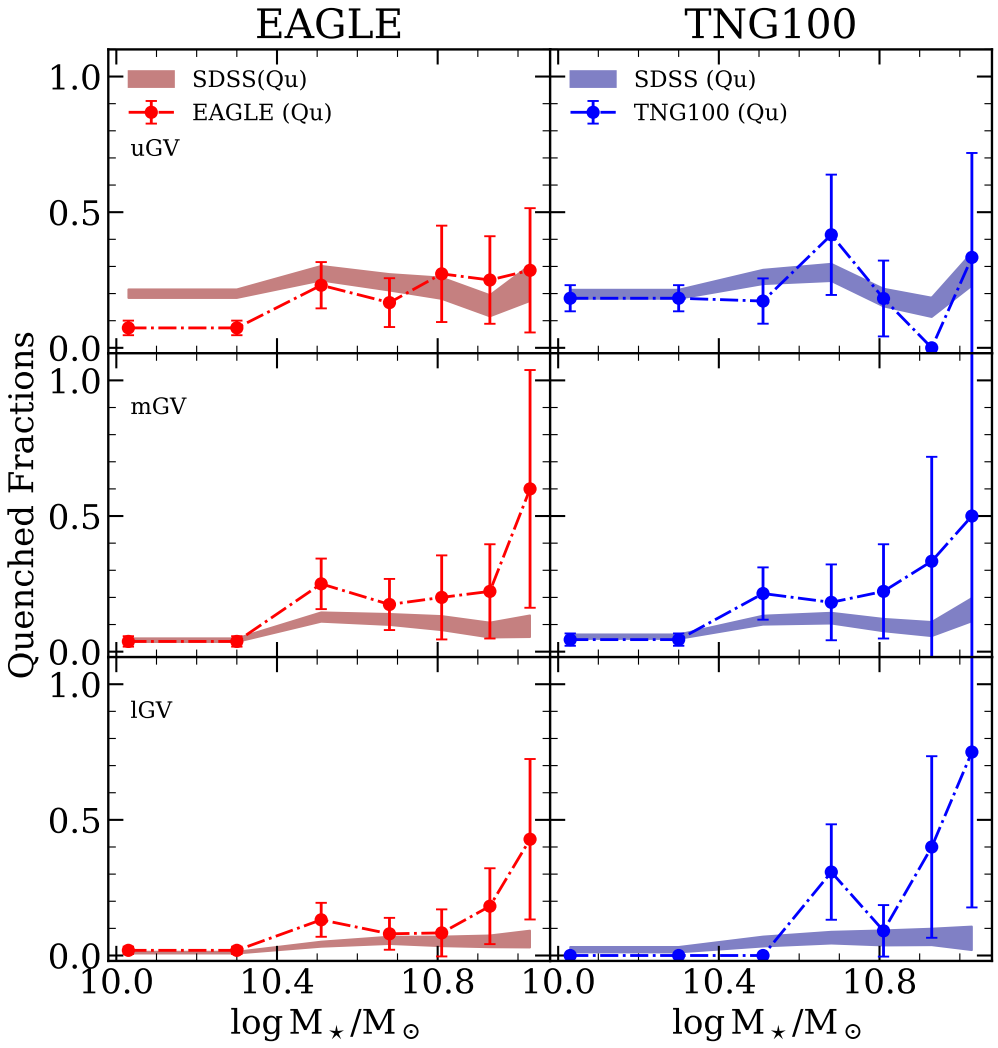

Figure 4.11: Comparison of the quenched fraction as a function of stellar mass in SDSS (filled) and simulations (dashed). The left and right panels show the results for EAGLE and TNG100 data, respectively. Quiescent galaxies in SDSS are selected via the BPT classification (-1, corresponding to no emission line detectable). Simulated quiescent galaxies are selected using the criteria stated in Tab. 4.2. From bottom to top, each panel corresponds to the lGV, mGV and uGV.

with respect to all galaxy types (concerning nebular emission). The SDSS galaxies are flagged as quenched if their BPT classification is -1 (i.e. no detected emission line). For the simulations, a quenched galaxy follows the criteria shown in Tab. 4.2, namely: $\log(\lambda_{\rm Edd}) < -4.2$ and $\log {\rm sSFR} \leq -11.0$. The filled and dashed lines show results for SDSS and simulations. Left and right panels show the results for EAGLE and TNG100, respectively. From bottom to top, the panels represent the lGV, mGV and uGV, evolving from the part of the GV closest to the BC towards the RS. This figure, along with Fig. 4.10 allows us to provide an explanation for our results. Both EAGLE and TNG100 show an overall agreement with respect to their SDSS counterpart, where there is an increase in GV quiescent galaxies with stellar mass. In lGV and mGV, we find a good qualitative agreement between both simulations and observations. The simulations produce a higher quenched fraction with increasing stellar mass. The exception to this is the uGV, where there is a constant fraction of quenched galaxies. Both simulations are able to reproduce a trend matching the observations. Both EAGLE and TNG100 simulations also produce a similar rate of increase in the quiescent population. Note the general low fraction of Q galaxies in the GV. This is owing to GV being mostly populated by LINER and Seyfert-type galaxies (Martin et al., 2007; Angthopo et al., 2019), further indicating the importance of having the correct subgrid physics for AGN feedback in hydrodynamical simulations.

The slower quenching leads to younger stellar components in TNG100 than EAGLE, thus we find younger luminosity-weighted average ages for TNG100, $t_{fid} = 2.98 \pm 0.08\,{\rm Gyr}$, than EAGLE, $t_{fid} = 3.77 \pm 0.33\,{\rm Gyr}$, (Fig. 4.6). The rapid change in the quenched fraction of GV galaxies and the higher number of galaxies with zero SFR (Fig. 4.5) provides an explanation for the observed excess of Q GV galaxies in TNG100 (Fig. 4.4); with respect to SDSS and EAGLE. Furthermore, the number of galaxies with zero SFR increases as we go from lGV to the uGV. This occurs at stellar masses above $\gtrsim 10^{10.5}{\rm M}_{\odot}$, where the kinetic feedback is switched on, thus suggesting the excess of kinetic feedback at late times might be the reason for this behaviour. This is supported when we study the re-

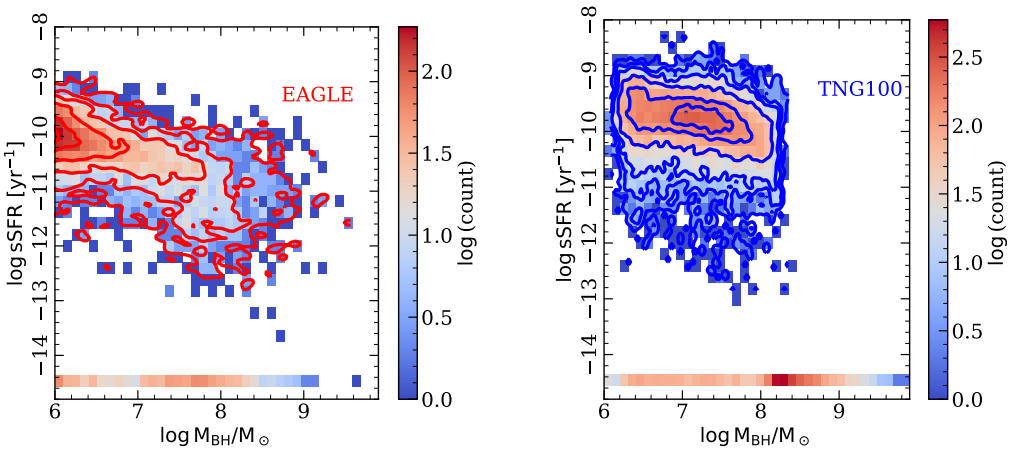

Figure 4.12: Distribution of galaxies in EAGLE (left) and TNG100 (right) in the black hole mass vs specific star formation (within 3 kpc) diagram. The contours outline the density of galaxies in a given area. The density plot indicates the number of galaxies in a given area, where the redder areas are occupied by a higher number of galaxies than the bluer regions. Note, the galaxies with $\log \mathrm{sSFR} = -14.5 [\mathrm{yr}^{-1}]$ corresponds to galaxies with SFR$= 0$.

lation between sSFR and black hole mass between the two simulations, as seen in Fig. 4.12. EAGLE (left panel) shows that an increase black hole mass results in the steady decrease of sSFR, where galaxies still have some ongoing SFR at high black hole masses, $\log \mathrm{m_{BH}/M_\odot} \gtrsim 8.0$. However, in TNG100 (right panel), we find a distribution focused around two points, where a clear divide can be seen around $\log \mathrm{m_{BH}/M_\odot} \sim 8.0$, where the AGN is thought to change from thermal to kinetic feedback. On the one hand at low black hole masses, where they experience thermal feedback, we find many galaxies with on-going star formation, with a dense region around $\log(\mathrm{sSFR/yr^{-1}}) \sim -10$. On the other hand, when the black hole mass goes above $\log \mathrm{m_{BH}/M_\odot} \gtrsim 8.0$, we find most of the SFR$= 0$, set our $\log(\mathrm{sSFR/yr^{-1}}) = -14.5$. This further supports the claim that kinetic feedback implemented in TNG100 is too powerful. Note there are some galaxies with some SFR, above the $10^{8.0}\mathrm{M_\odot}$ black hole mass, however this could be where galaxies experience rejuvenation as stated in Nelson et al. (2018). Such events are thought to be prominent at high stellar mass, $\gtrsim 10^{11.0}\mathrm{M_\odot}$, beyond the stellar mass interval explored in our study.

4.5.3 Subgrid interpretation

We explore in this section the details of the subgrid physics implemented in the simulations that could give rise to the differences presented above. Given the mass range we are studying, a valid assumption is to consider AGN feedback as responsible for the mismatch. Previous work in the literature noted a strong dependence of quenching within the stellar mass values studied (Kewley et al., 2006; Croton et al., 2006; Hopkins et al., 2006). For galaxies with stellar mass lower than $10^{9.7}$M$_\odot$, EAGLE finds very low AGN activity and most quenching is due to stellar feedback or environment (see, e.g. Crain et al., 2015). Above $10^{9.7}$M$_\odot$ – corresponding to the mass range probed in this study – EAGLE galaxies quench star formation via AGN feedback (Bower et al., 2017). Note even within this regime, EAGLE has two distinct intervals where the SMBH grows at different rate compared to the stellar mass. If the stellar mass is $10^{9.7}$ <M$_\star$/M$_\odot$ < $10^{10.3}$, EAGLE has slow growth in SMBH, while more massive galaxies undergo a rapid increase in the super-massive black hole accretion rate (Wright et al., 2019). This coincides with the same mass regime where we see a drastic increase in the fraction of Q galaxies, with an excess over the observed constraint. Therefore we can assume the increase in SMBH accretion rate, while self-regulated, could be too rapid.

In TNG100, both the black hole mass and the Eddington ratio have a strong dependence on how much energy is injected back onto the environment and in which form. In TNG100, primarily the AGN feedback, particularly the kinetic BH-driven winds, have been demonstrated to suppress star formation above $10^{10.5}$ M$_\odot$ (Weinberger et al., 2017; Nelson et al., 2018; Terrazas et al., 2020; Davies et al., 2020; Donnari et al., 2021a), hence the choices in subgrid physics of SMBH seed, growth or feedback are probably the cause of the discrepancies we have seen in this analysis. Specifically at the massive end, $\gtrsim 10^{10.5}$M$_\odot$, we find a substantial difference between SDSS and TNG100, where the simulation switches from predominantly thermal feedback:

$$\Delta\dot{E}_{therm} = \varepsilon_{\mathrm{f},high}\varepsilon_r\dot{M}_{\mathrm{BH}}c^2, \tag{4.10}$$

to kinetic feedback:

$$\Delta\dot{E}_{\mathrm{k}in} = \varepsilon_{\mathrm{f},kin}\dot{M}_{\mathrm{BH}}c^2, \tag{4.11}$$

thus injecting a higher amount of energy onto the interstellar medium (ISM) (Weinberger et al., 2017). Therefore we suspect that the kinetic feedback, along with the delay in SMBH growth imposed by the higher thresholds in the choice of seed mass, may be responsible for the over-quenching found in GV galaxies (see also Li et al., 2019, who found a similar discrepancy). At fixed stellar mass, the black hole mass in TNG100 is greater than the estimates derived from observations (see Fig. 4.13 and Li et al., 2019), hence we should expect the energy output, as shown in Eq. 4.11, to be overestimated in this simulation. The overmassive black holes could also lead to the overquenching in the quasar mode as well, as more energy is injected to the surrounding ISM, thus yielding a higher fraction of Q galaxies in the GV. Moreover, Terrazas et al. (2020) found a sharp decline in the SFR at $\mathrm{M}_\star \sim 10^{10.5}\mathrm{M}_\odot$, which corresponds roughly to the black hole mass of $\mathrm{M}_{BH} \sim 10^{8.0}\mathrm{M}_\odot$ in TNG100, further supporting this assumption and what we see in Fig. 4.12. Note this sharp decline in star formation could mean TNG100 galaxies feature more rapid quenching timescales, compared to both EAGLE and SDSS. However the bulk of the quenched galaxies might reside already in the RS, rather than the GV. At the same time, the dependence of the quenched fraction with stellar mass in TNG100 matches the SDSS data, when a different definition is adopted to classify star-forming and quiescent galaxies in the general population (Donnari et al., 2021b). In contrast, EAGLE's stellar mass vs black hole mass relation, Fig. 4.13, finds good agreement with observations. However, we still find inconsistencies in the quenched fraction between observation and simulation, within GV, suggesting the parameters, which have been fine tuned for the AGN feedback "subgrid" physics to be too powerful. Moreover, the use of one mode of AGN feedback, regardless of the stellar mass might be too simplistic.

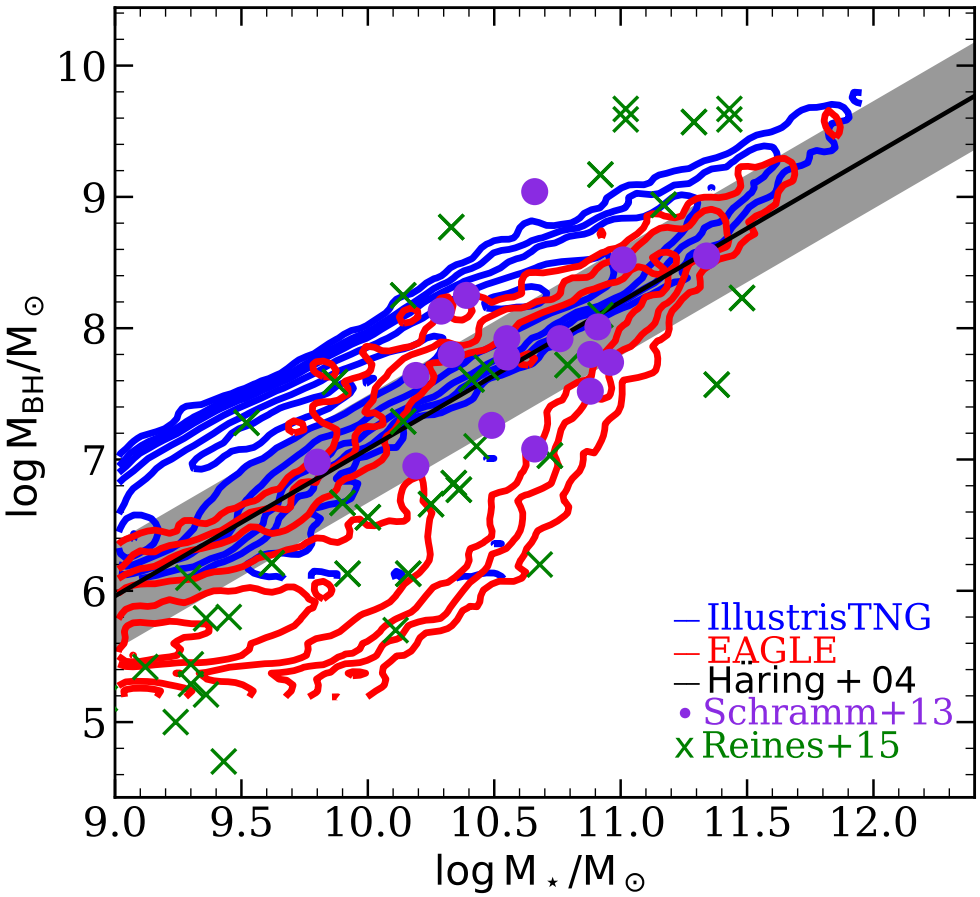

Figure 4.13: The relation between total stellar and black hole mass for EAGLE and TNG100, shown in red and blue, respectively. The purple and green data points outline the observed stellar and black hole mass, obtained from Schramm and Silverman (2013) and Reines and Volonteri (2015), respectively. Finally the black line with shaded area shows the relation obtained in Häring and Rix (2004).

4.6 Conclusions

We make use of a recent definition of GV galaxies based on 4000Å break strength, which uses SDSS classic spectra, and a probabilistic approach to separate BC, GV and RS (see Chapter 3 for more details), to explore two of the latest, state-of-the-art cosmological hydrodynamical simulations: EAGLE, (RefL0100N1504), and IllustrisTNG (TNG100-1). We model the simulated galaxies to obtain a set of mock spectra without accounting for the effects of dust and by including the contribution from all the stellar particles in a cylinder within 3 kpc galacto-centric radius to

mimic the 3 arcsec (diameter) SDSS fibre aperture. We make use of the E-MILES population synthesis models (Vazdekis et al., 2016) to create the spectra. The study projects the simulated data on the observationally motivated plane, comparing these simulations with high quality spectroscopic data from the classic SDSS survey (e.g. Abolfathi et al., 2018).

The galaxy samples need to be homogenised to avoid selection biases. Although we homogenise in the stellar mass range $9 \lesssim \log \mathrm{M}_\star/\mathrm{M}_\odot \lesssim 12$, our analysis focuses on a narrower region, $10.03 \lesssim \log \mathrm{M}_\star/\mathrm{M}_\odot \lesssim 11.03$, which is the stellar mass range obtained by converting velocity dispersion to stellar mass. Regarding nebular activity, that allows us to classify the observed spectra, we define a number of criteria based on the sSFR and the Eddington ratio of SMBH growth to separate the simulated galaxies into Seyfert AGN, LINER, Q or SF. We use the global fractions of the homogenised observational sample to define the constraints, and focus on differences in the trends with respect to stellar mass. Despite the different subgrid physics implemented in these two simulations, we find similar constraints in EAGLE and TNG100 (Tab. 4.2).

A reasonable agreement is found in general between observations and simulations, where the simulations are able to produce the bimodal distribution on the $\mathrm{D}_n(4000)$ vs stellar mass plane. Both EAGLE and TNG100 correctly produce the location of the BC. However EAGLE features a RS that appears too high regarding the 4000Å break strength (by $\Delta\mathrm{D}_n(4000) \sim +0.1$ dex), while TNG100 produces a RS with an even higher discrepancy ($\Delta\mathrm{D}_n(4000) \sim +0.2$ dex). Furthermore, as previously noted, both simulations produce a RS with a shallower gradient compared to SDSS constraints, with TNG100 producing the flattest RS (Fig. 4.3). Such a disagreement in the RS is expected to produce a similar mismatch in the GV, the main focus of our analysis. Due to the sparsity of the GV in optical bands, we only focus on 10.82% EAGLE and 4.91% IllustrisTNG galaxies of the homogenised samples. Even so, the analysis yields large constraining capabilities to improve the simulations. We emphasize that the analysis of GV galaxies provides a fundamental constraint beyond the *zeroth order* constraints such as the galaxy stellar mass function,

the Tully-Fisher relation, or the mass-metallicity relation, and focuses narrowly on the subgrid physics that regulates the SFH of galaxies via feedback. Our analysis, based on the dust-resilient $D_n(4000)$ index provides a robust definition of the green valley and is complementary to previous comparisons, such as, e.g., Trayford et al. (2015, 2017); Nelson et al. (2018) for the galaxy colour or SFR vs. galaxy stellar mass planes across the simulated galaxy populations.

We find both EAGLE and TNG100 overproduce (underproduce) the fraction of Q (SF) galaxies in the lGV and mGV[1] in galaxies with stellar mass $10^{11.0}M_{\odot}$. Moreover, the overproduction of quiescent GV galaxies is more prevalent in TNG100 than EAGLE (Fig. 4.4), supported by the comparison of sSFR. While both EAGLE and TNG100 produce galaxies with sSFR marginally greater, by ~ 0.1 dex, than the observations, they match the overall trend. However, both models still show overquenching as there are greater fractions of fully quenched galaxies with respect to the observations (Fig. 4.5). Furthermore, a comparison between simulations shows TNG100 produces more completely quenched galaxies than EAGLE. Note, by using a different definition of the SFR, Donnari et al. (2021a) have found good agreement with SDSS in the general galaxy population, i.e. not focusing on the GV, to better than 10 per cent, in the transitional mass scale of $10^{10-11}M_{\odot}$.

Despite EAGLE having a lower fraction of Q GV galaxies than TNG100, we find they produce overall older GV galaxies, both in luminosity and mass weighting, and undergo more rapid quenching at high stellar mass. In comparison to the observations, both simulations produce older luminosity-weighted stellar ages. EAGLE and TNG100 produce up to 3.5 Gyr and up to 2.8 Gyr older galaxies, respectively, with a dependence on stellar mass. EAGLE yields a steeper gradient of the correlation between luminosity-weighted average age and stellar mass, whereas TNG100 is able to produce a slope that roughly matches the SDSS-based constraints. The luminosity-weighted quenching timescale (τ_Q) shows a more extended transition time in simulations with respect to the SDSS data, a result that is reversed in mass-

[1] lGV, mGV and uGV represent the lower-, mid- and upper- green valley, defined as three terciles of the 4000Å break strength distribution within bins at fixed stellar mass

weighted τ_Q (Fig 4.8 and 4.9). However both simulations are able to reproduce the observational trend, more specifically a decrease in the mass-weighted quenching timescale with respect to stellar mass.

Finally, at the massive end, $10^{10.5-11.0}M_{\odot}$, EAGLE GV galaxies undergo more rapid quenching compared to TNG100 (Fig. 4.10). Both simulations show signs of overquenching, where, at higher stellar mass $10^{10.5-11.0}M_{\odot}$, there is a higher quenched fraction with respect to SDSS. While both over-produce quenched galaxies, we find a larger discrepancy between TNG100 and SDSS, up to 0.62 (fractional excess), compared to EAGLE and SDSS, with a difference up to 0.50 (Fig. 4.11). This shows that while TNG100 galaxies tend to quench at later times than EAGLE, they also quench more efficiently on the GV. This suggests that EAGLE allows for later episodes of star formation, when measured using the instantaneous SFR, which gives results that appear to be more in agreement with constraints from the SDSS sample (Fig. 4.5). Along with Fig. 4.12, previous multiple studies have noted the strong quenching nature of the kinetic black hole-driven winds (Terrazas et al., 2020; Davies et al., 2020), therefore we ascribe this difference to AGN feedback, which sterilises the ISM of TNG100 galaxies, resulting in an excess of quiescent galaxies on the GV. This chapter illustrates the power of the green valley – defined by use of the 4000Å break strength – as a key laboratory where feedback prescriptions can be put to the test on state-of-the-art simulations of galaxy formation.

Chapter 5

Testing the role of AGN feedback on "twin galaxies"

5.1 Introduction

In this thesis, we have explored the stellar populations of GV galaxies, defined using a novel method, through the use of the 4000Å break, uncovering the importance and abundance of AGN in the GV (see Chapter 3). Furthermore, we also make use of state-of-the-art hydrodynamical simulations to study how well the simulations are able to reproduce the observational trends in Chapter 4. There we find that the quenching mechanisms implemented in simulations to be too efficient, specifically for high mass systems, $M_\star \gtrsim 10^{10.5} M_\odot$, where AGN is thought to be essential in quenching of star formation. Furthermore, the study of super massive black hole (SMBH) and AGN in simulations have shown them to be essential for the formation of quiescent galaxies at high stellar mass (Trayford et al., 2017; Pillepich et al., 2018a; Nelson et al., 2018; Terrazas et al., 2020). Therefore, in this chapter we focus on a direct study of the effect of AGN on their stellar populations through the use of the "Twin" concept introduced in del Moral-Castro et al. (2019), whose sample was then expanded in del Moral-Castro et al. (2020). From the study of these "Twin" galaxies, they analyse the dimensionless spin parameter (λ_R) defined in Emsellem et al. (2007). The main result find bars to play an important role, where AGN galaxy with a bar have a higher λ_R compared to their SF twin with a bar 56%

of the time. When considering only unbarred galaxies, AGN galaxies have a higher λ_R greater than their SF twin 100% of the time, giving rise to the hypothesis that AGN galaxies may have a different SFH than their SF twin counterpart.

The material in this chapter is taken from *Testing the role of AGN on the star formation and metal enrichment of "twin galaxies"*, Angthopo et al. (Submitted to MNRAS).

5.2 Methodology

5.2.1 CALIFA data and twin galaxy selection

For the selection of twins, which refers to two galaxies that are almost identical in overall appearance and are similar in general properties, such as mass, luminosity, ellipticity and morphology, we make use of the 3D optical data (third data release) of the Calar Alto Legacy Integral Field Area survey (hereafter CALIFA, Sánchez et al., 2012, 2016). The CALIFA survey observed ~ 667 galaxies within redshift $0.005 \lesssim z \lesssim 0.03$. The parent sample was reduced to 404 galaxies by Méndez-Abreu et al. (2017), who disregarded those that presented signs of interaction, merging activity, or had a high inclination angle ($i > 70^{\rm o}$), for a reliable characterisation of morphology. Furthermore, they also check for the presence of bright stars that could contaminate the systems. For each target that we choose to study, the survey provides three data cubes: V500, V1200, and COMBO. The V500 data cubes have low spectral resolution, covering a wavelength range of $3745 < \lambda < 7500\,$Å with $R \sim 850$ at $\lambda \sim 5000\,$Å. The V1200 data cubes have higher resolution but cover a narrower spectral window, $3650 < \lambda < 4840\,$Å with $R \sim 1650$ at $\lambda \sim 4500\,$Å. The COMBO data cubes are a combination of the high and low resolution data cubes, where the high resolution spectra, via convolution with a smoothing kernel, are degraded to match the lowest resolution spectra of the sample. The combined data cubes are produced to overcome the vignetting affecting the other sets.

We give below a brief description of the selection process of twin galaxies - differing in nuclear activity. More details can be found in the papers presenting the original definition (del Moral-Castro et al., 2019, 2020). We start with the se-

lection of the AGN sample, identified with the ratios of emission line luminosities, applying the standard BPT classification method (Baldwin et al., 1981) to the central spaxel. The lines are isolated making use of the fitting codes pPXF (Cappellari and Emsellem, 2004) and Gandalf (Sarzi et al., 2006; Falcón-Barroso et al., 2006). An AGN is selected if the data meet the required criteria for a Seyfert galaxy in all four different BPT diagrams - three defined in Kewley et al. (2001) and one defined in Cid Fernandes et al. (2010), that compare the line ratios [OIII]/Hβ, [NII]/Hα, [SII]/Hα, [OI]/Hα, and [OIII]/[OII]. The AGN galaxies are included in the sample only if they are considered to be isolated. Following the isolation criteria detailed in Barrera-Ballesteros et al. (2014), from the whole CALIFA sample, galaxies are discarded if they meet all three criteria: (i) they have neighbouring galaxies within 250 kpc (ii) they have neighbours with a systemic velocity difference smaller than 1000 km s^{-1} (iii) their SDSS r-band magnitude difference, with the neighbouring galaxy, is less than 2 mag. The original sample was assembled to study the resolved galactic properties (del Moral-Castro et al., 2019). This original sample was expanded upon, where the differences in angular momentum was explored (del Moral-Castro et al., 2020). In addition, only galaxies with a spiral morphology, and types Sa/SBa to Sbc/SBbc are included, thus enforcing a "simpler" mass assembly history, rejecting the effect of major mergers. This selection criteria yielded 19 AGN galaxies.

To find the corresponding twin galaxies to these AGN (hereafter identified as SF galaxies[1]), a control sample of star forming galaxies were selected. For the SF galaxy to be considered a twin, firstly they have to be isolated and have to match the Hubble morphology of the AGN galaxy. In addition, the stellar mass difference between AGN and SF galaxies has to be $\Delta\log(M_\star/M_\odot) \lesssim 0.25$ dex, the absolute magnitude difference $\Delta M_r \lesssim 0.70$ mag, the difference in SDSS-r band disc ellipticity $\Delta\varepsilon \lesssim 0.2$. The selected candidates are then visually inspected to ensure similarity before they are selected as twins. These criteria were imposed in del Moral-Castro et al. (2020), however we further restrict the stellar mass difference

[1] However, note that the AGN galaxies in these systems also feature ongoing star formation. This is just a convention to identify the different twin members.

Table 5.1: List of twin galaxies, identified to be visually indistinguishable, where both are star-forming galaxies but only one of them has an AGN (we refer to the other one as SF). Columns 1 and 2 shows the galaxy ID and morphological classification, taken from Walcher et al. (2014), respectively. Col. 3 shows whether the galaxy has been identified to be an AGN or SF galaxy (del Moral-Castro et al., 2020), where AGN galaxy also has evidence of on-going star formation. Col. 4 indicates the twin number a galaxy belongs to. Cols. 5 and 6 lists the total stellar mass (Walcher et al., 2014) and the central velocity dispersion (measured within a 3 arcsec aperture), which was derived in del Moral-Castro et al. (2020), respectively. Finally, col. 7 shows the physical scale.

Galaxy (1)	Morph. (2)	Type (3)	Twin (4)	$\log M_\star/M_\odot$ (5)	σ (km/s) (6)	scale (pc/″) (7)
			Group 1			
NGC2253	SBbc	SF	1	10.50	109.1	257
NGC1093	SBbc	AGN	1	10.43	107.4	349
NGC5947	SBbc	SF	1	10.56	119.3	402
NGC6004	SBbc	SF	1	10.63	100.8	301
NGC2906	Sbc	AGN	3	10.46	114.0	165
NGC0001	Sbc	SF	3,4	10.58	131.9	305
NGC2916	Sbc	AGN	4	10.64	149.6	276
			Group 2			
NGC2639	Sa	AGN	2	11.09	210.8	247
NGC0160	Sa	SF	2,6	10.99	216.1	349
NGC7311	Sa	AGN	6	10.96	206.9	310
			Group 3			
NGC7466	Sbc	AGN	7	10.68	128.7	509
NGC5980	Sbc	SF	7,8	10.69	121.8	320
UGC00005	Sbc	AGN	8	10.74	117.9	485
			Group 4			
NGC6394	SBbc	AGN	5	10.86	105.8	596
UGC12810	SBbc	SF	5	10.81	114.0	543

to $\Delta\log(M_\star/M_\odot) \lesssim 0.20$ dex and introduce a velocity dispersion constraint, where the difference in velocity dispersion in the central region, within a 3 arcsec aperture, $\Delta\sigma \leq 30$ km/s. Note the velocity dispersion constraint is less than the typical measurement error in CALIFA, however this hard constraint on σ further ensures that these twin pairs, AGN and SF, galaxies are as similar as possible as σ is thought to be one of the fundamental parameters of galaxy evolution (Graves et al., 2010; Ferreras et al., 2019). The final sample comprises 8 AGN galaxies in total and 10 twin pairs – note that sometimes one SF can be associated to more than one AGN galaxy as twin. Tab. 5.1 shows the twin sample. From left to right each column shows the

galaxy name with their morphological classification, their "status" (AGN/SF), the twin pair identification number for this work, stellar mass, velocity dispersion and their scale, i.e. the mapping from an angular measurement (arcsec) to a physical length (kpc). Finally, the sample is separated into four groups, based on the properties of the evolutionary diagram, discussed below. Note, to treat each group as a unique set, we ensure that each of the SF galaxies only belongs to one group.

For the galaxies used, we display the stamp-like images (Figs. 5.1 and 5.2), obtained from the CALIFA collaboration using SDSS images, of the various twins. Each row corresponds to a twin pairing, where the left-most galaxy is an AGN, while the rest are SF. This shows the SF galaxy to be visually indistinguishable from the AGN galaxies. Furthermore, it displays the similarity in colour and morphology. Finally, for the different groups identified, see Sec. 5.3.1 for details of the group, we have framed the respective twins accordingly, where Group 1, 2, 3 and 4 twins are framed in black, red, blue and green, respectively.

5.2.2 Assessing the effect of aperture

Note for our twin galaxies, we make 3 sets of data, within different aperture radii, in order to explore the effect of AGN activity on its host galaxy. An example of the 3 apertures we have chosen to analyse the stellar populations is shown in Fig. 5.3, quoted in terms of radius, R$\leq 1.5''$ (top), R≤ 2.2 kpc (middle) and R$\leq 1.5\mathrm{R}_{eff}$ (bottom). We have chosen these 3 apertures for two reasons; (i) to determine of stellar population differences between Twin galaxies, which enable us to study the extent of impact of the AGN (i.e. if we find a substantial difference between AGN and SF galaxies in the outer region, this indicates that its effect can be global) (ii) the R≤ 2.2 kpc specifically enables us to compare with the SDSS data set. Finally, the spectra from individual spaxels, with S/N≥ 3 per spaxel, are summed up within each aperture, leading to a high signal to noise ratio, S/N≥ 100 per spaxel. Additionally, the spectra are brought to rest-frame using the velocity maps computed in del Moral-Castro et al. (2020).

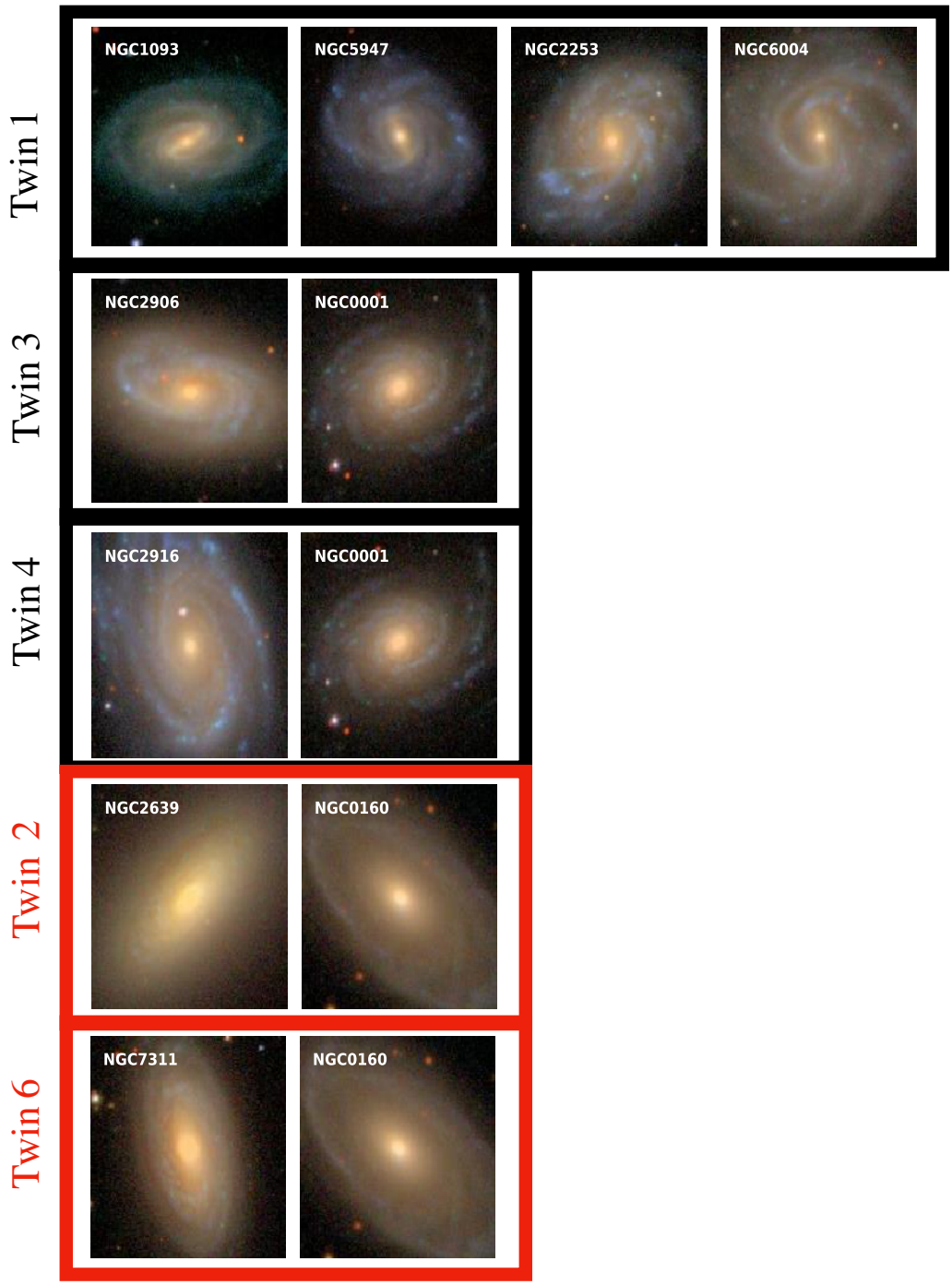

Figure 5.1: Stamp like SDSS images of AGN galaxies (left column) and their SF twin(s). Each of the image has a field of view of $90'' \times 90''$, where North is up and East is left. The different coloured frames separate the twins into their respective groups. For example, the black and red frames indicate Group 1 and Group 2 twins, respectively.

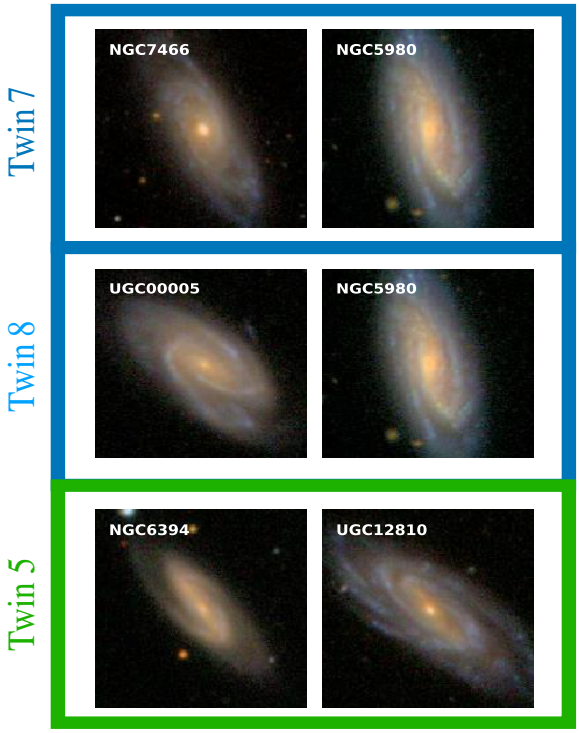

Figure 5.2: Continuation of Fig. 5.1. Here we show the images of the remaining groups, where the blue and green frames indicate groups 3 and 4, respectively.

5.2.3 Nebular emission correction

Before proceeding with the analysis of the stellar populations, we must ensure we can measure the spectral features accurately. By construction, this sample comprises of disc galaxies, i.e. Sa/SBa to Sbc/SBbc, hence these galaxies have strong emission lines. We correct for nebular emission following the methodology outlined in La Barbera et al. (2013), where we fit each of the observed spectra with linear superpositions of simple stellar populations from the Bruzual and Charlot (2003) population synthesis models, using STARLIGHT (Cid Fernandes et al., 2005). Note the use of different synthesis models, such as eMILES or FSPS (Vazdekis et al., 2016; Conroy and Gunn, 2010), are thought to produce very similar results. For each spectrum, the best fit is subtracted from the original one. The difference produces the nebular emission component, where the lines are fitted with a Gaussian function. The fitted lines are then removed from the original spectra. However, as

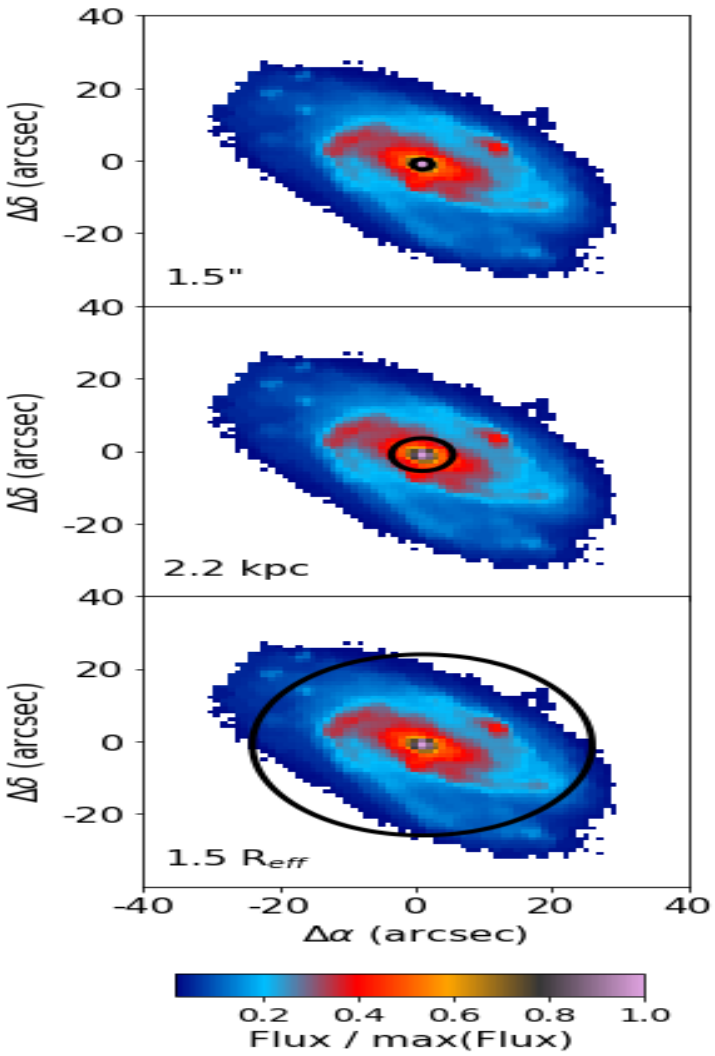

Figure 5.3: The map of stellar flux for one of our galaxies, namely UGC00005, constructed from a CALIFA survey data cube. Each panel shows the different apertures used for this study, where we sum the spectra from invidivual spaxels. *Top, middle* and *bottom:* panels show in black, the most central radial aperture, within R$\leq$1.5$''$, the intermediate radial aperture, which matches the SDSS fibre R$\leq$ 2.2 kpc, and the maximum radial aperture, R$\leq$ 1.5R$_{eff}$, respectively, which encapsulates the whole galaxy,

all the galaxies in the twin sample have strong emission lines, we opt not to measure the Hβ index in the analysis of populations, as the subtraction is expected to carry substantial systematic uncertainties.

5.2.4 SDSS reference sample

This chapter studies the properties of the sample of twin galaxies with respect to their evolutionary stage, using the methodology described in chapter 3 (based on

Angthopo et al., 2019). Here we briefly describe the methodology used to define the evolutionary sequence. We characterize the blue cloud (BC), green valley (GV) and red sequence (RS), with a large sample of galaxy spectra from SDSS (Gunn et al., 2006; Abolfathi et al., 2018). Moreover, the large sample maps the general distribution of galaxies at low redshift, that can be taken as reference to compare the properties of the twin AGN/SF sets. The SDSS data correspond to galaxies with a Petrosian r-band magnitude $14.5 < r_{AB} < 17.7$. The spectral coverage of the SDSS spectrograph spans from 3800-9200Å with resolution $R \equiv \lambda/\Delta\lambda$ of 1500 at 3800Å and 2500 at 9200Å (Smee et al., 2013). In order to remove a substantial bias from the fixed aperture, we restrict the redshift of the sample within $0.05 \lesssim z \lesssim 0.1$. Furthermore, for our measurements to be robust, we only select galaxies with high signal-to-noise ratio in the r band, SNr$\gtrsim 10$, leaving us with $\sim 228,000$ spectra. We make use of the GalSpecExtra catalogue (Brinchmann et al., 2004) to retrieve the stellar mass, BPT classification, and foreground dust. We calculate the $D_n(4000)$ strength using a slight variation of the definition from Balogh et al. (1999), in the same manner as Eq. 3.1 in Chapter 3. Note we also follow the methodology outlined in Chapter 3 for the definition the GV.

5.2.5 Identifying Type 2 AGN in SDSS spectra

In Section 5.3.2, we contrast the CALIFA-based sample of twin systems with the general galaxy population from SDSS. For this study, the AGN galaxies in CALIFA have been selected as type 2, whereas the SDSS sample is only classified, regarding AGN activity, through a simpler classification based on the BPT diagram, that does not distinguish between type 1 and type 2 AGN. We apply an additional selection criterion to those SDSS galaxies classified as having an AGN, to remove all possible type 1 AGN. The motivation for this is derived from recent studies indicating that type 1 and 2 AGN may not be just explained by a difference in orientation (see, e.g., Ramos Almeida et al., 2011; Villarroel and Korn, 2014; Spinoglio and Fernández-Ontiveros, 2021; Gkini et al., 2021), in contrast to the unification model (e.g., Antonucci, 1993).

Previous studies from the literature typically impose a threshold in the width

of the emission lines to discriminate between type 1 and 2 AGN. Here we follow an alternative approach. From the SDSS catalogues, we select the subset of SF (BPT classification = 1) and Seyfert AGN (BPT classification = 4) galaxies. In both sets, we measure the equivalent width of the Hα line from the MPA/JHU catalogue, and define a simple proxy of the relative amplitude of the line with respect to the continuum, as follows:

$$A_{H\alpha} = \frac{\phi_{H\alpha}^{max} - \mathscr{C}_{H\alpha}}{\mathscr{C}_{H\alpha}}, \tag{5.1}$$

where $\phi_{H\alpha}^{max}$ and $\mathscr{C}_{H\alpha}$ denote the flux of emission and continuum at the location of the Hα line ($\lambda = 6564.61$Å in vacuum), respectively. We divide the SF galaxies into different bins according to their EW(Hα) and calculate the mean (μ_{SF}) and standard deviation (σ_{SF}) of the distribution of $A_{H\alpha}$ values. These estimates are used to differentiate between type 1 and 2, so that a Seyfert AGN galaxy is considered type 2 if, for a given EW(Hα) its $A_{H\alpha}$ is located within $2\sigma_{SF}$ below the mean of the distribution of line amplitudes for the SF subset. This criterion results in 1,574 type 1 and 5,499 type 2 AGN galaxies – consistent with previous studies (Villarroel and Korn, 2014). The second motivation for the use of $2\sigma_{SF}$ in the classification is more empirical, where we argue that for a given EW(Hα), if the $A_{H\alpha}$ is too small, it must be due to the width of the line, i.e, corresponding to a type 1 AGN.

Fig. 5.4 illustrates this selection criterion. The blue, red and green data points show the distribution of SF, type 2 and type 1 Seyfert galaxies, respectively. Note, while our method is a crude approximation, visual inspection of the spectra of individual galaxies confirms a low level incidence of broad line AGN galaxies in our type 2 definition. Furthermore, for a more robust test, we plot the stacked spectra of SF (BPT = 1), type 1 and type 2 Seyfert AGN (BPT = 4). Fig. 5.5 shows the stacked spectra of SF, type 1 and 2 AGN for different bins of EW(Hα) in blue, green and red, respectively (following the same colour scheme as Fig. 5.4). For each bin, we make 50 stacks, consisting of 30% of type 1 and 2 AGN galaxies and 5% of SF galaxies; selected at random. We then plot the mean spectrum, where the error bar (filled colour) indicates the minimum and maximum flux in each stack at a given wavelength. The spectra are normalised in the displayed spectral window,

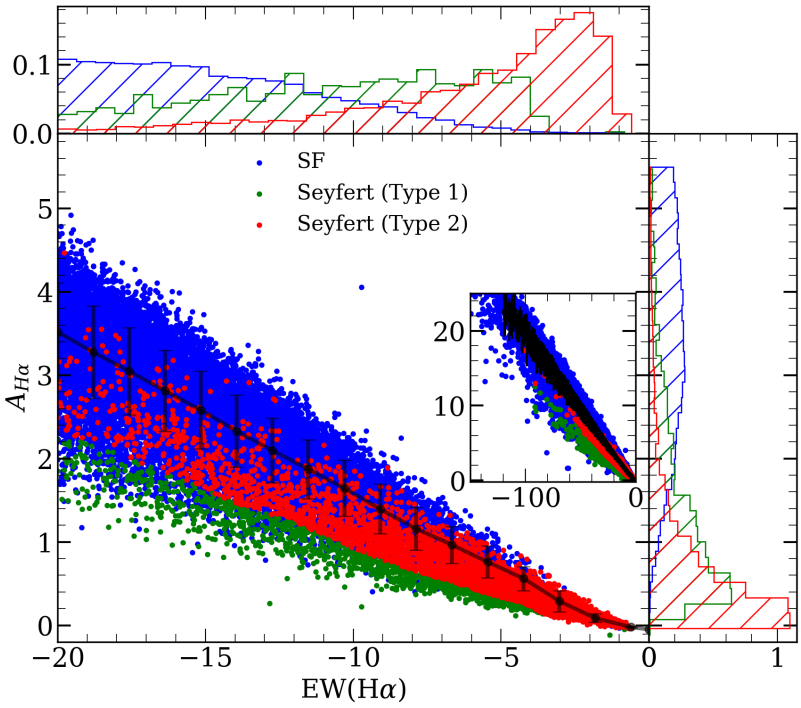

Figure 5.4: Scatter points show the distribution of SF (blue), type 1 AGN (green) and type 2 AGN (red), on the $A_{H\alpha}$ vs EW(Hα) plane. The inset shows the overall distribution of galaxies, whereas the central panel focuses on the region where we find the highest number of type 2 Seyfert galaxies. The black line shows the median $A_{H\alpha}$ of SF galaxies within different EW(Hα) bins, and the error bars map the 1 σ value of the SF galaxy distribution. We use 2 σ to discriminate between type 1 and type 2 AGN (see text for details). Finally, the top (EW(Hα)) and right ($A_{H\alpha}$) panels show the histogram of type 1 and 2 Seyfert AGN and SF galaxies, where the colouring system is the same as that of the scatter points.

dividing it by the minimum flux in each individual stack. The figure illustrates the expected trend, where galaxies classified as type 1 have a clear signature of a broad component. At the lowest EW(Hα), where we have the highest number of galaxies, we find the cleanest separation, where the green line features a wider Hα line compared to both red and blue lines. This is also evident at higher EW(Hα), but there are fewer galaxies with a broad component (type 1) in this case. It is possible that this procedure still suffers from some level of cross contamination. However, due to the wide distribution of SF galaxies, it is most likely that the method falsely flags type 2 AGN as type 1. We argue this false classification will only lower the number of galaxy samples therefore leaving the stellar population properties, in general,

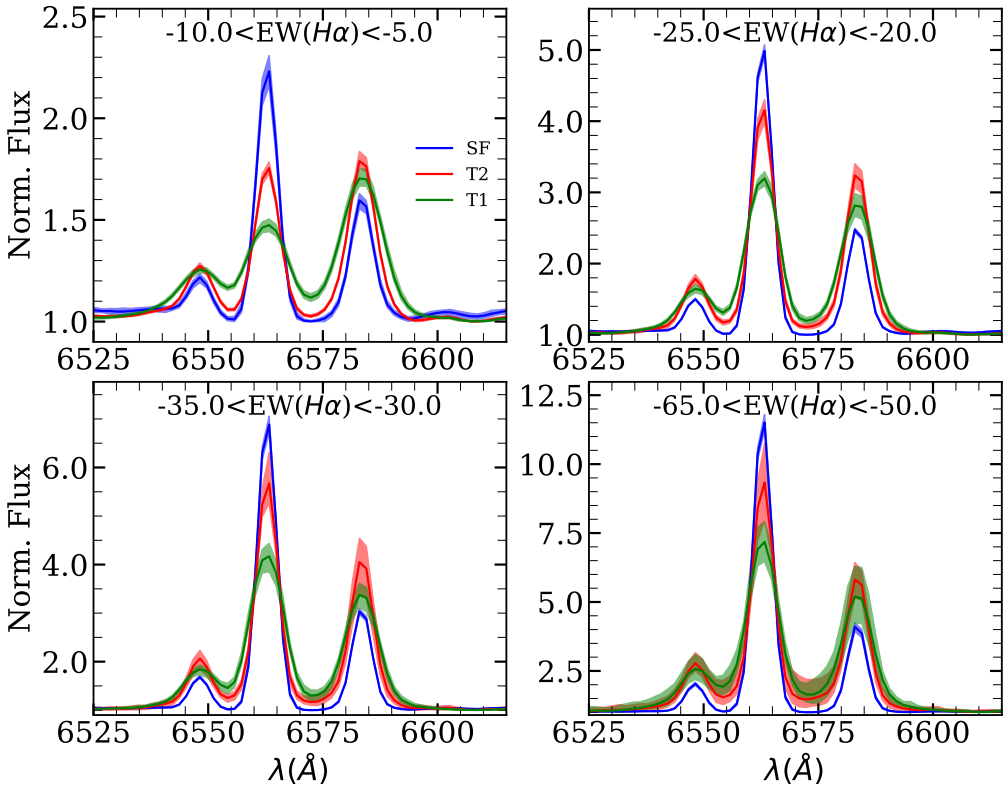

Figure 5.5: We present the stacked spectra of SF (blue) and Seyfert AGN galaxies. For Seyfert AGN, we divide them into type 1 (green, T1) and type 2 (red, T2), based on their EW(Hα) and $A_{H\alpha}$ values. We focus in a strong emission line region, Hα+[NII], where the stacks correspond to 30% (5%) of the total galaxies in the EW(Hα) bins.

unchanged.

5.3 Stellar population differences

In this section, we study various properties of the twin galaxy sample from integrated spectra within three different circular apertures. Additionally, we test the robustness and the statistical significance of the results by comparing them with a larger, general sample from SDSS. The redshift range of the SDSS and CALIFA samples is slightly different, therefore a selection bias could be present in the comparison as: i) the two samples correspond to different cosmic time, and/or ii) we are affected by an aperture bias, as we observe different regions of the galaxies. We argue cosmic time is not a major issue as it does not vary significantly between the

different redshift ranges probed by the samples, $\lesssim 1$ Gyr. Regarding the latter, we assess the effect by producing CALIFA spectra within apertures that are equivalent to the area covered (in physical size) by the $3''$ diameter of the fibers of the original SDSS spectrograph.

5.3.1 Differences in the evolutionary stage of twin galaxies

In order to compare the evolutionary stage of twin galaxies, we adopt the $D_n(4000)$-stellar mass plane in Figure 5.6 – instead of the standard colour-stellar mass diagram (Schawinski et al., 2014; Bremer et al., 2018). Each panel corresponds to a different twin. The blue, green and red filled regions depict the BC, GV and RS respectively; defined by the SDSS data (Chapter 3 and Angthopo et al., 2019). The black filled circles, grey squares and unfilled circles show the result for measurements within three different apertures, namely $1.5''$, 2.2 kpc, and $1.5\,R_{eff}$ (all defined by radius), respectively - Fig. 5.3 illustrates, for a single galaxy, the aforementioned apertures. The first one ($R \leq 1.5''$) concerns the data from the innermost region of the galaxies, thus studying the immediate vicinity where the AGN has the highest impact. It also takes into account the smearing of the point spread function. The $R \leq 2.2$ kpc is justified for a comparison between SDSS data and this sample, by matching the aperture size to the physical extent of the SDSS fibre at the median SDSS redshift ($z \sim 0.077$). Note the median redshift of the CALIFA survey is $z \sim 0.015$. The last choice of aperture ($1.5\,R_{eff}$) is meant to explore most of the galaxy, within the reach of the CALIFA survey. Note the $D_n(4000)$ measurements are carried out on spectra that have been smoothed to a common velocity dispersion, ~ 220 km/s (i.e. approximately the maximum value in the sample). In each twin, the AGN galaxy is shown in black, while the SF counterpart(s) are shown in blue, green or red. The strongest trend in this sample shows that 9 out of 10 twin pairs have an AGN with a greater 4000Å break than their SF counterparts, even amongst twin samples, in both their central regions ($1.5''$), and within 2.2 kpc, indicating the importance of AGN in quenching star formation (Schawinski et al., 2007; Bell, 2008). The case for a 2.2 kpc aperture – defined to match results with SDSS spectra – shows that most AGN galaxies, $\sim 71\%$, reside in the GV. Here we have identified galaxies as

residing in GV, even if they are slightly above BC or below RS; this is owing to us defining GV galaxies to be any galaxy that are not fully inside the RS or BC, due to low number statistics. Note using an alternate way to select GV galaxies, i.e. not overlapping the green region, finds only 3 of these Twin AGN galaxies to be in the GV. However, previous work from the literature based on SDSS, MaNGA and CALIFA data have also noted that a high fraction of AGN, specifically LINER galaxies occupy the GV (Martin et al., 2007; Sánchez et al., 2018; Angthopo et al., 2019; Lacerda et al., 2020). In addition, both AGN and SF galaxies show a decrease in 4000Å break strength radially outward, thus indicating older stellar populations in the centre, suggestive of inside-out quenching (Kelvin et al., 2018). The only exception to this trend is seen in the 3 SF galaxies belonging to twin 1 and twin 5, where the stellar populations within 2.2 kpc have a greater $D_n(4000)$ index than those within $1.5''$. All 4 SF galaxies are barred spiral galaxies, indicating younger stellar populations at the most central region. Note, del Moral-Castro et al. (2019) also found similar results in the pilot study regarding twin galaxies.

Using the aperture of the innermost region, i.e. $1.5''$, the twin(s) are binned into different groups (as labelled in Fig. 5.6), based on their location in the diagram. Group 1 (G1) consists of twins 1, 3 and 4, as their AGN galaxy resides in the RS, whereas their SF galaxies reside in either the BC or GV. Group 2 (G2) consists of twins 2 and 6, since both their AGN and SF galaxies are in the RS. Group 3 (G3) is made up of twins 7 and 8, as both AGN and SF galaxies reside in the GV/BC region. Finally, twin 5 alone is grouped in G4 as this is the only twin with the AGN galaxy in the GV, whereas its SF counterpart is clearly in the BC. The grouping is robust as it does not depend significantly on the adopted aperture. Using the $R \leq 2.2$ kpc spectra to define the groups, we find $\sim$22% of the grouping would change, as twin 4 would be on its own group and twin 5 would join twins 7 and 8. Similarly, using the $1.5\,R_{eff}$ aperture, the grouping structure would remain the same, but twins 5, 7 and 8 would be put together.

From these groups, we aim to test whether variations in stellar properties are caused either by the presence of an AGN, or by the galaxies being at different stages

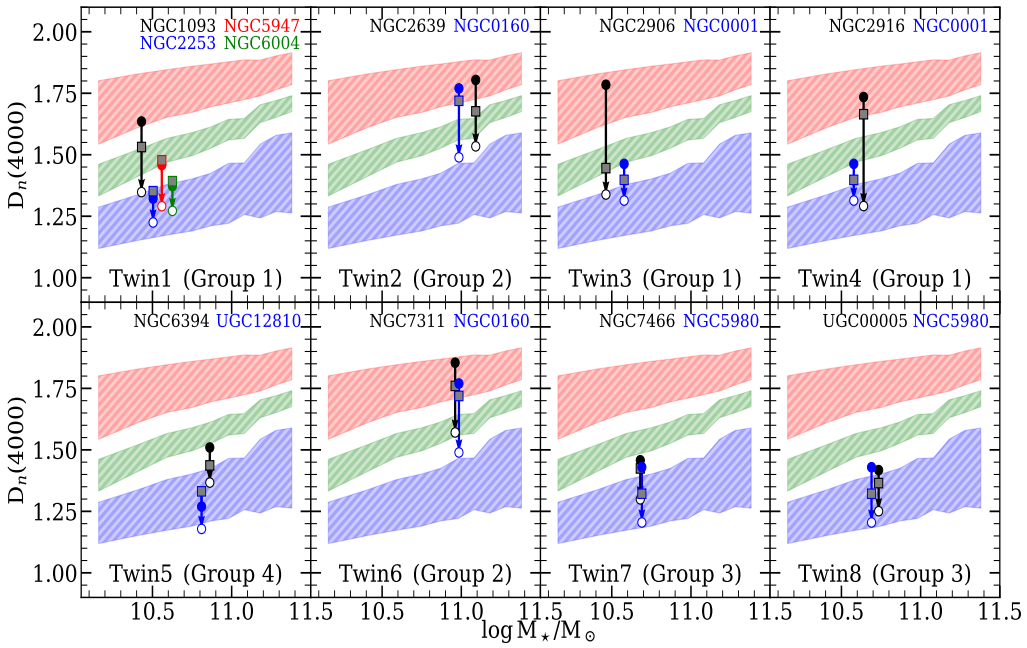

Figure 5.6: We display the location of our twin galaxies on the $D_n(4000)$ vs stellar mass plane. The blue, green and red filled regions respectively map the BC, GV and RS defined in chapter 4. In each panel, we show the twin galaxy pair, where galaxies hosting AGN are represented by black circles, and the coloured circles represent their SF counterparts. Note the $D_n(4000)$ are measured within $1.5''$ aperture (filled circle data points), similar to the PSF of CALIFA. The black gray and the unfilled circle shows the results within 2.2 kpc and $R \leq 1.5R_{eff}$, respectively. The uncertainties of the 4000Å break are calculated using a Monte Carlo realisation method, however it is minuscule, $\Delta D_n(4000) \leq 0.01$, due to the high singal to noise ratio of the spectra.

of evolution. It is evident for G1 that AGN galaxies are more evolved than SF galaxies within $1.5''$. Note that while the $D_n(4000)$ vs stellar mass diagram is a proxy of evolution, as galaxies are expected to transition from the BC to RS via the GV, the actual path could be complicated by rejuventaion events (Thomas et al., 2010). We argue that rejuvenation should not play an important role in our sample as (i) these galaxies are selected to be isolated, therefore it is unlikely they have undergone a major merging event. However recent minor mergers cannot be ruled out and (ii) state-of-the-art simulations, IllustrisTNG, have noted that rejuvenation events are more prominent at high stellar mass $\gtrsim 10^{11} M_{\odot}$ (Nelson et al., 2018), thus above the mass range probed by this sample.

5.3.2 Contrasting with the general galaxy population (SDSS)

Fig. 5.6 therefore suggests that AGN galaxies tend to be more evolved compared to their twin SF counterparts. In addition, previous works have noted AGN galaxies to be generally older than their SF counterpart, as AGNs mostly occupy GV, whereas most of SF galaxies are located in the BC (Sánchez et al., 2018; Lacerda et al., 2020). However, our result is more focused, as it targets sets of carefully defined pairs with very similar overall properties except for the presence of an AGN. Owing to the small sample size, we address now the statistical significance of our results, by comparing the sample with a large, general distribution of galaxies from the SDSS.

5.3.2.1 Line strengths

The differences found in Fig. 5.6 are still open to a potential sample selection effect. We need to assess whether the population properties of the twin galaxies is comparable with the general sample, i.e. are these galaxies a fair representation of their counterparts in SDSS, or are they statistical outliers? We compare key line strengths, $D_n(4000)$, $H\delta_A$ and [MgFe]$'$ within the 2.2 kpc aperture with respect to the distribution of galaxies in SDSS. We select spiral galaxies from SDSS, making use of the Galaxy Zoo catalogue (Lintott et al., 2008), choosing the spiral flag set to 1. Additionally, we do not smooth the spectra of the twin galaxies to $\sigma \sim 220$ km/s, unlike in previous and future sections, as the SDSS spectra are not smoothed either. Note, the smoothing has a small effect on the line strength, where we find the largest differences for [MgFe]$'$, with a maximum offset of $\sim$0.26 dex. Fig. 5.7 shows the distribution of 4000Å break strength for each twin – where the SDSS sample is restricted to the same stellar mass, within $\Delta \log M_\star/M_\odot = \pm 0.2$ dex of the AGN twin stellar mass. The vertical dashed lines locate the $D_n(4000)$ index for the twin galaxies: black for the AGN, coloured lines for SF systems. The solid blue and grey histograms show the distribution of SDSS galaxies classified as SF and type 2 Seyfert, respectively.

In G1, both twins 1 and 3 show the AGN galaxies close to the peak of the type 2 AGN distribution. In contrast, the AGN galaxy of twin 4 is offset with respect to the

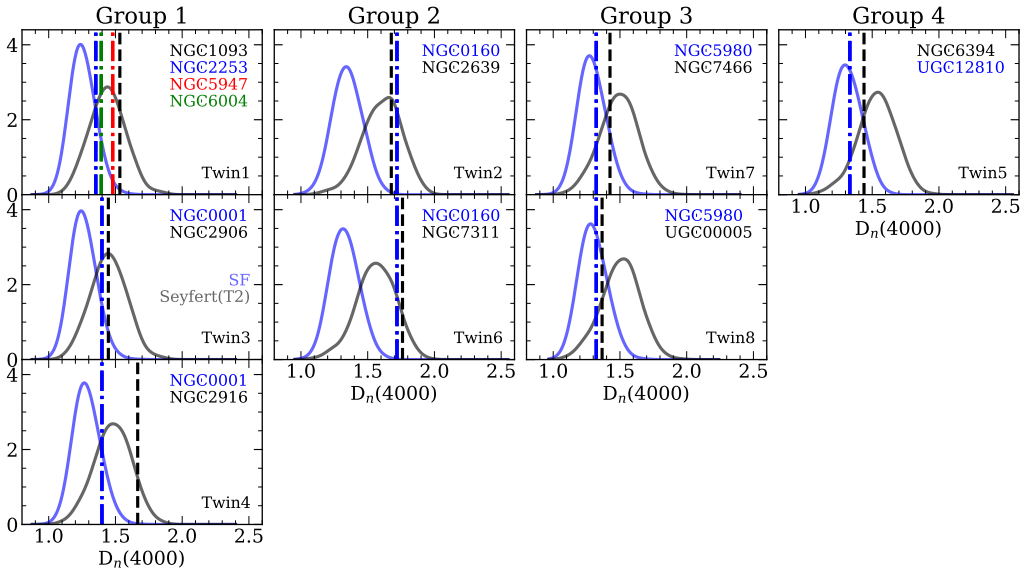

Figure 5.7: The general distribution of $D_n(4000)$ index for SF (blue kernel density estimation, KDE, histogram) and type 2 Seyfert AGN (gray KDE histograms) galaxies in SDSS. Note, the SDSS galaxies are selected to be within a range of stellar mass, that is compatible with the AGN galaxy of each twin. The black vertical lines in each panel indicate the 4000Å break for AGN, while the dashed-dotted lines, in diverse colours, show the line strength location of SF twins. Note, these line strengths are measured within 2.2 kpc aperture and their spectra have not been smoothed to a common velocity dispersion, unlike in previous sections. See text for details.

peak of the Seyfert distribution, by $\gtrsim 1\sigma$. SF galaxies in all 3 twins belonging to group 1 are more representative of the general sample, and are located towards the peak of the SDSS SF galaxy distribution. Note, while the corresponding histogram for the complete sample is not shown (to avoid overcrowding), it also peaks at the same location as the "SF" sample, indicating a high absolute number of SF galaxies within the chosen stellar mass. SF galaxies in G2 are located near the tail end of the SDSS SF galaxy distribution, whereas the AGN are neighbouring the peak of SDSS type 2 Seyfert distribution. Thus, while possible, such twin pairings are unlikely if extracted randomly from a larger, general sample. G3 and G4 show similar trends, to that of G1, where the 4000Å break of the AGN is located close to the peak of the distribution of Seyferts. For each twin, the SF galaxies tend to have their 4000Å break close to the peak of the SDSS SF distribution. Therefore, if we were to extend the sample to a larger survey, we would find that twins 1, 3, 4, 5, 7 and 8 are

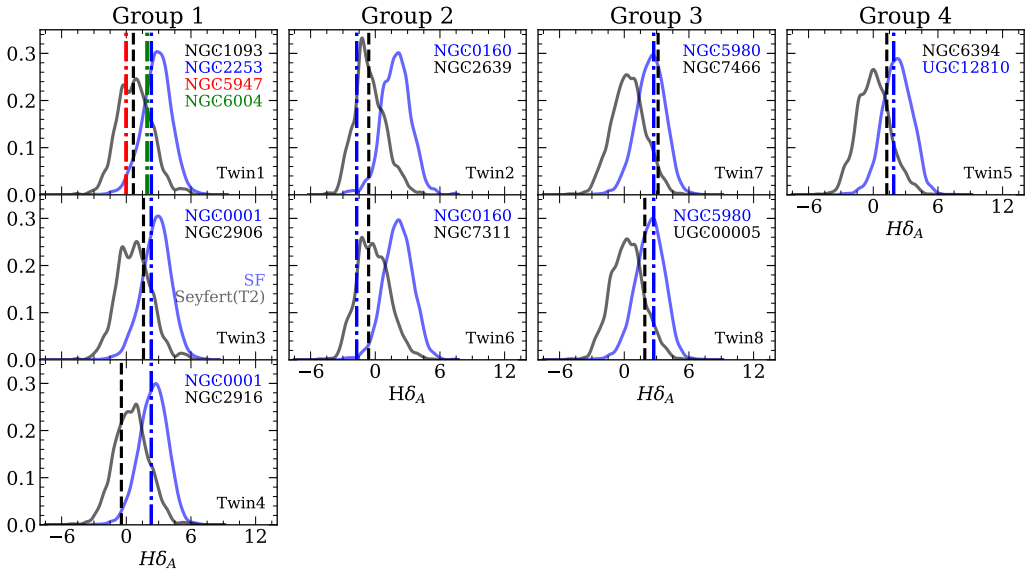

Figure 5.8: Same as Fig. 5.7 for the distribution of Hδ_A line strengths.

representative samples of the general population. Note, here we have assumed that twins at the peak of their respective distribution are more representative of twins on a larger sample, due to high number statistics. However, it is likely that for SF galaxies to be considered twins of AGN, such as for twins 2 and 6, they have to be away from the peak of their respective distribution, hence we require a larger twin sample to draw a strong conclusion.

Fig. 5.8 and Fig. 5.9 show the Hδ_A and [MgFe]$'$ distribution for AGN and SF galaxies, with the colour-coded vertical lines once more representing the individual measurements of galaxies in the twin samples. The SDSS distributions follow the same labelling system as Fig. 5.7. All twins in G1 have Hδ_A for AGN and SF galaxies compatible with respect to the SDSS distribution, with the exception of NGC5947 in twin 1. Similarly to $D_n(4000)$, the Hδ_A strength of SF galaxies in G2 are at the tail end of the distribution, while AGN galaxies are located closer to the peak of type 2 Seyfert AGN. G3 and G4 suggest a high likelihood of finding both AGN and SF galaxies with the observed Hδ_A, with the exception of twin 7 where the AGN is located $\gtrsim 1\sigma$ away from the peak of the distribution. For G1, G3 and G4, the [MgFe]$'$ index in both AGN and SF galaxies resembles that of the larger SDSS sample, once more with the exception of NGC5947. In comparison,

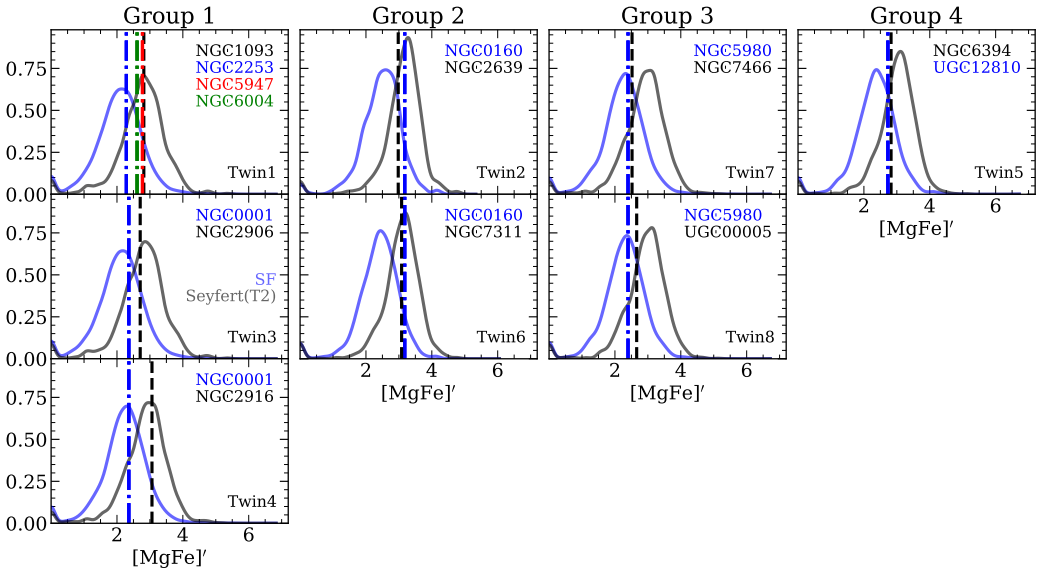

Figure 5.9: Same as Fig. 5.7 for the distribution of [MgFe]′ line strengths.

G2 shows the twin SF galaxy to deviate away from the peak location by $\gtrsim 1\sigma$, whereas the AGN galaxies appear closer to the peak of the distribution in type 2 Seyfert systems. The inclusion of Hδ_A and [MgFe]′ shows, given their position in the evolutionary sequence, how alike the twin galaxies are to a larger parent sample.

5.3.2.2 Testing the significance of the relative differences

We focus here on one key question: how significant is the difference found in the D$_n$(4000) vs stellar mass plane between the twin pairs, with respect to a random pairing of galaxies with similar mass? Additionally, are the differences between the twin pairings significant too, regarding Hδ_A and [MgFe]′. To answer such questions, we look at the relative difference in several spectral indices between the twin samples, measured within a 2.2 kpc aperture, and compare it with random pairings of galaxies with similar stellar mass (within $\Delta \log M_\star/M_\odot = \pm 0.2$ dex) from SDSS. We define the relative difference as follows:

$$\delta(\Psi) \equiv \frac{\Psi_1 - \Psi_2}{\Psi_1}, \tag{5.2}$$

where Ψ_1 and Ψ_2 are the line strengths of the galaxies in each pair. Note we use this definition for 4000Å break strength and [MgFe]′. However, this parameter can

vary largely when Ψ includes 'zero' as a possible measurement, i.e, the range of $H\delta_A$. Thus, we make an amendment to the relative difference defined as

$$\delta_r^v(\Psi) = \frac{\Psi_i - \Psi_j}{1 + |\Psi_j|}, \tag{5.3}$$

where Ψ, is $H\delta_A$ specifically, which varies from -6.0 to $+6.0$, with many galaxies having $H\delta_A$ close to 0, hence the inclusion of $1.0 + |\Psi_j|$ in the denominator, rather than simply Ψ_j, stops the $\delta_r^v(\Psi)$ from diverging greatly from 0.

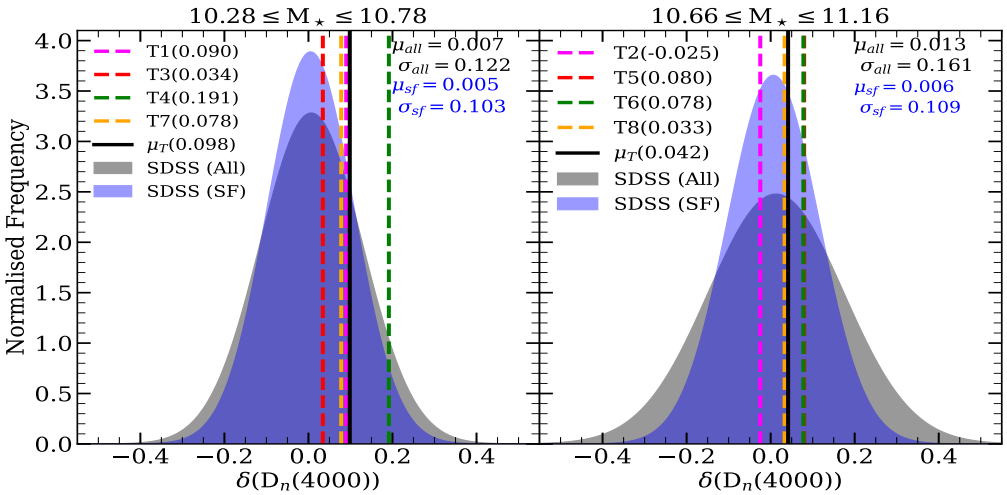

Figure 5.10: The blue (gray) shows the distribution of relative difference of the $D_n(4000)$ index between pairs of SF (SF and type 2 Seyfert AGN) galaxies from SDSS (assuming a Gaussian distribution). The vertical dashed lines show the relative difference between our twin samples, as labelled, and the black vertical line indicates the average relative difference of all twins in their respective panel. The panels are split according to their stellar mass, where left and right panels represents galaxies between $10.28 \lesssim \log M_\star/M_\odot \lesssim 10.78$ and $10.66 \lesssim \log M_\star/M_\odot \lesssim 11.16$, respectively.

Fig. 5.10 shows as vertical lines the observed relative difference in the twin sample, where the blue, red, green and orange lines show differences for individual twins, as labelled, while the black vertical line shows the average of the four twins. Note twin 1 has multiple pairs comprising of 1 AGN and 3 SF galaxies, therefore we show the average of the three pairs. The SDSS data are represented as a Gaussian distribution (i.e. taking the mean and standard deviation of the SDSS sample to produce a Gaussian equivalent). The blue distribution shows the result when selecting

random pairs from the subset of only SF galaxies, in SDSS and the grey distribution corresponds to random pairings that include SF and type 2 Seyfert AGN galaxies. Note these pairings can be SF-SF, SF-AGN or AGN-AGN. The figure is split according to stellar mass, where the left panel shows differences for SDSS galaxies within $10.28 \lesssim \log \mathrm{M}_\star/M_\odot \lesssim 10.78$ and the right panel shows differences within $10.66 \lesssim \log \mathrm{M}_\star/M_\odot \lesssim 11.16$. We find all twins (except twin 4) to have relative differences within 1σ (2σ) of the SDSS distribution for both SF and AGN galaxies. Note, while the variation seems to be statistically small, the relative difference is generally positive, suggesting the results found in Fig. 5.10 represent physical differences in the evolutionary stage of twin galaxies, so that galaxies hosting an AGN have stronger 4000Å break strengths than their SF counterparts - even when considering "twin" galaxies.

Fig. 5.11 shows the amended relative difference in $\mathrm{H}\delta_A$ (top panel) and the relative difference in $[\mathrm{MgFe}]'$ (bottom panel). The labelling and colour coding follows the same system presented in Fig. 5.10. Both figures further support the claim presented before, where we find the relative difference between twins to be statistically small, within 1σ, but of physical significance. For example, we find $\delta_r^{\nu}(\mathrm{H}\delta_A)$ values are consistently less than 0. Moreover, we find the same physical significance for metallicity sensitive index, as $\delta_r([\mathrm{MgFe}]') \gtrsim 0$. Both of these results suggest that, while at a small statistical significance, AGN are likely to be older and more metal rich; at least within 2.2 kpc. In the general sample, such trends are expected, even within similar stellar mass regime, however, we emphasize here that we are visually-selecting "twin" pairs, where SF closely resembles the overall properties of that of AGN galaxies. Finally, the analysis of average relative difference between the low mass regime, $10.28 \lesssim M_\star \lesssim 10.78\,\mathrm{M}_\odot$, and the high mass regime, $10.66 \lesssim M_\star \lesssim 11.16\,\mathrm{M}_\odot$, consistently finds lower mass twins to have greater difference, irrespective of the spectral indices.

5.3.3 Inner vs Outer regions

We consider now the difference in line strength between the smallest aperture, $1.5''$, and the largest one, extending to $1.5\,\mathrm{R}_{eff}$, by comparing the age-sensitive indices,

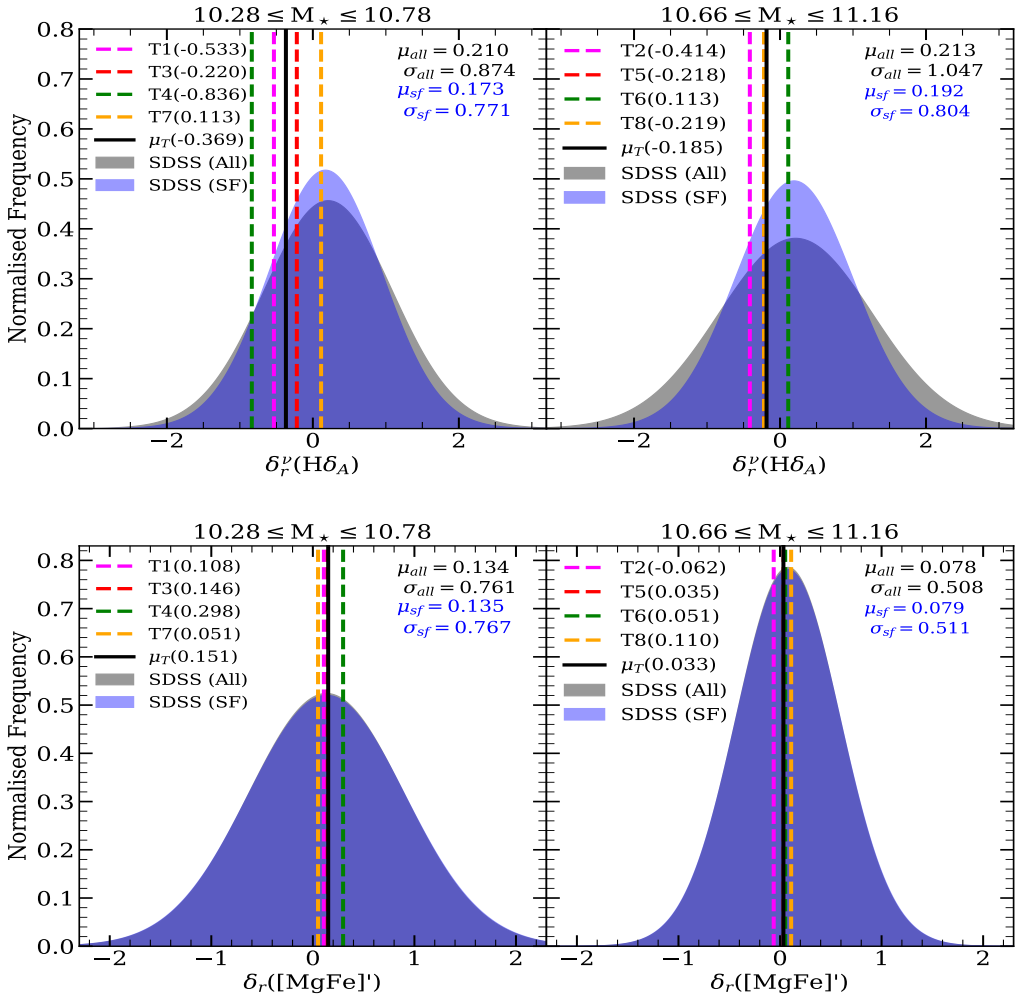

Figure 5.11: Same as Fig. 5.10 but for Hδ_A (top) and [MgFe]$'$ (bottom).

$D_n(4000)$ and Hδ_A, as well as the metallicity-sensitive index, [MgFe]$'$. We define the absolute difference between line strengths with respect to aperture as:

$$\Delta\Psi = \Psi(R \leq 1.5'') - \Psi(R \leq 1.5R_{eff}), \tag{5.4}$$

where Ψ represents the different indices – either $D_n(4000)$, Hδ_A or [MgFe]$'$.

5.3.3.1 Age Sensitive Indices

Fig. 5.12 shows $\Delta D_n(4000)$ vs ΔHδ_A for galaxies split in panels with respect to the four groups. The different colours denote different twins, as labelled. AGN galaxies are indicated by a circular data point, whereas SF galaxies are shown by a cross.

G1 galaxies – i.e. twins 1, 3 and 4 in the top-left panel, show a clean trend where galaxies hosting the AGN have a greater difference between the central and outer regions in both indices. AGN galaxies have a difference of $\Delta D_n(4000) \gtrsim 0.2$ and $\Delta H\delta_A \lesssim -2.6$. Both AGN and SF galaxies feature an older central part compared to the outer regions, favouring the idea of inside-out quenching (e.g. Spindler et al., 2018; Kelvin et al., 2018). In G2, twins 3 and 4, the $1.5\,R_{eff}$ aperture spectra show similar 4000Å break, regardless of galaxy type (see Fig. 5.6). In contrast, the SF systems have a consistently lower difference between central and outer apertures $\Delta D_n(4000) \lesssim 0.2$ and $\Delta H\delta_A \gtrsim -2.6$, indicating that the presence of an AGN preferentially quenches the central region. The G4 twins (bottom-right panel) show a similar trend, where the radial difference in 4000Å break strength is greater in the AGN system, although the difference here is more subtle. Note that G4 is defined by a twin where the AGN is in the "lower" part of the GV and the SF is in the BC. This figure shows that, in addition, the radial trends are shallower, and less distinguishable between AGN and SF galaxies.

G2 galaxies show substantial gradients, once more suggesting older populations in the central regions. However, there is no clear difference between AGN and SF members, a result that could be expected from the fact that G2 twins *both* have the central spectra in the RS, and the $1.5\,R_{eff}$ spectra in the upper portion of the BC. We can thus assume that the SF galaxy, while being classified as SF, is a system closer to the end of its star formation cycle. This is further supported by their earlier disc morphological classification (Sa). In a general context, group G2 is an anomaly in our sample, considering their SF galaxies are far from the peak of the general SF distribution in SDSS. In G3 both AGN and SF galaxies reside in the lower part of the GV. Here, a substantial difference is found in the radial gradient of 4000Å break strength, with larger variations in the SF systems with respect to the AGN, whereas $H\delta_A$ has similar variations within this group.

5.3.3.2 Metallicity Sensitive Indices

Fig. 5.13 shows the equivalent of Fig. 5.12, replacing $H\delta_A$ with the metallicity-sensitive index [MgFe]′, following the same labelling and colour coding. Once

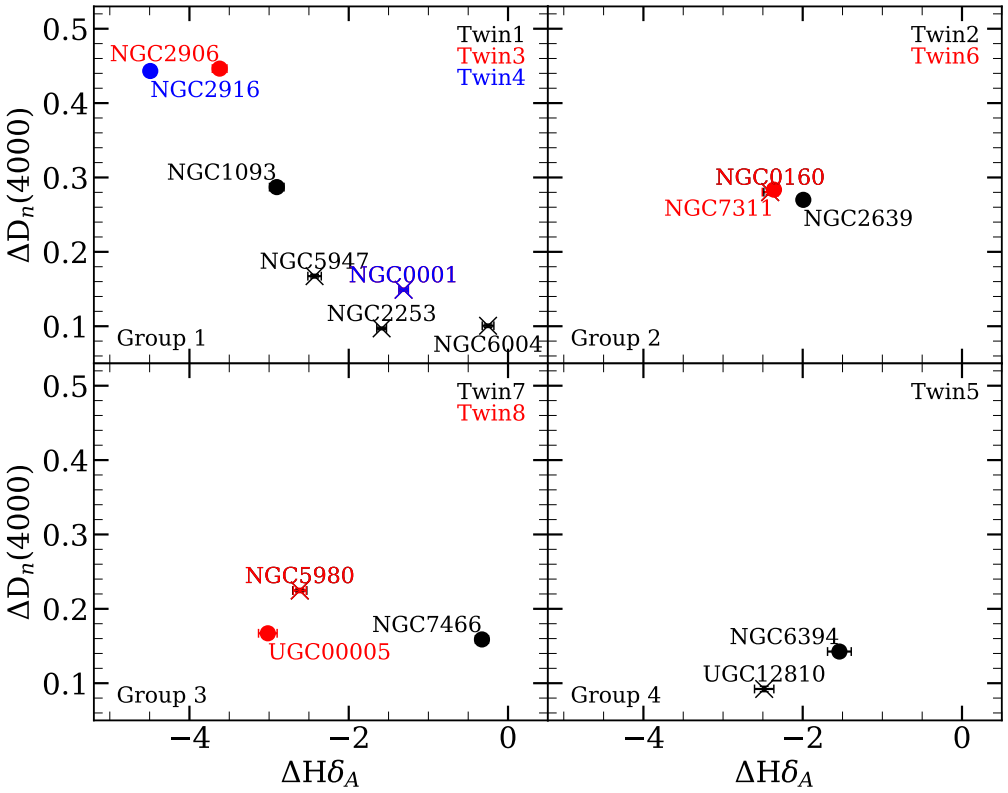

Figure 5.12: Difference in age-sensitive line strengths, $D_n(4000)$ and $H\delta_A$, between the central region (1.5″) and the largest aperture ($1.5\,R_{eff}$). In each panel, the circular and cross symbols show results for AGN and SF galaxies, respectively. We split the panels into four sets, depending on their group number (stated at the bottom left corner). Each colour identifies a different twin, as labelled within individual panels. Note we repeat some SF galaxies (NGC0160, NGC0001 and NGC5980), causing some overlapping of data points, as some twins have the same SF galaxy. However, their error bars might vary slightly between panels, as the uncertainties are calculated from a set of Monte Carlo realisations; i.e. same SF galaxy within different twin sets will have different errorbars but statistically similar.

more, G1 galaxies show the clearest trend, where AGN systems have a greater difference in $[MgFe]'$ ($\Delta[MgFe]' \gtrsim 0.6$), with respect to their SF twin counterpart ($\Delta[MgFe]' \lesssim 0.5$). This trend suggests a more metal rich population in the central regions regardless of galaxy type, as $\Delta[MgFe]' \gtrsim 0$, however, the AGN consistently have higher gradients. G3 and G4 galaxies show no clear difference between AGN and SF galaxies, given the error bars, but they consistently feature negative radial gradients in metallicity ($\Delta[MgFe]' \gtrsim 0.25$). A slightly more significant trend is

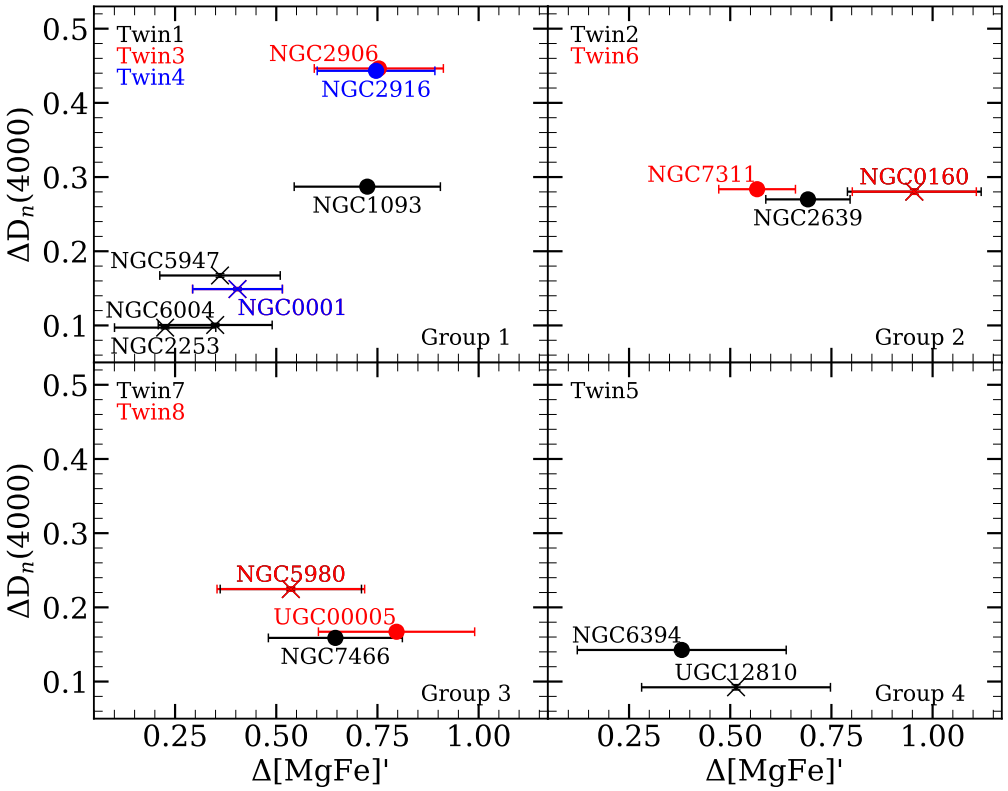

Figure 5.13: Same as Fig. 5.12, showing a line strength diagram comprising $D_n(4000)$, age sensitive index vs [MgFe]′, metallicity sensitive index.

shown in G2, where in both twins, SF galaxies have a greater difference between apertures, Δ[MgFe]′ $\gtrsim$0.8, compared to their AGN counterpart Δ[MgFe]′ $\lesssim$ 0.8. Note, there are large uncertainties associated to the data points.

These results suggest an alternative view of the radial extent of AGN feedback. If we were to believe low-to-intermediate AGN activity only affects the formation history within a relatively small region around the centre, we should consistently find greater differences in the AGN galaxy of each twin. The data are not conclusive, and reveals mixed distributions. Furthermore, del Moral-Castro et al. (in prep.) will investigate these results further using spectral fitting. The implications of this are discussed in Sec. 5.4.

5.3.4 SSP Parameters

In this section, the SSP equivalent ages and metallicites are estimated for the twin galaxies within the 3 different apertures. We make use of the MIUSCAT population

synthesis models (Vazdekis et al., 2012), constructing a grid consisting of 8192 synthetic spectra, 128 ages varying from 0.1 to 13.5 Gyr in a logarithmic scale. Similarly, the metallicity varies from [Z/H]=-2.0 to +0.2 also in log steps. The best fit to the SSPs adopts a χ^2 statistic defined as follows:

$$\chi^2(t,Z) = \Sigma_i \left[\frac{\Delta_i(t,Z)}{\sigma_i}\right]^2, \tag{5.5}$$

where $\Delta_i(t,Z) = O_i - M_i(t,Z) - \delta_i$ is the difference between the observed and model index with an offset (δ_i) for the ith index. This offset is introduced due to the high S/N in our observed spectra, at a level where the SSP models are not capable of fully reproducing all the details, such as the α/Fe abundance ratio. As we are interested more in the relative difference between AGN and their twin SF galaxies, this offset brings the model line strength values more in line with the observed results. The uncertainties $\sigma_i = \sqrt{\sigma_{i,err}^2 + (0.05O_i)^2}$, encapsulate both the statistical error in the index along with an extra term amounting to 5% of the index value. This way we account for both the systematics associated with our methodology and include a conservative uncertainty in our calculations. The χ^2 statistic involves a set of seven different spectral indices: $D_n(4000)$, $H\delta_A$ and $H\gamma_A$ (age sensitive indices), and Mgb, Fe5270, Fe5335 and [MgFe]$'$ (metallicity sensitive indices). The likelihood corresponding to the SSP-equivalent estimates of age and metallicity are obtained by marginalising over the unwanted parameter. While some indices are described as "age-sensitive" and others are "metallicity-sensitive", all of the indices suffer from the age-metallicity degeneracy (Worthey, 1994).

5.3.4.1 Age parameters

Figs. 5.14, 5.15 and 5.16 shows the SSP equivalent age for the central 1.5″, 2.2 kpc and 1.5 R_{eff} apertures, respectively. The black data points show the ages of the AGN galaxy in each twin, while the other colours represent the ages of SF galaxies. Circle, square, pentagon and triangle symbols denote G1, G2, G3 and G4, respectively. We find 80%, 40% and 60% of the AGN galaxies in the twin being equal or older than their SF counterpart for G1 galaxies inside of the 1.5″, 2.2 kpc and

1.5 R_{eff} apertures, respectively. In G2, AGN galaxies have equal or younger average ages compared to their SF counterpart 83% of the time, even though in the evolutionary sequence, within a 1.5″ aperture, we find these AGN to have a stronger 4000Å break. G3 twins show no clear trend in the inner regions (1.5″ and 2.2 kpc) but show older populations in AGN with respect to SF galaxies, for both twins, in the 1.5 R_{eff} aperture. G4 follows the opposite trend, where the AGN galaxy is older within both 1.5″ and 2.2 kpc apertures, but is younger, than the SF galaxy, when considering the largest aperture.

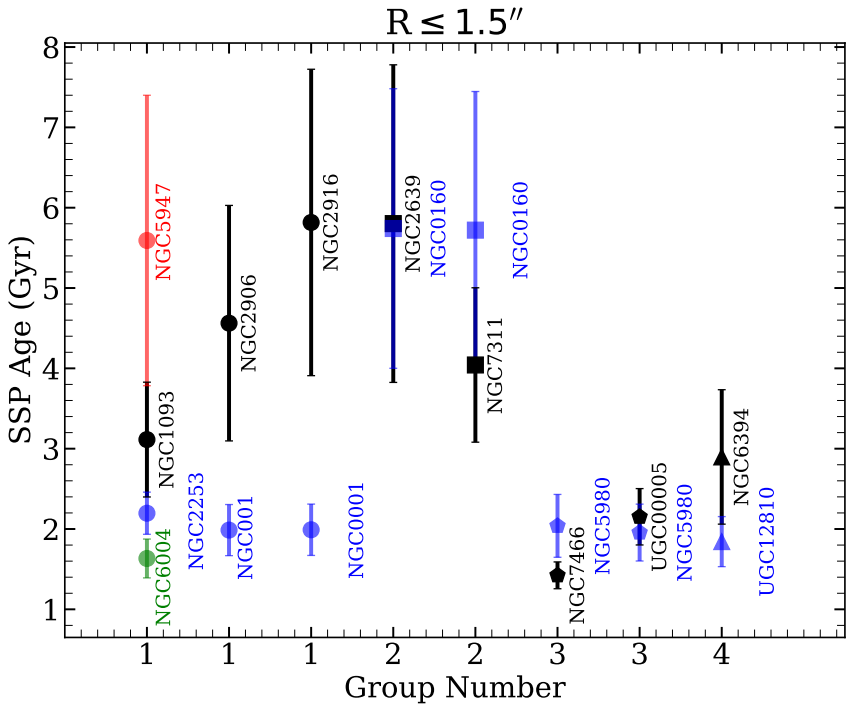

Figure 5.14: SSP equivalent average ages for the most central region (within 1.5″), for twin galaxies in all 4 groups. Note, circular, square, pentagon and triangle symbols identify G1, G2, G3 and G4 respectively. From left to right we show the ages for twins 1, 3, 4, 2, 6, 7, 8 and 5. In each instance, the black and colour data points show results for AGN and SF galaxies, respectively. For the errorbars, we make 100 Monte Carlo realisations of each spectra and calculate the χ^2 best fit, which is then used to calculate the normalised likelihood value. From this we obtain 1σ confidence level, shown by the errorbars on each data point.

If we consider all the twins in the different groups, in all apertures, we find that 50% of twins show equal or older populations in the AGN galaxies (70% in 1.5″, 30% within 2.2 kpc and 50% for the largest aperture). This indicates that the AGN

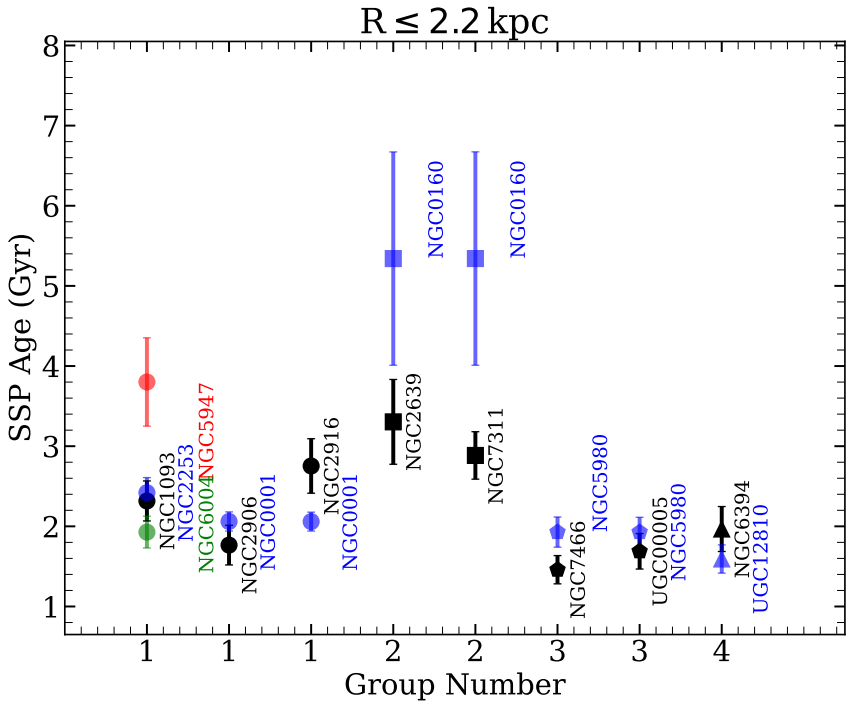

Figure 5.15: Same as Fig. 5.15 but within R≤2.2 kpc, to match the SDSS aperture.

exerts the most impact within the most central region of the galaxy.

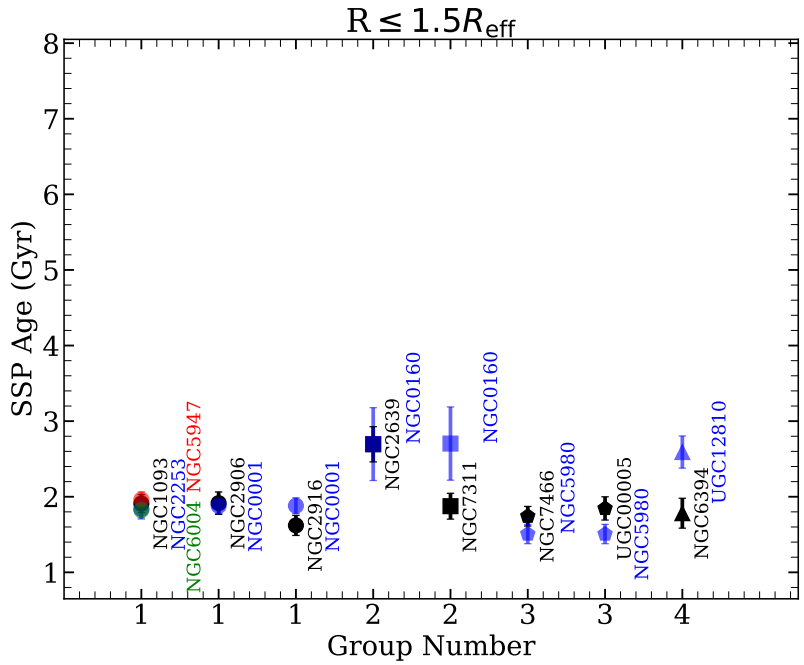

Figure 5.16: Same as Fig. 5.16 but within R≤1.5 R_{eff}.

5.3.4.2 Metallicity parameters

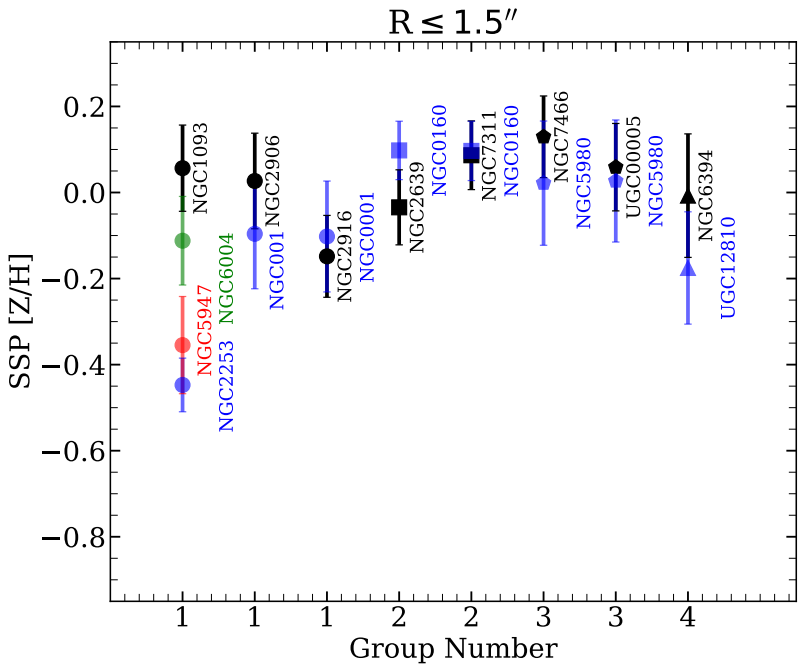

Figure 5.17: Same as Fig. 5.14 for the SSP equivalent metallicity of the twin pairs, within 1.5″, following an identical notation.

Figs. 5.17, 5.18 and 5.19 shows the SSP-equivalent metallicities, within the central 1.5″, 2.2 kpc, and 1.5 R_{eff} apertures, respectively. The symbols and colours are equivalent to those shown in Fig. 5.14. Similarly to the age estimates, within 1.5″, G1 galaxies have AGN that are more metal rich than the SF galaxies 80% of the time. G2 and G3 show no clear trend. Finally G4, also shows AGN galaxies to be more metal rich. In the 2.2 kpc aperture G1 and G3 host AGN galaxies that are equal or more metal rich than their SF counterpart 100% of the time. G4 shows the SF galaxy to be more metal rich, however the differences are within 1σ. For the more metal rich AGN galaxies, we sometimes find them to be younger than their SF counterpart, perhaps a sign of the age-metallicity degeneracy. However in section 5.5, we show the bivariate confidence levels in age and metallicity for 2 twins, rejecting a substantial bias from this degeneracy, specifically for twins where we find the AGN galaxy to be more metal rich. Therefore, at least within a 2.2 kpc aperture, the metallicity trend indicates that the presence of an AGN is potentially

related to a different star formation history, with respect to the SF counterpart. This is further backed up by the spectra in the largest aperture, 1.5 R_{eff} trends, where we find that the AGN galaxies in G1 and G4 are more metal rich compared to their SF counterpart. Note, while we find strong evidence showing AGN galaxies are likely to be more metal rich, some twins show large overlap between AGN and SF twins.

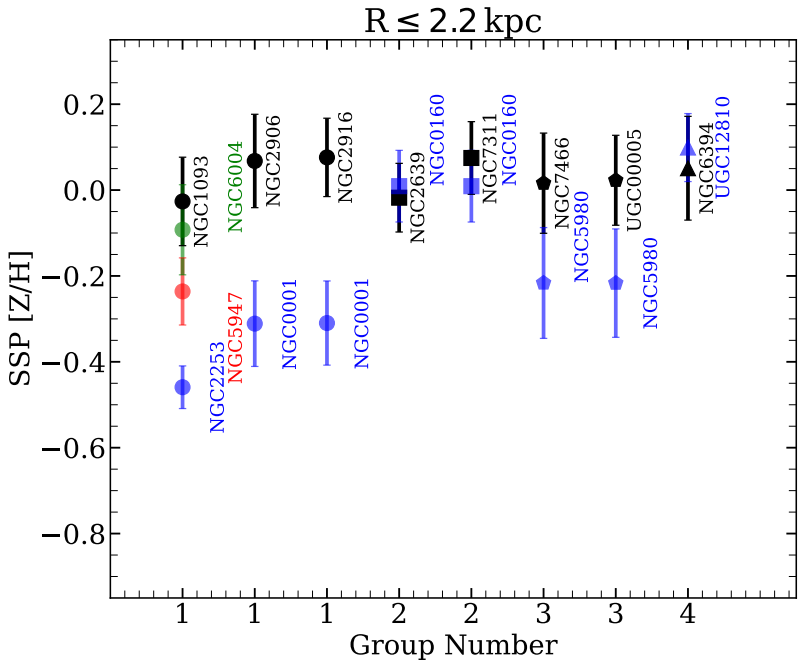

Figure 5.18: Equivalent figure to Fig. 5.15, with the same colour coding and labelling system, but for the SSP equivalent metallicity of the twin pairs, within R≤2.2 kpc, to match the SDSS aperture.

Furthermore, rather than looking at an individual group within a fixed aperture, if we look at all the different groups and in all apertures, we find AGN galaxies to be more metal rich 73% of the time compared to their SF counterparts. Breaking this into different apertures, we find 70%, 80% and 70% of AGN galaxies to be more metal rich in the 1.5″, 2.2 kpc, and 1.5 R_{eff}, respectively. Note, some of these galaxies have values, which are compatible within 1σ.

5.4 Discussion

This chapter explores the transitional role of AGN activity by analysing pairs of galaxies defined as twins, inasmuch as they feature similar large galaxy-scale prop-

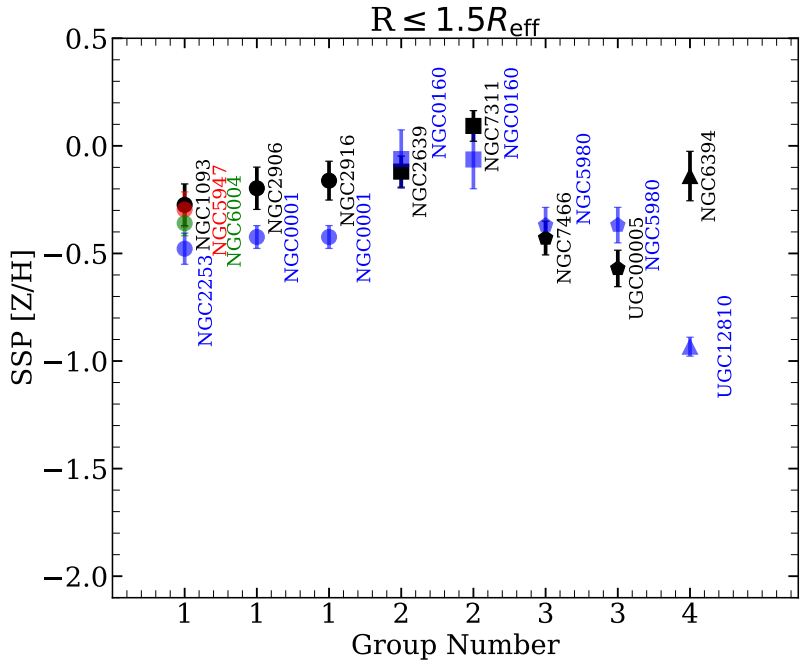

Figure 5.19: Same as Fig. 5.16 for the SSP equivalent metallicity of the twin pairs, within R≤1.5 R_{eff}, following an identical notation.

erties but one presents AGN activity and the other one does not. The definition of these twin pairs follows the methodology laid out in del Moral-Castro et al. (2020). In this section we discuss the potential implications of our results, from the radial influence of AGN activity on the galaxy, to testing two alternative hypotheses, either an "on-off" AGN switching mode, or the possibility of the twins having different evolutionary paths. Owing to the small sample size (10 twins comprising 8 AGN and 7 SF galaxies, noting that some AGN galaxies have multiple SF pairs), we mostly find mixed trends in the behaviour of the individual twins. A key reason for such difference could be due to their differing location on the evolutionary sequence, as galaxies on the BC have different stellar populations with respect to those on the GV or RS. Nevertheless, a statistical comparison of the CALIFA spectra measured within 2.2 kpc with respect to a more general sample from SDSS suggests that many of these twins – twin pair 1, 3, 4, 5, 7 and 8 – are representative of the larger sample, taken from SDSS (see Figs. 5.7, 5.8, and 5.9), thus providing strong motivation for similar studies in larger data sets.

5.5 Age-Metallicity Degeneracy

The line strengths are all prone to the age-metallicity degeneracy (Worthey, 1994), therefore affecting the estimation of our SSP equivalent ages and metallicities. This degeneracy implies that the effect of an old stellar population can be mimicked by a higher metallicity, producing very similar colours or even line strengths (Ferreras et al., 1999). To break such degeneracy, we make use of a battery of line strengths with different sensitivity to age and chemical composition. Our set of indices comprises: $D_n(4000)$, $H\delta_A$, $H\gamma_A$, Mgb, Fe5270, Fe5335 and [MgFe]$'$. The spectra have a high S/N, which helps to break such degeneracy. Fig. 5.20 shows a bivariate plot with the confidence levels for the SSP-equivalent age and metallicity of twins 5 and 8. The contours are shown – from the inside out – at the 1, 2, and 3 σ level. The solid red (dashed blue) contours correspond to the twin with (without) an AGN. A large overlap between these contours would mean a substantial age-metallicity degeneracy, so that the best-fit SSP parameters would be affected by it. We find no overlap between AGN and SF contours for twin 5, indicating that similar trends to twin 5 in R$\leq 1.5\,$Reff should be independent of the age-metallicity degeneracy. Twin 8 shows some level of overlap between the contours, indicating there might be some level of degeneracy, however within 1σ we find there to be no overlap in the confidence levels, therefore indicating that the difference in age/metallicity is robust. Furthermore, our χ^2 analysis consists of manually boosting the uncertainty by adding, in quadrature, 5% of the index value due to our models not being accurate enough to explain the observations. Therefore, our confidence levels should be tighter, thus breaking the age-metallicity degeneracy, as we are unlikely to have large overlaps on the contours.

5.5.1 Radial effect of AGN activity

Both AGN and SF galaxies present mostly older stellar populations in the inner part of the galaxy, with a decreasing gradient as we move radially out (Sec. 5.3), where AGN galaxies, generally, tend to be older and more metal rich compared to their twin SF – as shown by their stronger $D_n(4000)$, [MgFe]$'$ indices, and lower $H\delta_A$ - in agreement with del Moral-Castro et al. (in prep.), who adopt a full spectral

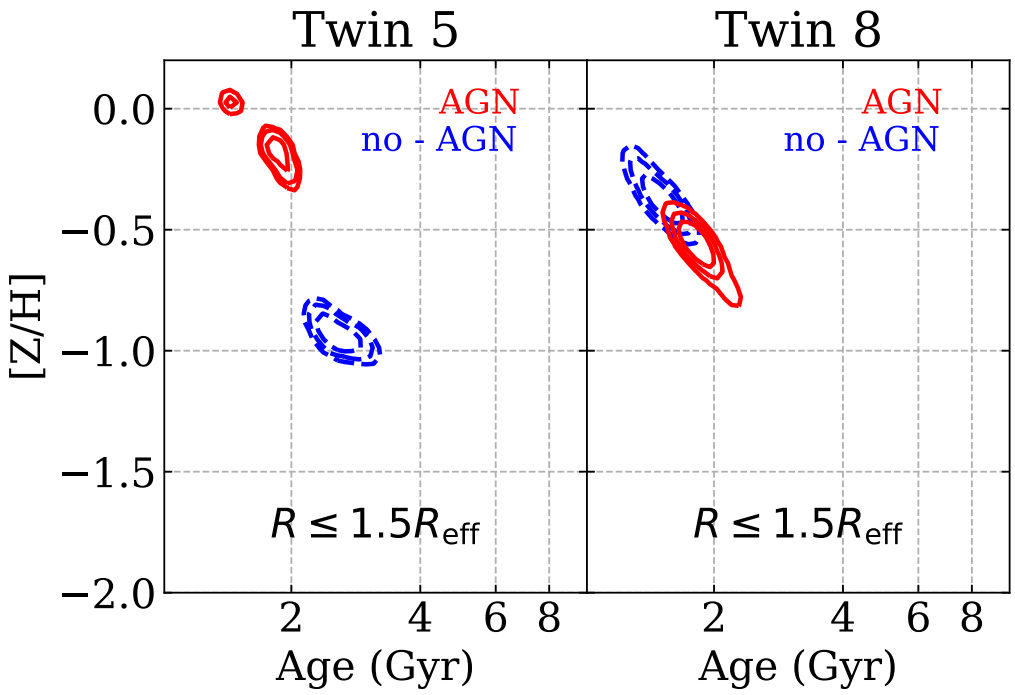

Figure 5.20: Contours of SSP-equivalent age and metallicity, denoting different confidence levels - from inside-out it indicates the 1, 2 and 3 σ levels. This figure shows the result for twin 8 galaxies, corresponding to the largest aperture ($R \leq 1.5\ R_{eff}$). The red solid and dashed blue contours show the results for the AGN and SF galaxy, respectively.

fitting approach. Sánchez et al. (2018) also find similar results in the MaNGA survey, using the derived star formation rate and gas density of their sample. Similarly, studies of stellar populations at different radii in CALIFA unveil similar trends, noting a decrease in age and metallicity for different types of galaxies at increasing radii (Bitsakis et al., 2019; Lacerna et al., 2020; Kalinova et al., 2021). All three results favour inside-out quenching (Lipari et al., 1994; Tacchella et al., 2015; Li et al., 2015; Breda et al., 2020), which suggests a galaxy may run out of gas without any interaction with other galaxies, involving internal processes, for instance, through secular evolution.

5.5.2 "On-off" AGN hypothesis

Here we invoke a simple "on-off" AGN mode to explain our results. This scenario is motivated by the fact that most galaxies experience AGN events but some happen to be in an active phase ("on" state), while others are dormant ("off" state). The

timescale of individual "on-off" events is expected to be around $\sim 10^5$ yr, where the whole life cycle lasts for $\sim 10^7 - 10^9$ yr (Schawinski et al., 2015). In such a cyclic behaviour, it is possible to explain the similarities and differences in twin pairs. G1 features the largest variation between AGN and SF systems, where AGN galaxies, measured within a $1.5''$ aperture, reside near the RS but SF galaxies reside either in the BC or GV. In addition, G1 twins display a greater radial difference between the central region and the largest aperture, $1.5\,R_{eff}$, for AGN galaxies, with respect to the SF counterparts (see Fig. 5.12 and Fig. 5.13). Fig. 5.14 also shows generally an older population in the central region for AGN galaxies with respect to their SF counterpart. Such behaviour seems antithetical to the "on-off" AGN mode, however it can still be applicable, provided the AGN twin has a different formation time compared to the SF equivalent. Therefore, these AGN galaxies may be in a state closer to the end of their AGN life cycle, whereas the SF galaxies – while still experiencing some form of AGN activity – have been formed in more recent cosmological times. The G4 twin further supports this idea, as the AGN is located close to the GV but their SF galaxy is located in the BC. However, since the AGN galaxy can be thought of as just entering the GV, we can assume it lies in a state more representative of the middle of its AGN life-cycle, resulting in similar properties between AGN and SF counterparts – unlike the G1 twins (see Fig. 5.12 and 5.13).

G2 and G3 twins have AGN and SF galaxies with more similar population properties, regardless of the aperture size. There is no clear distinction between AGN and SF galaxies at the central region or in the largest aperture (see Fig. 5.12 and 5.13), favouring the "on-off" AGN hypothesis. G2 and G3 twins show similar behaviour between their AGN and SF galaxies, however this could be due to different reasons. G2 twins are both old, have very weak Hα emission, and are classified as *Sa*, thus featuring prominent central bulges. These properties indicate that the AGN in G2 may be undergoing maintenance mode activity (Barišić et al., 2019), explaining the similarity found in the stellar populations of AGN and SF twin pairs. In contrast, G3 twins have strong Hα emission lines for both AGN and SF members

and they are classified as late spirals. Therefore rather than invoking maintenance mode, we can think of these galaxies as undergoing more active "on-off" events at the start or middle of the AGN life cycle. Additionally, the analysis of the SSP equivalent ages (Figs. 5.14, 5.15 and 5.16) gives no clear difference between AGN and SF galaxies. Note that previous studies, such as Lacerda et al. (2020) and Angthopo et al. (2019), noted AGN hosts are more evolved than SF galaxies, as the former are mainly located in the GV, whereas the latter mostly reside in the BC. However, in comparison between this targeted set of twin galaxies, such behaviour seems less clear. Within the "on-off" AGN hypothesis, this contrast could be due to their different formation times.

5.5.3 "no-AGN" hypothesis

At low and intermediate stellar mass ($M_\star \lesssim 10^{10.3} M_\odot$) there is ample evidence suggesting that stellar feedback and environmental mechanisms are sufficient to quench star formation (Feldmann et al., 2010; Naab et al., 2014), where we find greater relative difference in line strengths between AGN and their SF twin counterpart (see Fig. 5.10 and 5.11). However, at the massive end, AGN activity has been necessary to explain quiescent galaxies (Silk and Rees, 1998; Nelson et al., 2018). Thus, we propose an alternative simple model, which is an alternative to the "on-off" case, to explain the properties of the twin pairs. In the "no-AGN" hypothesis we assume that, within same stellar mass, some galaxies will quench their star formation through AGN activity while others will (i) not experience any AGN (ii) will not quench their SF through AGN but through different physical mechanisms. Therefore, galaxies that quench via AGN will have one set of signatures and galaxies quenching through stellar feedback, starvation or environmental effects would have a different set of signatures. This would be analogous to how different physical mechanisms could lead to different quenching timescales (Wright et al., 2019; Correa et al., 2019; Phillipps et al., 2019). Thus, the "no-AGN" hypothesis would imply that in twin galaxies, we should find statistically significant differences between the stellar populations of AGN and SF twin pairs. Previous work in the literature, such as del Moral-Castro et al. (2019) and del Moral-Castro et al. (2020),

have found strong evidence supporting the "no-AGN" hypothesis, where they find AGN galaxies to consistently display higher angular momentum than their SF counterpart. Note that variations in angular momentum are related to larger timescales, that cannot be explained in the context of a simple "on-off" AGN switch model (assuming similar formation time for these "twin" systems), as the AGN duty cycle is rather short-lived, of order $\sim 10^5$ yr. For such a short-lived cycle, we would expect rather small differences in line strengths, as stellar population indicators vary over timescales of order $\sim$100 Myr or more.

In this work, the analysis of G1 twins generally shows older populations in AGN galaxies. Fig. 5.12 shows the highest difference in the $D_n(4000)$ index, between the outer and inner regions, for galaxies in twins 3 and 4. This trend, while possible, would be unlikely, if we were to assume a simple "on-off" scenario. Furthermore, we find the biggest radial gradient in $H\delta_A$ between the $1.5''$ and $1.5\,R_{eff}$ apertures in the AGN galaxy. However as this index is sensitive to short timescales – with respect to 4000Å break strength – this is somewhat expected. The estimation of SSP metallicity, Figs. 5.17 and 5.18, shows AGN galaxies are generally more metal rich compared to their SF counterparts, within $1.5''$ and 2.2 kpc apertures. Once more, such variation in metallicity is expected over longer timescales, indicating a different chemical enrichment history, which implies timescales that are longer than those expected from the "on-off" AGN switching mode. The analysis of the G4 twin yields a similar result, where we find the metallicity of AGN galaxies consistently greater than their SF counterpart.

5.6 Summary

In this chapter, we have investigated the stellar population properties of a carefully defined sample of twin galaxies (del Moral-Castro et al., 2020), selected from the CALIFA IFU survey. Galaxies in twins are expected to appear undistinguishable from the point of view of size, mass, morphology and inclination, with the only difference being the presence or absence of an AGN. We project this sample onto a dust resilient evolutionary plane spanned by $D_n(4000)$ vs stellar mass; following the

methodology outlined in Chapter 3. The original 11 twin sample (20 twin pairs) is reduced to 8 twins (10 twin pairs), due to a new selection criteria restricting differences in velocity dispersion and stellar mass, to maximise the similarities between twins concerning the stellar populations. We study stacked spectra within three different apertures – the most central region, (R$\leq$1.5$''$), a region that matches, on average, the single fibre of the SDSS legacy spectra at $0.05 \lesssim z \lesssim 0.1$ (R$\leq$2.2 kpc), and a much more extended aperture, probing out to R$\leq$1.5R_{eff}. We find similar fractions of AGN (6/8 - *NGC1093, NGC2639, NGC2906, NGC2916, NGC6394 and NGC7466*) and SF (5/7 - *NGC5947, NGC2253, NGC6004, NGC2916, NGC0160*) galaxies to reside in the GV, within 2.2 kpc aperture. However, we find evidence of the role of AGN in quenching, as AGN galaxies in a twin system have greater $D_n(4000)$ than their SF counterpart 90% of the time, regardless of aperture size (Fig. 5.6).

The sample is divided into a set of groups depending on their location in this diagram (i.e. whether they live on the RS, GV, or BC). We base this classification on spectra in the most central (1.5,$''$) aperture as AGN activity is thought to impact more significantly the immediate vicinity. We grouped twins 1, 3 and 4 into group G1 as they all have their AGN in the RS, while the SF counterpart resides in the BC. Similarly, group G2 (twins 2 and 5) have their AGN in the RS but the SF system also resides in the RS. Group G3 (twins 7 and 8) have both AGN and SF in the GV. Finally, G4 (twin 5) has the AGN in the GV, while the SF galaxies are in the BC.

The twin sample is compared with a general distribution of galaxies from SDSS, with similar stellar mass. All twin AGN galaxies were selected in the CALIFA sample as type 2 Seyfert AGN, therefore, we need to select the same type in the SDSS sample. We separate type 1 and 2 AGN in the Seyfert sample from SDSS. This novel method makes use of the equivalent width of the Hα line in SF galaxies, to calibrate the peak of Hα emission in lines without a broad component. Twins 1, 3, 4, 5, 7 and 8 were found to be representative of galaxies from the larger SDSS sample (Fig. 5.7). Furthermore, relative difference, in line strengths, for twins are found to be within 3σ and all but one twin had difference within 1σ when com-

paring with the distribution of relative difference for random pairs (either SF-SF or SF-AGN) of SDSS galaxies (Fig. 5.10). Note, due to the small sample size, we do not find any strong conclusive results. However, we always find the relative variation for 4000Å break and [MgFe]′to be positive, $\gtrsim 0$, and Hδ_A to be negative, $\gtrsim 0$, indicating a consistent physical difference caused by AGN activity. This motivates the extension of this methodology to a larger sample to confirm whether such positive difference between "twin" samples is due to the effect of the AGN on the evolution of the star formation history of galaxies.

Analysis of a targeted set of line strengths showed a mixture of behaviour regarding the stellar populations. These results were discussed in the framework of two alternative hypotheses, one invoking "on-off" switching of the AGN, and the other assuming that some galaxies may not experience AGN activity at all. AGN galaxies generally have stronger 4000Å break and [MgFe]′ and weaker Hδ_A within 1.5″ and 2.2 kpc aperture – indicating an older and more metal rich population. However converting these line strengths to SSP equivalent ages and metallicities shows there is no clear trend in stellar age between AGN and SF galaxies (Figs. 5.14, 5.15 and 5.16). In contrast to age, 70%, 80% and 70% of AGN galaxies appear more metal rich within 1.5″, 2.2 kpc and 1.5 R_{eff} (Figs. 5.17, 5.18 and 5.19), respectively indicating AGN galaxies have a different star formation and chemical enrichment histories. Note we can rearrange the grouped twins into sets where groups 1 and 4, which have a bar, feature consistent differences between AGN and SF galaxies, mostly supporting the no-AGN theory, whereas groups 2 and 3, that lack barred galaxies, show more similarities than differences between AGN and SF galaxies, supporting the on-off AGN switching mode hypothesis. The diversity of the results in this sample shows the complex behaviour of AGN, thus no definitive conclusion can be drawn. However, this work provides a strong justification for a larger study that adopts the methodology implemented in this chapter to study the effect of AGN on the evolution of star formation in galaxies.

Chapter 6

Conclusion and Future Outlook

6.1 Thesis Summary

In the recent history, many strides have been made towards bettering our understand of galaxy formation and evolution. On the one hand, large surveys have enabled us to identify the key general trends of galaxies such as their stellar mass/luminosity function (Wyder et al., 2007; Faber et al., 2007), mass-metallicity relation (Gallazzi et al., 2005; Tremonti et al., 2004), their fundamental plane (Graves et al., 2010), etc. On the other hand, increase in computational power, thus leading to improvements in simulations, have enabled us to explain the observed trends using different modelling of the physical mechanisms. Combination of observation and simulations, has enabled us to further explore key aspects of galaxy evolution, such as their morphology density relation (Dressler, 1980; Dressler and Shectman, 1987), galactic kinematics (Ciotti and Bertin, 1999; Cappellari et al., 2011; Pillepich et al., 2019) or their bimodal distribution (Strateva et al., 2001; Baldry et al., 2004; Wyder et al., 2007); the latter being the focus of this thesis. From the exploration of this bimodal distribution, we have discovered a third region, which hosts transitioning galaxies (Baldry et al., 2004). Therefore, we can construct a simple evolutionary track to explain the formation and evolution of galaxies (see Fig. 1.5). The existence of a bimodal distribution enables us to categorise most galaxies in the observable universe into late-type galaxies (LTGs) and early-type galaxies (ETGs). LTGs are typically disc-like (many have spiral arms), have young average age, high star

formation and dust, are thought to mostly occupy the so called Blue Cloud (BC). In contrast ETGs host old stellar populations, are elliptical, have low to little on-going star formation and dust - mostly reside in a region known as the Red Sequence (RS). Finally, the region between BC and RS, which hosts galaxies that are in transition, is coined the GV. The BC, GV and RS have been defined using multiple galaxy parameters such as their colour-magnitude (CMD, Martin et al., 2007; Graves et al., 2007), UVJ bi-colour (Williams et al., 2009), colour-mass (Schawinski et al., 2014; Trayford et al., 2015; Bremer et al., 2018; Nelson et al., 2018) and SFR-mass (Salim et al., 2007; Koyama et al., 2019; Trussler et al., 2020) relations.

There are many studies on the region of GV, but each of the aforementioned are prone to substantial systematics as they either require some form of correction or modelling. For example, the use of colour to define BC, GV and RS, is heavily susceptible to the effects of dust extinction/attenuation (Cardelli et al., 1989; Fitzpatrick, 1999; Calzetti et al., 2000). The correction will be biased by the assumptions made, e.g. whether dust is modelled as being distributed around the galaxies homogeneously or more densely packed around star forming regions. The chemical composition of the dust grains will also affect the dust correction (Tress et al., 2018; Salim and Narayanan, 2020), as these parameters will change the slope of the dust extinction law. Therefore, dust correction carries a high level of systematics, see Fig. 3.22 in Chapter 3. In this thesis, we try to avoid some of these systematics by using a novel way of defining the evolutionary sequence, i.e. BC, GV and RS, through the use of the spectral index measured around the 4000Å break, known as the $D_n(4000)$ index. Being a spectral index, it is prone to the "Age-Metallicity" degeneracy (Worthey, 1994), so the variation in the evolutionary sequence could be due to the metallicity of the galaxy rather than their age; similar to what happens with colour. However, the $D_n(4000)$ index is measured over a shorter wavelength range than colour, so it is less sensitive to dust (see Fig. 3.22). If we consider the change in location of the BC, i.e. most dusty galaxies, we find $\delta D_n(4000)^{systematics}_{max} \sim 0.002$, where $\delta D_n(4000) = \Delta D_n(4000)^{MW} - \Delta D_n(4000)^{Calz}$, whereas $\delta col^{systematics}_{max} \sim 0.1$.

Due to its resilience to dust, we use the 4000Å break as a novel method to defining the GV, and compare this with a more traditional method, i.e. dust-corrected colour, see Fig. 3.5, in Chapter 3. For this, we divide the galaxies into different velocity dispersion bins. In each individual bin, we select Star-Forming (SF) and Quiescent (Q) galaxies, where we use the mean (μ_k) and standard deviation (s_k) within each bin (where k is BC, GV or RS), to model a probability distribution function of the BC ($\mathscr{P}_{BC}$) and RS ($\mathscr{P}_{RS}$) in the form of a Gaussian function. From this we define the midpoint of the GV, located at $\mathscr{P}_{BC}(\sigma;\pi) \equiv \mathscr{P}_{RS}(\sigma;\pi)$, where the width of GV equals $s_{GV}(\sigma;\pi) \equiv s_{RS}(\sigma;\pi)/2.0$. Note, as we follow a probabilistic approach, our selection of GV galaxies does not yield a unique solution (see Fig. 3.4).

Analysis of galaxies in transition, residing within GV, shows a high fraction of AGN in the lower (lGV) and upper (uGV) green valley (Fig. 3.8 - $f_{AGN} \sim 30\% - 50\%$) as well as the transition timescale for both 4000Å break and colour selection. In addition, previous studies, have found quenching timescales $\tau_Q \sim 1.0 - 5.0\,\mathrm{Gyr}$, where for low mass systems, $M_\star \lesssim 10^{9.8}\,\mathrm{M}_\odot$, it was thought that environment was the dominant form of quenching - i.e. ram pressure stripping, strangulation and galaxy harassment. For intermediate stellar mass systems, $M_\star \sim 10^{9.8} - 10^{10.3}\,\mathrm{M}_\odot$, stellar feedback and AGN are thought to quench the star formation, which have a longer timescale than for lower stellar mass. Finally, most massive systems, $M_\star \gtrsim 10^{10.3}\,\mathrm{M}_\odot$, have the shortest quenching timescales and are thought to quench their star formation predominantly through mix of major mergers and AGN (Wright et al., 2019; Phillipps et al., 2019). Note, in each of the stellar mass bins, there is also a spread in the quenching timescale, owing to their morphology, where ETGs will experience faster quenching compared to LTGs (Schawinski et al., 2014). This behaviour is also seen in our studies, for both selection methods (Chapter 3), when contrasting the transition timescale, Δt_{SSP}, where for stacks consisting of only quiescent galaxies we find a shorter transition timescale, which is representative of ETGs, (Fig. 3.12, where $\Delta t_{SSP} \sim$1.0-3.5 Gyr) compared to stacks that include SF, LINER and Q galaxies - these stacks can be thought of as a proxy of LTGs - (Fig. 3.12,

where Δt_{SSP} ∼0.5-5.0 Gyr). Note, similar to Wright et al. (2019), we also find a heavy dependency between velocity dispersion and transition timescale - suggesting different modes of quenching.

Both selection methods of GV galaxies find qualitative agreement in galactic properties for general trends, although a more detailed analysis of the stellar population showed important differences. To the zeroth order, the most obvious difference is a cleaner stratification between the different evolutionary regions in $D_n(4000)$ compared to colour selection. We are also able to identify more nuanced differences between the two selection criteria. For example, the use of the 4000Å break to select transitioning galaxies revealed a more homogeneous stellar population regarding different types of galaxies, i.e. Star-Forming (SF), LINER AGN or Quiescent (Q) - see Figs. 3.10 and 3.11. The higher difference in line strengths when using colour selection rather than $D_n(4000)$ shows that even when we do correct for dust, this might not be the *true* correction, hence, galaxies that should belong in the BC are found instead in the GV. Moreover, studying the stellar ages of the galaxies in lGV, middle (mGV) GV and uGV, we find lower differences between the populations in lGV and mGV compared to uGV, for 4000Å break selection (see Figs. 3.9, 3.16 and 3.17), implying a non-linear transition from BC to RS. Such behaviour suggests that the transition from BC to GV occurs more rapidly with respect to the transition between GV or RS. Note, this behaviour is not present in the colour-based selection, possibly from contamination of populations from different regions, due to dust, making the transition more homogeneous.

In Chapter 4 we turned our attention to two state-of-the-art simulations, EAGLE and IllustrisTNG, testing how well they are able to reproduce the observed trends with regards to BC, GV and RS. Note similar studies were done in Trayford et al. (2015, 2017), for EAGLE, and Nelson et al. (2018), for TNG100, finding a good qualitative agreement between observation and simulations, when using colour, (g-r). To begin with, we carry out a similar analysis, but on the stellar mass vs $D_n(4000)$ plane, where we find both simulations are able to reproduce the location of the BC. However, both simulations produced too many galaxies with

stronger 4000Å break than seen in (SDSS) observations, thus failing to match the location of GV and RS (see Fig. 4.3). TNG100 produced more galaxies with stronger 4000Å break, $\Delta D_n(4000) \sim +0.2$ dex, compared to EAGLE, $\Delta D_n(4000) \sim +0.1$ dex, suggesting a stronger quenching in TNG100 than EAGLE and SDSS. We also find the slope of the RS to be shallower in both simulations compared to SDSS, where, again, TNG100 finds a flatter slope than EAGLE - this behaviour was faulted to the mismatch in the mass-metallicity relation (MZR) in simulations (Schaye et al., 2015; Nelson et al., 2018). As the discrepancy affects the RS, but not the BC, this suggests the star formation subgrid physics is correct. However, this mismatch concerns the quenching mechanism in simulations. Thus, we choose to focus and study the variation of stellar populations in GV. To the zeroth order, we examined the capability of simulations to reproduce the fraction of different types of galaxies as seen in the observations, within the same region. For the observations, the different types of galaxies are based on their emission line ratios, i.e. through the BPT classification system (Baldwin et al., 1981), whereas for simulations, we define the different types of galaxies based on their Eddington ratio, λ_{Edd}, and specific star formation rate, sSFR, to match the observational fractions for the homogenised sample; see Tab. 4.2 for the selection/definition criteria for different types of galaxies. Both λ_{Edd} and sSFR, were fine tuned to produce the same fraction of SF, Q, Seyfert AGN and LINER AGN for the homogenised sample of simulations and observations. Both simulations were able to reproduce the fraction of LINER and Seyfert galaxies irrespective of stellar mass or GV region, however at the high stellar mass regime, $M_\star \gtrsim 10^{10.5} M_\odot$, they overproduce the fraction of Q galaxies (Figs. 4.2 and 4.11). Such behaviour suggests an overquenching of galaxies in simulations.

The overquenching in simulations were further supported when studying the luminosity weighted average ages of galaxies, where EAGLE (TNG1000) produced systematically older galaxies than seen in observation, $\sim +3.77 \pm 0.33\,(+2.98 \pm 0.08)$ Gyr. In contrast, there was good agreement between the mass weighted average ages of observations and simulations. Note, our results showed a higher fraction of quiescent galaxies in TNG100 compared to EAGLE, however the EAGLE

galaxies were found to be older. The study of their SFH showed good agreement between EAGLE and TNG100 at low mass, where we also found good agreement in the fraction of quiescent galaxies between simulations, but for more massive systems, it revealed that the quenching of star formation started at an earlier time in EAGLE compared to TNG100, but TNG100 had more rapid and stronger quenching events, inhibiting any star formation in the recent past (Fig. 4.10). There could be multiple reasoning for such a behaviour, where one hypothesis could be due to the SMBH and subgrid physics regarding AGN feedback. Specifically, EAGLE has a lower threshold halo mass to convert a gas particle to a black hole, with a lower black hole seed mass, compared to TNG100, explaining the earlier onset of quenching. The higher threshold mass explains the later onset of quenching in TNG100. Additionally, the higher black hole seed mass and the two modes of AGN feedback, thermal and kinetic feedback, where the latter an order of magnitude more efficient causing it to inject a large quantity of energy into the surrounding, causing a very rapid quenching of star formation and prevents further star formation. This hypothesis is supported as we see a lack of star forming galaxies with a high black hole mass (see Fig. 4.12 and Terrazas et al., 2020; Davies et al., 2020).

In our study of GV galaxies, the importance of AGN was consistently iterated, both from observations and simulations (chapter 2, 3 and 4). Hence, chapter 5 analyses the properties of galaxies hosting AGN and their effect on the host's stellar population more directly. This studies "twin" galaxies, following the pilot study of del Moral-Castro et al. (2019, 2020). We select pairs of galaxies, with similar overall properties - i.e., stellar mass, velocity dispersion, magnitude in r band, morphology and inclination - but one hosts an AGN and the other is simple star forming. For each galaxy, the stellar populations within 3 distinct radii apertures are analysed - R$\leq 1.5''$, R≤ 2.2kpc and R$\leq 1.5\,\mathrm{R}_{eff}$. For each of the apertures we studied the location of "twin" galaxies, both AGN and SF, on the evolutionary sequence, consistently finding AGN galaxies to be more evolved than their SF "twin" counterpart (see Fig. 5.6). Additionally, similar to previous studies carried out using SDSS (Martin et al., 2007; Angthopo et al., 2019), CALIFA (Lacerda et al.,

2020) and MANGA (Sánchez et al., 2018) survey, we find most of our AGN galaxies, within R$\leq$ 2.2 kpc, to be located in the GV. Furthermore, we used the innermost aperture to divide the twins into different groups - depending on their position in the evolutionary sequence. This yielded 4 distinct groups. Furthermore, a comparison of spectral indices - $D_n(4000)$, $H\delta_A$ and [MgFe]$'$- with SDSS galaxies suggested the AGN to be older or more metal rich than their SF, even amongst "twin" pairs, suggesting this behaviour to be physical - seen in Figs. 5.10 and 5.11.

Finally, the difference between AGN and their SF twin were tested against two hypothesis, "on-off" switching of the AGN or no-AGN. The former would mean that there are more similarities between the twins than differences, whereas the latter would exhibit the opposite trend. We found, owing to the small sample, a mixed signal supporting both hypotheses. The study of SSP equivalent stellar ages found no clear trend between AGN and SF galaxies, however, the SSP equivalent metallicities found AGN galaxies to be more metal rich compared to their SF twin. Note, the variation in metallicity supports the no-AGN hypothesis, as such differences accumulate over a long period of time, hence indicating a different SFH. Nevertheless, such trends can be explained within the "on-off" scenario assuming that AGN galaxies have an earlier formation time compared to their SF twin.

6.2 Implications

To summarise, this thesis makes use of a novel definition of GV, defined using the spectroscopic index 4000Å break, and compares it against a traditional method, based on colour. Moving forward, this novel method provides a new avenue upon which one can define the GV, with little systematics associated to it. Moreover, this definition is timely as many spectroscopic surveys will be available in the near future, such as WAVES (Driver et al., 2019) , WEAVE (Dalton, 2016), DESI (DESI Collaboration et al., 2016) or MSE (McConnachie et al., 2016). From each of these surveys, we can measure the 4000Å break. Such definition of the GV finds a more homogeneous population among different galaxy types, therefore enabling a cleaner study of stellar population properties. A further implication of our study is related

to state-of-the-art hydrodynamical simulations, where we find in both EAGLE and TNG100, the subgrid physics of AGN feedback to be too powerful. Hence, for future runs of such simulations, further fine tuning is required in the subgrid physics. Finally, our work from Chapter 4 hints towards a different way of looking at the SMBH and AGN feedback, where we try to explain the observed behaviour between "twin" samples using two "opposite end spectrum" hypotheses - "on-off" AGN or not-AGN. While, we have a small statistical sample, the implication of this chapter can be thought of as a fundamental way to understand the role of AGN feedback on the star formation history of galaxies.

6.3 Future work

In this thesis we have explored many avenues regarding the evolution of galaxies, using a novel definition of GV. In our analysis, we do not discriminate between the different types of environment. As mentioned in Chapter 1, the environment that a galaxy resides in can determine the key properties of galaxies. One such key result the existence of the morphology-density relation (Dressler, 1980), which finds high number of elliptical galaxies in high-density environments and low-density regions to be mostly dominated by disc type galaxies. The existence of such relation has been explored in two main contexts: "Is such a relation due to intrinsic properties, in regards to their early stages of formation?" or "do such relations come about due to external factors, i.e. galaxy-galaxy interactions?". Further studies of galaxies and their environment have found evidence supporting both results where (i) low mass systems seem to be affected more by their environment (ii) the impact of environment also depends on whether the galaxy is a central (the most massive galaxy in a group) or a satellite (all other galaxies in a group) (Peng et al., 2010; Pasquali et al., 2012; La Barbera et al., 2014; Pasquali, 2015). Galaxies in a cluster/group environment happen to be redder, more metal rich, older and with a lower star formation rate (Kauffmann et al., 2004), as they are thought to quench faster through processes such as strangulation and ram pressure stripping (Gunn and Gott, 1972; Balogh et al., 2000; Balogh and Morris, 2000; Trussler et al., 2020). On

the other hand, galaxies in the field or in voids, i.e. sparser environments, tend to have a more extend period of star formation, hence resulting in slower quenching timescales. Physical mechanisms such as supernovae and weak AGN are thought to be the dominant form of quenching in these galaxies (Wright et al., 2019; Lacerda et al., 2020).

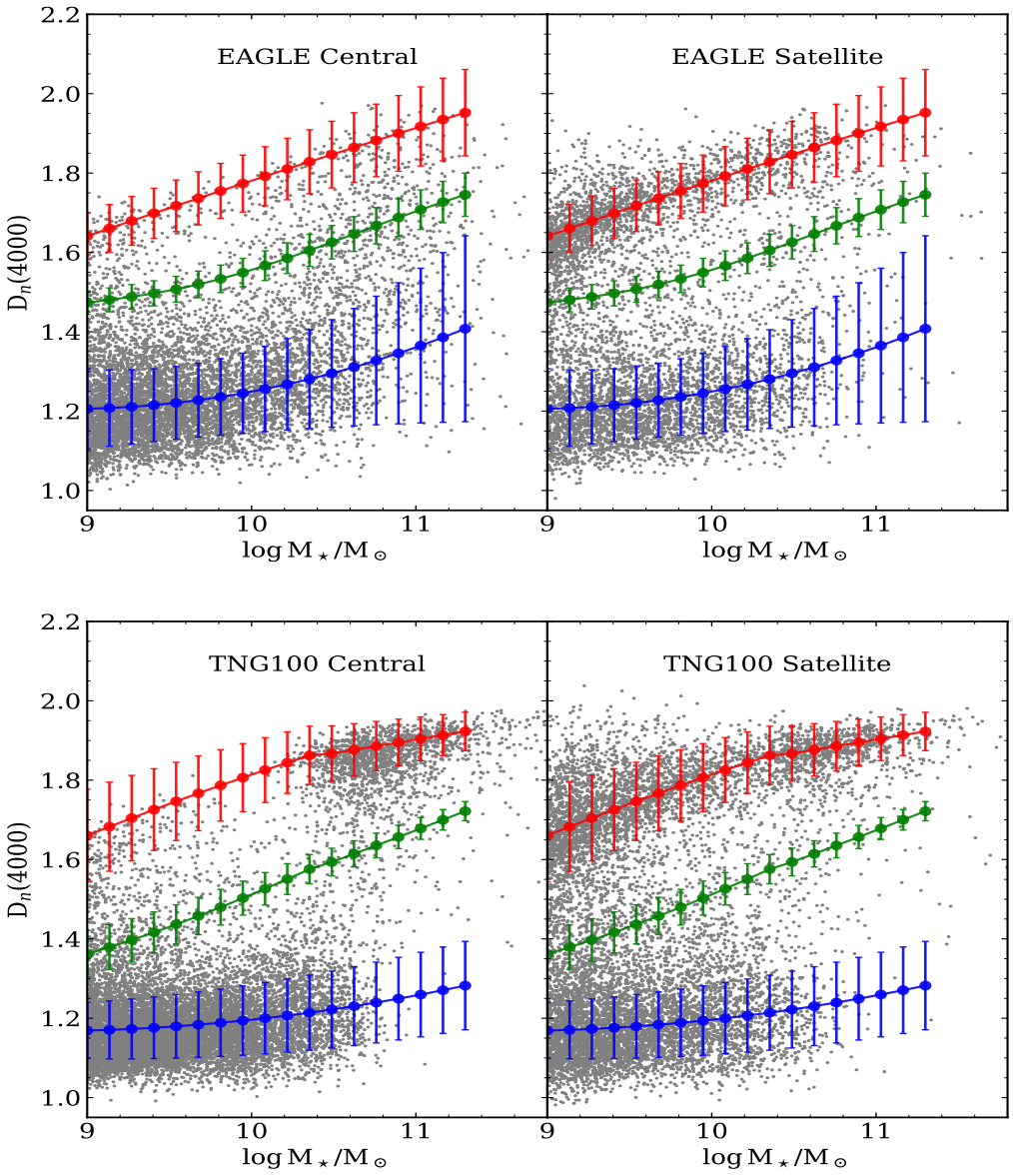

Figure 6.1: BC, GV and RS defined for EAGLE (top) and TNG100 (bottom), shown by blue, green and red data points respectively. The scatter points show the simulated galaxies, where left and right panels show centrals and satellites, respectively.

In Chapter 3, we discussed the possibility of defining the BC, GV and RS using simulations rather than observations. Therefore, a future project could consist of the analysis of transitioning galaxies selected from a GV defined by simulations, as in Wright et al. (2019). Fig. 6.1 presents such exercise, where we make use of the sSFR to identify SF and Q galaxies within different stellar mass bins, after which we follow a similar approach as outlined in chapter 2 to define BC, GV and RS. However, we carry out an additional step, where we find a best fit for a polynomial function to express the BC, GV and RS. Note in TNG100, for the RS specifically, we combine two polynomial functions below and above $M_\star \sim 10^{10.5} M_\odot$, as one function yields a RS that does not follow the distribution. From this we find different functional forms and locations for GV and RS between the two simulations. Additionally, we find the view of BC, GV and RS changes depending on whether the galaxy is central or satellite and depending on the simulation. Note we have a very sparse Central RS in EAGLE, whereas TNG100 shows a high density of RS centrals around $M_\star \sim 10^{10.5} M_\odot$. Therefore, future studies can analyse the stellar population properties, such as their quenching timescales, and SFHs, to explain the differences in evolutionary sequence between the two selection criteria; especially with respect to environment. Furthermore, we can compare this with central and satellite estimates from SDSS.

The first order approximation simply analyses the difference in galactic and stellar population properties for centrals and satellites. However, with access to advanced simulations and high quality observations, we are able to carry out a more in-depth analysis of galaxies and their environment. One such study makes use of the mean infall time of a galaxy into a group/cluster to study the effect of environment (Pasquali et al., 2019). Note, the mean infall time (T_{inf}), indicates how long it has been since a galaxy has come inside the virial radius of a cluster. Fig. 6.2, shows a projected phase space (PPS) diagram, made up of V_{LOS}/σ (line of site velocity over group velocity dispersion) and R_{proj}/R_{vir} (projected group-centric radius of the galaxy normalised by virial radius). The colour coding shows the infall time (T_{inf}), where each of the black lines indicate different zones. These zones divide the PPS

diagram into different sections based on the infall time of the galaxy. Zone 1 hosts galaxies, which have the earliest infall time, thus have been in a cluster environment for the longest time. Zone 9 have galaxies which have "fallen" in most recently.

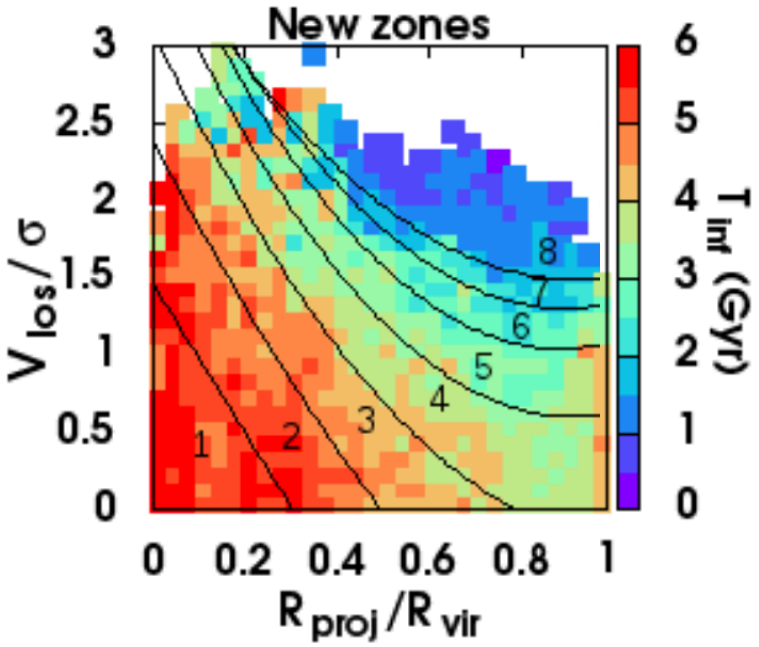

Figure 6.2: The projected phase space diagram of galaxies mapped with respect to infall time, obtained from simulations. Each zones from 1 to 9 indicate a different mean infall time as denoted by the colour bar on the right. This figure is an amended version from Pasquali et al. (2019).

While the PPS diagram regions are constructed using simulations, the y and x axis can be calculated for observational data. Therefore, we make use of the PPS diagram to study the effect of environment and infall time on SDSS galaxies. We obtain the different regions (in phase space) from a catalogue constructed by Sampaio et al. (2021) based on the groups catalogue of Yang et al. (2007). Note, galaxies which have a very high R_{proj}/R_{vir} can be thought of as field galaxies, i.e. do not belong to any group. Fig. 6.3 presents the fraction of galaxies in these zones and fields for different velocity dispersion bins. The red, green and blue indicate different regions the PPS diagram, as labelled. The black lines (indicated to be "All") represent the field galaxies. From top to bottom, we show the results for RS, GV and BC (where each region is defined following the steps outline in Chapter 2). Similar to

previous studies (Kauffmann et al., 2004; Pasquali et al., 2012; La Barbera et al., 2014), we also find galaxies with low velocity dispersion to be more affected by environment - indicated by a large scatter in the fractions, whereas for galaxies with high velocity dispersion we see a convergence in fractions, regardless of their environment. Furthermore, it is also evident that most low mass BC galaxies belong to the field, whereas low mass RS galaxies mostly happen to be in the very central regions, Zone $1-3$, of clusters/group.

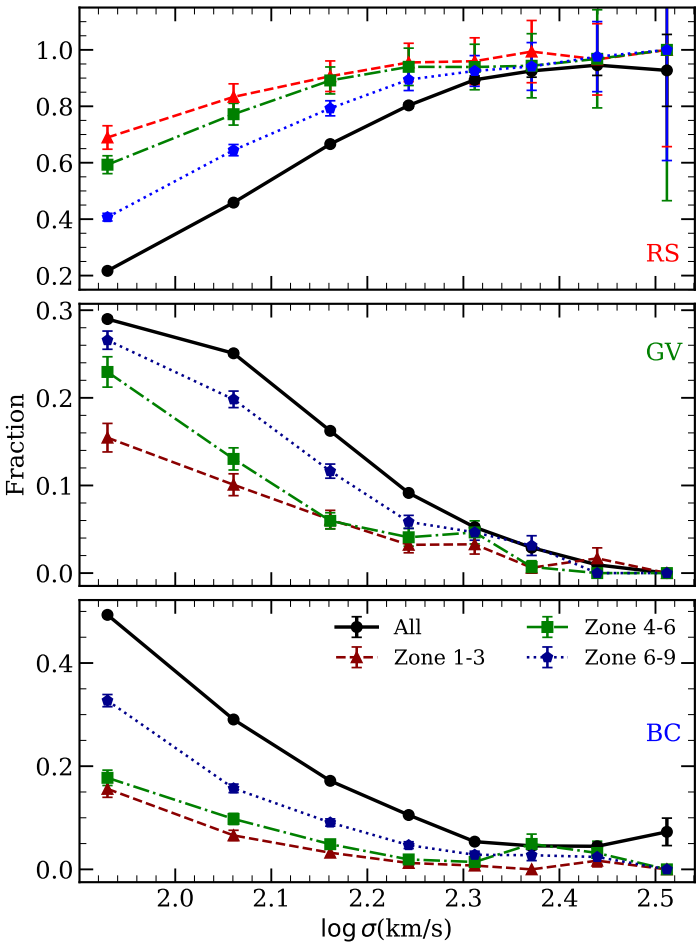

Figure 6.3: The fractions of galaxies in different infall time zones (proxy for group/cluster environment) shown by red, green and blue data points, and in field environments (shown by black data points). *Top, middle* and *bottom:* panels show the fractions for RS, GV and BC, respectively. Note, for individual stellar mass bins the summation of fractions in BC, GV and RS equals to one.

Further work on such topic requires the study of different types of galaxies, i.e. AGN, Q, SF or LINER, in different zones at different phase of the evolutionary

sequence. Furthermore, we are also able to determine whether these galaxies are centrals and satellites, identified in Yang et al. (2007), enabling us to relate them to their environment and evolutionary sequence. Additionally, future work could also consist of using intermediate-high redshift survey data such as LEGA-C (van der Wel et al., 2016), SUBARU (Sugai et al., 2012), JWST (Gardner et al., 2006), to study the properties of galaxies at higher redshift. These studies can be contrasted with galactic properties at low redshift as a way of studying galaxies in different evolutionary stages. Additionally, some surveys probe galaxies at intermediate redshifts in different environment, enabling us to study their properties at the initial stages, before a galaxy experiences the effect of both its environment and secular evolution: such effects are very challenging to disentangle in low redshift galaxies. Additionally, we can also see in detail how the evolutionary sequence truly changes at different cosmic time. For example both Wright et al. (2019) and Correa et al. (2019) use the EAGLE simulation to study BC, GV and RS within different redshift bins, $z \sim 1.0$, finding the RS to become more sparse at higher redshift.

In addition to the analysis of stellar populations at higher redshift, we can also make use of the integral field spectroscopy (IFS) data from surveys such as SAMI (Croom et al., 2012, 2021), CALIFA (Sánchez et al., 2012), MUSE (Bacon et al., 2014, 2017) and MAGPI (Foster et al., 2021). From such surveys we are able to study radial trends of galactic properties, such as their age and metallicity, as we move away from the central region. Such analysis can improve our knowledge regarding inside-out quenching. For example, we can select BC, GV and RS galaxies, identified within their central regions, and analyse how their radial gradients might change in different evolutionary stages. Furthermore, in dense environments, we can also study population variations in the outer regions of galaxies to study the frequency of outside-in quenching and mergers. Finally, we can also identify AGN galaxies to study the extent of their impact.

Bibliography

Abadi Mario G., Moore Ben, and Bower Richard G. (1999), "Ram pressure stripping of spiral galaxies in clusters." *MNRAS*, 308, 947–954.

Abolfathi B., Aguado D. S., Aguilar G., Allende Prieto C., Almeida A., Ananna T. T., Anders F., Anderson S. F., Andrews B. H., Anguiano B., et al. (2018), "The Fourteenth Data Release of the Sloan Digital Sky Survey: First Spectroscopic Data from the Extended Baryon Oscillation Spectroscopic Survey and from the Second Phase of the Apache Point Observatory Galactic Evolution Experiment." *ApJ*, 235, 42.

Abraham R. G. (1998), "Perspectives in Physical Morphology." *ArXiv Astrophysics e-prints*.

Angthopo J., Negri A., Ferreras I., de la Rosa I. G., Dalla Vecchia C., and Pillepich A. (2021), "Evaluating hydrodynamical simulations with green valley galaxies." *MNRAS*, 502, 3685–3702.

Angthopo James, Ferreras Ignacio, and Silk Joseph (2019), "Exploring a new definition of the green valley and its implications." *MNRAS*, 488, L99–L103.

Angthopo James, Ferreras Ignacio, and Silk Joseph (2020), "A detailed look at the stellar populations in green valley galaxies." *MNRAS*.

Antonucci Robert (1993), "Unified models for active galactic nuclei and quasars." , 31, 473–521.

Baade D., Meisenheimer K., Iwert O., Alonso J., Augusteijn T., Beletic J., Bellemann H., Benesch W., Böhm A., Böhnhardt H., et al. (1999), "The Wide Field

Imager at the 2.2-m MPG/ESO telescope: first views with a 67-million-facette eye." *The Messenger*, 95, 15–16.

Bacon R., Vernet J., Borisova E., Bouché N., Brinchmann J., Carollo M., Carton D., Caruana J., Cerda S., Contini T., et al. (2014), "MUSE Commissioning." *The Messenger*, 157, 13–16.

Bacon Roland, Conseil Simon, Mary David, Brinchmann Jarle, Shepherd Martin, Akhlaghi Mohammad, Weilbacher Peter M., Piqueras Laure, Wisotzki Lutz, Lagattuta David, et al. (2017), "The MUSE Hubble Ultra Deep Field Survey. I. Survey description, data reduction, and source detection." , 608, A1.

Baldry I. K., Glazebrook K., Brinkmann J., Ivezić Ž., Lupton R. H., Nichol R. C., and Szalay A. S. (2004), "Quantifying the Bimodal Color-Magnitude Distribution of Galaxies." *ApJ*, 600, 681–694.

Baldwin J. A., Phillips M. M., and Terlevich R. (1981), "Classification parameters for the emission-line spectra of extragalactic objects." *PASP*, 93, 5.

Balogh M. L., Morris S. L., Yee H. K. C., Carlberg R. G., and Ellingson E. (1999), "Differential Galaxy Evolution in Cluster and Field Galaxies at z$\sim$0.3." *ApJ*, 527, 54–79.

Balogh Michael L. and Morris Simon L. (2000), "Hα photometry of Abell 2390." *MNRAS*, 318, 703–714.

Balogh Michael L., Navarro Julio F., and Morris Simon L. (2000), "The Origin of Star Formation Gradients in Rich Galaxy Clusters." *ApJ*, 540, 113–121.

Barišić Ivana, van der Wel Arjen, van Houdt Josha, Maseda Michael V., Bell Eric F., Bezanson Rachel, Chang Yu-Yen, Röttgering Huub, van de Ven Glenn, and Wu Po-Feng (2019), "An Absence of Radio-loud Active Galactic Nuclei in Geometrically Flat Quiescent Galaxies: Implications for Maintenance-mode Feedback Models." *ApJL*, 872, L12.

Barnes Joshua E. and Hernquist Lars (1998), "Transformations of galaxies. ii. gas-dynamics in merging disk galaxies: Addendum." *The Astrophysical Journal*, 495, 187.

Barrera-Ballesteros J. K., Falcón-Barroso J., García-Lorenzo B., van de Ven G., Aguerri J. A. L., Mendez-Abreu J., Spekkens K., Lyubenova M., Sánchez S. F., Husemann B., et al. (2014), "Kinematic alignment of non-interacting CALIFA galaxies. Quantifying the impact of bars on stellar and ionised gas velocity field orientations." , 568, A70.

Belfiore Francesco, Maiolino Roberto, Maraston Claudia, Emsellem Eric, Bershady Matthew A., Masters Karen L., Yan Renbin, Bizyaev Dmitry, Boquien Médéric, Brownstein Joel R., et al. (2016), "SDSS IV MaNGA - spatially resolved diagnostic diagrams: a proof that many galaxies are LIERs." *MNRAS*, 461, 3111–3134.

Bell Eric F. (2008), "Galaxy Bulges and their Black Holes: a Requirement for the Quenching of Star Formation." *ApJ*, 682, 355–360.

Bell Eric F., McIntosh Daniel H., Katz Neal, and Weinberg Martin D. (2003), "The Optical and Near-Infrared Properties of Galaxies. I. Luminosity and Stellar Mass Functions." *ApJ*, 149, 289–312.

Benitez N., Dupke R., Moles M., Sodre L., Cenarro J., Marin-Franch A., Taylor K., Cristobal D., Fernandez-Soto A., and Mendes de Oliveira C. (2014), "J-PAS: The Javalambre-Physics of the Accelerated Universe Astrophysical Survey." *arXiv e-prints*, arXiv:1403.5237.

Bernardi M. et al. (2003), "Early-Type Galaxies in the Sloan Digital Sky Survey. IV. Colors and Chemical Evolution." *AJ*, 125, 1882–1896.

Bitsakis T., Sánchez S. F., Ciesla L., Bonfini P., Charmandaris V., Cervantes Sodi B., Maragkoudakis A., Diaz-Santos T., and Zezas A. (2019), "The integrated properties of the CALIFA galaxies: model-derived galaxy parameters and quenching of star formation." *MNRAS*, 483, 370–380.

Blanton M. R. and Roweis S. (2007), "K-Corrections and Filter Transformations in the Ultraviolet, Optical, and Near-Infrared." , 133, 734–754.

Bondi H. and Hoyle F. (1944), "On the mechanism of accretion by stars." *MNRAS*, 104, 273.

Bower R. G., Benson A. J., Malbon R., Helly J. C., Frenk C. S., Baugh C. M., Cole S., and Lacey C. G. (2006), "Breaking the hierarchy of galaxy formation." *MNRAS*, 370, 645–655.

Bower R. G., Lucey J. R., and Ellis R. S. (1992a), "Precision photometry of early-type galaxies in the Coma and Virgo clusters : a test of the universality of the colour-magnitude relation - II. Analysis." *MNRAS*, 254, 601.

Bower Richard G., Lucey J. R., and Ellis Richard S. (1992b), "Precision photometry of early-type galaxies in the Coma and Virgo clusters : a test of the universality of the colour-magnitude relation - I. The data." *MNRAS*, 254, 589–600.

Bower Richard G., Schaye Joop, Frenk Carlos S., Theuns Tom, Schaller Matthieu, Crain Robert A., and McAlpine Stuart (2017), "The dark nemesis of galaxy formation: why hot haloes trigger black hole growth and bring star formation to an end." *MNRAS*, 465, 32–44.

Brammer G. B., Whitaker K. E., van Dokkum P. G., Marchesini D., Labbé I., Franx M., Kriek M., Quadri R. F., Illingworth G., Lee K. S., et al. (2009), "The Dead Sequence: A Clear Bimodality in Galaxy Colors from z = 0 to z = 2.5." *ApJL*, 706, L173–L177.

Breda Iris, Papaderos Polychronis, Gomes Jean Michel, Vílchez José Manuel, Ziegler Bodo L., Hirschmann Michaela, Cardoso Leandro S. M., Lagos Patricio, and Buitrago Fernando (2020), "Stellar age gradients and inside-out star formation quenching in galaxy bulges." , 635, A177.

Bremer M. N., Phillipps S., Kelvin L. S., De Propris R., Kennedy R., Moffett A. J., Bamford S., Davies L. J. M., Driver S. P., Häußler B., et al. (2018), "Galaxy and

Mass Assembly (GAMA): Morphological transformation of galaxies across the green valley." *MNRAS*, 476, 12–26.

Brinchmann J., Charlot S., White S. D. M., Tremonti C., Kauffmann G., Heckman T., and Brinkmann J. (2004), "The physical properties of star-forming galaxies in the low-redshift Universe." *MNRAS*, 351, 1151–1179.

Bruzual G. (1983), "Spectral evolution of galaxies. I. Early-type systems." , 273, 105–127.

Bruzual G. and Charlot S. (2003), "Stellar population synthesis at the resolution of 2003." *MNRAS*, 344, 1000–1028.

Calzetti Daniela, Armus Lee, Bohlin Ralph C., Kinney Anne L., Koornneef Jan, and Storchi-Bergmann Thaisa (2000), "The Dust Content and Opacity of Actively Star-forming Galaxies." *ApJ*, 533, 682–695.

Calzetti Daniela, Kinney Anne L., and Storchi-Bergmann Thaisa (1994), "Dust Extinction of the Stellar Continua in Starburst Galaxies: The Ultraviolet and Optical Extinction Law." *ApJ*, 429, 582.

Cappellari M. and Emsellem E. (2004), "Parametric Recovery of Line-of-Sight Velocity Distributions from Absorption-Line Spectra of Galaxies via Penalized Likelihood." , 116, 138–147.

Cappellari Michele, Emsellem Eric, Krajnović Davor, McDermid Richard M., Scott Nicholas, Verdoes Kleijn G. A., Young Lisa M., Alatalo Katherine, Bacon R., Blitz Leo, et al. (2011), "The ATLAS^{3D} project - I. A volume-limited sample of 260 nearby early-type galaxies: science goals and selection criteria." *MNRAS*, 413, 813–836.

Cardelli J. A., Clayton G. C., and Mathis J. S. (1989), "The relationship between infrared, optical, and ultraviolet extinction." *ApJ*, 345, 245–256.

Cenarro A. J., Peletier R. F., Sánchez-Blázquez P., Selam S. O., Toloba E., Cardiel N., Falcón-Barroso J., Gorgas J., Jiménez-Vicente J., and Vazdekis A. (2007),

"Medium-resolution Isaac Newton Telescope library of empirical spectra - II. The stellar atmospheric parameters." *MNRAS*, 374, 664–690.

Cervantes J. L. and Vazdekis A. (2009), "An optimized Hβ index for disentangling stellar population ages." , 392, 691–704.

Chabrier Gilles (2003), "Galactic Stellar and Substellar Initial Mass Function." , 115, 763–795.

Charlot Stéphane and Fall S. Michael (2000), "A Simple Model for the Absorption of Starlight by Dust in Galaxies." *ApJ*, 539, 718–731.

Cid Fernandes R., Mateus A., Sodré L., Stasińska G., and Gomes J. M. (2005), "Semi-empirical analysis of Sloan Digital Sky Survey galaxies - I. Spectral synthesis method." *MNRAS*, 358, 363–378.

Cid Fernandes R., Stasińska G., Mateus A., and Vale Asari N. (2011), "A comprehensive classification of galaxies in the Sloan Digital Sky Survey: how to tell true from fake AGN?" *MNRAS*, 413, 1687–1699.

Cid Fernandes R., Stasińska G., Schlickmann M. S., Mateus A., Vale Asari N., Schoenell W., and Sodré L. (2010), "Alternative diagnostic diagrams and the 'forgotten' population of weak line galaxies in the SDSS." *MNRAS*, 403, 1036–1053.

Ciotti L. and Bertin G. (1999), "Analytical properties of the $R^{1/m}$ law." , 352, 447–451.

Ciotti Luca, Pellegrini Silvia, Negri Andrea, and Ostriker Jeremiah P. (2017), "The Effect of the AGN Feedback on the Interstellar Medium of Early-Type Galaxies:2D Hydrodynamical Simulations of the Low-Rotation Case." *ApJ*, 835, 15.

Conroy Charlie and Gunn James E. (2010), "The Propagation of Uncertainties in Stellar Population Synthesis Modeling. III. Model Calibration, Comparison, and Evaluation." *ApJ*, 712, 833–857.

Conselice Christopher J. (2003), "The Relationship between Stellar Light Distributions of Galaxies and Their Formation Histories." *ApJ*, 147, 1–28.

Correa Camila A., Schaye Joop, and Trayford James W. (2019), "The origin of the red-sequence galaxy population in the EAGLE simulation." *MNRAS*, 484, 4401–4412.

Crain Robert A., Schaye Joop, Bower Richard G., Furlong Michelle, Schaller Matthieu, Theuns Tom, Dalla Vecchia Claudio, Frenk Carlos S., McCarthy Ian G., Helly John C., et al. (2015), "The EAGLE simulations of galaxy formation: calibration of subgrid physics and model variations." *MNRAS*, 450, 1937–1961.

Crockett R. M., Shabala S. S., Kaviraj S., Antonuccio-Delogu V., Silk J., Mutchler M., O'Connell R. W., Rejkuba M., Whitmore B. C., and Windhorst R. A. (2012), "Triggered star formation in the inner filament of Centaurus A." *MNRAS*, 421, 1603–1623.

Croom Scott M., Lawrence Jon S., Bland-Hawthorn Joss, Bryant Julia J., Fogarty Lisa, Richards Samuel, Goodwin Michael, Farrell Tony, Miziarski Stan, Heald Ron, et al. (2012), "The Sydney-AAO Multi-object Integral field spectrograph." *MNRAS*, 421, 872–893.

Croom Scott M. et al. (2021), "The SAMI Galaxy Survey: the third and final data release." *MNRAS*.

Croton Darren J., Springel Volker, White Simon D. M., De Lucia G., Frenk C. S., Gao L., Jenkins A., Kauffmann G., Navarro J. F., and Yoshida N. (2006), "The many lives of active galactic nuclei: cooling flows, black holes and the luminosities and colours of galaxies." *MNRAS*, 365, 11–28.

Dalla Vecchia Claudio and Schaye Joop (2012), "Simulating galactic outflows with thermal supernova feedback." *MNRAS*, 426, 140–158.

Dalton G. (2016), "WEAVE: The Next Generation Spectroscopy Facility for the WHT." In *Multi-Object Spectroscopy in the Next Decade: Big Questions, Large Surveys, and Wide Fields* (I. Skillen, M. Balcells, and S. Trager, eds.), volume 507 of *Astronomical Society of the Pacific Conference Series*, 97.

Dashyan Gohar, Choi Ena, Somerville Rachel S., Naab Thorsten, Quirk Amanda C. N., Hirschmann Michaela, and Ostriker Jeremiah P. (2019), "AGN-driven quenching of satellite galaxies." *MNRAS*, 1710.

Davies Jonathan J., Crain Robert A., Oppenheimer Benjamin D., and Schaye Joop (2020), "The quenching and morphological evolution of central galaxies is facilitated by the feedback-driven expulsion of circumgalactic gas." *MNRAS*, 491, 4462–4480.

Davis M., Guhathakurta P., Konidaris N. P., Newman J. A., Ashby M. L. N., Biggs A. D., Barmby P., Bundy K., Chapman S. C., Coil A. L., et al. (2007), "The All-Wavelength Extended Groth Strip International Survey (AEGIS) Data Sets." *ApJL*, 660, L1–L6.

Davis Marc, Faber Sandra M., Newman Jeffrey, Phillips Andrew C., Ellis Richard S., Steidel Charles C., Conselice C., Coil Alison L., Finkbeiner D. P., Koo David C., et al. (2003), "Science Objectives and Early Results of the DEEP2 Redshift Survey." In *Discoveries and Research Prospects from 6- to 10-Meter-Class Telescopes II* (Puragra Guhathakurta, ed.), volume 4834 of *Society of Photo-Optical Instrumentation Engineers (SPIE) Conference Series*, 161–172.

de la Rosa Ignacio G., La Barbera Francesco, Ferreras Ignacio, and de Carvalho Reinaldo R. (2011), "The link between the star formation history and [/fe]." *Monthly Notices of the Royal Astronomical Society: Letters*, 418, L74–L78.

Dekel A. and Silk J. (1986), "The Origin of Dwarf Galaxies, Cold Dark Matter, and Biased Galaxy Formation." *ApJ*, 303, 39.

del Moral-Castro I., García-Lorenzo B., Ramos Almeida C., Ruiz-Lara T., Falcón-Barroso J., Sánchez S. F., Sánchez-Blázquez P., Márquez I., and Masegosa J.

(2019), "Spotting the differences between active and non-active twin galaxies on kpc-scales: a pilot study." *MNRAS*, 485, 3794–3815.

del Moral-Castro I., García-Lorenzo B., Ramos Almeida C., Ruiz-Lara T., Falcón-Barroso J., Sánchez S. F., Sánchez-Blázquez P., Márquez I., and Masegosa J. (2020), "Larger λ_R in the disc of isolated active spiral galaxies than in their non-active twins." , 639, L9.

DESI Collaboration et al. (2016), "The DESI Experiment Part I: Science,Targeting, and Survey Design." *arXiv e-prints*, arXiv:1611.00036.

Dodge Yadolah (2008), *Kolmogorov–Smirnov Test*, 283–287. Springer New York, New York, NY.

Donnari Martina, Pillepich Annalisa, Joshi Gandhali D., Nelson Dylan, Genel Shy, Marinacci Federico, Rodriguez-Gomez Vicente, Pakmor Rüdiger, Torrey Paul, Vogelsberger Mark, et al. (2021a), "Quenched fractions in the IllustrisTNG simulations: the roles of AGN feedback, environment, and pre-processing." *MNRAS*, 500, 4004–4024.

Donnari Martina, Pillepich Annalisa, Nelson Dylan, Marinacci Federico, Vogelsberger Mark, and Hernquist Lars (2021b), "Quenched fractions in the IllustrisTNG simulations: comparison with observations and other theoretical models." *MNRAS*, 506, 4760–4780.

Donnari Martina, Pillepich Annalisa, Nelson Dylan, Vogelsberger Mark, Genel Shy, Weinberger Rainer, Marinacci Federico, Springel Volker, and Hernquist Lars (2019), "The star formation activity of IllustrisTNG galaxies: main sequence, UVJ diagram, quenched fractions, and systematics." *MNRAS*, 485, 4817–4840.

Dressler A. (1980), "Galaxy morphology in rich clusters: implications for the formation and evolution of galaxies." *ApJ*, 236, 351–365.

Dressler Alan and Shectman Stephen A. (1987), "Systematics of the 4000 Angstrom Break in the Spectra of Galaxies." , 94, 899.

Driver S. P., Liske J., Davies L. J. M., Robotham A. S. G., Baldry I. K., Brown M. J. I., Cluver M., Kuijken K., Loveday J., and McMahon R. (2019), "4MOST Consortium Survey 7: Wide-Area VISTA Extragalactic Survey (WAVES)." *The Messenger*, 175, 46–49.

Eales S. A. et al. (2018), "The causes of the red sequence, the blue cloud, the green valley, and the green mountain." *MNRAS*, 481, 1183–1194.

Emsellem Eric, Cappellari Michele, Krajnović Davor, van de Ven Glenn, Bacon R., Bureau M., Davies Roger L., de Zeeuw P. T., Falcón-Barroso Jesús, Kuntschner Harald, et al. (2007), "The SAURON project - IX. A kinematic classification for early-type galaxies." *MNRAS*, 379, 401–417.

Faber S. M. and Jackson R. E. (1976), "Velocity dispersions and mass-to-light ratios for elliptical galaxies." *ApJ*, 204, 668–683.

Faber S. M., Willmer C. N. A., Wolf C., Koo D. C., Weiner B. J., Newman J. A., Im M., Coil A. L., Conroy C., Cooper M. C., et al. (2007), "Galaxy Luminosity Functions to z˜1 from DEEP2 and COMBO-17: Implications for Red Galaxy Formation." *ApJ*, 665, 265–294.

Falcón-Barroso Jesús, Bacon Roland, Bureau Martin, Cappellari Michele, Davies Roger L., de Zeeuw P. T., Emsellem Eric, Fathi Kambiz, Krajnović Davor, Kuntschner Harald, et al. (2006), "The SAURON project - VII. Integral-field absorption and emission-line kinematics of 24 spiral galaxy bulges." *MNRAS*, 369, 529–566.

Feldmann R., Carollo C. M., Mayer L., Renzini A., Lake G., Quinn T., Stinson G. S., and Yepes G. (2010), "The Evolution of Central Group Galaxies in Hydrodynamical Simulations." *ApJ*, 709, 218–240.

Ferreras I., Charlot S., and Silk J. (1999), "The Age and Metallicity Range of Early-Type Galaxies in Clusters." *ApJ*, 521, 81–89.

Ferreras I., La Barbera F., de la Rosa I. G., Vazdekis A., de Carvalho R. R., Falcón-Barroso J., and Ricciardelli E. (2013a), "Systematic variation of the stellar initial mass function with velocity dispersion in early-type galaxies." *MNRAS*, 429, L15–L19.

Ferreras I., Sharples R., Dunlop J. S., Pasquali A., La Barbera F., Vazdekis A., Khochfar S., Cropper M., Cimatti A., Cirasuolo M., et al. (2013b), "Chronos: A NIR spectroscopic galaxy survey. From the formation of galaxies to the peak of activity." *arXiv e-prints*, arXiv:1306.6333.

Ferreras Ignacio (2019), *Fundamentals of Galaxy Dynamics, Formation and Evolution*. UCL Press, London.

Ferreras Ignacio, Scott Nicholas, La Barbera Francesco, Croom Scott, van de Sande Jesse, Hopkins Andrew, Colless Matthew, Barone Tania M., d'Eugenio Francesco, Bland-Hawthorn Joss, et al. (2019), "The SAMI galaxy survey: stellar population radial gradients in early-type galaxies." *MNRAS*, 489, 608–622.

Fitzpatrick Edward L. (1999), "Correcting for the effects of interstellar extinction." *Publications of the Astronomical Society of the Pacific*, 111, 63.

Foster C., Mendel J. T., Lagos C. D. P., Wisnioski E., Yuan T., D'Eugenio F., Barone T. M., Harborne K. E., Vaughan S. P., Schulze F., et al. (2021), "The MAGPI survey: Science goals, design, observing strategy, early results and theoretical framework." , 38, e031.

Furlong M., Bower R. G., Theuns T., Schaye J., Crain R. A., Schaller M., Dalla Vecchia C., Frenk C. S., McCarthy I. G., Helly J., et al. (2015), "Evolution of galaxy stellar masses and star formation rates in the eagle simulations." *MNRAS*, 450, 4486–4504.

Gabor J. M., Davé R., Finlator K., and Oppenheimer B. D. (2010), "How is star formation quenched in massive galaxies?" *MNRAS*, 407, 749–771.

Gaibler V., Khochfar S., Krause M., and Silk J. (2012), "Jet-induced star formation in gas-rich galaxies." *MNRAS*, 425, 438–449.

Gallazzi A., Charlot S., Brinchmann J., White S. D. M., and Tremonti C. A. (2005), "The ages and metallicities of galaxies in the local universe." *MNRAS*, 362, 41–58.

Galliano F., Galametz M., and Jones A. P. (2018), "The Interstellar Dust Properties of Nearby Galaxies." , 56, 673–713.

Gardner Jonathan P., Mather John C., Clampin Mark, Doyon Rene, Greenhouse Matthew A., Hammel Heidi B., Hutchings John B., Jakobsen Peter, Lilly Simon J., Long Knox S., et al. (2006), "The James Webb Space Telescope." , 123, 485–606.

Genel Shy, Vogelsberger Mark, Springel Volker, Sijacki Debora, Nelson Dylan, Snyder Greg, Rodriguez-Gomez Vicente, Torrey Paul, and Hernquist Lars (2014), "Introducing the Illustris project: the evolution of galaxy populations across cosmic time." *MNRAS*, 445, 175–200.

Georgakakis A., Aird J., Schulze A., Dwelly T., Salvato M., Nandra K., Merloni A., and Schneider D. P. (2017), "Observational constraints on the specific accretion-rate distribution of X-ray-selected AGNs." *MNRAS*, 471, 1976–2001.

Girardi L., Bressan A., Bertelli G., and Chiosi C. (2000), "Evolutionary tracks and isochrones for low- and intermediate-mass stars: From 0.15 to 7 M_{sun}, and from Z=0.0004 to 0.03." *A&AS*, 141, 371–383.

Gkini Anamaria, Plionis Manolis, Chira Maria, and Koulouridis Elias (2021), "Host galaxy and orientation differences between different types of AGN." *arXiv e-prints*, arXiv:2101.01481.

Gonçalves T. S., Martin D. C., Menéndez-Delmestre K., Wyder T. K., and Koekemoer A. (2012), "Quenching Star Formation at Intermediate Redshifts: Downsizing of the Mass Flux Density in the Green Valley." *ApJ*, 759, 67.

Graves G. J., Faber S. M., and Schiavon R. P. (2009), "Dissecting the Red Sequence. I. Star-Formation Histories of Quiescent Galaxies: The Color-Magnitude versus the Color-σ Relation." *ApJ*, 693, 486–506.

Graves Genevieve J., Faber S. M., and Schiavon Ricardo P. (2010), "Dissecting the red sequence. iv. the role of truncation in the two-dimensional family of early-type galaxy star formation histories." *The Astrophysical Journal*, 721, 278.

Graves Genevieve J., Faber S. M., Schiavon Ricardo P., and Yan Renbin (2007), "Ages and abundances of red sequence galaxies as a function of liner emission-line strength." *ApJ*, 671, 243.

Gültekin K., Richstone D. O., Gebhardt K., Lauer T. R., Tremaine S., Aller M. C., Bender R., Dressler A., Faber S. M., Filippenko A. V., et al. (2009), "The M-σ and M-L Relations in Galactic Bulges, and Determinations of Their Intrinsic Scatter." *ApJ*, 698, 198–221.

Gunn J. E., Siegmund W. A., Mannery E. J., Owen R. E., Hull C. L., Leger R. F., Carey L. N., Knapp G. R., York D. G., Boroski W. N., et al. (2006), "The 2.5 m Telescope of the Sloan Digital Sky Survey." , 131, 2332–2359.

Gunn James E. and Gott III J. Richard (1972), "On the Infall of Matter Into Clusters of Galaxies and Some Effects on Their Evolution." *ApJ*, 176, 1.

Habouzit Mélanie, Genel Shy, Somerville Rachel S., Kocevski Dale, Hirschmann Michaela, Dekel Avishai, Choi Ena, Nelson Dylan, Pillepich Annalisa, Torrey Paul, et al. (2019), "Linking galaxy structural properties and star formation activity to black hole activity with IllustrisTNG." *MNRAS*, 484, 4413–4443.

Häring Nadine and Rix Hans-Walter (2004), "On the Black Hole Mass-Bulge Mass Relation." *ApJL*, 604, L89–L92.

Hathi N. P., Ferreras I., Pasquali A., Malhotra S., Rhoads J. E., Pirzkal N., Windhorst R. A., and Xu C. (2009), "Stellar Populations of Late-Type Bulges at z 1 in the Hubble Ultra Deep Field." *ApJ*, 690, 1866–1882.

Heckman Timothy M., Kauffmann Guinevere, Brinchmann Jarle, Charlot Stéphane, Tremonti Christy, and White Simon D. M. (2004), "Present-Day Growth of Black Holes and Bulges: The Sloan Digital Sky Survey Perspective." *ApJ*, 613, 109–118.

Hernán-Caballero A. et al. (2013), "SHARDS: stellar populations and star formation histories of a mass-selected sample of 0.65 z 1.1 galaxies." *MNRAS*, 434, 2136–2152.

Hirschmann Michaela, Charlot Stephane, Feltre Anna, Naab Thorsten, Choi Ena, Ostriker Jeremiah P., and Somerville Rachel S. (2017), "Synthetic nebular emission from massive galaxies - I: origin of the cosmic evolution of optical emission-line ratios." *MNRAS*, 472, 2468–2495.

Ho L. C. (2008), "Nuclear activity in nearby galaxies." , 46, 475–539.

Ho Luis C. (2009), "Radiatively Inefficient Accretion in Nearby Galaxies." *ApJ*, 699, 626–637.

Hogg David W., Baldry Ivan K., Blanton Michael R., and Eisenstein Daniel J. (2002), "The K correction." *arXiv e-prints*, astro-ph/0210394.

Hopkins P. F., Hernquist L., Cox T. J., Di Matteo T., Robertson B., and Springel V. (2006), "A Unified, Merger-driven Model of the Origin of Starbursts, Quasars, the Cosmic X-Ray Background, Supermassive Black Holes, and Galaxy Spheroids." *ApJ*, 163, 1–49.

Hopkins Philip F., Hernquist Lars, Cox Thomas J., and Kereš Dušan (2008), "A Cosmological Framework for the Co-Evolution of Quasars, Supermassive Black Holes, and Elliptical Galaxies. I. Galaxy Mergers and Quasar Activity." *ApJ*, 175, 356–389.

Hubble E. P. (1926a), "A spiral nebula as a stellar system: Messier 33." *ApJ*, 63.

Hubble E. P. (1926b), "Extragalactic nebulae." *ApJ*, 64.

Johnston Kathryn V., Sigurdsson Steinn, and Hernquist Lars (1999), "Measuring mass-loss rates from Galactic satellites." *MNRAS*, 302, 771–789.

Kalinova V., Colombo D., Sánchez S. F., Kodaira K., García-Benito R., González Delgado R., Rosolowsky E., and Lacerda E. A. D. (2021), "Star formation quenching stages of active and non-active galaxies." *arXiv e-prints*, arXiv:2101.10019.

Kauffmann G., White S. D. M., Heckman T. M., Ménard B., Brinchmann J., Charlot S., Tremonti C., and Brinkmann J. (2004), "The environmental dependence of the relations between stellar mass, structure, star formation and nuclear activity in galaxies." *MNRAS*, 353, 713–731.

Kauffmann G. et al. (2003), "Stellar masses and star formation histories for 10^5 galaxies from the Sloan Digital Sky Survey." *MNRAS*, 341, 33–53.

Kauffmann Guinevere, Heckman Timothy M., White Simon D. M., Charlot Stéphane, Tremonti Christy, Brinchmann Jarle, Bruzual Gustavo, Peng Eric W., Seibert Mark, Bernardi Mariangela, et al. (2003), "Stellar masses and star formation histories for 105 galaxies from the sloan digital sky survey." *Monthly Notices of the Royal Astronomical Society*, 341, 33–53.

Kaviraj S., Laigle C., Kimm T., Devriendt J. E. G., Dubois Y., Pichon C., Slyz A., Chisari E., and Peirani S. (2017), "The Horizon-AGN simulation: evolution of galaxy properties over cosmic time." *MNRAS*, 467, 4739–4752.

Keel W. C., Banfield J. K., Medling A. M., and Neff S. G. (2019), "Optical Detection of Star Formation in a Cold Dust Cloud in the Counterjet Direction of Centaurus A." *AJ*, 157, 66.

Kelvin L. S., Bremer M. N., Phillipps S., James P. A., Davies L. J. M., De Propris R., Moffett A. J., Percival S. M., Baldry I. K., Collins C. A., et al. (2018), "Galaxy and Mass Assembly (GAMA): variation in galaxy structure across the green valley." *MNRAS*, 477, 4116–4130.

Kennicutt Jr. Robert C. (1998), "Star Formation in Galaxies Along the Hubble Sequence." *ARA&A*, 36, 189–232.

Kewley L. J., Dopita M. A., Sutherland R. S., Heisler C. A., and Trevena J. (2001), "Theoretical Modeling of Starburst Galaxies." *ApJ*, 556, 121–140.

Kewley Lisa J., Groves Brent, Kauffmann Guinevere, and Heckman Tim (2006), "The host galaxies and classification of active galactic nuclei." *MNRAS*, 372, 961–976.

Kormendy J. (1977), "Brightness distributions in compact and normal galaxies. II. Structure parameters of the spheroidal component." *ApJ*, 218, 333–346.

Koyama Shuhei, Koyama Yusei, Yamashita Takuji, Hayashi Masao, Matsuhara Hideo, Nakagawa Takao, Namiki Shigeru V., Suzuki Tomoko L., Fukagawa Nao, Kodama Tadayuki, et al. (2019), "Do Galaxy Morphologies Really Affect the Efficiency of Star Formation During the Phase of Galaxy Transition?" *ApJ*, 874, 142.

Kroupa P. (2001), "On the variation of the initial mass function." *MNRAS*, 322, 231–246.

Kroupa Pavel (2002), "The Initial Mass Function of Stars: Evidence for Uniformity in Variable Systems." *Science*, 295, 82–91.

Kuntschner Harald and Davies Roger L. (1998), "The ages and metallicities of early-type galaxies in the Fornax cluster." , 295, L29–L33.

La Barbera F., Ferreras I., Vazdekis A., de la Rosa I. G., de Carvalho R. R., Trevisan M., Falcón-Barroso J., and Ricciardelli E. (2013), "SPIDER VIII - constraints on the stellar initial mass function of early-type galaxies from a variety of spectral features." *MNRAS*, 433, 3017–3047.

La Barbera F., Lopes P. A. A., de Carvalho R. R., de La Rosa I. G., and Berlind A. A. (2010), "SPIDER - III. Environmental dependence of the Fundamental Plane of early-type galaxies." *MNRAS*, 408, 1361–1386.

La Barbera F., Pasquali A., Ferreras I., Gallazzi A., de Carvalho R. R., and de la Rosa I. G. (2014), "SPIDER - X. Environmental effects in central and satellite early-type galaxies through the stellar fossil record." *MNRAS*, 445, 1977–1996.

Lacerda Eduardo A. D., Sánchez Sebastián F., Cid Fernandes R., López-Cobá Carlos, Espinosa-Ponce Carlos, and Galbany L. (2020), "Galaxies hosting an active galactic nucleus: a view from the CALIFA survey." *MNRAS*, 492, 3073–3090.

Lacerna I., Ibarra-Medel H., Avila-Reese V., Hernández-Toledo H. M., Vázquez-Mata J. A., and Sánchez S. F. (2020), "SDSS-IV MaNGA: Global and local stellar population properties of elliptical galaxies." , 644, A117.

Lee Gwang-Ho, Hwang Ho Seong, Lee Myung Gyoon, Ko Jongwan, Sohn Jubee, Shim Hyunjin, and Diaferio Antonaldo (2015), "Galaxy Evolution in the Mid-infrared Green Valley: A Case of the A2199 Supercluster." *ApJ*, 800, 80.

Lee Seong-Kook, Ferguson Henry C., Somerville Rachel S., Wiklind Tommy, and Giavalisco Mauro (2010), "The Estimation of Star Formation Rates and Stellar Population Ages of High-redshift Galaxies from Broadband Photometry." *ApJ*, 725, 1644–1651.

Li Cheng, Wang Enci, Lin Lin, Bershady Matthew A., Bundy Kevin, Tremonti Christy A., Xiao Ting, Yan Renbin, Bizyaev Dmitry, Blanton Michael, et al. (2015), "P-MaNGA: Gradients in Recent Star Formation Histories as Diagnostics for Galaxy Growth and Death." *ApJ*, 804, 125.

Li Shuang-Liang and Xie Fu-Guo (2017), "A strong negative correlation between radio loudness R_{UV} and optical-to-X-ray spectral index α_{ox} in low-luminosity AGNs." *MNRAS*, 471, 2848–2855.

Li Yuan, Habouzit Melanie, Genel Shy, Somerville Rachel, Terrazas Bryan A., Bell Eric F., Pillepich Annalisa, Nelson Dylan, Weinberger Rainer, Rodriguez-Gomez Vicente, et al. (2019), "Correlations Between Black Holes and Host Galaxies in the Illustris and IllustrisTNG Simulations." *arXiv e-prints*, arXiv:1910.00017.

Lintott Chris J., Schawinski Kevin, Slosar Anže, Land Kate, Bamford Steven, Thomas Daniel, Raddick M. Jordan, Nichol Robert C., Szalay Alex, Andreescu Dan, et al. (2008), "Galaxy Zoo: morphologies derived from visual inspection of galaxies from the Sloan Digital Sky Survey." *MNRAS*, 389, 1179–1189.

Lipari Sebastian, Colina Luis, and Macchetto F. (1994), "Galaxies with Extreme Infrared and Fe II Emission. I. Markarian 231: The Signature of a Young Infrared QSO." *ApJ*, 427, 174.

Lotz Jennifer M., Primack Joel, and Madau Piero (2004), "A New Nonparametric Approach to Galaxy Morphological Classification." , 128, 163–182.

Mahoro Antoine, Pović Mirjana, and Nkundabakura Pheneas (2017), "Star formation of far-IR AGN and non-AGN galaxies in the green valley: possible implication of AGN positive feedback." *MNRAS*, 471, 3226–3233.

Mahoro Antoine, Pović Mirjana, Nkundabakura Pheneas, Nyiransengiyumva Beatrice, and Väisänen Petri (2019), "Star formation in far-IR AGN and non-AGN galaxies in the green valley - II. Morphological analysis." *MNRAS*, 485, 452–463.

Man Zhong-yi, Peng Ying-jie, Kong Xu, Guo Ke-xin, Zhang Cheng-peng, and Dou Jing (2019), "The dependence of AGN activity on environment in SDSS." *MNRAS*, 488, 89–98.

Maraston Claudia (2005), "Evolutionary population synthesis: models, analysis of the ingredients and application to high-z galaxies." *MNRAS*, 362, 799–825.

Marinacci Federico, Vogelsberger Mark, Pakmor Rüdiger, Torrey Paul, Springel Volker, Hernquist Lars, Nelson Dylan, Weinberger Rainer, Pillepich Annalisa, Naiman Jill, et al. (2018), "First results from the IllustrisTNG simulations: radio haloes and magnetic fields." *MNRAS*, 480, 5113–5139.

Martin D. Christopher, Fanson James, Schiminovich David, Morrissey Patrick, Friedman Peter G., Barlow Tom A., Conrow Tim, Grange Robert, Jelinsky

Patrick N., Milliard Bruno, et al. (2005), "The Galaxy Evolution Explorer: A Space Ultraviolet Survey Mission." *ApJL*, 619, L1–L6.

Martin D. Christopher, Wyder Ted K., Schiminovich David, Barlow Tom A., Forster Karl, Friedman Peter G., Morrissey Patrick, Neff Susan G., Seibert Mark, Small Todd, et al. (2007), "The UV-optical galaxy color-magnitude diagram. III. constraints on evolution from the blue to the red sequence." *ApJ*, 173, 342–356.

Matteucci Francesca and Recchi Simone (2001), "On the Typical Timescale for the Chemical Enrichment from Type Ia Supernovae in Galaxies." *ApJ*, 558, 351–358.

McAlpine S., Helly J. C., Schaller M., Trayford J. W., Qu Y., Furlong M., Bower R. G., Crain R. A., Schaye J., Theuns T., et al. (2016), "The EAGLE simulations of galaxy formation: Public release of halo and galaxy catalogues." *Astronomy and Computing*, 15, 72–89.

McConnachie Alan W., Babusiaux Carine, Balogh Michael, Caffau Elisabetta, Côté Pat, Driver Simon, Robotham Aaron, Starkenburg Else, Venn Kim, and Walker Matthew (2016), "A concise overview of the Maunakea Spectroscopic Explorer." *arXiv e-prints*, arXiv:1606.00060.

McIntosh Daniel H., Wagner Cory, Cooper Andrew, Bell Eric F., Kereš Dušan, Bosch Frank C. van den, Gallazzi Anna, Haines Tim, Mann Justin, Pasquali Anna, et al. (2014), "A new population of recently quenched elliptical galaxies in the sdss." *Monthly Notices of the Royal Astronomical Society*, 442, 533–557.

McKinley B., Tingay S. J., Carretti E., Ellis S., Bland-Hawthorn J., Morganti R., Line J., McDonald M., Veilleux S., Wahl Olsen R., et al. (2018), "The jet/wind outflow in Centaurus A: a local laboratory for AGN feedback." *MNRAS*, 474, 4056–4072.

McLure R. J., Pentericci L., Cimatti A., Dunlop J. S., Elbaz D., Fontana A., Nandra K., Amorin R., Bolzonella M., Bongiorno A., et al. (2018), "The VANDELS ESO public spectroscopic survey." *MNRAS*, 479, 25–42.

Mendez Alexander J., Coil Alison L., Lotz Jennifer, Salim Samir, Moustakas John, and Simard Luc (2011), "AEGIS: The Morphologies of Green Galaxies at 0.4 ¡ z ¡ 1.2." *ApJ*, 736, 110.

Méndez-Abreu J., Ruiz-Lara T., Sánchez-Menguiano L., de Lorenzo-Cáceres A., Costantin L., Catalán-Torrecilla C., Florido E., Aguerri J. A. L., Bland-Hawthorn J., Corsini E. M., et al. (2017), "Two-dimensional multi-component photometric decomposition of CALIFA galaxies." , 598, A32.

Mo H., van den Bosch F., and S. White (2010), *Galaxy formation and evolution*. Cambridge University Press, Cambridge New York.

Naab Thorsten, Oser L., Emsellem E., Cappellari Michele, Krajnović D., McDermid R. M., Alatalo K., Bayet E., Blitz L., Bois M., et al. (2014), "The ATLAS^{3D} project - XXV. Two-dimensional kinematic analysis of simulated galaxies and the cosmological origin of fast and slow rotators." *MNRAS*, 444, 3357–3387.

Naab Thorsten and Ostriker Jeremiah P. (2017), "Theoretical Challenges in Galaxy Formation." *ARA&A*, 55, 59–109.

Naiman Jill P., Pillepich Annalisa, Springel Volker, Ramirez-Ruiz Enrico, Torrey Paul, Vogelsberger Mark, Pakmor Rüdiger, Nelson Dylan, Marinacci Federico, Hernquist Lars, et al. (2018), "First results from the IllustrisTNG simulations: a tale of two elements - chemical evolution of magnesium and europium." *MNRAS*, 477, 1206–1224.

Nelson Dylan, Pillepich Annalisa, Springel Volker, Pakmor Rüdiger, Weinberger Rainer, Genel Shy, Torrey Paul, Vogelsberger Mark, Marinacci Federico, and Hernquist Lars (2019a), "First results from the TNG50 simulation: galactic outflows driven by supernovae and black hole feedback." *MNRAS*, 490, 3234–3261.

Nelson Dylan, Pillepich Annalisa, Springel Volker, Weinberger Rainer, Hernquist Lars, Pakmor Rüdiger, Genel Shy, Torrey Paul, Vogelsberger Mark, Kauffmann Guinevere, et al. (2018), "First results from the IllustrisTNG simulations: the galaxy colour bimodality." *MNRAS*, 475, 624–647.

Nelson Dylan, Springel Volker, Pillepich Annalisa, Rodriguez-Gomez Vicente, Torrey Paul, Genel Shy, Vogelsberger Mark, Pakmor Ruediger, Marinacci Federico, Weinberger Rainer, et al. (2019b), "The IllustrisTNG simulations: public data release." *Computational Astrophysics and Cosmology*, 6, 2.

Pasquali A. (2015), "How environment drives galaxy evolution: Lessons learnt from satellite galaxies." *Astronomische Nachrichten*, 336, 505.

Pasquali A., Smith R., Gallazzi A., De Lucia G., Zibetti S., Hirschmann M., and Yi S. K. (2019), "Physical properties of SDSS satellite galaxies in projected phase space." *MNRAS*, 484, 1702–1723.

Pasquali Anna, Gallazzi Anna, Fontanot Fabio, van den Bosch Frank C., De Lucia Gabriella, Mo H. J., and Yang Xiaohu (2010), "Ages and metallicities of central and satellite galaxies: implications for galaxy formation and evolution." *MNRAS*, 407, 937–954.

Pasquali Anna, Gallazzi Anna, and van den Bosch Frank C. (2012), "The gas-phase metallicity of central and satellite galaxies in the Sloan Digital Sky Survey." *MNRAS*, 425, 273–286.

Peng Y., Maiolino R., and Cochrane R. (2015), "Strangulation as the primary mechanism for shutting down star formation in galaxies." , 521, 192–195.

Peng Ying-jie, Lilly Simon J., Kovač Katarina, Bolzonella Micol, Pozzetti Lucia, Renzini Alvio, Zamorani Gianni, Ilbert Olivier, Knobel Christian, Iovino Angela, et al. (2010), "Mass and Environment as Drivers of Galaxy Evolution in SDSS and zCOSMOS and the Origin of the Schechter Function." *ApJ*, 721, 193–221.

Phillipps S., Bremer M. N., Hopkins A. M., De Propris R., Taylor E. N., James P. A., Davies L. J. M., Cluver M. E., Driver S. P., Eales S. A., et al. (2019), "Galaxy and Mass Assembly (GAMA): time-scales for galaxies crossing the green valley." *MNRAS*, 485, 5559–5572.

Pillepich Annalisa, Nelson Dylan, Hernquist Lars, Springel Volker, Pakmor Rüdiger, Torrey Paul, Weinberger Rainer, Genel Shy, Naiman Jill P., Marinacci Federico, et al. (2018a), "First results from the IllustrisTNG simulations: the stellar mass content of groups and clusters of galaxies." *MNRAS*, 475, 648–675.

Pillepich Annalisa, Nelson Dylan, Springel Volker, Pakmor Rüdiger, Torrey Paul, Weinberger Rainer, Vogelsberger Mark, Marinacci Federico, Genel Shy, van der Wel Arjen, et al. (2019), "First results from the TNG50 simulation: the evolution of stellar and gaseous discs across cosmic time." *MNRAS*, 490, 3196–3233.

Pillepich Annalisa, Springel Volker, Nelson Dylan, Genel Shy, Naiman Jill, Pakmor Rüdiger, Hernquist Lars, Torrey Paul, Vogelsberger Mark, Weinberger Rainer, et al. (2018b), "Simulating galaxy formation with the IllustrisTNG model." *MNRAS*, 473, 4077–4106.

Planck Collaboration, Ade P. A. R., Aghanim N., Alves M. I. R., Armitage-Caplan C., Arnaud M., Ashdown M., Atrio-Barandela F., Aumont J., Aussel H., et al. (2014), "Planck 2013 results. I. Overview of products and scientific results." *A&A*, 571, A1.

Planck Collaboration, Ade P. A. R., Aghanim N., Arnaud M., Ashdown M., Aumont J., Baccigalupi C., Banday A. J., Barreiro R. B., Bartlett J. G., et al. (2016), "Planck 2015 results. XIII. Cosmological parameters." *A&A*, 594, A13.

Poggianti B. M. and Barbaro G. (1997), "Indicators of star formation: 4000 Å break and Balmer lines." , 325, 1025–1030.

Ramos Almeida C., Levenson N. A., Alonso-Herrero A., Asensio Ramos A., Rodríguez Espinosa J. M., Pérez García A. M., Packham C., Mason R., Radomski J. T., and Díaz-Santos T. (2011), "Testing the Unification Model for Active Galactic Nuclei in the Infrared: Are the Obscuring Tori of Type 1 and 2 Seyferts Different?" *ApJ*, 731, 92.

Reines Amy E. and Volonteri Marta (2015), "Relations between Central Black Hole Mass and Total Galaxy Stellar Mass in the Local Universe." *ApJ*, 813, 82.

Richstone D. O. (1976), "Collisions of galaxies in dense clusters. II. Dynamical evolution of cluster galaxies." *ApJ*, 204, 642–648.

Roche N., Bernardi M., and Hyde J. (2009), "Spectral-based k-corrections and implications for the colour-magnitude relation of E/S0s and its evolution." *MNRAS*, 398, 1549–1562.

Rogers Ben, Ferreras Ignacio, Pasquali Anna, Bernardi Mariangela, Lahav Ofer, and Kaviraj Sugata (2010), "The role of environment on the formation of early-type galaxies." *MNRAS*, 405, 329–339.

Rosas-Guevara Y. M., Bower R. G., Schaye J., Furlong M., Frenk C. S., Booth C. M., Crain R. A., Dalla Vecchia C., Schaller M., and Theuns T. (2015), "The impact of angular momentum on black hole accretion rates in simulations of galaxy formation." *MNRAS*, 454, 1038–1057.

Rowlands K., Wild V., Bourne N., Bremer M., Brough S., Driver S. P., Hopkins A. M., Owers M. S., Phillipps S., Pimbblet K., et al. (2018), "Galaxy And Mass Assembly (GAMA): The mechanisms for quiescent galaxy formation at z$<$1." *MNRAS*, 473, 1168–1185.

Saha M. N. (1921), "On a Physical Theory of Stellar Spectra." *Proceedings of the Royal Society of London Series A*, 99, 135–153.

Salim S. (2014), "Green Valley Galaxies." *Serb. Astron. J.*, 189, 1–14.

Salim Samir, Dickinson Mark, Michael Rich R., Charlot Stéphane, Lee Janice C., Schiminovich David, Pérez-González Pablo G., Ashby Matthew L. N., Papovich Casey, Faber S. M., et al. (2009), "Mid-IR Luminosities and UV/Optical Star Formation Rates at z $<$ 1.4." *ApJ*, 700, 161–182.

Salim Samir and Narayanan Desika (2020), "The Dust Attenuation Law in Galaxies." , 58, 529–575.

Salim Samir, Rich R. Michael, Charlot Stéphane, Brinchmann Jarle, Johnson Benjamin D., Schiminovich David, Seibert Mark, Mallery Ryan, Heckman Timothy M., Forster Karl, et al. (2007), "UV Star Formation Rates in the Local Universe." *ApJ*, 173, 267–292.

Salpeter Edwin E. (1955), "The Luminosity Function and Stellar Evolution." *ApJ*, 121, 161.

Sampaio V. M., de Carvalho R. R., Ferreras I., Laganá T. F., Ribeiro A. L. B., and Rembold S. B. (2021), "Investigating the projected phase space of Gaussian and non-Gaussian clusters." *MNRAS*, 503, 3065–3080.

Sánchez S. F., Avila-Reese V., Hernandez-Toledo H., Cortes-Suárez E., Rodríguez-Puebla A., Ibarra-Medel H., Cano-Díaz M., Barrera-Ballesteros J. K., Negrete C. A., Calette A. R., et al. (2018), "SDSS IV MaNGA - Properties of AGN Host Galaxies." , 54, 217–260.

Sánchez S. F., García-Benito R., Zibetti S., Walcher C. J., Husemann B., Mendoza M. A., Galbany L., Falcón-Barroso J., Mast D., Aceituno J., et al. (2016), "CALIFA, the Calar Alto Legacy Integral Field Area survey. IV. Third public data release." , 594, A36.

Sánchez S. F., Kennicutt R. C., Gil de Paz A., van de Ven G., Vílchez J. M., Wisotzki L., Walcher C. J., Mast D., Aguerri J. A. L., Albiol-Pérez S., et al. (2012), "CALIFA, the Calar Alto Legacy Integral Field Area survey. I. Survey presentation." , 538, A8.

Sánchez-Blázquez P., Peletier R. F., Jiménez-Vicente J., Cardiel N., Cenarro A. J., Falcón-Barroso J., Gorgas J., Selam S., and Vazdekis A. (2006), "Medium-resolution Isaac Newton Telescope library of empirical spectra." *MNRAS*, 371, 703–718.

Sansom A. E. and Northeast M. S. (2008), "Bimodality in low-luminosity E and S0 galaxies." *MNRAS*, 387, 331–343.

Sarzi Marc, Falcón-Barroso Jesús, Davies Roger L., Bacon Roland, Bureau Martin, Cappellari Michele, de Zeeuw P. Tim, Emsellem Eric, Fathi Kambiz, Krajnović Davor, et al. (2006), "The SAURON project - V. Integral-field emission-line kinematics of 48 elliptical and lenticular galaxies." *MNRAS*, 366, 1151–1200.

Schawinski K., Kaviraj S., Khochfar S., Yoon S. J., Yi S. K., Deharveng J. M., Boselli A., Barlow T., Conrow T., Forster K., et al. (2007), "The Effect of Environment on the Ultraviolet Color-Magnitude Relation of Early-Type Galaxies." *ApJ*, 173, 512–523.

Schawinski Kevin, Koss Michael, Berney Simon, and Sartori Lia F. (2015), "Active galactic nuclei flicker: an observational estimate of the duration of black hole growth phases of $\sim 10^5$ yr." *MNRAS*, 451, 2517–2523.

Schawinski Kevin et al. (2014), "The green valley is a red herring: Galaxy zoo reveals two evolutionary pathways towards quenching of star formation in early- and late-type galaxies." *MNRAS*, 440.

Schaye J. et al. (2015), "The EAGLE project: simulating the evolution and assembly of galaxies and their environments." *MNRAS*, 446, 521–554.

Schaye Joop and Dalla Vecchia Claudio (2008), "On the relation between the Schmidt and Kennicutt-Schmidt star formation laws and its implications for numerical simulations." *MNRAS*, 383, 1210–1222.

Schechter P. (1976), "An analytic expression for the luminosity function for galaxies." *ApJ*, 203, 297–306.

Schiminovich David, Wyder Ted K., Martin D. Christopher, Johnson Benjamin. D., Salim Samir, Seibert Mark, Treyer Marie A., Budavári Tamás, Hoopes Charles, Zamojski Michel, et al. (2007), "The UV-Optical Color Magnitude Diagram. II. Physical Properties and Morphological Evolution On and Off of a Star-forming Sequence." *ApJ*, 173, 315–341.

Schramm Malte and Silverman John D. (2013), "The Black Hole-Bulge Mass Relation of Active Galactic Nuclei in the Extended Chandra Deep Field-South Survey." *ApJ*, 767, 13.

Schulze A., Bongiorno A., Gavignaud I., Schramm M., Silverman J., Merloni A., Zamorani G., Hirschmann M., Mainieri V., Wisotzki L., et al. (2015), "The cosmic growth of the active black hole population at 1 <z <2 in zCOSMOS, VVDS and SDSS." *MNRAS*, 447, 2085–2111.

Sersic Jose Luis (1968), *Atlas de Galaxias Australes*.

Shankar F., Lapi A., Salucci P., De Zotti G., and Danese L. (2006), "New Relationships between Galaxy Properties and Host Halo Mass, and the Role of Feedbacks in Galaxy Formation." *ApJ*, 643, 14–25.

Sijacki Debora, Springel Volker, Di Matteo Tiziana, and Hernquist Lars (2007), "A unified model for AGN feedback in cosmological simulations of structure formation." *MNRAS*, 380, 877–900.

Sijacki Debora, Vogelsberger Mark, Genel Shy, Springel Volker, Torrey Paul, Snyder Gregory F., Nelson Dylan, and Hernquist Lars (2015), "The Illustris simulation: the evolving population of black holes across cosmic time." *MNRAS*, 452, 575–596.

Silk Joseph and Rees Martin J. (1998), "Quasars and galaxy formation." , 331, L1–L4.

Simard Luc, Willmer Christopher N. A., Vogt Nicole P., Sarajedini Vicki L., Phillips Andrew C., Weiner Benjamin J., Koo David C., Im Myungshin, Illingworth Garth D., and Faber S. M. (2002), "The DEEP Groth Strip Survey. II. Hubble Space Telescope Structural Parameters of Galaxies in the Groth Strip." *ApJ*, 142, 1–33.

Smee Stephen A. et al. (2013), "The Multi-object, Fiber-fed Spectrographs for the

Sloan Digital Sky Survey and the Baryon Oscillation Spectroscopic Survey." *AJ*, 146, 32.

Smethurst R. J., Lintott C. J., Simmons B. D., Schawinski K., Marshall P. J., Bamford S., Fortson L., Kaviraj S., Masters K. L., Melvin T., et al. (2015), "Galaxy Zoo: evidence for diverse star formation histories through the green valley." *MNRAS*, 450, 435–453.

Somerville Rachel S. and Davé Romeel (2015), "Physical Models of Galaxy Formation in a Cosmological Framework." , 53, 51–113.

Somerville Rachel S., Hopkins Philip F., Cox Thomas J., Robertson Brant E., and Hernquist Lars (2008), "A semi-analytic model for the co-evolution of galaxies, black holes and active galactic nuclei." *MNRAS*, 391, 481–506.

Spindler Ashley, Wake David, Belfiore Francesco, Bershady Matthew, Bundy Kevin, Drory Niv, Masters Karen, Thomas Daniel, Westfall Kyle, and Wild Vivienne (2018), "SDSS-IV MaNGA: the spatial distribution of star formation and its dependence on mass, structure, and environment." *MNRAS*, 476, 580–600.

Spinoglio L. and Fernández-Ontiveros J. (2021), "AGN types and unification model." *IAU Symposium*, 356, 29–43.

Springel V., Pakmor R., Pillepich A., Weinberger R., Nelson D., Hernquist L., Vogelsberger M., Genel S., Torrey P., Marinacci F., et al. (2018), "First results from the IllustrisTNG simulations: matter and galaxy clustering." *MNRAS*, 475, 676–698.

Springel Volker (2005), "The cosmological simulation code GADGET-2." *MNRAS*, 364, 1105–1134.

Springel Volker (2010), "E pur si muove: Galilean-invariant cosmological hydrodynamical simulations on a moving mesh." *MNRAS*, 401, 791–851.

Springel Volker and Hernquist Lars (2003), "Cosmological smoothed particle hydrodynamics simulations: a hybrid multiphase model for star formation." *MNRAS*, 339, 289–311.

Steinhauser Dominik, Schindler Sabine, and Springel Volker (2016), "Simulations of ram-pressure stripping in galaxy-cluster interactions." , 591, A51.

Strateva I. et al. (2001), "Color Separation of Galaxy Types in the Sloan Digital Sky Survey Imaging Data." *AJ*, 122, 1861–1874.

Sugai Hajime, Karoji Hiroshi, Takato Naruhisa, Tamura Naoyuki, Shimono Atsushi, Ohyama Youichi, Ueda Akitoshi, Ling Hung-Hsu, Vital de Arruda Marcio, Barkhouser Robert H., et al. (2012), "Prime focus spectrograph: Subaru's future." In *Ground-based and Airborne Instrumentation for Astronomy IV* (Ian S. McLean, Suzanne K. Ramsay, and Hideki Takami, eds.), volume 8446 of *Society of Photo-Optical Instrumentation Engineers (SPIE) Conference Series*, 84460Y.

Sutherland Ralph S. and Dopita M. A. (1993), "Cooling Functions for Low-Density Astrophysical Plasmas." *ApJ*, 88, 253.

Tacchella S., Carollo C. M., Renzini A., Förster Schreiber N. M., Lang P., Wuyts S., Cresci G., Dekel A., Genzel R., Lilly S. J., et al. (2015), "Evidence for mature bulges and an inside-out quenching phase 3 billion years after the Big Bang." *Science*, 348, 314–317.

Taylor Edward N. et al. (2015), "Galaxy and mass assembly (gama): deconstructing bimodality – i. red ones and blue ones." *MNRAS*, 446, 2144–2185.

Terrazas Bryan A., Bell Eric F., Pillepich Annalisa, Nelson Dylan, Somerville Rachel S., Genel Shy, Weinberger Rainer, Habouzit Mélanie, Li Yuan, Hernquist Lars, et al. (2020), "The relationship between black hole mass and galaxy properties: examining the black hole feedback model in IllustrisTNG." *MNRAS*, 493, 1888–1906.

Thomas D., Greggio L., and Bender R. (1999), "Constraints on galaxy formation from alpha-enhancement in luminous elliptical galaxies." *MNRAS*, 302, 537–548.

Thomas D., Maraston C., and Bender R. (2003), "Stellar population models of Lick indices with variable element abundance ratios." *MNRAS*, 339, 897–911.

Thomas D., Maraston C., Bender R., and Mendes de Oliveira C. (2005), "The Epochs of Early-Type Galaxy Formation as a Function of Environment." *ApJ*, 621, 673–694.

Thomas Daniel, Maraston Claudia, and Korn Andreas (2004), "Higher-order Balmer line indices in α/Fe-enhanced stellar population models." , 351, L19–L23.

Thomas Daniel, Maraston Claudia, Schawinski Kevin, Sarzi Marc, and Silk Joseph (2010), "Environment and self-regulation in galaxy formation." *MNRAS*, 404, 1775–1789.

Trager S. C., Worthey G., Faber S. M., Burstein D., and González J. J. (1998), "Old Stellar Populations. VI. Absorption-Line Spectra of Galaxy Nuclei and Globular Clusters." *ApJ*, 116, 1–28.

Trayford J. W., Theuns T., Bower R. G., Crain R. A., Lagos C. d. P., Schaller M., and Schaye J. (2016), "It is not easy being green: the evolution of galaxy colour in the EAGLE simulation." *MNRAS*, 460, 3925–3939.

Trayford James W., Camps Peter, Theuns Tom, Baes Maarten, Bower Richard G., Crain Robert A., Gunawardhana Madusha L. P., Schaller Matthieu, Schaye Joop, and Frenk Carlos S. (2017), "Optical colours and spectral indices of z = 0.1 eagle galaxies with the 3D dust radiative transfer code skirt." *MNRAS*, 470, 771–799.

Trayford James W., Theuns Tom, Bower Richard G., Schaye Joop, Furlong Michelle, Schaller Matthieu, Frenk Carlos S., Crain Robert A., Dalla Vecchia

Claudio, and McCarthy Ian G. (2015), "Colours and luminosities of z = 0.1 galaxies in the EAGLE simulation." *MNRAS*, 452, 2879–2896.

Tremonti Christy A., Heckman Timothy M., Kauffmann Guinevere, Brinchmann Jarle, Charlot Stéphane, White Simon D. M., Seibert Mark, Peng Eric W., Schlegel David J., Uomoto Alan, et al. (2004), "The Origin of the Mass-Metallicity Relation: Insights from 53,000 Star-forming Galaxies in the Sloan Digital Sky Survey." *ApJ*, 613, 898–913.

Tress Mónica et al. (2018), "SHARDS: constraints on the dust attenuation law of star-forming galaxies at z 2." *MNRAS*, 475, 2363–2374.

Trussler James, Maiolino Roberto, Maraston Claudia, Peng Yingjie, Thomas Daniel, Goddard Daniel, and Lian Jianhui (2020), "Both starvation and outflows drive galaxy quenching." *MNRAS*, 491, 5406–5434.

Tully R. B. and Fisher J. R. (1977), "Reprint of 1977A&A....54..661T. A new method of determining distance to galaxies." , 500, 105–117.

Valiante E., Smith M. W. L., Eales S., Maddox S. J., Ibar E., Hopwood R., Dunne L., Cigan P. J., Dye S., Pascale E., et al. (2016), "The Herschel-ATLAS data release 1 - I. Maps, catalogues and number counts." *MNRAS*, 462, 3146–3179.

van den Bosch Frank C., Aquino Daniel, Yang Xiaohu, Mo H. J., Pasquali Anna, McIntosh Daniel H., Weinmann Simone M., and Kang Xi (2008), "The importance of satellite quenching for the build-up of the red sequence of present-day galaxies." *MNRAS*, 387, 79–91.

van der Wel A., Noeske K., Bezanson R., Pacifici C., Gallazzi A., Franx M., Muñoz-Mateos J. C., Bell E. F., Brammer G., Charlot S., et al. (2016), "The VLT LEGA-C Spectroscopic Survey: The Physics of Galaxies at a Lookback Time of 7 Gyr." *ApJ*, 223, 29.

van Dokkum Pieter G., Labbé Ivo, Marchesini Danilo, Quadri Ryan, Brammer Gabriel, Whitaker Katherine E., Kriek Mariska, Franx Marijn, Rudnick Gregory,

Illingworth Garth, et al. (2009), "The NEWFIRM Medium-Band Survey: Filter Definitions and First Results." , 121, 2.

Vazdekis A., Koleva M., Ricciardelli E., Röck B., and Falcón-Barroso J. (2016), "UV-extended E-MILES stellar population models: young components in massive early-type galaxies." *MNRAS*, 463, 3409–3436.

Vazdekis A., Ricciardelli E., Cenarro A. J., Rivero-González J. G., Díaz-García L. A., and Falcón-Barroso J. (2012), "MIUSCAT: extended MILES spectral coverage - I. Stellar population synthesis models." *MNRAS*, 424, 157–171.

Villarroel Beatriz and Korn Andreas J. (2014), "The different neighbours around Type-1 and Type-2 active galactic nuclei." *Nature Physics*, 10, 417–420.

Vogelsberger Mark, Genel Shy, Springel Volker, Torrey Paul, Sijacki Debora, Xu Dandan, Snyder Greg, Nelson Dylan, and Hernquist Lars (2014), "Introducing the Illustris Project: simulating the coevolution of dark and visible matter in the Universe." *MNRAS*, 444, 1518–1547.

Walcher C. J., Wisotzki L., Bekeraité S., Husemann B., Iglesias-Páramo J., Backsmann N., Barrera Ballesteros J., Catalán-Torrecilla C., Cortijo C., del Olmo A., et al. (2014), "CALIFA: a diameter-selected sample for an integral field spectroscopy galaxy survey." , 569, A1.

Walker Lisa May, Butterfield Natalie, Johnson Kelsey, Zucker Catherine, Gallagher Sarah, Konstantopoulos Iraklis, Zabludoff Ann, Hornschemeier Ann E., Tzanavaris Panayiotis, and Charlton Jane C. (2013), "The Optical Green Valley versus Mid-infrared Canyon in Compact Groups." *ApJ*, 775, 129.

Weinberger Rainer, Springel Volker, Hernquist Lars, Pillepich Annalisa, Marinacci Federico, Pakmor Rüdiger, Nelson Dylan, Genel Shy, Vogelsberger Mark, Naiman Jill, et al. (2017), "Simulating galaxy formation with black hole driven thermal and kinetic feedback." *MNRAS*, 465, 3291–3308.

Weinberger Rainer, Springel Volker, Pakmor Rüdiger, Nelson Dylan, Genel Shy, Pillepich Annalisa, Vogelsberger Mark, Marinacci Federico, Naiman Jill, Torrey Paul, et al. (2018), "Supermassive black holes and their feedback effects in the IllustrisTNG simulation." *MNRAS*, 479, 4056–4072.

Whitaker K. E., Labbé I., van Dokkum P. G., Brammer G., Kriek M., Marchesini D., Quadri R. F., Franx M., Muzzin A., Williams R. J., et al. (2011), "The NEWFIRM Medium-band Survey: Photometric Catalogs, Redshifts, and the Bimodal Color Distribution of Galaxies out to z ˜ 3." *ApJ*, 735, 86.

Wilkinson David M., Maraston Claudia, Goddard Daniel, Thomas Daniel, and Parikh Taniya (2017), "FIREFLY (Fitting IteRativEly For Likelihood analYsis): a full spectral fitting code." *MNRAS*, 472, 4297–4326.

Williams R. J., Quadri R. F., Franx M., van Dokkum P., and Labbé I. (2009), "Detection of Quiescent Galaxies in a Bicolor Sequence from Z = 0-2." *ApJ*, 691, 1879–1895.

Worthey Guy (1994), "Comprehensive Stellar Population Models and the Disentanglement of Age and Metallicity Effects." *ApJ*, 95, 107.

Worthey Guy and Ottaviani D. L. (1997), "Hγ and Hδ Absorption Features in Stars and Stellar Populations." , 111, 377–386.

Wright Edward L., Eisenhardt Peter R. M., Mainzer Amy K., Ressler Michael E., Cutri Roc M., Jarrett Thomas, Kirkpatrick J. Davy, Padgett Deborah, McMillan Robert S., Skrutskie Michael, et al. (2010), "The Wide-field Infrared Survey Explorer (WISE): Mission Description and Initial On-orbit Performance." , 140, 1868–1881.

Wright Ruby J., Lagos Claudia del P., Davies Luke J. M., Power Chris, Trayford James W., and Wong O. Ivy (2019), "Quenching time-scales of galaxies in the EAGLE simulations." *MNRAS*, 487, 3740–3758.

Wu Po-Feng, Nelson Dylan, van der Wel Arjen, Pillepich Annalisa, Zibetti Stefano, Bezanson Rachel, D'Eugenio Francesco, Gallazzi Anna, Pacifici Camilla, Straatman Caroline M. S., et al. (2021), "Towards precise galaxy evolution: a comparison between spectral indices of $z \sim 1$ galaxies in the IllustrisTNG simulation and the LEGA-C survey." *arXiv e-prints*, arXiv:2108.10455.

Wyder Ted K., Martin D. Christopher, Schiminovich David, Seibert Mark, Budavári Tamás, Treyer Marie A., Barlow Tom A., Forster Karl, Friedman Peter G., Morrissey Patrick, et al. (2007), "The UV-Optical Galaxy Color-Magnitude Diagram. I. Basic Properties." *ApJ*, 173, 293–314.

Yang Xiaohu, Mo H. J., van den Bosch Frank C., Pasquali Anna, Li Cheng, and Barden Marco (2007), "Galaxy Groups in the SDSS DR4. I. The Catalog and Basic Properties." *ApJ*, 671, 153–170.

York D. G. et al. (2000), "The Sloan Digital Sky Survey: Technical Summary." *AJ*, 120, 1579–1587.